Towards Sustainable Electrosynthesis of Industrially Valuable Small Molecules

by

Jonathan Francis Melville

B.S. Chemistry
University of California, Berkeley (2016)

Submitted to the Department of Chemistry
in partial fulfillment of the requirements for the degree of

Doctor of Philosophy in Chemistry

at the

MASSACHUSETTS INSTITUTE OF TECHNOLOGY

June 2021

Author .....
Department of Chemistry
May 21, 2021

Certified by .....
Yogesh Surendranath
Paul M. Cook Career Development Associate Professor of Chemistry
Thesis Supervisor

Accepted by .....
Adam P. Willard
Associate Professor of Chemistry
Graduate Officer

This doctoral thesis has been examined by a Committee of the Department of Chemistry as follows:

Professor Daniel Suess .....
Chairman, Thesis Committee
Class of '48 Career Development Assistant Professor of Chemistry

Professor Yogesh Surendranath .....
Thesis Supervisor
Paul M. Cook Career Development Associate Professor of Chemistry

Professor Yuriy Román .....
Member, Thesis Committee
Professor of Chemical Engineering

Towards Sustainable Electrosynthesis of Industrially Valuable Small Molecules

by

Jonathan Francis Melville

Submitted to the Department of Chemistry
on May 21, 2021, in partial fulfillment of the
requirements for the degree of
Doctor of Philosophy in Chemistry

Abstract

The decarbonization of legacy industrial processes calls for substantial advances in our ability to apply sustainably generated electricity as a means of making and breaking arbitrary chemical bonds. The development of such carbon-neutral systems demands the design of efficient and selective electrocatalysts with an eye towards economic viability and industrial operability. In this work, we present three electrochemical processes at varying degrees of practical maturity with theoretical applicability to a zero-carbon future economy:

In **Chapter 2**, we rigorously interrogate the electrolysis of molten condensed phosphate salts to white phosphorus, a valuable specialty chemical currently generated by energy-intensive carbothermal reduction. We demonstrate that the reduction of phosphate to phosphorus occurs near the limit of energetic and atom efficiency, portending future application as a milder and possibly carbon-neutral route for industrial phosphorus synthesis.

In **Chapter 3**, we investigate the electrochemical reduction of nitrogen to ammonia, whose current production is dependent on the reforming of methane. We examine the fundamental challenges intrinsic to this challenging reactivity, and highlight the amplification of catalyst selectivity at elevated pressures, a strategy which is showcased on a novel copper nitride electrode with exceptional selectivity towards nitrogen reduction in aqueous media.

In **Chapter 4**, we discuss electrochemical methane monofunctionalization as a strategy for gas-to-liquid conversion, capable of valorizing methane flare streams economically inaccessible by incumbent industrial chemistries. We devise a process scheme for methane gas-to-liquid electroconversion with capacity for real-world implementation, which maximizes overall carbon efficiency by minimizing distillative overheads.

The development of sustainable processes for generation of energy-dense fuels or valuable refined chemicals is ultimately reliant upon the application of efficient electrocatalysts for selectively employing electrons to rearrange chemical bonds. With this work, we demonstrate the rich potential for electrochemistry to unlock future routes to desirable industrial reactivities.

Thesis Supervisor: Yogesh Surendranath
Title: Paul M. Cook Career Development Associate Professor of Chemistry

Respective Contributions

This thesis contains work that was obtained collaboratively with other researchers at the Massachusetts Institute of Technology (Andrew Licini, Prof. Christopher Hendon, Dr. Matt O'Reilly, and Dr. Patrick Smith) and the MIT Energy Initiative (Randall Field). In particular, the following contributions are noted:

In **Chapter 2**, Andrew Licini designed the molten-salt electrochemical reactor, collected the P_4 in CS_2 ^{31}P NMR spectrum **Figure 2-13**, and collected the graphite counter-electrode gas chromatography data in **Table 2.1**.

In **Chapter 4**, Prof. Christopher Hendon performed DFT studies to calculate bond-dissociation energies of functionalized methane products. Dr. Matt O'Reilly collected the ^{1}H NMR **Figure 4-1** displaying electrochemical methane functionalization by $CoSO_4$. Randall Field calculated all process flow energetic demands.

In **Appendix A**, Dr. Patrick Smith collected all XPS spectra on metal-electroplated graphite electrodes for phosphate reduction.

In **Appendix C**, Randall Field modeled all stream tables and associated process flow diagrams for methane functionalization systems.

Acknowledgments

It occurs to me that there exists in theory some maximum length that is socially acceptable for a thesis acknowledgments section – a length which is, perhaps, drastically exceeded here. For this I make no apology, as the number of persons to whom I owe this degree is, far from a mark of shame, a point of distinct pride.

To my family.

To my mom, Monica Melville, first and foremost. My mom has defined my understanding of family for as long as I've been alive, and for that reason I could not imagine anyone else filling this space, first among the first of my many acknowledgments. More than anything else, my mom taught me to make the world a better place. It is her influence that motivates all of my student activism, advocacy, and care work. More than that, it is her deeply inculcated values – her idealism and environmentalism – that drove me pursue chemistry in the first place. Mom: I love you so much. I would not be who I am today – nor where I am today – were it not for your unequivocal love and relentless support.

To my dad, Navin Melville. My dad has shaped my many eccentricities – my hobbies, interests, quirks, and general affect – more than any other single person. He buried me in Dungeons & Dragons sourcebooks and Isaac Asimov novels, while brainwashing me into thinking that math puzzles were fun and Linux was a good operating system. When I was a kid, I would tell my dad that I was going to grow up and get a PhD, and he would jokingly respond that if I did, he would go back to grad school with me. I suppose that it's now clear that I was serious about grad school even at a young age, but don't worry, Dad, I'm not going to hold you to that old promise – just between you and me, I think grad school would be a suboptimal career decision at this point. Dad: thank you for fostering my creativity and intellectual curiosity and empowering me to pursue my passions. It is because of you that I get to be a person I can be proud of; I can only hope that I will continue to make you proud, too.

To my brother, Dominic Melville. My brother is shrewd and ingenious, and I could not have anticipated how much growing up with him kept me on my toes and motivated my continuous self-education. I am incredibly lucky that, unlike me, he has chosen to take his considerable talents into the field of engineering – because it means I have an excuse not to compete against him intellectually, because it means I won't have to be the designated family IT person, and because it guarantees at least one of us will be employable. Dom: thank you for being a calm voice of reason, for always giving me hardware advice, and for being my brother, through thick and thin. Go Bears!

To my aunt and uncle, Shiamin Melville & Dr. Raj Melville. Thank you so much for taking me under your wings and helping my parents vicariously support me from across the country. Thank you especially for all the times you successfully pried me away from my oh-so-important, can't-possibly-wait research with promises of fancy dinners and complimentary drinks. It turns out I would never regret taking time away from my work to spend with family.

To my uncle, Dr. Prem Melville, who some eight years ago wagered that I would switch majors away from chemistry before finishing my undergraduate studies at Berkeley – thereby

ensuring that I would complete not only my bachelor's degree, but also a doctorate in chemistry, just to win an argument as thoroughly as possible. Prem Uncle: you owe me $20.

And to all my aunties, uncles, cousins, nieces, nephews, and niblings. It has been said that family is our bridge to the past and our link to the future. I can say without question that our past is rich, and our future is bright.

To my friends.

To Leena Yin. Leena is my best friend and it's not even close.[i] She is simply at the top of all of the charts that matter: number of collective ears pierced together (4), number of unprompted care packages sent during the writing of this thesis (3), number of rescued cats to whom I am apparently uncle (2), and number of shared brain cells (1). I cannot count the number of times I have nearly fallen apart throughout this grueling five-year ordeal, only to be picked back up by a timely and extemporaneous phone call or mushily sentimental letter from my best friend, whom I can only presume picked up a subconscious distress call transmitted by our unbreakable rapport through the psychic æther of the universe. Leena: I can't believe how far we have come, and how much we have to look forward to. I don't know how many other ways I can say "thank you for being you". Please give Stella & Po an extra treat from their Uncle Jo.[ii]

To James Connor Gilhula. Connor has been my best chum here at MIT, and there is no doubt in my mind that I would not have reached the end of this arduous journey without his constant support and unconditional friendship, which he provided even when I did not deserve it. Clongus: I will always remember our many late nights toiling away in the Room, practicing high fives, raiding La Verde's, beaning each other with foam balls, substituting butter for creamer, and occasionally even working. What is memory, after all?

To Ai Bui and Davi da Silva. It is exceedingly challenging for me to describe my bond with Ai and Davi without using the phrase 'found family', as if this acknowledgments section were a cheesy AO3 fic. Ai: I am so, so proud of you. When we first met, you were already one of the strongest people I knew, and you have come so far and grown so much since. You are unstoppable, every second of time I have spent with you has been worth it, and I'm so excited for what comes next for you. Davi: what the hell is MIT. I'm glad we both made it out alive to write a juicy tell-all exposé. You're gonna be an amazing doctor. Eat shit :)

To William 'Jaundice' Howland, Lydia 'Beanstown' Pazienza, and Bryan 'Justice' Tang. Thank you all for being my favorite nuclear nonproliferation advocates. I couldn't ask for a better set of armchair epidemiologist drinking buddies. Sorry we Jumanji'ed the planet.

To Raymond Liu, Jessica Beard, Lucy Shen, Maggie Tsai, Giulio Zhou, Sam Alterman, May Hong, Whitney DiMeo, David Gygi, and Emily Thai. Thank you all for being there for me and supporting me through the living hell that is grad school. I could not have done it without friends like you all over the country.

[i] Sorry not sorry, to everyone else reading this.

[ii] Yes, every time you read this.

To my labmates.

To Drs. Anna Wuttig, Sterling Chu, Youngmin Yoon, Megan Jackson, Sahr Khan, Seokjoon Oh, Bing Yan, and Soyoung Kim. You are the brave pioneers that came before me and, out of nothing, carved out the Surendranath Group as I know it. When I came to MIT, I had already decided I would prioritize choosing a lab where the students were friendly, kind, respectful, and happy. You were those students, and I'm beyond grateful for the culture you built which guided me here in the first place.

To Drs. Ryan Bisbey, Michael Pegis, Patrick Smith, and Daniel Bregante, and Profs. Christopher Hendon and Alex Murray. Thank you all for your mentorship, insightful perspective, and guidance, both inside the lab and out of it. I wish you all the best of success in your promising future careers.

To Dr. Corey Kaminsky. I will always treasure our snappy and frequently infuriating repartee. Your hard-earned experience and insightful perspective make you a formidable scientist, and I know the future holds great things for you. Beamtime trips have been a highlight of my PhD, and you have been a highlight of that highlight.

To Alexander 'Sasha' Alabugin. You are immensely clever and perceptive, entertainingly offbeat and nonconformist in all the best ways. One day we will play that game of Microscope.

To Travis Marshall-Roth. I could not have wished for a better officemate. You are talented, hardworking, and brilliant, but more importantly, you are humble, empathetic, and supportive. Never change, and never give up.

To Jaeyune Ryu. You are a true pal and despite your unceasing work ethic, you never hesitated to take time out of your day to help me with my science. You are incredibly modest, so I am sure you will demur, but you are indisputably among the best researchers I know, and certainly an even better drinking buddy.

To Andrew Licini. You are possibly the most kind-hearted person I have ever called friend, and I owe you a debt of gratitude for all of your crucial work underpinning the molten-phosphate project. More than being a good scientist, however, you are a good person. You deserve good things and I know you will find them.

To Onyu Jung, Thejas Wesley, An Chu, Sophia Weng, Wei Lun 'James' Toh, Noah Lewis, Deiaa Harraz, and Kunal Lodaya. You are the future of the group, and with folks like you I have no doubt our future is auspicious. You are all sharp, hardworking, funny, and caring. I know that your research is all going to turn out great, because you are all great scientists. Whenever I needed help, you guys were always there for me, and I know you'll keep supporting and cherishing each other into the future. Be sure to post some absolute bangers on the Twitter account for me.

To my neighbors.

To Rich Swartwout, David Ramsay, Victoria Beja-Glasser & Justin Porter, Dr. Sam & Kay Chevalier, Lauren Stopfer, Erika DeBenedictis, Mary Tellers, Aditya Bhattaru, and Davi da

Silva (again). Through the many GRTs[iii] that came before me, I have learned and lived so much. It is a demanding job and I have only been able to do it for so long because of you. It may be rose-tinted glasses or COVID burnout, but the halcyon days of the 2018-2019 East Campus house team will always be sweetest to me.

To David Ramsay, Dustin Hayden, Hugh Ebdy, Phillip Daniel, Mohammed Toure, Peter Sharpe, and Amanda Fike. To the many GRTs that will come after me, I can only hope that I have helped prepare you in some small way for this beautiful, terrible job. You are all excellent people and I have full faith that with your support and stewardship, EC will rise again like a phoenix, the eternal kingdom that it once was and always will be, a bustling hub of anarchy, counterculture, self-expression, student advocacy, and hand-foot-mouth disease. On second thought, see if you can get rid of the hand-foot-mouth disease.

To Prof. Sandy Alexandre, Prof. Rob Miller, Prof. Eden & Dr. Cristian Medina, Alexandria Clyburn, and Carrie Wicks. A majority of what makes East Campus great is the students, but at some point I figured out that the senior house team – y'all – are the reason EC has been able to *stay* great for so long. It's a thankless job, and one that I feel a vanishingly small group of people have the necessary perspective to properly appreciate. But I've been around long enough, and I have that perspective, and I appreciate it. I've seen the things you people do for these students. I've seen you fight for them, I've seen you fight for us, and I've seen you fight for this community. So thank you: thanks for standing up for our little island, thanks for always looking out for us GRTs and giving us the tools to support our kids, thanks for all the times you had the hard conversations that no one ever wants to have, thanks for all the 3 AM Dean on Call texts, and thanks for the free haircuts. Please never stop fighting to improve this place we all love, while sheltering that spark that makes EC special.

To the East Campus facilities team: Joe, Bobby, Evelina, Jiaro, Oliar, Edgar, Mohammad, Tess, and Balmiro. Thank you for all your hard work holding this ramshackle building together and keeping it livable these many years, an unequivocally herculean feat. Thank you even more for your continuous support and friendship, which in particular kept me sole company for a long many months in Summer 2020. You are collectively the bones of EC, the deep-rooted skeletal system which holds everything together. Without your tireless labor and kind spirits, there would not be an East Campus for me to call home.

To Allysa Allen, Samantha Amey-Gonzalez, Ivan Tadeu Ferreira Antunes Filho, Emile Augustine, Ilani Axelrod-Freed, Avital Baral, Samuel Bruce, Shane Campbell, Emily Caragay, Zawad Chowdhury, Julia Clarke, James Collier, Kenneth Cox, Christian Cruz Matias, Jensen Curtiss, Christian de Weck, Sarah Dohadwala, Barış Ekim, Juan Ferrua, Amanda Fike, Zoe Fisher, Ying Gao, Madeline Garcia, Juan Garcia, Michael Gilbert, Conrad Goffinet, Richard Gong, Colin Greybosh, Emma Griffiths, Maks Groom, Emily Haig, Dana Haig, Sang Eun Han, Madee Haworth, Tomas Herrera, Kristine Hocker, William Hu, Alula Hunsen, Jrew Hutchison, Johnson Huynh, Samuel Ingersoll, Ibuki Iwasaki, Adriana Jacobsen, Isaiah Jeremie, Devin King-Roberts, Kai Kloepfer, Karina Lara, Jonathan Ledet, Ivy Li, Jeffery Li, Yihong Li, Kristie Lino, Emily Liu, Daniel Liu, Alexis Lopez, Carolyn Lu, Elizabeth Martin, Noah McDaniel, Hadrian Merced Hernandez, Jacob Miske, Andi Mitchell,

[iii] Yes, I said 'GRT' and not 'GRA', and I will die on this hill, god dammit. This is because, in my first year as a GRT, one of my residents nicknamed me 'Jort' (i.e. 'Jo-R-T'), a sobriquet I have embraced wholeheartedly ever since. In my third year as a GRT, 'Graduate Resident Tutor' became 'Graduate Resident Advisor', presumably because we never actually did any tutoring – but 'Jora' doesn't have the same ring to it.

Soma Mitra-Behura, Bethany Moore, Quynh Nguyen, Avery Nguyen, Joseph Ntaimo, John Paris, Matisse Peppet, Anthony Polese, Caroline Powers, Suparnamaaya Prasad, Kaitlyn Przydzial, Danielle-Joy Rodriguez, Anthony Roman, Uma Roy, Emma Rutkowski, Sagnik Saha, Hannah Savoldy, J Shelly, Amy Shim, Margaret Shutts, Veronika Silkin, Taylor Sims, Mimi Suarez, Allison Tam, Shoki Taniura, Yanisa Techagumthorn, Jimmy Tran, Christopher Vargas, Brendan Vaughan, Julie Vaughn, Sarah Weidman, Melissa White, Laurel Wright, Christopher Xu, Byron Xu, Chun-Chen Yao, Catherine Yao, Julian Yocum, Hung-Hsun Yu, Jennifer Yu, Sara Zangi, Vera Zarubin, Franklin Zhang, Madeline Zhang, Jingyi Zhao, George Zheng, and Willie Zhu. I have said it a hundred times and I will say it again: I have no doubt in my mind that, twenty years from now, my fondest memories of MIT will be of those I spent with all of you. Luckily for me, you've gifted me with no shortage of memorable events: a plethora of early mornings frying sausages and baking tots for finals breakfast; a disused pump organ hauled across the city and up four flights of stairs; numerous hard-won Green Building Challenges; a trash sack filled with mystery Taco Bell; hundreds of cocoa screams, always on the dot; an ice cream puzzlehunt stretching across Camberville; many a rambunctious dinner at Dumpling House; at least one Hall-Party-That-Shall-Not-Be-Named. Thank you for putting up with my wacky antics and deranged mastery of Google Forms. You are good kids, the best kids, and I can only hope that my tenure on Slugfest has meant to some of you some small fraction of what it has meant to me. I love you all, I am so proud of each and every one of you, and please never hesitate to look me up, reach out, and keep in touch.

To my compatriots.

To AC, AD, AK, AR, AS, AT, BC, BG, BL, CM, CR, DC, DD, EB, GN, HK, JR, KC, KR, LM, LP, MD, MS, MP, NS, NK, PM, PP, PR, TW, TZ, WB, ZM, and everyone else. My work in student activism has shaped my future more than possibly any other aspect of grad school, and for that I must thank you all for helping me realize the unexplored passion that now shapes my future career. Of the many remnants of my five-year tenure at MIT, I have little doubt that the time spent working alongside you has been the most meaningful. You are the best people and your solidarity has been a privilege I will cherish forever.

To my mentors.

To Prof. Jeff Long, Dr. Matt Kapelewski, and the rest of the Long Group at UC Berkeley. Thank you for setting me on the right path and teaching me everything I know, as well as a good number of things I never bothered to learn and therefore to this day do not know. It boggles my mind to imagine how different my life would be had you not chosen to take a lost and clueless undergraduate like me under your wings. I will always hold a special place in my heart for Berkeley, for the College of Chemistry, and for the Long Group, and as long as you keep inviting me to reunion parties I am going to keep showing up.

To Profs. Dan Suess and Yuriy Román. Thank you for your guidance, advocacy, and insight serving on my thesis committee. My life as a graduate student has been eased in part because I am privileged to have a thesis committee and chair that I trust to support and mentor me.

To Prof. Yogi Surendranath. Anyone who has heard me pontificating about what makes for a great academic adviser has heard me talk about Yogi. Although I joined Yogi's group in no small part because of his excellent taste in South Asian catering for recruitment events,[iv] it is his forthright and genuinely caring mode of mentorship that truly sets him apart from the pack. At times in my academic career, I have been cynical of the numerous systemic issues that plague many STEM disciplines – unhealthy work-life balance, a disregard for mental health, a pernicious centering of narratives that too often pushes away marginalized voices. As an adviser, Yogi gives me hope that science can be better, that academia can treat people like human beings, and that a research lab can be successful by bringing together a wonderful group of nerds of all persuasions, motivated as much by each other as by the childlike wonder that enraptured us all with science in the first place. If that is a description of Yogi's group, then Yogi is surely the Alpha Nerd, and the group's idiosyncratic nature is as much a reflection of his approach to science as anything else. Yogi taught me never to let a fear of asking a dumb question keep me from asking a good question. He taught me to ask hard questions, and to not be afraid of doing the difficult work of answering them. I am immensely grateful for his mentoring and scholarship, and I am proud to carry onwards the flame of the Surendranath Group.

[iv] For more information, please refer to `https://masalachaat.wordpress.com/`.

Table of Contents

List of Figures

List of Schemes

List of Tables

List of Abbreviations

AC	alternating current
ADP	adenosine diphosphate
APG	associated petroleum gas
ATP	adenosine triphosphate
BCZYZ	$BaCe_{0.5}Zr_{0.3}Y_{0.16}Zn_{0.04}O_{3-\delta}$
BDE	bond dissociation energy
BE	bulk electrolysis
BMP	Bosch-Meiser process
C_{dl}	double-layer capacitance
CI	current interrupt
CNG	compressed natural gas
CNT	carbon nanotube
COVID-19	coronavirus disease 2019
CV	cyclic voltammetry
DC	direct current
$\Delta G^{\ominus}$	standard-state Gibbs free energy change
ΔH°	standard enthalpy change
DLC	double-layer capacitance
DME	dimethyl ether
DMS	dimethyl sulfate

E_a	activation energy
ECSA	electrochemical surface area
$[eFAP]^-$	tris(pentafluoroethyl) trifluorophosphate
EIS	electrochemical impedance spectroscopy
E°	standard cell potential
EPOC	electrochemical promotion of catalysis
FCP	Frank-Caro process
FE%	Faradaic efficiency
FeFe	iron-iron nitrogenase
FTO	fluorine-doped tin oxide
FTP	Fischer-Tropsch process
GC	gas chromatography
γ-CD	γ-cyclodextrin
GTL	gas-to-liquid
HBP	Haber-Bosch process
HER	hydrogen evolution reaction
HOR	hydrogen oxidation reaction
HTFA	trifluoroacetic acid
ID	inner diameter
LCS	lost carbonate sintering
LNG	liquified natural gas
LSV	linear-sweep voltammogram
MBS	methyl bisulfate
MeCN	acetonitrile
MMO	methane monooxygenase
MoFe	molybdenum-iron nitrogenase
MOR	methane oxidation reaction

$[C_2mpyr]^+$	N-ethyl-N-methylpyrrolidinium
MSA	methylsulfonic acid
MTG	methanol-to-gasoline
NEMCA	non-Faradaic electrochemical modification of catalytic activity
NMR	nuclear magnetic resonance
NP	nanoparticle
NRR	nitrogen reduction reaction
OAL	overall length
OCP	open-circuit potential
OD	outer diameter
OER	oxygen evolution reaction
ORR	oxygen reduction reaction
$[P_{6,6,6,14}]^+$	trihexyl(tetradecyl) phosphonium
PBS	phosphate-buffered saline
PC	propylene carbonate
PDC	phosphorus-derived chemical
PEBCD	poly(N-ethyl-benzene-1,2,4,5-tetracarboxylic diimide)
PFA	perfluoroalkoxy alkane
P_i	inorganic phosphate
PIL	protic ionic liquid
ppm	parts per million
PRR	phosphate reduction reaction
psi	pound-force per square inch
psig	pound-force per square inch gauge
R_{ct}	charge-transfer resistance
RHE	reversible hydrogen electrode
RLS	rate-limiting step

R_u	uncompensated resistance
S10PP	sodium decapolyphosphate
S3MP	sodium trimetaphosphate
S3PP	sodium tripolyphosphate
S4PP	sodium tetrapolyphosphate
sccm	standard cubic centimetres per minute
SDC	samarium-doped ceria
SHE	standard hydrogen electrode
SMR	steam methane reforming
SOP	sodium orthophosphate
TBA	tetra-*n*-butylammonium
TBAOH	tetra-*n*-butylammonium hydroxide
TBATMP	tetra-*n*-butylammonium trimetaphosphate
TPP	triphenylphosphine
VFe	vanadium-iron nitrogenase
WGS	water-gas shift
XPS	x-ray photoelectron spectroscopy

Chapter 1

Introduction

Greenhouse gas emissions, particularly carbon dioxide (CO_2) and methane (CH_4), are the primary drivers of anthropogenic global warming due to increased radiative forcing.[1] As such, international climate targets designed to mitigate the environmental, economic, and sociocultural ramifications of climate change necessarily demand severe reductions of global greenhouse gas emissions. Meeting such benchmarks, such as limiting the degree of mean global temperature rise to 1.5 °C, might require the complete elimination of all anthropogenic CO_2 emissions by as soon as 2040 (an implausibly ambitious goal);[2] milder targets such as 2 °C of mean warming might push this deadline back to 2060, while still entailing a dramatic restructuring of the global energy economy.[3, 4] Despite substantial advances in the field of renewable energy, it is clear that dramatic improvements in our ability to apply sustainably produced electricity to effect desired chemical transformations are needed to achieve full decarbonization within the 21st century.

A core presupposition for a decarbonized global economy is a largely[i] renewable energy sector. Though clearly a herculean undertaking, there is evidence of promising progress towards this goal: in the United States, capacity-weighted average construction costs for so-

[i] Increased use of practices such as afforestation or developing technologies such as carbon capture and storage, or deployment of nuclear power stations, may supplement renewable energy generation in a carbon-neutral economy; however, projected investment in these strategies may be broadly understood to be subsidiary to continued renewable-energy growth in reaching global net-zero emissions.[5–13]

lar photovoltaic systems dropped by 50% from 2013 to 2018,[14] and growth in renewables (particularly solar and wind) is projected to outpace all other energy sources, accounting for nearly 60% of all cumulative capacity additions from 2020 to 2050.[15] China, the world's largest emitter of CO_2, has pledged to reach zero-carbon by 2060,[16], while the United States (the second-largest emitter) has targeted carbon-neutrality by 2050.[17] Achieving these goals would require exceeding even optimistic projections of renewable electricity growth, which estimate that renewables will comprise some 42% of U.S. electricity production by 2050.[15] Nevertheless, there are clear political and economic reasons to believe that sustainably produced electricity will occupy an expanding portion of global energy production in the coming decades, as the cost of renewable electricity continues to decrease[18] and public pressure for meaningful climate action increases.[19–21]

Despite this, a fully renewable global energy sector constitutes a *necessary but insufficient* precondition for achieving a zero-emission economy. A substantial proportion of anthropogenic carbon emissions originate from sectors that are "difficult to decarbonize", including load-following electricity (12% of global CO_2 emissions), iron & steel production (5% of global emissions), cement production (4%), shipping (3%), aviation (2%), and long-distance road transport (1%).[22] While, in a renewable-powered economy, the decarbonization of some 70% of emissions sources (such as heating, lighting, and motor vehicles) is as simple as electrification of these processes, *deep decarbonization* of the remaining 30% of emissions sources – from industrial processes to long-haul transportation to reliable load-following electricity generation – will necessitate groundbreaking advances in our ability to bring low-cost sustainable electricity to bear as a means of selectively making and breaking chemical bonds.

This may be broadly understood through the relationships depicted in **Figure 1-1**. While the nascent renewable economy is increasingly providing zero-carbon routes to performing desirable work (for example, in the increasing ubiquity of electric vehicles), commercial application of renewable energy to directly generate value-added products or energy-dense chemical fuels will require paradigm shifts in our understanding of electrochemistry.

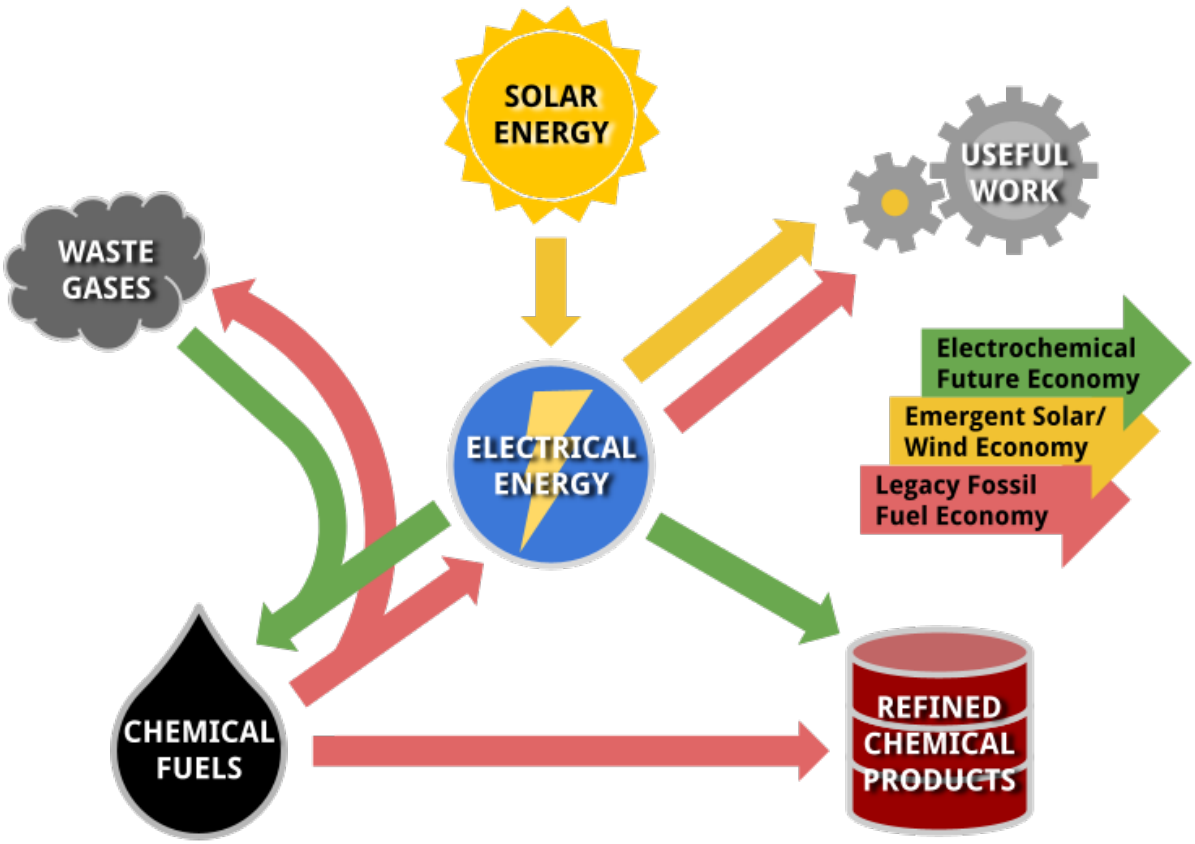

Figure 1-1. Relational diagram of energy inputs and outputs in the legacy hydrocarbon economy, the nascent renewable economy, and a hypothetical future electrochemical economy.

The incumbent routes for generation of high-quality steel or metallurgical-grade silicon are highly representative of the scientific challenge in decarbonizing industries. Both are resources highly critical for any developed economy: the former used in vast quantities for all manner of construction, the latter necessary not only for high-tech semiconductors but also (ironically) the burgeoning photovoltaic industry. Both materials are produced by processes that are fundamentally *carbothermal*, relying upon the action of elemental carbon (in the form of coke) as a chemical reducing agent at temperatures well in excess of 1000 °C. It is no coincidence that China accounted for 68% of all global silicon production[23] and 53% of all global steel production in 2020,[24] the latter in particular singlehandedly comprising some 15% of the nation's CO_2 footprint.[25–29] In principle, these are simple electron-transfer processes; there is no fundamental reason why carbon must be used as the

reductant (necessarily entailing the emission of CO_2) instead of the direct electrochemical application of reducing electrons.[ii] In practice, while the electrosynthesis of iron [37, 38] and silicon [39, 40] are active research thrusts, our understanding of the underlying electrochemistry has yet to evolve to the point where such processes can compete economically with incumbent coal-fired carbothermic chemistry, even though raw electrons in the form of electricity are among the cheapest available industrial reducing agents (**Table 1.1**).

Reagent	**Cost** ($/mol)
electrons[iii]	0.006
H_2	0.006
O_2	0.006
H_2O_2	0.038
Na metal	0.075
Mg metal	0.079
Zn metal	0.086
N_2H_4	0.14
$Na_2S_2O_4$	0.25
$Na_2Cr_2O_7$	0.39
$KMnO_4$	0.45
$NaBH_4$	1.70
$SnCl_2$	2.80

Table 1.1. Cost of industrial redox agents, in US dollars per mole of electron-equivalents. Adapted from Ullman's Encyclopedia of Industrial Chemistry, 7th ed.[41]

Meanwhile, the electrochemical conversion of waste gases to chemical fuels (for example,

[ii] Indeed, this is functionally how aluminum is made industrially today via the Hall-Héroult process.[30–32] At its core, the reason why aluminum is generated by electrochemical methods where iron and silicon are produced carbothermally may be understood by looking at their standard reduction potentials. Where the reduction $Fe_2O_3 + 3\,H_2O + 6\,e^- \longrightarrow Fe + 6\,OH^-$ occurs at $E^\circ = -0.89\,V$ vs. reversible hydrogen electrode (RHE) and $SiO_2 + 4\,H^+ + 4\,e^- \longrightarrow Si + 2\,H_2O$ occurs at $E^\circ = -0.91\,V$ vs. RHE, the reduction of aluminum $Al^{3+} + 3\,e^- \longrightarrow Al$ does not occur until $E^\circ = -1.662\,V$! This is why the first recorded 'smelting' of aluminum metal did not occur until 1824, when Hans Ørsted (and subsequently Friedrich Wöhler) bent potassium amalgam ($E^\circ = -2.931\,V$) to the task.[33] For several decades, these exotic conditions meant aluminum was rarer and more expensive than gold – indeed, the French emperor Napoleon III apocryphally ordered royal jewelry and cutlery forged of the metal.[34] This changed somewhat in 1859, when Étienne Henry Sainte-Claire Deville reproduced Wöhler's process with cheaper sodium metal ($E^\circ = -2.71\,V$), bringing the price of aluminum down to about that of silver.[35] Even still, aluminum was considered a precious enough metal that an aluminum cap was chosen to top the Washington Monument when it was completed in 1884.[36] Two years later, Hall and Héroult independently discovered their eponymous process and, with the help for Carl Bayer's process for bauxite refining, globally cratered the aluminum market in less than a decade. As of 2021, the price of silver is practically unchanged from 1884, at about $26/oz (adjusting for inflation). The price of aluminum is about $0.07/oz. *See also:* footnote *vi* on page 54.

[iii] At a typical industrial electricity pricing of 0.06 $/kWh @ 3.5 V.

the reduction of carbon dioxide to hydrocarbons) may serve to address two fundamental flaws in the development of grid-scale renewable-energy systems: intermittancy and availability. The specific energy of such fuels is orders of magnitude greater than competing energy storage techniques, a fact which explains almost singlehandedly the incredible inertia of the fossil fuel economy. By storing excess electrical energy in chemical bonds, the easily transported fuels can be readily provided for as-needed use, thereby generating reliable load-following electricity via processes compatible with the legacy hydrocarbon economy. In conjunction with this, electrochemical processes capable of mediating the oxidation of chemical fuels directly into waste gases and electrical energy (i.e., fuel cells) may obviate the need for messy combustion entirely.[42–45]

In this work, we present three electrochemical processes at varying degrees of intellectual and practical maturity with hypothetical future application in a zero-carbon future economy:

In **Chapter 2**, we rigorously interrogate for the first time the electrolysis of molten condensed phosphate salts to elemental phosphorus, a valuable industrial product and chemical precursor which is currently generated by carbothermal reduction. We demonstrate that the reduction of phosphate to white phosphorus occurs near the limits of thermodynamic, electrokinetic, and atom efficiency, portending future application as a milder and potentially carbon-neutral route towards the generation of this ubiquitous specialty chemical.

In **Chapter 3**, we investigate the electrochemical reduction of nitrogen to ammonia, a crucial commodity chemical for fertilizer production with further potential applications as a hydrogen-dense chemical fuel. We discuss the fundamental challenges that continue to stymie advancements in this storied field, and highlight in particular the potential for elevated pressures of reaction to amplify catalyst selectivity. We showcase this strategy on a novel copper nitride electrode with exceptional selectivity towards nitrogen reduction in aqueous media, thereby presenting conceivable new strategies towards future electrocatalyst systems with eventual potential for practical application.

Finally, in **Chapter 4** we discuss electrochemical routes for selective methane monofunc-

tionalization, with an eye towards valorizing flared natural gas streams by conversion into marketable liquid fuels. We investigate the chemical feasibility of multiple product separation strategies from an electrochemical reactor, and construct closed flow-stream analyses to assess the economic viability of these product separations strategies. Ultimately, we present a chemical process scheme for methane gas-to-liquid electrofunctionalization with potential for real-world implementation which aims to minimize distillative overheads in order to maximize the overall carbon efficiency of the system.

The development of sustainable processes for generation of energy-dense fuels or valuable refined chemicals is ultimately reliant upon the application of efficient electrocatalysts for selectively employing electrons to rearrange chemical bonds. This can take the form of electrochemical alternatives to legacy carbothermal processes, alternative routes to generating valuable fuels or chemicals from ubiquitous reagents, or novel schemes for applying existing electrocatalysts to valorize wasted process streams. Collectively, these works demonstrate the rich potential for electrochemistry to unlock future routes to desirable industrial reactivities.

References

[1] IPCC, *Climate Change 2013 - The Physical Science Basis: Working Group I Contribution to the Fifth Assessment Report of the Intergovernmental Panel on Climate Change*; IPCC Assessment Report 5, 2014.

[2] IPCC, *Global Warming of 1.5°C. An IPCC Special Report on the Impacts of Global Warming of 1.5°C above Pre-Industrial Levels and Related Global Greenhouse Gas Emission Pathways, in the Context of Strengthening the Global Response to the Threat of Climate Change, Sustainable Development, and Efforts to Eradicate Poverty*; IPCC Special Report, 2018.

[3] Rogelj, J.; Schaeffer, M.; Meinshausen, M.; Knutti, R.; Alcamo, J.; Riahi, K.; Hare, W. *Environ. Res. Lett.* **2015**, *10*, 105007.

[4] Matthews, H. D.; Caldeira, K. *Geophys. Res. Lett.* **2008**, *35*.

[5] Gabrielli, P.; Gazzani, M.; Mazzotti, M. *Ind. Eng. Chem. Res.* **2020**, *59*, 7033–7045.

[6] Rubin, E. S.; Mantripragada, H.; Marks, A.; Versteeg, P.; Kitchin, J. *Prog. Energy Combust. Sci.* **2012**, *38*, 630–671.

[7] Jones, W. D. *J. Am. Chem. Soc.* **2020**, *142*, 4955–4957.

[8] van Vuuren, D. P.; Deetman, S.; van Vliet, J.; van den Berg, M.; van Ruijven, B. J.; Koelbl, B. *Clim. Change* **2013**, *118*, 15–27.

[9] Kheshgi, H.; de Coninck, H.; Kessels, J. *Mitig. Adapt. Strateg. Glob. Change.* **2012**, *17*, 563–567.

[10] Rhodes, J. S.; Keith, D. W. *Clim. Change* **2008**, *87*, 321–328.

[11] Smith, P.; Porter, J. R. *Glob. Change Biol. Bioenergy* **2018**, *10*, 428–431.

[12] Fajardy, M.; Köberle, A.; Mac Dowell, N.; Fantuzzi, A. *BECCS Deployment: A Reality Check*; Briefing Paper 28, 2018.

[13] Terlouw, T.; Bauer, C.; Rosa, L.; Mazzotti, M. *Energy Environ. Sci.* **2021**, *14*, 1701–1721.

[14] U. S. Energy Information Administration, *A Guide to EIA Electric Power Data*; 2018; p 18.

[15] U. S. Energy Information Administration, *Annual Energy Outlook 2021 with Projections to 2050*; 2021.

[16] Mallapaty, S. *Nature* **2020**, *586*, 482–483.

[17] Plumer, B. To Cut Emissions to Zero, U.S. Needs to Make Big Changes in Next 10 Years. 2020.

[18] U. S. Solar Energy Technologies Office, *Solar Energy Technologies Office: SunShot 2030 Goals*; 2016.

[19] Steentjes, K.; Pidgeon, N.; Poortinga, W.; Corner, A.; Arnold, A.; Böhm, G.; Poumadère, M.; Ruddat, M.; Scheer, D.; Tvinnereim, E. *European Perceptions of Climate Change: Topline Findings of a Survey Conducted in Four European Countries in 2016.*; 2017.

[20] Pew Research Center, Environmental Protection Rises on the Public's Policy Agenda As Economic Concerns Recede. 2020.

[21] Marquart-Pyatt, S. T.; Qian, H.; Houser, M. K.; McCright, A. M. *Int. J. Sociol.* **2019**, *49*, 1–26.

[22] Davis, S. J. et al. *Science* **2018**, *360*.

[23] Schnebele, E. K. *Silicon Commodities Report*; USGS Mineral Commodity Summaries 2021, 2021.

[24] World Steel Association, *2020 Global Crude Steel Production*; Global Crude Steel Production 2020, 2021.

[25] Lee, A. China Mulls Tax Overhaul for Steel in Push to Meet Green Goals. 2021.

[26] Chow, M.; Zhang, E. China's Crude Steel Output to Peak around 2025 – Govt Consultancy. 2021.

[27] Zheng, X.; Lu, Y.; Yuan, J.; Baninla, Y.; Zhang, S.; Stenseth, N. C.; Hessen, D. O.; Tian, H.; Obersteiner, M.; Chen, D. *Proc. Nat. Acad. Sci.* **2020**, *117*, 29–36.

[28] Yue, D.; You, F.; Darling, S. B. *Sol. Energy* **2014**, *105*, 669–678.

[29] Brandt, B.; Kletzer, E.; Pilz, H.; Hadzhiyska, D.; Seizov, P. *Silicon-Chemistry Carbon Balance: An Assessment of Greenhouse Gas Emissions and Reductions*; 2012.

[30] Haupin, W. E. *J. Chem. Educ.* **1983**, *60*, 279.

[31] Prasad, S. *J. Braz. Chem. Soc.* **2000**, *11*, 245–251.

[32] Frank, W. B.; Haupin, W. E.; Vogt, H.; Bruno, M.; Thonstad, J.; Dawless, R. K.; Kvande, H.; Taiwo, O. A. *Ullmann's Encyclopedia of Industrial Chemistry*; Wiley-VCH, 2009.

[33] Wöhler, F. *Ann. Phys. (Berl.)* **1827**, *87*, 146–161.

[34] Venetski, S. *Metallurgist* **1969**, *13*, 451–453.

[35] Deville, H. S.-C. *De l'aluminium: ses propriétés, sa fabrication et ses applications*; Mallet-Bachelier, 1859.

[36] Binczewski, G. J. *JOM* **1995**, *47*, 20–25.

[37] Licht, S.; Wu, H. *J. Phys. Chem. C* **2011**, *115*, 25138–25147.

[38] Li, H. *Int. J. Electrochem. Sci.* **2019**, *14*, 11267–11278.

[39] Dong, Y.; Slade, T.; Stolt, M. J.; Li, L.; Girard, S. N.; Mai, L.; Jin, S. *Angew. Chem.* **2017**, *129*, 14645–14649.

[40] Nohira, T.; Yasuda, K.; Ito, Y. *Nat. Mater.* **2003**, *2*, 397–401.

[41] Wendt, H.; Vogt, H.; Kreysa, G.; Kolb, D. M.; Engelmann, G. E.; Ziegler, J. C.; Goldacker, H.; Jüttner, K.; Galla, U.; Schmieder, H.; Steckhan, E. *Ullmann's Encyclopedia of Industrial Chemistry*, seventh ed.; Wiley-VCH, 2003.

[42] Evans, A.; Strezov, V.; Evans, T. J. *Renew. Sust. Energy Rev.* **2012**, *16*, 4141–4147.

[43] Olabi, A. G. *Energy* **2017**, *136*, 1–6.

[44] Castillo, A.; Gayme, D. F. *Energy Convers. Manag.* **2014**, *87*, 885–894.

[45] Ould Amrouche, S.; Rekioua, D.; Rekioua, T.; Bacha, S. *Int. J. Hydrog. Energy* **2016**, *41*, 20914–20927.

Chapter 2

Highly Efficient Electrosynthesis of White Phosphorus from Molten Condensed Phosphate Salts

Contents

2.1 Introduction

Elemental white phosphorus (P_4) is a crucial feedstock for the multibillion-dollar phosphorus-derived chemical (PDC) industry, spanning everything from herbicides to food additives. Currently, industrial P_4 production is gated by the infrastructurally demanding reduction of phosphate rock by carbon coke in an arc furnace at temperatures of up to 1500 °C. The electrochemical reduction of phosphate salts presents a promising alternative for white phosphorus production scalable for point-of-use manufacture; however, this process has never been rigorously studied, owing to systemic complexities intrinsic to the exotic conditions necessary for such reactivity. Through the application of cutting-edge cell design techniques operating at the limits of practicable laboratory-scale electroanalysis, we interrogate this process for the first time, revealing a highly efficient and potentially carbon-neutral replacement for industrial phosphorus production under considerably milder conditions than the incumbent carbothermal process.

2.1.1 The Global Role of Phosphates

Of the major elements that govern the reproduction and growth of most organisms, phosphorus is notable in the aeonian length of its biogeochemical cycle. Unlike most other biogenic elements such as nitrogen, carbon, or sulfur, natural phosphorus compounds do not exist in the gas phase, and as such, atmospheric equilibration of ecological phosphorus is practically nonexistent. Rather, environmental phosphorus exists solely in the solid or aqueous phases, as phosphate rock or dissolved ocean phosphates, respectively.[1] While the erosion and runoff of terrestrial phosphate rock to soluble phosphates is a comparatively rapid process, occurring over the lifespan of individual plants and animals, the converse process – that of soluble phosphate sedimentation and lithification – occurs only on a geologic timescale, entailing millions of years of diagenesis and tectonic uplift to regenerate new phosphate rock ready to be weathered anew.[2] As a result, phosphorus exists as a limiting nutrient for many organ-

isms, especially plants, and the ecological carrying capacity of these species is inextricably linked to the equilibrium of the phosphorus cycle and the bioavailability of phosphorus.[3–6]

It is for these reasons that the application of external phosphates, whether artificially or naturally generated, is closely tied to the history of human agriculture. Phosphate-rich mud and sewage have been applied as fertilizers for millennia, and guano was a primary source for agricultural phosphates for roughly a century[i] following the dawn of the Industrial Revolution and prior to the development of processes for artificial phosphate production. These obsoleting processes – the wet process for phosphate production, and the Haber and Ostwald processes for nitrate production – have been called "detonators of the population explosion" for their role in underpinning crop productivities capable of sustaining previously unthinkable human populations.[12–15]

These artificial processes for converting phosphate rock to soluble phosphates also have had the unintended consequence of drastically accelerating the depletion of mineralized phosphate deposits to dissolved ocean phosphates, constituting an obliteration of the natural phosphorus cycle. As a result, phosphate rock is functionally a nonrenewable resource, and much like guano before it, it will eventually run out; estimates for 'peak phosphorus' range from 2030 to 2300.[16] While the precise timescale of phosphorus depletion remains hotly debated, it is clear that the future will demand new methodologies for effecting conversions of phosphate species. In the short term, new, efficient routes are needed to streamline existing phosphorus refining processes, as global demand for phosphorus increases every year. In the

[i] Guano in particular was a strategically crucial resource for the entire 19th century due to its high content of phosphates and nitrates, valuable not just as a fertilizer but as an important source of saltpetre for gunpowder. The mining and processing of guano is therefore central to the histories of many South American, Caribbean, and Pacific Island countries throughout the 1800s, as European powers and the United States struggled to exert control over regions of guano production. Though occasionally manifesting as colonial autarky, epitomized in Peru's several-decade 'Guano Era', imperialism and exploitation are fundamental throughlines of the historical guano trade, from the use of enslaved African and blackbirded indigenous labour in the dangerous process of guano mining, to the Spanish-South American 'Chincha Islands War' (that ended the Peruvian Guano Era), to the annexation by the United States of nearly one hundred 'guano islands' in the Pacific and Caribbean under the Guano Islands Act of 1856. Even as the advent of processes for generating artificial nitrates and phosphates in the early 20th century cratered international demand for guano, the environmental ramifications of the guano trade linger to this day, such as in island nations like Kiribati and Nauru where over 80% of land area was strip-mined for guano, inducing catastrophic ecosystem collapse.[7–11]

long term, processes capable of concentrating and replenishing bioavailable phosphorus from oceanic sinks are necessary in order to close the phosphorus cycle on a human timescale, which will necessarily require substantial advances in the field of phosphorus chemistry.[17]

2.1.2 Industrial Methods for Processing Phosphate

Contextualized by this history, the processing of raw phosphate rock around the globe represents a $50 billion-dollar annual industry, a figure which comprises the mining of over 250 million tons of phosphorite each year as well as the summary processing of this material into fertilizers and other PDCs. By mass, the overwhelming majority (approximately 95%) of this phosphate is refined through the so-called *wet process* into phosphoric acid (H_3PO_4) for use in fertilizers, to the tune of 90 million tons of phosphoric acid per year. However, while the annual production of 1 million tons of elemental P_4 from phosphate rock via the *thermal process* represents a comparatively small fraction of all phosphorus processing by mass, it occupies an outsize proportion of the financial footprint of the phosphorus industry, representing some $12.5 billion dollars of the $50 billion-dollar industry. As depicted in **Figure 2-1**, this figure encompasses the production of food-grade phosphate additives, ubiquitous chemical reagents, various materials additives and stabilizers, as well as an assortment of herbicides, insecticides, rodenticides, and other fumigants.[12, 18, 19]

2.1.2.1 The Wet Process

In its most basic formulation, the wet process relies upon the treatment of phosphate rock – typified here as calcium fluorophosphate ($Ca_5(PO_4)_3F$, also known as fluorapatite) – with sulfuric acid, producing phosphoric acid, calcium sulfate dihydrate ($CaSO_4 \cdot 2\,H_2O$, more commonly known as gypsum), and hydrogen fluoride (**Equation 2.1**). The insoluble gypsum is readily filtered off with other particulates such as silica (which will react with any produced HF to precipitate sodium fluorosilicate, Na_2SiF_6), producing an outflow stream of aqueous phosphoric acid, at dilutions ranging from 35% to 70% H_3PO_4. This phosphoric acid is then

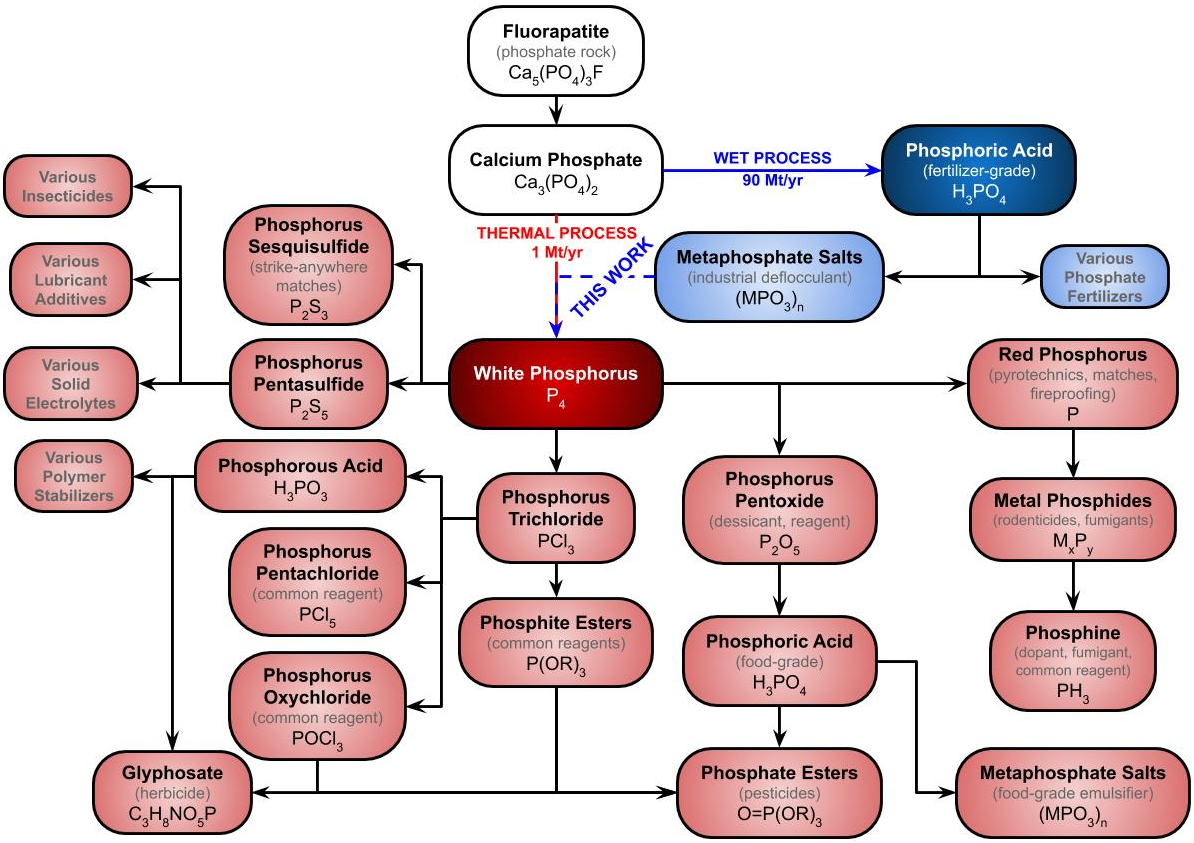

Figure 2-1. Chemical products map of phosphorus-derived chemicals industry.

concentrated up to the desired formulation by evaporation.

$$\mathrm{Ca_5(PO_4)_3F + 5\,H_2SO_4 + 10\,H_2O \longrightarrow 3\,H_3PO_4 + 5\,CaSO_4 \cdot 2\,H_2O + HF} \qquad (2.1)$$

While cheap and efficient, the wet process contains no separative stages by which insoluble impurities might be removed. As a result, virtually all solubilizable trace metal impurities in the source phosphate rock are transmitted to the final phosphoric acid product. Wet-process H_3PO_4 may vary wildly in color from green to brown due to concentrations of ions such as Na^+, Mg^{2+}, Ca^{2+}, Al^{3+}, Fe^{2+}, and Fe^{3+} up to several percent, and (depending on the origin of the raw phosphate rock) trace heavy metal contaminants such as Cd^{2+}, Pb^{4+}, or As^{3+} may be present in concentrations as high as 150 parts per million (ppm).[20–23]

For this reason, while wet-process phosphoric acid is considered an acceptable precursor for fertilizers and some industrial applications, it is not appropriate for human consumption or specialty chemical production; rather, high-purity H_3PO_4 for these purposes is synthesized via elemental white phosphorus from the thermal process (*vide infra*). Furthermore, while the presence of toxic heavy metals in wet-process phosphoric acid has long been deemed to be below the level of human risk, increasingly stringent restrictions, e.g. on cadmium content in fertilizers sold within the European Union, may provoke assessment of further routes to remediation of wet-process phosphoric acid, or perhaps alternative routes entirely. [24, 25]

2.1.2.2 The Thermal Process

By contrast, the thermal process (sometimes called the Wöhler process, pictured in **Figure 2-2**) produces extremely high-purity white phosphorus, owing primarily to the intrinsic separations process that occurs as molecular P_4 is vaporized and recondensed in a product stream. As seen in **Equation 2.2**, this reaction consumes calcium phosphate, silicon dioxide, and elemental carbon (in the form of coke) and produces carbon monoxide and calcium

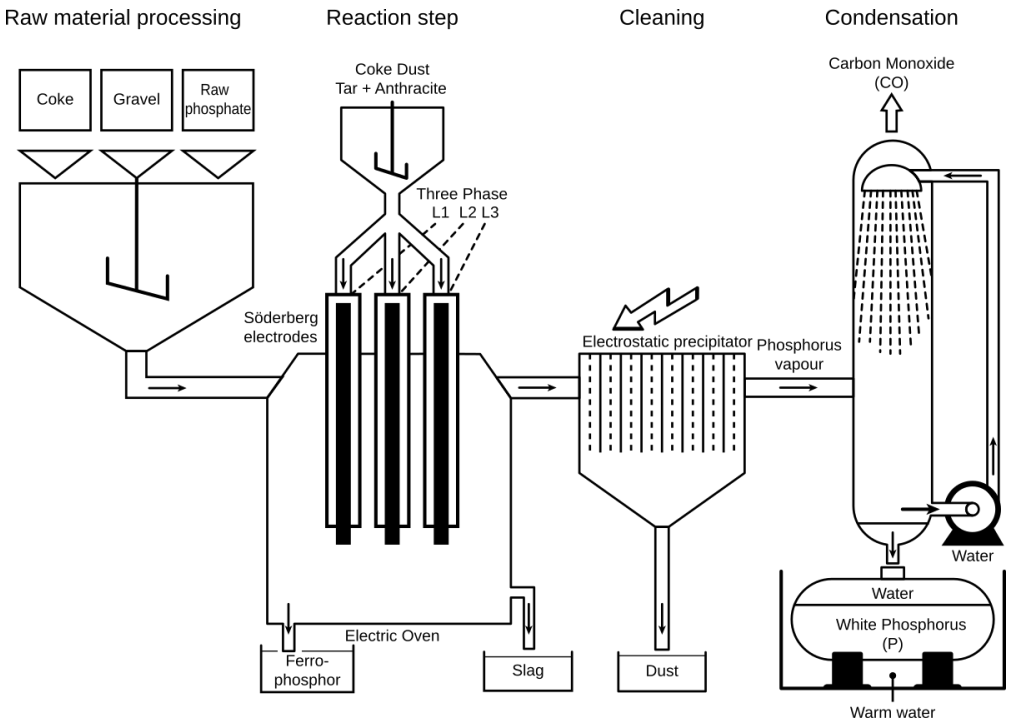

Figure 2-2. Diagram of thermal process P_4 production plant. Adapted with permission from *Phosphorus Production* by Vollrath Hopp.[26]

silicate in addition to P_4.[ii]

$$2\,Ca_3(PO_4)_2 + 6\,SiO_2 + 10\,C \xrightarrow[1500\ ^\circ C]{\text{arc furnace}} 6\,CaSiO_3 + 10\,CO + P_4 \tag{2.2}$$

The Arc Furnace The most notable aspect of the thermal process is indisputably the almost inconceivably high temperature of reaction, generally ranging from 1400-1500 °C. Such temperatures are necessary to soften the reactant fluorapatite (MP 1660 °C) and silica (MP 1710 °C) to the point where they can be chemically reduced by coke. These temperatures are accessed through the use of an arc furnace, in which three coal-tar "Söderberg" electrodes are extruded into a reactor melt while passing currents in excess of 60 kA. These extreme currents, corresponding to areal densities as high as $5\,A{\cdot}cm^{-2}$, produce electric arcs

[ii] For the purposes of simplicity, the full reaction from calcium fluorophosphate is omitted here. While a naïve analysis of the role of fluoride might suggest the formation of SiF_4 gas, this reaction only occurs to a fraction of its theoretical stoichiometry, with 80-90% of fluoride equivalents retained as fluorosilicates in the calcium slag. While the potential value of this byproduct stream is realized in some industrial layouts, by neutralization to pure sodium fluorosilicate (Na_2SiF_6) for water fluoridation, commercialization of this side reaction is by and large considered unreliable and unnecessary.

that are capable of reaching temperatures as high as 3000 °C through Ohmic heating. It is this intense process that contributes greatly to the net furnace power demand, which typically ranges from 50 MW to 70 MW. Of this power demand, only a minority (approximately 45%) is directly consumed by the desired process of P_4 generation; electrical, radiative, and cooling losses altogether account for another 15%, while a full 40% of the reactor's energy usage is depleted by the heat content of the silicate slag and waste gases, as well as any undesired products such as ferrophosphorus. Despite the considerable inefficiencies induced by the heat content of the slag, attempts to eliminate this sunk cost have thus far remained unsuccessful, and it is generally regarded as an unsolved problem in the field.[27]

Carbon Monoxide as Terminal Reductant As a redox reaction in which P^{V} is formally reduced to $P^{(0)}$, the role of carbon coke as a chemical reducing agent also warrants further examination. As an electron source, each $C^{(0)}$ atom possesses four valence electrons available for reducing action before it reaches its stable C^{IV} closed-shell configuration, typically in the form of carbon dioxide, CO_2. It is noteworthy, then, that the thermal process as previously formulated only permits the formation of carbon monoxide (CO), representing a two-electron oxidation from $C^{(0)}$ to C^{II}; the evolved monoxide must then be further burned off in to produce the terminal carbon dioxide. This constraint arises due to the oxidative instability of CO_2 relative to P_4 at temperatures above 650 °C; CO is the only oxocarbon sufficiently inert to phosphorus to enable coexistence in a gaseous product stream. As a direct result, the reaction stoichiometry of carbon is twice what a naïve electron-counting might suggest, functionally doubling the carbon footprint of the thermal process owing solely to the inability for this chemical redox process to effectively separate the oxidative and reduced reaction products.[27–30]

The Role of Silicon Dioxide Silicon dioxide, too, plays a critical function that justifies its disproportionate contribution to the substantial inefficiencies of the thermal process. As a source of phosphorus, the orthophosphate ion PO_4^{3-} is enriched in both negative charge

and oxygen atoms; correspondingly, any process that liberates neutral elemental phosphorus species must also expel anionic oxygen equivalents – oxide ions – due to simple principles of atom and charge conservation. In this framework, silicon dioxide is an *oxide acceptor* – absorbing produced O^{2-} through the formation of metasilicate ions, corresponding to a simple stoichiometry $SiO_2 + O^{2-} \longrightarrow {SiO_3}^{2-}$. Precipitating with calcium as $CaSiO_3$, this partial reaction is the primary driver of slag formation in the thermal process, to the tune of 7.7 tons of slag per ton of produced P_4. In addition to the additional infrastructural complexities entailed by slag separation and processing, the heat content of this material alone is responsible for some 30% of energy consumption by the overall process.[27, 29]

2.2 Results and Discussion

2.2.1 System Design for High-Temperature Electroanalysis

The electrolysis of molten phosphate salts presents an attractive route to addressing many of these issues simultaneously. Condensed phosphate species such as sodium trimetaphosphate ($[NaPO_3]_3$; MP 628 °C) are cheap, synthetically accessible from wet-process phosphoric acid, and electrochemically active at far milder temperatures than that of the thermal-process arc furnace.[iii] Electrochemical methods are inherently amenable to spatial separation of cathodic and anodic half-reactions, allowing for the production of oxidative products such as CO_2 or O_2 that would react with P_4 in a non-separated setup. Finally, condensed phosphate species such as metaphosphates are themselves intrinsic oxide acceptors through their phosphoryl anhydride linkages, which cleave to terminal orthophosphates in accordance with the stoichiometry ${PO_3}^- + O^{2-} \longrightarrow {PO_4}^{3-}$. As pictured in **Scheme 2.1**, these phosphoryl anhydride linkages can then be replenished by the addition and subsequent dehydration of phosphoric acid, in net effecting the electrolysis of phosphoric acid to white phospho-

[iii] The minimum temperature of reaction may be further reduced through the use of eutectic solutions; a 64:36 mol:mol mixture of $LiPO_3$ and KPO_3 exhibits melt onset at 518 °C,[31] well within the capabilities of concentrated solar thermal energy collectors.[32]

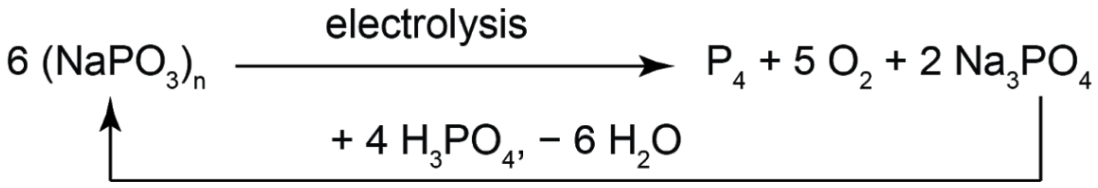

Scheme 2.1. Electrolysis of sodium metaphosphate.

rus, oxygen, and water (**Equation 2.3**). In this manner, valuable P_4 might be accessed in a mild, potentially carbon-neutral process from wet-process phosphoric acid, thereby bypassing the thermal process entirely.

$$4\,H_3PO_4 \longrightarrow P_4 + 5\,O_2 + 6\,H_2O \tag{2.3}$$

Setting aside the non-redox dehydration reaction, this process can, like all electrochemical reactions, be split into anodic and cathodic half-reactions, corresponding to the oxidation of O^{2-} to molecular O_2 (**Equation 2.4**) and the reduction of $PO_3{}^-$ to P_4 (**Equation 2.5**).

$$2\,O^{2-} \longrightarrow O_2 + 4\,e^- \tag{2.4}$$

$$4\,PO_3{}^- + 20\,e^- \longrightarrow P_4 + 12\,O^{2-} \tag{2.5}$$

Being the fundamental reaction by which P^V is reduced to $P^{(0)}$, this latter half-reaction, henceforth phosphate reduction reaction (PRR), is of central and irreplaceable importance to any P_4 electrosynthesis from phosphate salts. Although the first record of this reduction dates back to 1931, and electrochemistry in condensed phosphate melts briefly sustained a small research community in the late 1960s–early 1970s,[iv] these literature reports do not detail the efficiency or selectivity of the process. This is in large part due to the systemic complexities intrinsic to electroanalysis under the extreme conditions of reaction, as well as the highly

[iv] While some reports deal solely with the electrolysis of metaphosphate ions, several others are more concerned with the anodic reaction of oxygen evolution or the application of these melts as a supporting electrolyte, in large part due to the ability of these highly oxidizing media to dissolve most metal oxides – from aluminum to uranium.[31, 33] *See also:* footnote *vi* on page 54.

sensitive nature of the pyrophoric P_4 product. Revisiting this exotic system for the first time in half a century and applying modern principles of electrochemical reactor design and analysis, we quantitate the near-perfect thermodynamic and kinetic efficiencies of PRR, and illuminate the key role of phosphoryl anhydride linkages in promoting this reactivity.[31, 33–41]

2.2.1.1 Reactor Design

An electrochemical reactor (**Figure 2-3**) was designed from the ground up to accommodate the electroanalysis of a molten-salt system while maintaining separation of cathodic and anodic gas flowstreams. The main reactor body consisted of a closed-end alumina tube, to which a machined stainless-steel cap with four Swagelok™ Ultra-Torr® fittings could be attached. These fittings, as well as the junction between the reactor head and body, were sealed with DuPont™ Kalrez® perfluoroelastomer o-rings (temperature rated to 325 °C). Of the four fittings, three (of $\frac{1}{4}$" diameter) held alumina-sheathed electrodes, while the remainder (of $\frac{3}{4}$" diameter) held the isolated counter compartment and electrode (*vide infra*).

Crucible Selection The bottom of the electrochemical reactor contained a conical glassy carbon electrode (60 mL, 52 mm outer diameter (OD), part #39006KT from Alfa Aesar), so chosen for its inertness to the metaphosphate melt and the temperatures of reaction while under inert atmosphere. Between experiments, the crucible was polished with 800 grit sandpaper and an alumina powder slurry, then rinsed with reagent grade water (Millipore Type 1, 18.2 MΩ·cm resistivity), thereby ensuring that the fused melts could be easily separated from the crucible post-reaction.

Counter Compartment For all experiments performed in this document, the counter compartment consisted of a single-bore alumina tube ($\frac{3}{4}$" OD, $\frac{1}{2}$" inner diameter (ID), 18" overall length (OAL), part #AL-T-N3/4-N1/2-18 by AdValue Technologies). Following the conclusion of these experiments, it was discovered that a clear fused quartz tube (19 mm OD, 15 mm ID, 1219 mm OAL, part #FQ-T-19-15-4 by AdValue Technologies, subsequently

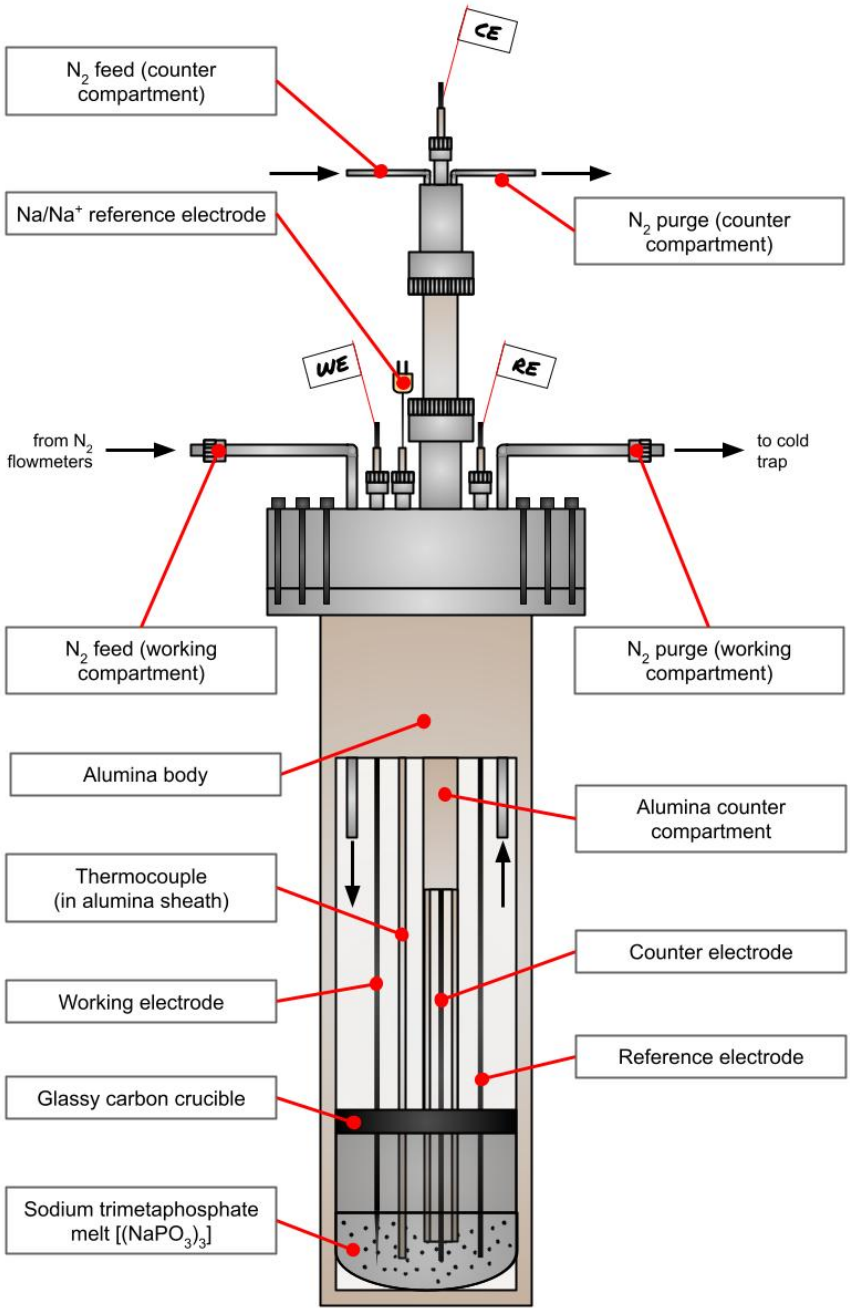

Figure 2-3. Schematic of third-generation cell for high-temperature molten-salt electroanalysis.

cut into 16"-long segments) was better suited to this task, being more resistant to oxidative attack by the metaphosphate melt as well as transparent to allow for examination of the internal counterelectrode contacts.

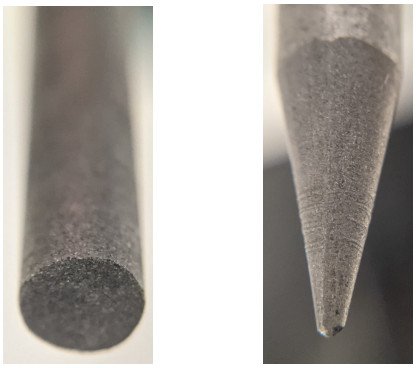

(a) **(b)**

Figure 2-4. Graphite working-electrodes morphologies: **(a)** an unaltered rod and **(b)** a sharpened rod to militate P_4 bubble formation.

2.2.1.2 Working Electrode

Unless indicated otherwise, the working electrode for all experiments was a graphite rod (Spectro-Grade[v], $\frac{3}{16}$" diameter, 12" OAL, part# 70231 by Electron Microscopy Sciences), the end sharpened to a point in a pencil sharpener (**Figure 2-4b**) and subsequently polished clean by a Kimberly-Clark Professional™ Kimtech Science™ Kimwipe™ Delicate Task Wiper (henceforth 'Kimwipe™') to exfoliate potential trace metal impurities. To prevent shorting of the electrode against the conductive reactor head, a single-bore alumina tube ($\frac{1}{4}$" OD, $\frac{3}{16}$" ID, part #AL-T-N1/4-N3/16-12 by AdValue Technologies, cut to an OAL of approximately 4 inches) was used as an electrode sheath. The graphite electrode was flame-sealed to the electrode sheath by using a blowtorch to dab molten sodium metaphosphate salt to the alumina sheath, adhering it to the graphite electrode.

[v] Total impurity level <2 ppm, individual element impurity levels <1 ppm.

2.2.1.3 Counter Electrode

Unless indicated otherwise, the working electrode for all experiments was a graphite[vi] rod (Spectro-Grade, $\frac{1}{4}$" diameter, 12" OAL, part #70230 by Electron Microscopy Sciences™), the end polished clean by a Kimwipe™ to exfoliate potential impurities.

2.2.1.4 Reference Electrode

As a graphite electrode does not exist in thermodynamic equilibrium with the metaphosphate medium, it is impossible to define a precise potential for a graphite used as a reference electrode in this system. For this reason, it is most accurately described as a pseudoreference electrode: though it returns a stable potential in a quiescent melt for even long timescales, the precise value of this potential cannot be determined without comparison to an external "true" reference system. As a result, the pseudoreference potential can (and does) shift, both within an experiment (due to local variations in melt composition induced by electrochemical action) and between experiments (due to alterations in the bulk composition of the melt), as seen in **Figure 2-5**.

For this reason, the graphite pseudoreference electrode is calibrated before and after each experiment against an externally stable liquid-sodium Na/Na^+ absolute reference electrode (S4 Na/Al by Ionotec Ltd.). The solid-electrolyte junction of the sodium electrode is unstable to the metaphosphate melt at timescales longer than a few minutes, precluding its use as a full-time reference electrode. This combined Na/Na^+-calibrated graphite reference electrode system, collectively constituting a quasireference electrode, is stable to oxidative attack from

[vi] Graphite was chosen as a sacrificial anode in this work, which focuses primarily on investigating the cathodic reduction of phosphate to elemental phosphorus; the development of robust anodes capable of zero-carbon oxygen evolution reaction (OER) in molten oxide melts without corrosion remains a longstanding challenge in the field. Indeed, among what few molten-salt electrolyses that find industrial use today – such as the Hall-Héroult process – sacrificial carbon counter electrodes are employed despite the carbon cost they entail. While numerous factors contribute to the lack of non-sacrificial anodes for such processes – among them, cost, overpotential for OER, electrical conductivity, ease of fabrication, thermal stability, and mechanical strength – by far the principal barrier may be understood to be inadequate inertness to the highly oxidizing molten-salt electrolyte, which will dissolve most any anode under working conditions. This is true for the molten Na_3AlF_6 electrolyte of the Hall process, and it is true for the molten condensed phosphates described here.[42–44] *See also:* footnote *ii* on page 36.

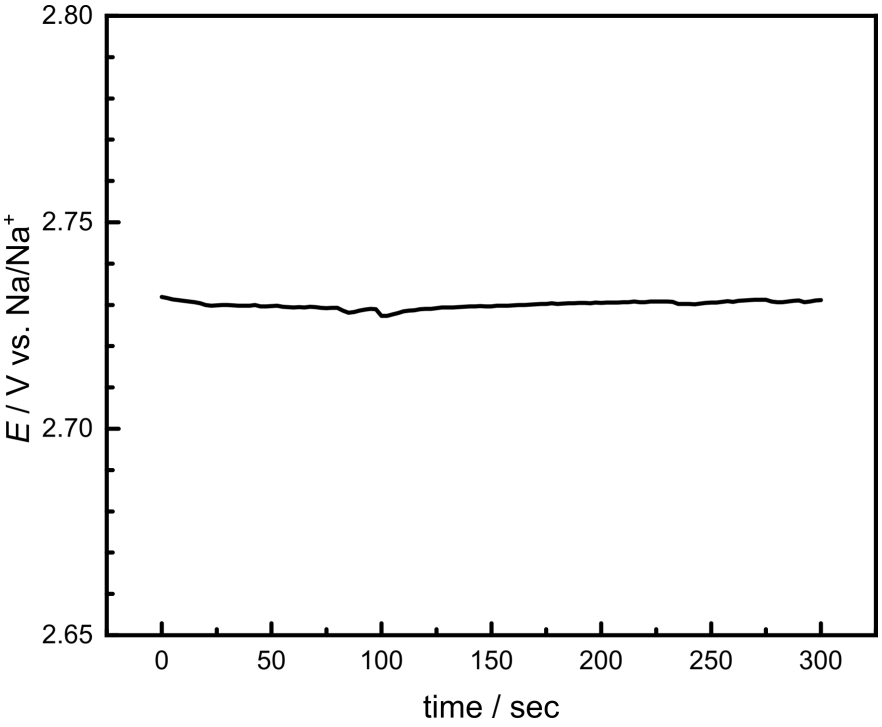

Figure 2-5. 5-minute open-circuit potential trace of graphite pseudoreference electrode against a Na/Na^+ absolute reference electrode.

the melt while enabling comparative analysis of electrochemical potentials across a variety of melt compositions.[45]

Graphite Pseudoreference Unless indicated otherwise, the working electrode for all experiments was a graphite rod (Spectro-Grade, $\frac{3}{16}$" diameter, 12" OAL, part #70231 by Electron Microscopy Sciences™), the end polished clean by a Kimwipe™ to exfoliate potential impurities. To prevent shorting of the electrode against the conductive reactor head, a single-bore alumina tube ($\frac{1}{4}$" OD, $\frac{3}{16}$" ID, part #AL-T-N1/4-N3/16-12 by AdValue Technologies, cut to an OAL of approximately 4 inches) was used as an electrode sheath. The graphite electrode was flame-sealed to the electrode sheath by using a blowtorch to dab molten sodium metaphosphate salt to the alumina sheath, adhering it to the graphite electrode.

Liquid Sodium Electrode The liquid sodium reference electrode (**Figure 2-6**) was custom-ordered from the UK electroceramics company Ionotec Ltd. under the product des-

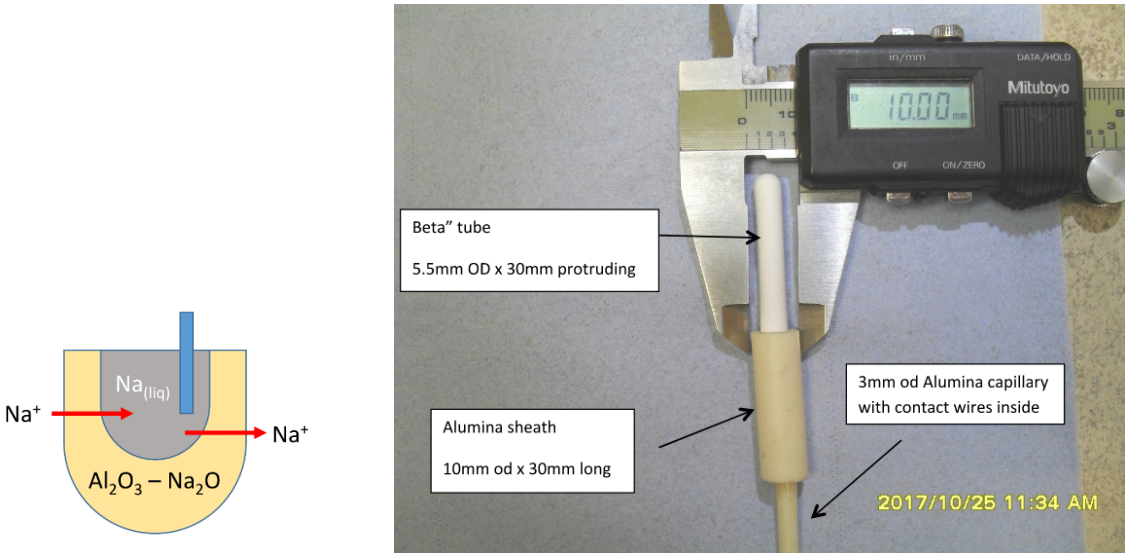

Figure 2-6. Ionotec Ltd. S4 Na/Al liquid sodium reference electrode.

ignation S4 Na/Al: Na beta-alumina reference electrode, 4.0 mm ID x 70 mm length x 0.6 mm wall thickness. The electrode terminus was filled with carbon fiber and hermetically sealed and terminated with 80 mm of 0.5 mm-diameter Pt wire attached to a 300 mm long nichrome wire. A protective alpha-alumina tube (250 mm long) was glazed to the OD of the sensor head and a protective alpha-alumina collar, 8 mm OD, was cemented over the joint between the sensor head and the 250 mm tube, such that the exposed length of the beta-alumina tube was 30 mm.

2.2.1.5 Gas Flowthrough Setup

In order to account for potential gas flow losses due to loss of o-ring seal integrity at temperature, a gas flowthrough setup (**Figure 2-7**) was constructed to enable quantitation of N_2 gas flow into and out of the electrochemical reactor, utilizing acrylic valved bead flowmeters (part #PB-3246040 by Cole-Parmer Scientific™) leading into and out of both the working and counter electrode compartments. Working compartment flowmeters were rated for between 40 to 600 standard cubic centimetres per minute (sccm), while counter compartment flowmeters were rated for between 10 and 50 sccm. At typical flowrates of 40 sccm through

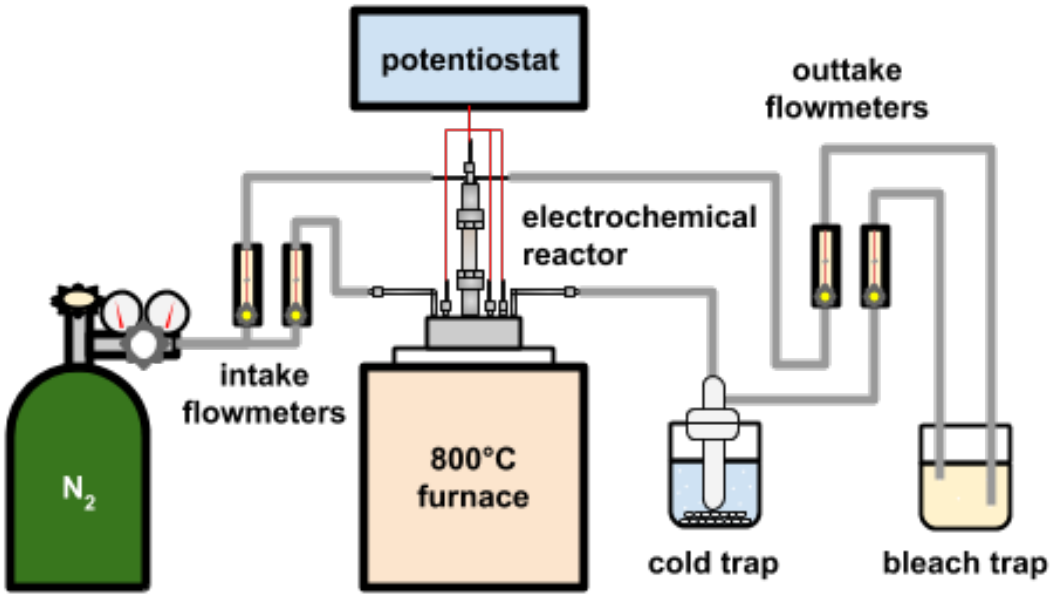

Figure 2-7. Diagram of total PRR electroanalytical setup, configured for P_4 capture and quantitation.

the counter compartment and 400 sccm through the working compartment, temperature effects due to volumetric expansion were found to be within the error of the system. In quantitating P_4 yield for calculating Faradaic efficiency (FE%), observed yield was normalized by working compartment gas outflow as a fraction of working compartment gas inflow (see page 84). For analysis of counter electrode outflow streams, gas chromatography (GC) analysis was performed by injection into a Multi-Gas Analyzer (#3; SRI Instruments) equipped with a thermal conductivity detector, methanizer, and flame ionization detector in series after Molsieve 13x and Hayesep D Columns.

2.2.1.6 Product Capture

Evolved phosphorus was collected from three primary locations: the cold trap, the bleach trap, and the reactor head. The cold trap, immersed in a dry ice/acetone bath at -78 °C, was the primary method of capture and the only method by which molecular P_4 could be collected. To mitigate photoconversion of P_4 to polymeric red phosphorus, the bleach trap was wrapped in aluminum foil; following an experiment, the valves were sealed and the cold

trap was pumped into a N_2 glovebox, within which P_4 samples for ^{31}P NMR could be prepared. The terminal bleach trap sometimes accumulated measurable quantities of phosphorus in the form of oxidized polyphosphate species, presumably formed when by the oxidation of gaseous P_4 bubbles that escaped from the cold trap. Finally, polymeric red phosphorus deposits on the reactor interior (see **Figure 2-12** on page 62), formed when the reactor head cooled below the 280.5 °C boiling point of P_4, could be collected for quantification by dissolution with bleach, which likewise oxidizes red phosphorus to soluble polyphosphates.

2.2.2 Molten Phosphate Reduction is Highly Selective for P_4

2.2.2.1 Voltammetric Behaviour of Metaphosphate Melt

With this electroanalytic system, we can begin to assess the selectivity of the cathodic reaction by applying increasingly cathodic potentials in a linear-sweep voltammogram (LSV), as seen in **Figure 2-8**. We observe the onset of a substantial reductive current at approximately +2.4 V against a Na/Na^+ reference electrode. We cannot observe a peak to this reductive feature within the current range accessible by our potentiostat; as our electrolyte is itself our reactant, we cannot reach a region of local depletion that characterizes a typical voltammetric peak feature. Instead, we observe a characteristic ongoing reductive feature more typically associated as a "solvent window" in conventional electrolytes.

Having established the presence of a feature indicative of reductive solvent decomposition, we can further probe our system through cyclic voltammetry (CV), as seen in **Figure 2-9**. For a sharpened graphite working electrode in a sodium metaphosphate melt, we observe that the onset of the cathodic feature displays a linear relation between current density and the square root of voltammetric scanrate, indicative of the participation of a freely-diffusing redox species as per the Randles-Ševčík equation. Returning from our reductive trace, we notice an immediate coupled oxidative feature at approximately +2.5 V vs. Na/Na^+, with a stark scanrate dependence; though prominent at $100\,mV{\cdot}s^{-1}$, it is practically nonexistent at $10\,mV{\cdot}s^{-1}$. This suggests the formation of a transient reduced species at the electrode

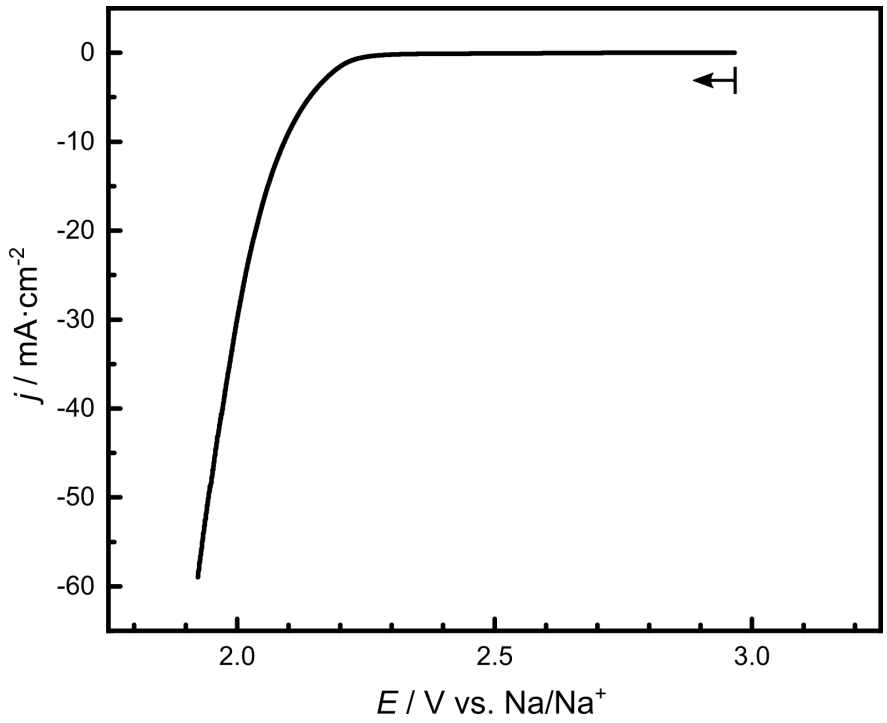

Figure 2-8. Reductive linear sweep voltammogram of a sharpened graphite electrode in molten sodium trimetaphosphate at a scanrate of $100\,\mathrm{mV{\cdot}s^{-1}}$.

interface, such as a gas bubble that will diffuse away at low scanrates. Finally, past +3.0 V vs. Na/Na^+ we observe an irreversible oxidative feature with minimal scanrate dependence, which we assign to the oxidation of our graphite electrode. GC analysis of the anodic gas stream from our graphite counter electrode indicates a mixture of 96.3% CO_2 and 3.7% CO – corresponding to an electron efficiency of 3.93 electrons per atom of carbon – and sustained electrolysis at this potential will result in visible corrosion of the otherwise-inert graphite.

2.2.2.2 Chronopotentiometric Electrolysis of Metaphosphate Melt

The graphite electrode is stable to high cathodic current densities (up to $300\,\mathrm{mA{\cdot}cm^{-2}}$) for timescales of several hours with no visible corrosion nor decrease in electrochemical surface area, though convolution may occur following prolonged electrolyses at high current densities owing to solution crossover of partially-oxidized graphite particles from the counter electrode. Upon sustained electrolysis at reductive potentials below +2.4 V vs. Na/Na^+ (**Figure 2-10**), yellow-white crystals (**Figure 2-11a**) are observed to grow in the cold trap connected to

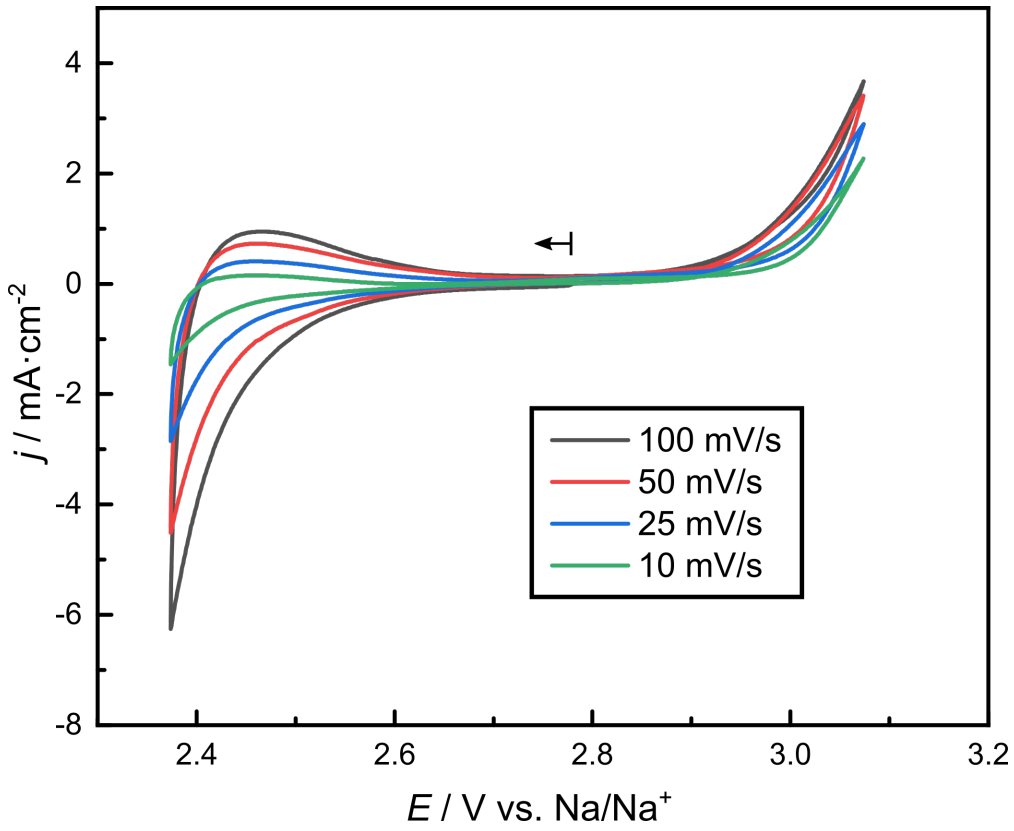

Figure 2-9. Cyclic voltammetry of a sharpened graphite electrode in molten sodium trimetaphosphate at scanrates are 10 $mV \cdot s^{-1}$, 25 $mV \cdot s^{-1}$, 50 $mV \cdot s^{-1}$ and 100 $mV \cdot s^{-1}$.

the working compartment outflow stream; if exposed to air, these crystals will immediately ignite. If the glass trap is not lined with aluminum foil, these crystals will slowly decay over the course of a few hours into a reddish-brown coating (**Figure 2-11b**), consistent with the photoconversion of molecular white phosphorus to polymeric red phosphorus.

2.2.2.3 Phosphorus Analysis and Quantitation

Protected from photoconversion by foil and transferred into an inert nitrogen atmosphere, these waxy white crystals may be dissolved in carbon disulfide for ^{31}P nuclear magnetic resonance (NMR) against a triphenylphosphine (TPP) internal standard (**Figure 2-13**), against which is evinced a chemical shift of approximately -510 ppm vs. 85% H_3PO_4, highly characteristic for white phosphorus.[46]

Additional accumulations of red phosphorus may collect on surfaces near the top of the

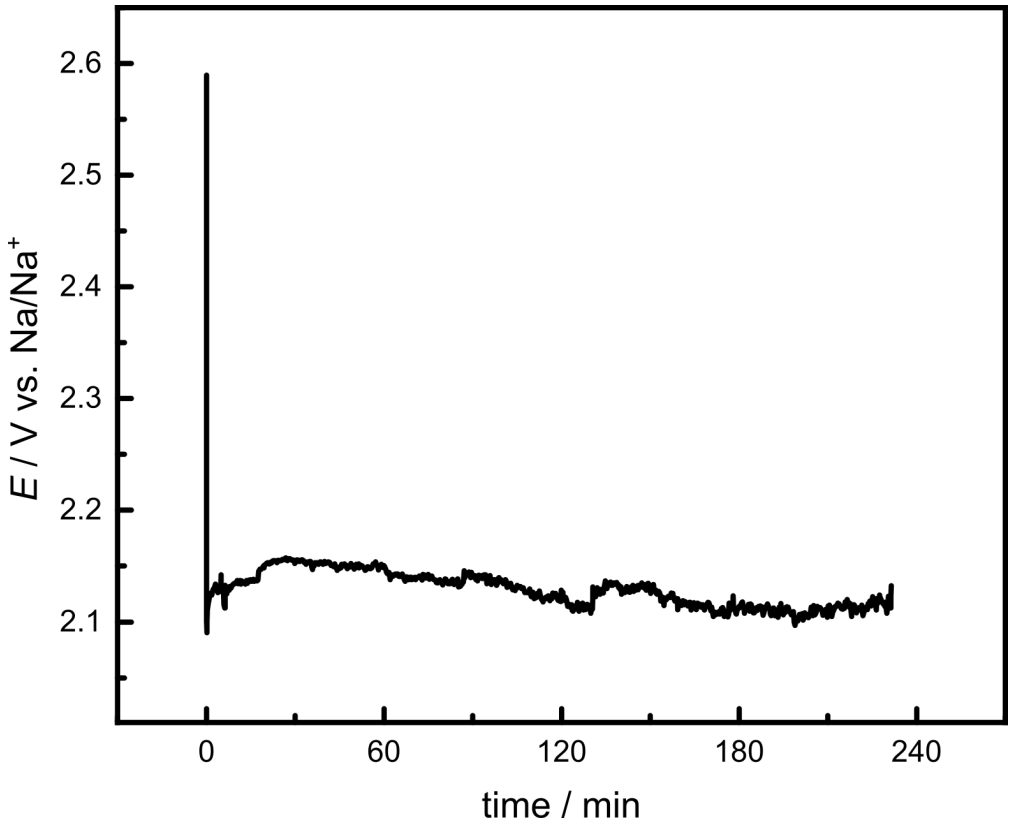

Figure 2-10. 4-hour potential trace of molten sodium trimetaphosphate electrolysis at a fixed current density of 48 $\mathrm{mA{\cdot}cm^{-2}}$.

(a)

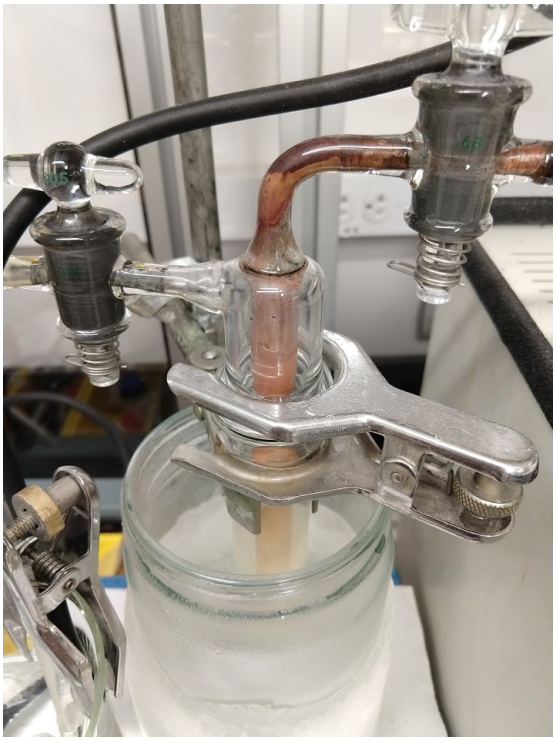

(b)

Figure 2-11. **(a)** Yellow-white crystals of white phosphorus are observed to form in the cold trap upon sustained electrolysis. **(b)** Upon exposure to light, electrogenerated white phosphorus will photoconvert to polymeric red phosphorus.

(a)

(b)

Figure 2-12. Post-electrolysis accumulation of red phosphorus on reactor body **(a)** and head **(b)** interiors.

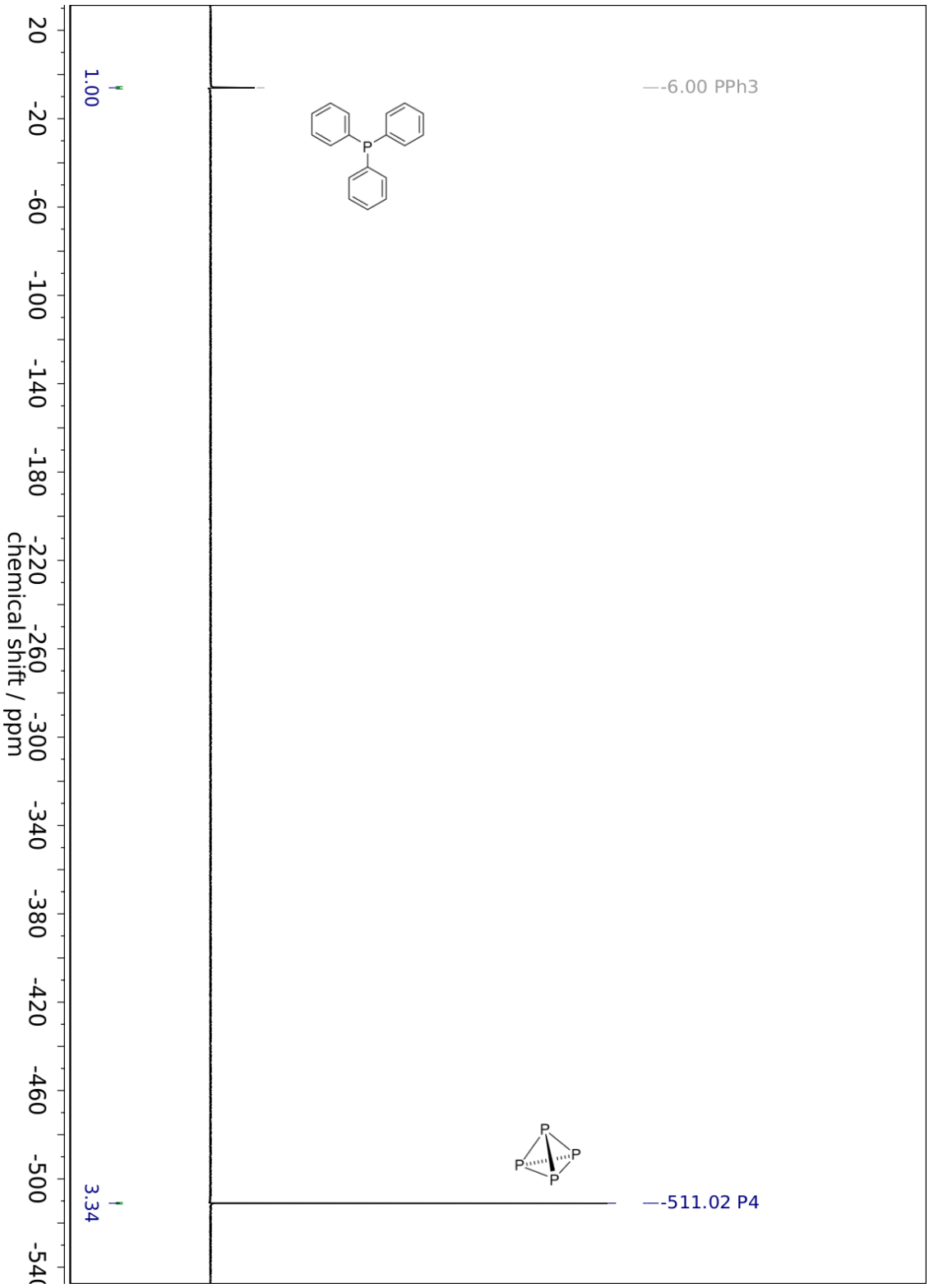

Figure 2-13. ^{31}P NMR spectrum of electrogenerated P_4 dissolved in CS_2 against a TPP internal standard.

reactor (**Figure 2-12**). Combining this phosphorus with P_4 collected from the cold trap and quantitating using ^{31}P NMR against an internal standard of phosphonoacetic acid, we observe a peak FE% for PRR of 64.5% for the four-hour galvanostatic electrolysis pictured in **Figure 2-10**. Normalizing this FE% by a 68% gasflow retention rate out of the reactor, thereby accounting for P_4 losses due to imperfect reactor sealing at temperature, we note a peak FE% of 95% for P_4 evolution. However, due to the imperfect function of the DuPont™ Kalrez® o-rings, which are only temperature rated up to 300 °C, lower gasflow-normalized Faradaic efficiencies in the range of 60-80% may be observed, presumably due to oxidative consumption of reduced phosphorus species prior to their removal from the cell.

Taken together, these data indicate definitively that PRR is the sole cathodic process of metaphosphate electrolysis, that P_4 is the primary reductive product of PRR, and that the reduction of metaphosphate to P_4 occurs in near-quantitative yield, with FE% for the process approaching unity.

2.2.3 Phosphate Reduction Occurs Reversibly at Near-Zero Overpotential

2.2.3.1 Strategies for Assessing E°

Calculation of overpotential for PRR in this system necessarily requires an assessment of the thermodynamic reduction potential E° for the $PO_3^- \rightleftharpoons P_4$ redox couple under these conditions, as former is defined in terms of the latter:

$$E = E^\circ + \eta. \tag{2.6}$$

Owing to the reliance of the preceding polarographic reports on pseudoreference electrodes such as bare graphite, we cannot rely upon prior literature values and must estimate this potential ourselves. Unfortunately, this is not as trivial an evaluation to perform as it may first appear. As cell potential is defined as the change in free energy per coulomb of

charge transferred, the standard cell potential (E°) is related to the reaction's standard-state Gibbs free energy change ($\Delta G^\ominus$) by the equation:

$$\Delta G^\ominus = -nFE^\circ, \tag{2.7}$$

where n is the number of electrons transferred and $F = 96\,485\,\mathrm{C{\cdot}mol^{-1}}$ is the Faraday constant. The observed equilibrium potential is then determined by the Nernst equation

$$E = E^\circ - \frac{RT}{nF}\ln Q, \tag{2.8}$$

where $R = 8.314\,\mathrm{J{\cdot}mol^{-1}{\cdot}K^{-1}}$ is the ideal gas constant and $Q = \frac{\prod_i^{\mathrm{red}} a_i^{\nu_i}}{\prod_j^{\mathrm{ox}} a_j^{\nu_j}}$ is the reaction quotient at the temperature of interest T. This approach is hampered, however, by an inability to determine $\Delta G^\ominus$ without knowledge of the specific species and reduced products associated with this electrochemical feature, which is impossible to determine *a priori*. Even making assumptions about the reaction in question, an attempt to calculate $\Delta G^\ominus$ by Hess' Law

$$\Delta G^\ominus_{\mathrm{reaction}} = \sum \Delta_f G^\ominus_{\mathrm{products}} - \sum \Delta_f G^\ominus_{\mathrm{reactants}} \tag{2.9}$$

is stymied by a lack of necessary thermochemical reference data on the enthalpies and entropies of formation for specific condensed phosphate species, as well as the enthalpies and entropies of fusion so as to account for the melting process.

The only remaining approach is to empirically determine E from electroanalytical data. The relationship between the cathodic current density j and the overpotential η is defined by the Tafel equation:

$$\eta = -\frac{RT\ln 10}{\beta nF}\log_{10}\left[\frac{j}{j_0}\right], \tag{2.10}$$

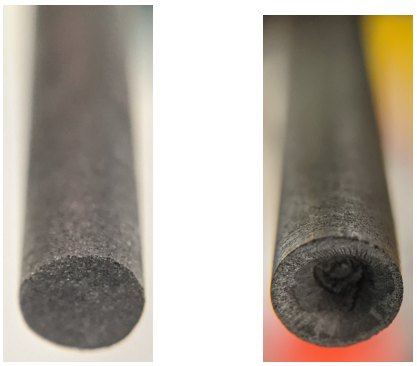

(a) **(b)**

Figure 2-14. Graphite working-electrode morphologies: **(a)** an unaltered rod, and **(b)** a hollowed rod to induce P_4 bubble trapping.

where β is the *symmetry factor*[vii] for a single-step electrochemical reaction in which n electrons are transferred and j_0 is the exchange-current density, defined as the equilibrium current density at net zero overpotential, at which the magnitudes of anodic and cathodic current are equal, thereby evincing no net electrolysis.[48] This is equivalent to the open-circuit potential (OCP) by definition; plugging **Equation 2.6** into **Equation 2.10** for $\eta = 0$, we have $j = j_0$ and hence $E^\circ = E_{\text{oc}}$.

2.2.3.2 The Hollowed-Electrode Method for Measuring E°

By this reasoning, if we can produce a system containing both reducible PO_3^- and oxidizable P_4 in equilibrium with each other, the OCP will equal E°. However, as P_4 is a gas at this temperature, it does not readily remain at equilibrium and will instead bubble free of the electrode interface. This is functionally the inverse problem to that of bubble convolution of electrode surface area (see **Figure 2-4** on page 53), and accordingly it has an inverse solution; by carving out the bottom of a flat graphite electrode (**Figure 2-14**), we can create a hollow capable of trapping a bubble of evolved P_4 gas, thereby establishing a $PO_3^- \rightleftharpoons P_4$ equilibrium at the graphite-metaphosphate-phosphorus triple phase boundary.

We can assess the efficacy of this approach by generating a P_4 bubble in the hollow of our

[vii] A number between 0 and 1, corresponding to the relative position of the activated complex as a fraction of the reaction coordinate from reduced to oxidized species. Experimentally determined symmetry factors almost always range from 0.4 to 0.6, and hence β is typically assumed to be 0.5 in nearly all cases.[47]

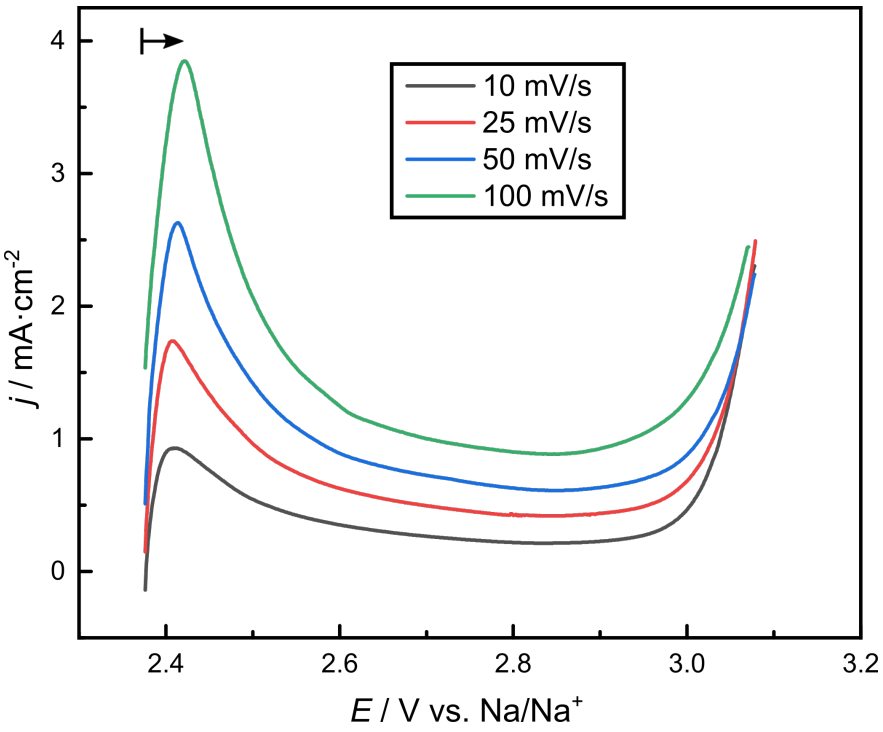

Figure 2-15. LSV traces of a hollowed graphite electrode following a 1-minute galvanostatic electrolysis at $-10\,\mathrm{mA{\cdot}cm^{-2}}$, scanning oxidatively from OCP at scanrates of $10\,\mathrm{mV{\cdot}s^{-1}}$, $25\,\mathrm{mV{\cdot}s^{-1}}$, $50\,\mathrm{mV{\cdot}s^{-1}}$ and $100\,\mathrm{mV{\cdot}s^{-1}}$.

working electrode and scanning oxidatively from OCP, from which we would expect to see an anodic feature analogous to that seen in our cyclic voltammogram (**Figure 2-9** on page 60) at approximately +2.45 V vs. Na/Na^+. This is accomplished by galvanostatic electrolysis at an equivalent potential previously established to accord with the electrochemical generation of P_4, followed by a scanrate-dependent LSV as pictured in **Figure 2-15**. We observe an oxidative peak, again at approximately +2.45 V vs. Na/Na^+, with no further features until the previously assigned graphite oxidation peak beyond +3.0 V vs. Na/Na^+.

While highly suggestive that the voltammetric feature at +2.45 V vs. Na/Na^+ corresponds with the oxidation of P_4, this evidence does not by itself preclude the possibility that residual partially-reduced intermediate species are being produced at the electrode surface and subsequently reoxidized. As not all P_4 we are generating electrolytically will be trapped in the electrode hollow (both due to its limited volume and the electrolyte contact with the outer surface of the hollowed electrode), we cannot exclude this prospect by simple charge

Figure 2-16. A hollowed graphite working electrode, with the produced cavity smeared with red phosphorus for nonfaradaic *in situ* P_4 generation.

integration analysis. Instead, to definitively address this edge possibility, we can exploit the thermal depolymerization of red phosphorus to white phosphorus to nonfaradaically generate a P_4 bubble without the possibility of generating partially-reduced intermediate species, by loading the cavity of a hollowed graphite electrode with red phosphorus (**Figure 2-16**) and performing an analogous oxidative LSV sweep as soon as it is lowered into the electrolyte medium. The result, seen in **Figure 2-17a**, shows a high correlation between the oxidative peaks of nonfaradaically generated P_4 and our presumptive electrosynthesized P_4, allowing us at last to confidently assign the anodic feature at +2.45 V vs. Na/Na^+ to P_4 oxidation and thereby assess the thermodynamic E° for PRR.

We can further assess the efficacy of the hollowed-electrode experiment by comparing the OCP traces for a resting sharpened sharpened electrode, a sharpened electrode following electrolysis, a hollowed electrode following electrolysis, and a hollowed electrode following electrolysis. While resting OCP for a quiescent electrode hovers around +2.7 V vs. Na/Na^+, both post-electrolysis and red phosphorus-dosed electrodes initially exhibit OCP values near +2.4 V vs. Na/Na^+. While the post-electrolysis potential of a sharpened electrode rises rapidly over the course of several minutes towards that of the control electrode, both hollowed electrode traces remain roughly steady around +2.4 V vs. Na/Na^+. The hollowed-electrode

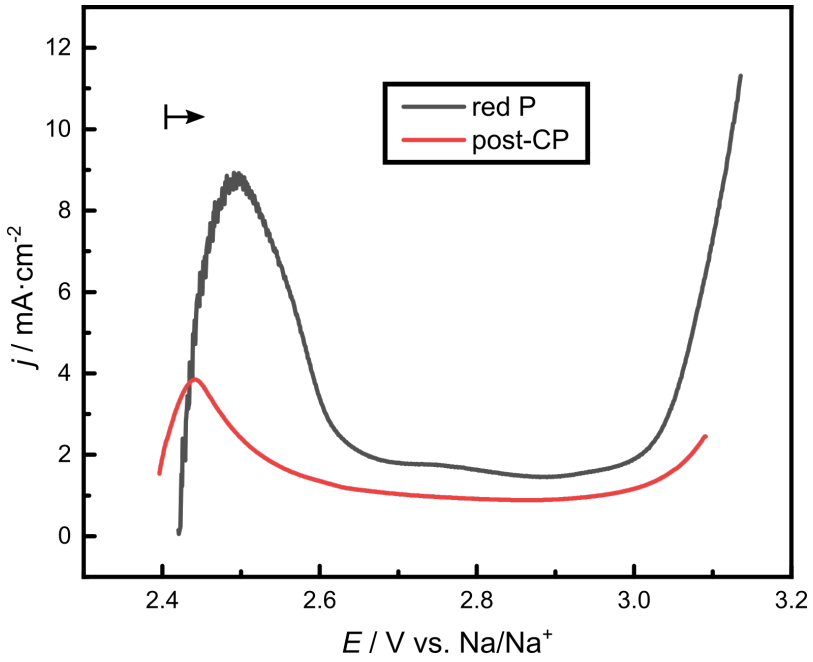

(a) LSV traces of a hollowed graphite electrode following a 1-minute galvanostatic electrolysis at $-10\,\mathrm{mA{\cdot}cm^{-1}}$ (red), and a hollowed graphite electrode coated in red phosphorus (black), scanning oxidatively from OCP at $100\,\mathrm{mV{\cdot}s^{-1}}$.

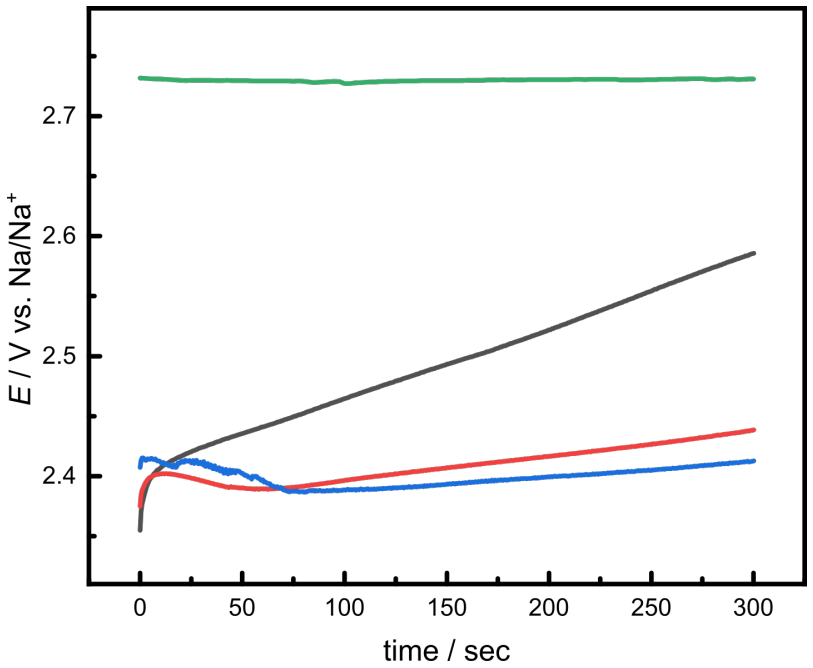

(b) 5-minute OCP traces of a resting sharpened graphite electrode (green), sharpened (black) and hollowed (red) graphite electrodes following 1-minute galvanostatic electrolyses at $-10\,\mathrm{mA{\cdot}cm^{-2}}$, and a hollowed graphite electrode coated in red phosphorus (blue).

Figure 2-17. **(a)** LSV and **(b)** OCP traces comparing electrogenerated P_4 to P_4 generated by thermal depolymerization of red phosphorus.

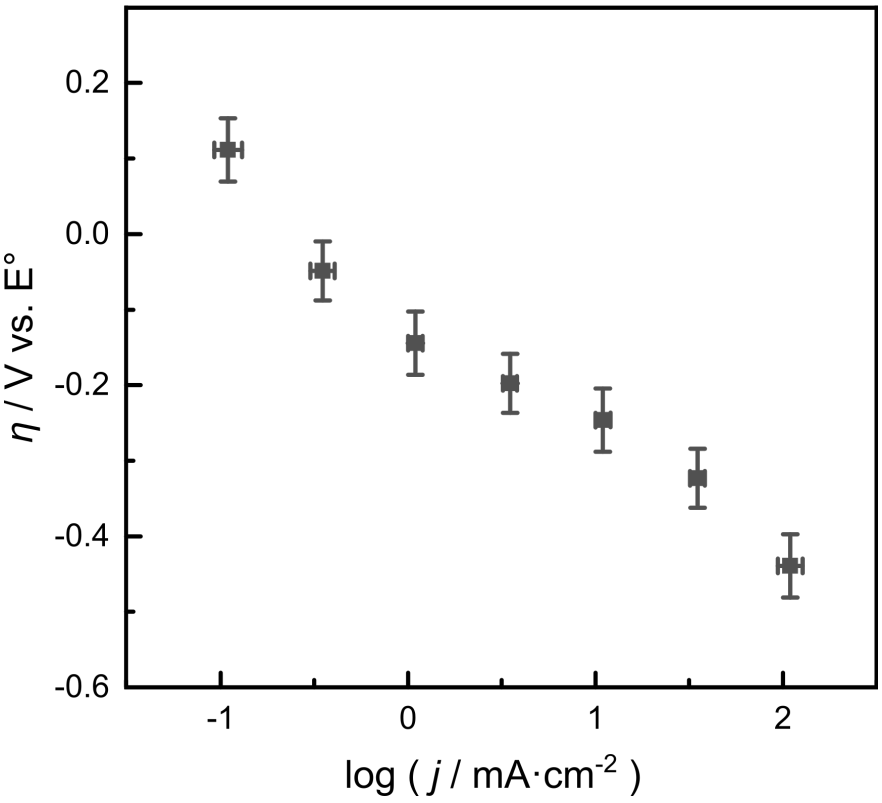

Figure 2-18. Plot of phosphate reduction overpotential in molten sodium trimetaphosphate as a function of current density. The Tafel slope is $150\,\mathrm{mV{\cdot}dec^{-1}}$. Error bars represent 95% confidence intervals computed from a set of eight independent experimental setups, each reproduced in triplicate.

potential trace appears to be characterized by a slight *decrease* in potential over the course of approximately a minute, following which the potential will begin to creep back upwards, albeit at a markedly slower rate than for a sharpened electrode. This phenomenon may be due to equilibration time for an evolved P_4 bubble in the electrode hollow to reach steady-state, as it is likely in both the electrosynthesized and chemically-generated cases that the evolved quantity of P_4 greatly exceeds the volume of the electrode hollow.

2.2.3.3 Mechanistic Tafel Analysis of Phosphate Reduction

Taking the post-electrolysis OCP value as E° for PRR in this system, we can at last construct a diagram relating the overpotential of phosphate reduction as a function of steady-state

galvanostatic current density, revealing the activation-controlled[viii] Tafel plot **Figure 2-18**. In the macropolarization regime in which PRR takes place, the observed Tafel slope is $150\,\mathrm{mV{\cdot}dec^{-1}}$. By generalizing the Tafel equation (**Equation 2.10**) to a multistep case, we have

$$\eta = -\frac{RT\ln 10}{\alpha F}\log_{10}\left[\frac{j}{j_0}\right], \tag{2.11}$$

in which the single-step symmetry factor-adapted electron transfer number βn is replaced by the multi-step *transfer coefficient* α:

$$\alpha = \frac{\gamma}{\nu} + r\beta, \tag{2.12}$$

where γ is the number of electrons transferred prior to the rate-limiting step (RLS), ν is the stoichiometric number of the reaction, r is the number of electrons transferred in the RLS, and β is the symmetry factor of the RLS.[47, 49] At 800 °C, this corresponds to a Tafel slope[ix]

$$b_{800\ ^\circ\mathrm{C}} = \frac{\partial\eta}{\partial(\log j)} = \frac{212.9\,\mathrm{mV{\cdot}dec^{-1}}}{\alpha}. \tag{2.13}$$

This observed Tafel slope of $150\,\mathrm{mV{\cdot}dec^{-1}}$ then corresponds to a transfer coefficient $\alpha \approx 1.4$. Knowing that symmetry factors are typically in the range 0.4–0.6, that single-step multielectron transfers are exceedingly uncommon, and presuming that the reduction of a single PO_3^- unit necessitates $\nu = 1$, by far the most reasonable assignment to make is $\gamma = 1$ and $r = 1$, corresponding to a 1-electron pre-rate-limiting electron transfer followed by a second rate-limiting 1-electron transfer. This would correspond to a reduction from formal P^{V} to P^{IV} to P^{III}, from which further reduction to $P^{(0)}$ may occur electrochemically or by disproportionation.[50]

[viii] Subsequent computational analysis would reconcile the activation-controlled Tafel curves seen here with the diffusion-controlled voltammograms seen in **Figure 2-9** on page 60; see **Section 2.2.3.5** on page 72.

[ix] Functionally a linearization parameter that falls out of the Butler-Volmer equation in the high-overpotential limit, the Tafel slope is most commonly reported in units of $\mathrm{mV{\cdot}dec^{-1}}$, conveying the overpotential increase necessary to induce an order-of-magnitude increase in current density.

2.2.3.4 Potential Mechanism for Phosphate Reduction

We can extrapolate from this analysis a potential mechanism for the net reduction of metaphosphate to white phosphorus. As detailed in **Appendix A.1.1** on page 188, a metaphosphate unit, having two phosphoryl anhydride linkages, may in net accept an oxide equivalent to form a free orthophosphate ion (**Equation 2.14**). Our Tafel analysis suggests the initial steps of reaction are in net the two-electron reduction of metaphosphate, which would be sufficient to induce the rate-limiting formation of a surface-bound phosphite species ${}^{\star}PO_2{}^{-}$, as seen in **Equation 2.15**. From this point two post-RLS mechanisms are possible: the disproportionation of bound phosphite (P^{III}) to molecular $P^{(0)}$ and metaphosphate (P^{V}), with associated release of two oxide equivalents (**Equation 2.16**) or the electrochemical reduction of bound phosphite (P^{III}) to molecular $P^{(0)}$, with associated release of eight oxide equivalents (**Equation 2.17**); however, in both cases, the overall stoichiometry of the cathodic reduction of metaphosphate to form P_4 with associated phosphoryl anhydride cleavage to orthophosphates (**Equation 2.18**) is identical.

$$[PO_3]^- + O^{2-} \longrightarrow PO_4{}^{3-} \tag{2.14}$$

$$[PO_3]^- + 2\,e^- \longrightarrow {}^{\star}PO_2{}^- + O^{2-} \tag{2.15}$$

$$10\,{}^{\star}PO_2{}^- \longrightarrow P_4 + 6\,[PO_3]^- + 2\,O^{2-} \tag{2.16}$$

$$4\,{}^{\star}PO_2{}^- + 12\,e^- \longrightarrow P_4 + 8\,O^{2-} \tag{2.17}$$

$$16\,[PO_3]^- + 20\,e^- \longrightarrow P_4 + 12\,PO_4{}^{3-} \tag{2.18}$$

2.2.3.5 Computational Modeling of Predicted PRR Mechanism

To assess the plausibility of our putative mechanism and reconcile the activation-controlled current-overpotential relation in **Figure 2-18** on page 70 with the diffusion-controlled voltammograms seen in **Figure 2-9** on page 60, we employed Gamry™ Elchsoft™ DigiElch® Elec-

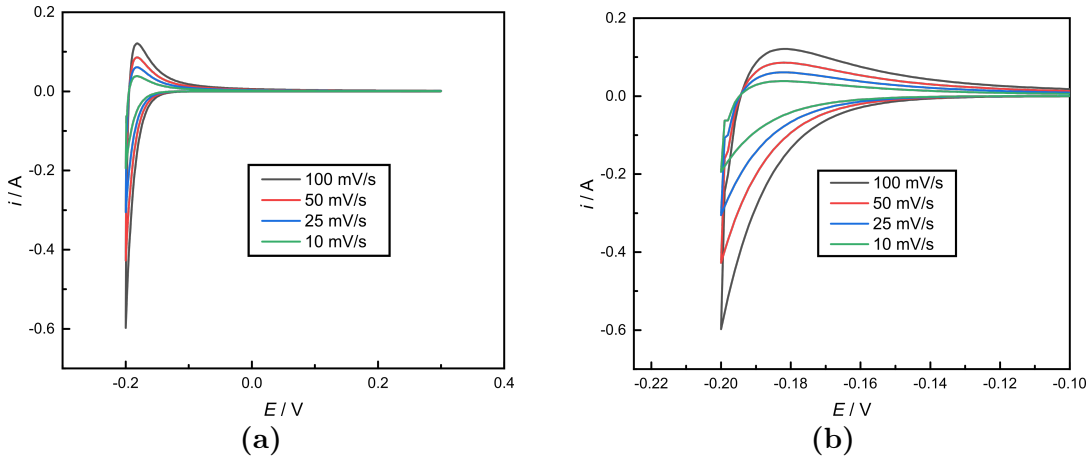

Figure 2-19. Computationally modeled cyclic voltammograms, simulated by Gamry™ Elchsoft™ DigiElch® Electrochemical Simulation Software, for a putative phosphate reduction mechanism consisting of two consecutive rapid electron-transfer steps followed by a comparatively slow chemical disproportionation. **(a)** displays the full CV simulation, while **(b)** displays a zoomed view of the simulated reductive feature.

trochemical Simulation Software to simulate hypothetical cyclic voltammetric behavior, as seen in **Figure 2-19**. For this simulation, we modeled an EEC mechanism consisting of two consecutive fast electron-transfer steps followed by a comparatively slow chemical disproportionation. The first electron transfer (representing the reduction of $P^{V} \longrightarrow P^{IV}$) occurred at an arbitrarily-selected potential of $E^{\circ} = 0\,\text{V}$ and a rapid $k_s = 1 \times 10^{5}\,\text{cm}{\cdot}\text{s}^{-1}$, while the second electron transfer (representing the reduction of $P^{IV} \longrightarrow P^{III}$) was chosen to occur at $E^{\circ} = -0.1\,\text{V}$ with a slightly slower $k_s = 1 \times 10^{4}\,\text{cm}{\cdot}\text{s}^{-1}$; both reactions utilized a default symmetry factor[vii] of $\beta = 0.5$. The subsequent chemical reaction (representing the disproportionation of $P^{III} \longrightarrow P^{(0)}$) was modeled as a slow forward equilibrium with $k_f = 1 \times 10^{-4}$ and $K_{eq} = 1$. To represent the metaphosphate melt, the starting conditions for the simulation began at a concentration of 100 M for the simulated P^{V} species, which possessed a rapid diffusion coefficient of $10\,\text{cm}^2{\cdot}\text{s}^{-1}$. All other species began at a starting concentration of zero; the P^{IV} and P^{III} species were assigned a sluggish diffusion coefficient of $1 \times 10^{-20}\,\text{cm}^2{\cdot}\text{s}^{-1}$ to represent the likely surface-bound nature of these partially-reduced intermediates, while the terminal $P^{(0)}$ species had a modestly faster diffusion coefficient of $1 \times 10^{-5}\,\text{cm}^2{\cdot}\text{s}^{-1}$ to represent P_4 bubbling in the viscous electrolyte media.

The simulated voltammograms seen in **Figure 2-19** correspond exceedingly well with the diffusion-controlled voltammograms seen in **Figure 2-9** on page 60, from the square-root scanrate dependence of the reductive current densities right down to the presence of a scanrate-independent 'isosbestic point'[x] on the back oxidation trace, where the voltammetric traces intersect at $j = 0$ at all scanrates. These simulations resolve the apparent aberration implied by a diffusion-controlled cyclic voltammogram with an activation-controlled Tafel curve by suggesting the latter voltammetric scanrate dependence is associated not with the diffusion limitation of a reactant species, but variable back-oxidation rates of a diffusion-limited *product* species (P_4 oxidation) in a highly reversible redox equilibrium with catalytic metaphosphate reduction. This is enabled by low gas solubility and product diffusion coefficients in the metaphosphate electrolyte, which means that slower scanrates have a greater buildup of reduced products near the electrode surface. As a result, a lower $j = j_{red} - j_{ox}$ value is observed at lower scanrates not due to reduced diffusion-limited j_{red}, but *increased* diffusion-limited j_{ox}.

2.2.4 Phosphoryl Anhydride Linkages Promote Phosphate Reduction

Thanks to our robust electroanalytical system and Na/Na^+ quasireference electrode, which allow for reproducible and comparable electroanalysis across varying melt compositions, we can assess the phosphate reduction reaction as a function of the phosphoryl anhydride linkage concentration of the melt. As detailed in **Appendix A.1.1** on page 188, this concentration is inversely related to the oxide content of the melt. As oxide equivalents do not exist in this system as free O^{2-} ions, the melt's oxide content is instead defined in terms of the distribution of branching, bridging, terminal, and free phosphate species, corresponding

[x] 'Isosbestic point' is a spectroscopic term, denoting a wavelength at which the absorbance of a sample is constant over the course of a chemical reaction. As such, this voltammetric feature is not in any sense a *true* isosbestic point – the word itself meaning 'equal extinguishability', thereby relatively inextricable from its spectroscopic context – rather, the term is used here merely by purpose of analogy.

respectively to ultraphosphates, metaphosphates, paraphosphates, and orthophosphates . The production of a single oxide equivalent is analogous to the cleavage of two ultraphosphate groups to a metaphosphate, two metaphosphates to paraphosphates, or two paraphosphates to orthophosphates. In a melt, these moieties will rapidly interconvert with an equilibrium distribution that is a function of temperature; however, the total concentration of phosphoryl anhydride linkages, being an inverse measure of the oxide content of the melt, will remain constant in a quiescent solution.

By exploiting the rapid interconversion of phosphate ions in a molten salt, melts with phosphoryl anhydride concentrations ranging from $5.4\,\mathrm{mol{\cdot}kg^{-1}}$ to $9.8\,\mathrm{mol{\cdot}kg^{-1}}$ may be synthesized by dosing pure sodium trimetaphosphate with sodium orthophosphate (see **Table A.2** on page 192). Phosphoryl anhydride concentrations below $5.4\,\mathrm{mol{\cdot}kg^{-1}}$ were inaccessible, as their melting points are above the 800 °C temperature used for all experiments in this study; future studies may access lower values of phosphoryl anhydride concentrations at higher reaction temperatures[xi], or higher values through the dosing of sodium trimetaphosphate with phosphoric anhydride.

The anhydride concentrations $9.8\,\mathrm{mol{\cdot}kg^{-1}}$, $8.3\,\mathrm{mol{\cdot}kg^{-1}}$, $6.4\,\mathrm{mol{\cdot}kg^{-1}}$ and $5.4\,\mathrm{mol{\cdot}kg^{-1}}$ correspond respectively to the phosphoryl anhydride contents of sodium trimetaphosphate (S3MP), sodium decapolyphosphate (S10PP), sodium tetrapolyphosphate (S4PP), and sodium tripolyphosphate (S3PP). For each melt, we measure the E° for PRR using the hollowed-electrode methodology described on page 66 with electrogenerated P_4. We also collect cyclic voltammograms and chronopotentiometric Tafel data.

One of the first things we observe is a dramatic shift in the resting potential of our graphite electrode against the Na/Na^+ quasireference, as depicted in **Figure 2-20**. This suggests that the action of our observed graphite pseudoreference potential is also oxide- (and hence, anhydride-) dependent. Accordingly, we observe a decrease in the oxidative feature previously observed at +3.0 V vs. Na/Na^+, consistent with our assignment of this

[xi] The next lowest polyphosphate ion, the dipolyphosphate (or pyrophosphate), melts at 988 °C; pure sodium orthophosphate melts at 1583 °C.

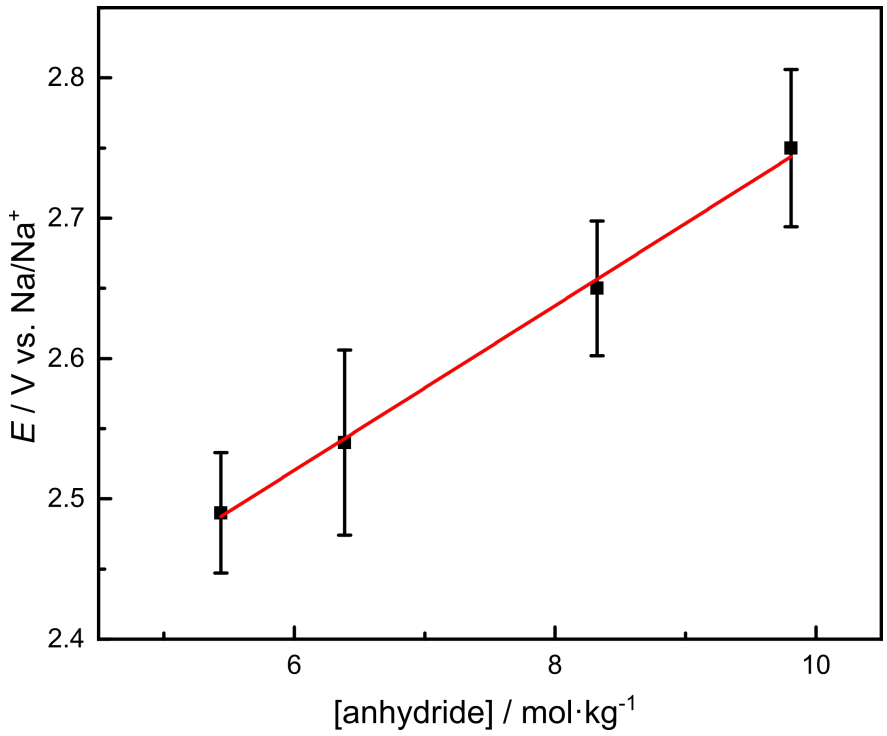

Figure 2-20. Plot of graphite pseudoreference potential against Na/Na^+ as a function of phosphoryl anhydride linkage concentration. Error bars represent 95% confidence intervals computed from a set of three independent measurements.

wave with the oxide-consuming anodic reaction of graphite to produce CO_2.

Where the increased melt oxide content induces the systematically less-anodic oxidation of graphite, it demands correspondingly more-cathodic reduction potentials for PRR. Both potential shifts are similar in magnitude and direction, with the net effect being the apparent shift in the system's effective solvent window by approximately 250 mV cathodic as phosphoryl anhydride concentration decreases from 9.8 $mol \cdot kg^{-1}$ to 5.4 $mol \cdot kg^{-1}$.

Comparing cyclic voltammetry data (**Figure 2-21**) for four condensed-phosphate melts, we observe a dramatic reduction in the resting potential of our graphite electrode against the Na/Na^+ quasireference as phosphoryl anhydride concentration decreases. This suggests that the fundamental reaction associated with our graphite pseudoreference potential is also anhydride- (and hence, oxide-) dependent. Accordingly, we observe a decrease in the oxidative feature previously observed at 3.0 V vs. Na/Na^+, consistent with our assignment of this wave with the oxide-consuming anodic reaction of graphite to produce CO_2.

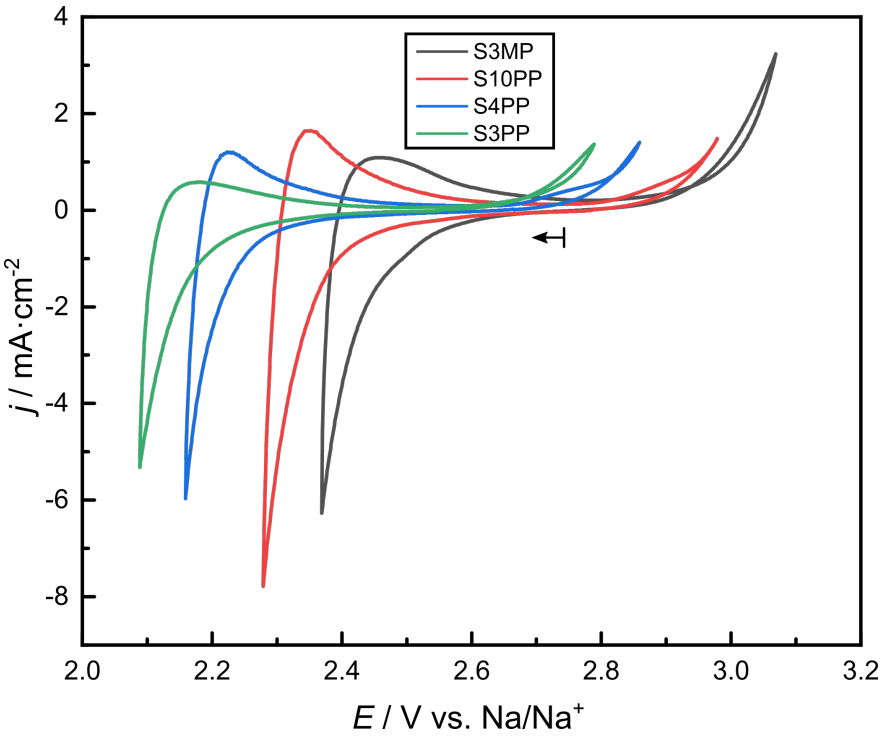

Figure 2-21. 100 mV·s^{-1} cyclic voltammograms of sodium trimetaphosphate (black), decapolyphosphate (red), tetrapolyphosphate (blue), and tripolyphosphate (green) melts.

Where the increased melt oxide content induces the systematically less-anodic oxidation of graphite, it demands correspondingly more-cathodic reduction potentials for PRR. Both potential shifts are similar in magnitude and direction, with the net effect being the apparent shift in the system's effective solvent window by approximately 250 mV cathodic as phosphoryl anhydride concentration decreases from 9.8 mol·kg^{-1} to 5.4 mol·kg^{-1}. We highlight especially that this trend is only observable due to our Na/Na^{+} reference; prior literature reports, owing to their reliance on graphitic pseudoreference electrodes, would observe no apparent shift in the phosphate reduction or carbon oxidation potentials, as they remain roughly constant relative to the graphite pseudoreference.

While Tafel behavior (**Figure 2-22**) is consistent (within error) in the low-current density regime, overpotentials for PRR increase dramatically as a function of anhydride concentration at higher current densities, consistent with a local depletion effect at the electrode surface. In addition to the previously observed 150 mV·dec^{-1} Tafel slope in pure metaphos-

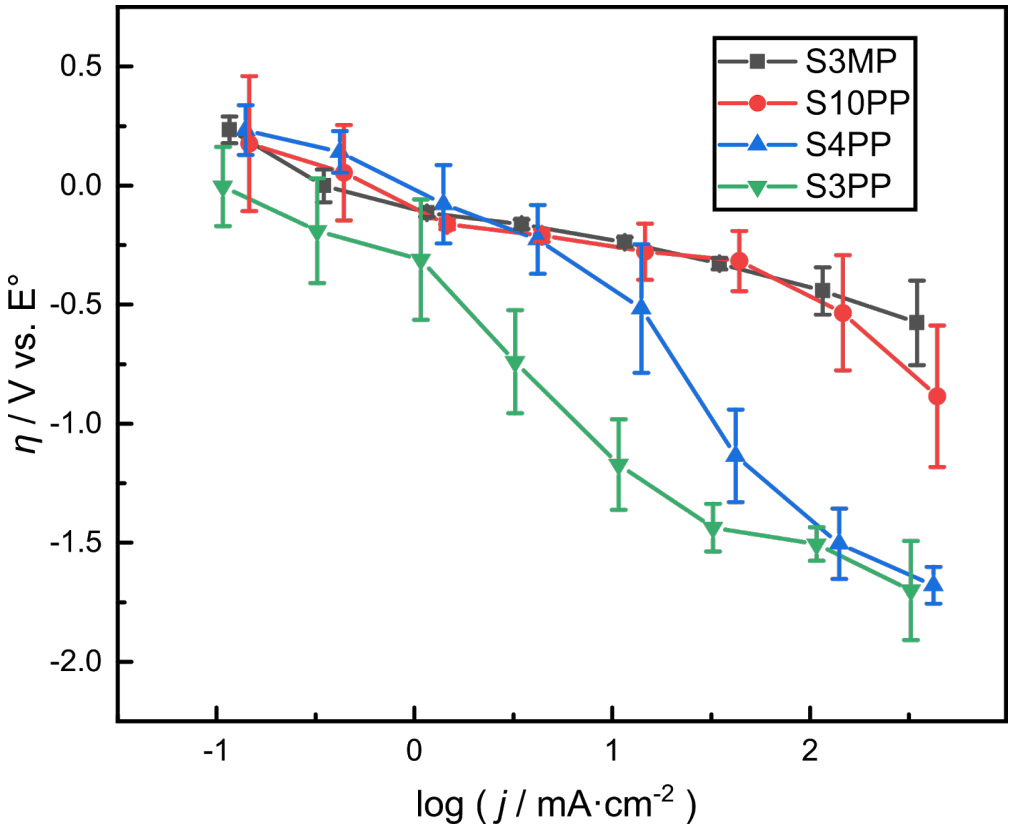

Figure 2-22. Plot of phosphate reduction overpotential as a function of current density in molten sodium trimetaphosphate (S3MP), sodium decapolyphosphate (S10PP), sodium tetrapolyphosphate (S4PP), and sodium tripolyphosphate (S3PP) melts. Error bars represent 95% confidence intervals computed from a set of three independent experimental setups, measurements for each setup themselves being reproduced in triplicate.

phate, we note in the low-anhydride melts an apparent parallel curve with apparent slope $150\,\mathrm{mV{\cdot}dec^{-1}}$ at overpotentials around $-1.5\,\mathrm{V}$. These potentials and this slope correlate well with prior literature reports of the 2-electron reduction of orthophosphate to surface-bound phosphite: $\mathrm{PO_4}^{3-} + 2\,\mathrm{e}^- \longrightarrow {}^{\star}\mathrm{PO_2}^- + 2\,\mathrm{O}^{2-}$.[39, 40]

We conclude that high local concentrations of phosphoryl anhydride linkages are crucial to promoting the low-overpotential reduction of metaphosphate over the energy-intensive reduction of orthophosphate, and that a high bulk concentration of phosphoryl anhydride linkages is necessary to preclude depletion effects at larger current densities. We further note that the reduction of orthophosphate may itself be occurring at low overpotentials relative to the thermodynamic potential for the reduction $\mathrm{PO_4}^{3-} + 2\,\mathrm{e}^- \longrightarrow \mathrm{PO_3}^{3-} + \mathrm{O}^{2-}$; unfortunately, we cannot assess this thermodynamic potential empirically from a triple-phase hollowed-electrode experiment as we can for the metaphosphate, as a pure sodium orthophosphate (SOP) melt (MP 1583 °C) is inaccessible at the temperatures of reaction. However, unlike the condensed phosphate species, thermochemical reference data on the enthalpies and entropies of formation[51–56] does allow us to estimate an E° value of approximately -1.9 V vs. RHE for this reaction using Hess' law (**Equation 2.9**) and the Nernst relation (**Equation 2.7**). This value is necessarily an approximation, as RHE is an aqueous formalism and cannot be compared directly to a liquid sodium electrode in a metaphosphate melt. Nevertheless, assuming analogous graphitic pseudoreference potentials (a large assumption, indeed), this value broadly falls within the range at which we might expect a zero-overpotential reduction of orthophosphate based on our Tafel data in **Figure 2-22**.

2.3 Concluding Remarks

Herein, we have elaborated a robust electroanalytical system for reproducibly interrogating the high-temperature reduction of condensed-phosphate molten salts to phosphorus, specifically addressing systemic flaws in the half-century-old electrochemical literature that pre-

clude product identification, product quantitation, separated counter/working gas flow analysis, and absolute potential referencing. For the first time, we demonstrate unambiguously that the sole product of this reduction is molecular white phosphorus and that the electrogeneration of this species proceeds at Faradaic efficiencies approaching unity. Through creative product dosing and trapping methodologies, we assess the thermodynamic potential for phosphate reduction, and further demonstrate that this process occurs at low overpotentials approaching the limit of electrochemical reversibility. Finally, we educe the crucial role of phosphoryl anhydride linkages as oxide acceptors in this process, identifying separate two-electron reduction mechanisms for orthophosphate and metaphosphate as a function of local phosphoryl anhydride linkage concentration at the electrode surface.

White phosphorus remains an irreplaceable precursor to numerous value-added chemicals, yet its synthesis has long been inextricable from the inefficient and intrinsically carbonaceous thermal process. With this work, we illuminate a truly sustainable alternative that exploits the immense economies of scale of phosphate fertilizer production to access the entire suite of phosphorus-derived chemicals. The ubiquitous starting material and comparatively mild conditions of reaction present the attractive possibility of point-of-use P_4 generation at existing fine chemical factories, obviating the need for transport and storage of this hazardous substance. In a completely decarbonized economy, electrolytic phosphorus synthesis may one day 'short-circuit' the thermal process entirely.

2.4 Experimental Details

All electrochemical experiments were conducted at a temperature of 800 °C using a Biologic VSP potentiostat using IR compensation values of no more than 20% for noncapacitive voltammetric studies (see **Appendix A.2** on page 193). Except where specified otherwise, a graphite electrode was employed as a pseudoreference electrode for all experiments, the potential of which was retroactively corrected for against a Na/Na^+ reference that was briefly

(15 seconds – 2 minutes) dipped into the melt before and after each experiment.

2.4.1 Calculation of Electrochemical Surface Area

Observed currents i were normalized to areal current densities j using electrochemical surface areas (ECSAs) assessed by methodologies explicated by Yoon and coworkers.[57] For bare graphite electrodes, specific capacitance values in aqueous solution were found to be approximately $20\,\mu F{\cdot}cm^{-2}$ relative to the geometric surface area, well in line with literature reports.[58] Within the melt, specific capacitances of approximately $100\,\mu F{\cdot}cm^{-2}$ for graphite were determined empirically from geometric surface area. Having determined these values, the ECSAs of an electrode could be determined in terms of the double-layer capacitances (DLCs) of the electrode, both in the melt preceding and following every experiment, as well as within the melt to assess the depth of electrode immersion and ensure the absence of a short between an electrode and the glassy carbon crucible.

DLC values were assessed by CV scans spanning $\pm 50\,mV$ around the solution OCP at scanrates of $10\,mV{\cdot}s^{-1}$, $20\,mV{\cdot}s^{-1}$, $30\,mV{\cdot}s^{-1}$, $40\,mV{\cdot}s^{-1}$ and $50\,mV{\cdot}s^{-1}$ at IR compensations of 80%. The resultant capacitive CV traces were used to calculate the total capacitive current i, as the difference of the cathodic current i_c and the anodic current i_a. These currents are related to the overall electrode capacitance C by the relation

$$C = \frac{1}{2}\frac{\partial(i_a - i_c)}{\partial(\text{scan rate})}. \tag{2.19}$$

Hence, the electrode capacitance (and hence ECSA) could be determined by plotting the capacitive currents as a function of scan rate and dividing the slope of the resulting linear fit, as demonstrated in **Figure 2-23**.

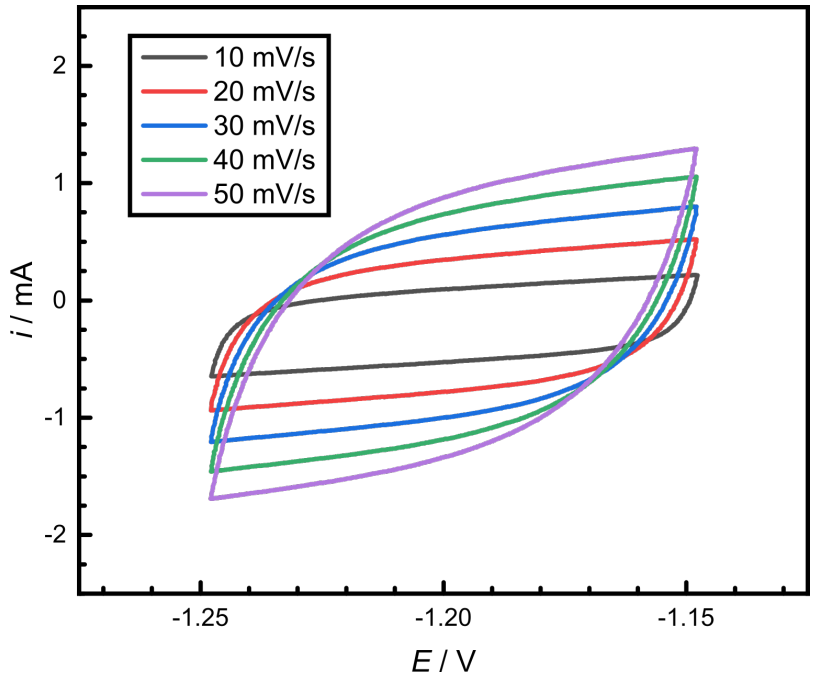

(a) Representative cyclic voltammograms of a graphite electrode scanning ±50 mV around OCP at scanrates of 10 $mV \cdot s^{-1}$, 20 $mV \cdot s^{-1}$, 30 $mV \cdot s^{-1}$, 40 $mV \cdot s^{-1}$ and 50 $mV \cdot s^{-1}$. Electrolyte is 0.1 M aqueous sodium perchlorate solution.

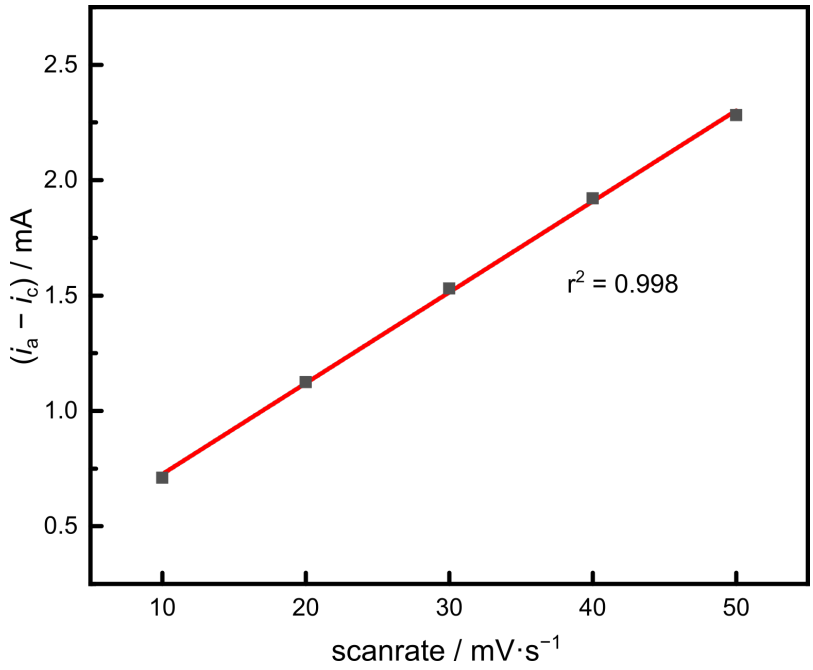

(b) Representative linear fit for scanrate dependence of capacitive current at OCP in **(a)**. At an aqueous specific capacitance of 20 $\mu F \cdot cm^{-2}$, this slope corresponds to an electrode surface area of 1.08 cm^2.

Figure 2-23. Methodology for capacitive ECSA determination.

2.4.2 ^{31}P NMR Analysis and Quantitation

^{31}P NMR spectra were recorded with either Bruker AVANCE-400 or Bruker AVANCE-Neo-500 spectrometers and processed using MestReNova software. ^{31}P shifts are given in ppm with respect to externally referenced triphenylphosphine (TPP) (δ = -6.0 ppm) or phosphonoacetic acid (δ = -17.0 ppm). Coupling constants are reported as J-values in Hz.

2.4.2.1 ^{31}P NMR Identification of P_4

For the collection of ^{31}P NMR spectra of molecular P_4, such as that seen in **Figure 2-13** on page 63, the reactor cold trap (wrapped in aluminum foil) was sealed following a bulk electrolysis (typically around 50 mA·cm^{-2} for several hours). The cold trap was then pumped into a N_2 glovebox, where the contents of the trap were dissolved with approximately 2 mL carbon disulfide (CS_2) along with a known quantity of TPP (as an internal standard) as well as approximately 25 mg (0.072 mmol) of chromium(III) acetylacetonate as a paramagnetic relaxation agent. The sample was then transferred to a J. Young tube for ^{31}P NMR analysis. To ensure full spin relaxation for quantitation, a delay time of 10.0 s was used.

2.4.2.2 Quantitative ^{31}P NMR

Quantitative ^{31}P NMR techniques were applied for the calculation of total reduced phosphorus yield. Phosphorus residues may be collected from three primary locations: the cold trap, the bleach trap, and the accretions within the reactor head. As we have already established the identity of the reduced phosphorus species to be P_4 with the preceding NMR evidence, here we dissolve all products in a 7.4% w/w aqueous solution of sodium hypochlorite to facilitate the quantitation of all reduced products. This bleach solution is capable of dissolving red phosphorus accretions such as those depicted in **Figure 2-11b** and **Figure 2-12** on page 62, oxidizing the elemental phosphorus up to soluble ortho- and polyphosphate species. These products may then be quantified by aqueous ^{31}P NMR against an internal standard of phosphonoacetic acid, again using a delay time of 10.0 s to ensure full spin re-

laxation for quantitation. For quantitation of phosphorus in the bleach trap, an aliquot is taken and analyzed against a phosphonoacetic acid internal standard to determine the concentration of phosphorus in the bleach trap, which is then multiplied by the volume of the trap. The total phosphorus content in the bleach trap, cold trap, and reactor head are then totaled together for assessment of the overall phosphorus yield N_{P}.

2.4.2.3 Calculation of Faradaic Efficiency

The Faradaic efficiency (FE%) of a process, also known as the overall current efficiency, may be understood as the fraction of the total charge passed that proceeds towards a desired reaction:

$$\mathrm{FE}\% = \frac{Q_{\mathrm{desired}}}{Q_{\mathrm{total}}}.$$

In this regard it is equivalent to the time integral of instantaneous current efficiency

$$\int_0^t \frac{i_{\mathrm{desired}}}{i_{\mathrm{total}}} dt,$$

and as such may be understood to represent the selectivity of an electrochemical process: the rate of the desired electrochemical transformation as a proportion of all applied current.[48]

We may assess Q_{PRR} in coulombs for phosphate reduction from the total molar quantity of phosphorus N_{P} collected in the cold trap, bleach trap, and reactor head:

$$Q_{\mathrm{PRR}} = N_{\mathrm{P}} \times \frac{5\,\mathrm{mol\ e^-}}{1\,\mathrm{mol\ P}} \times 96\,485\,\mathrm{C{\cdot}mol^{-1}}.$$

We can then normalize this observed value by the gas flow fraction $\frac{m_{\mathrm{out}}}{m_{\mathrm{in}}}$ (as measured by the flow meters described in **Section 2.2.1.5** on page 56) to account for product losses from o-ring leakage, all of which occurs within the cell's working compartment:

$$Q_{\mathrm{PRR,actual}} = Q_{\mathrm{PRR,observed}} \div \frac{m_{\mathrm{out}}}{m_{\mathrm{in}}}.$$

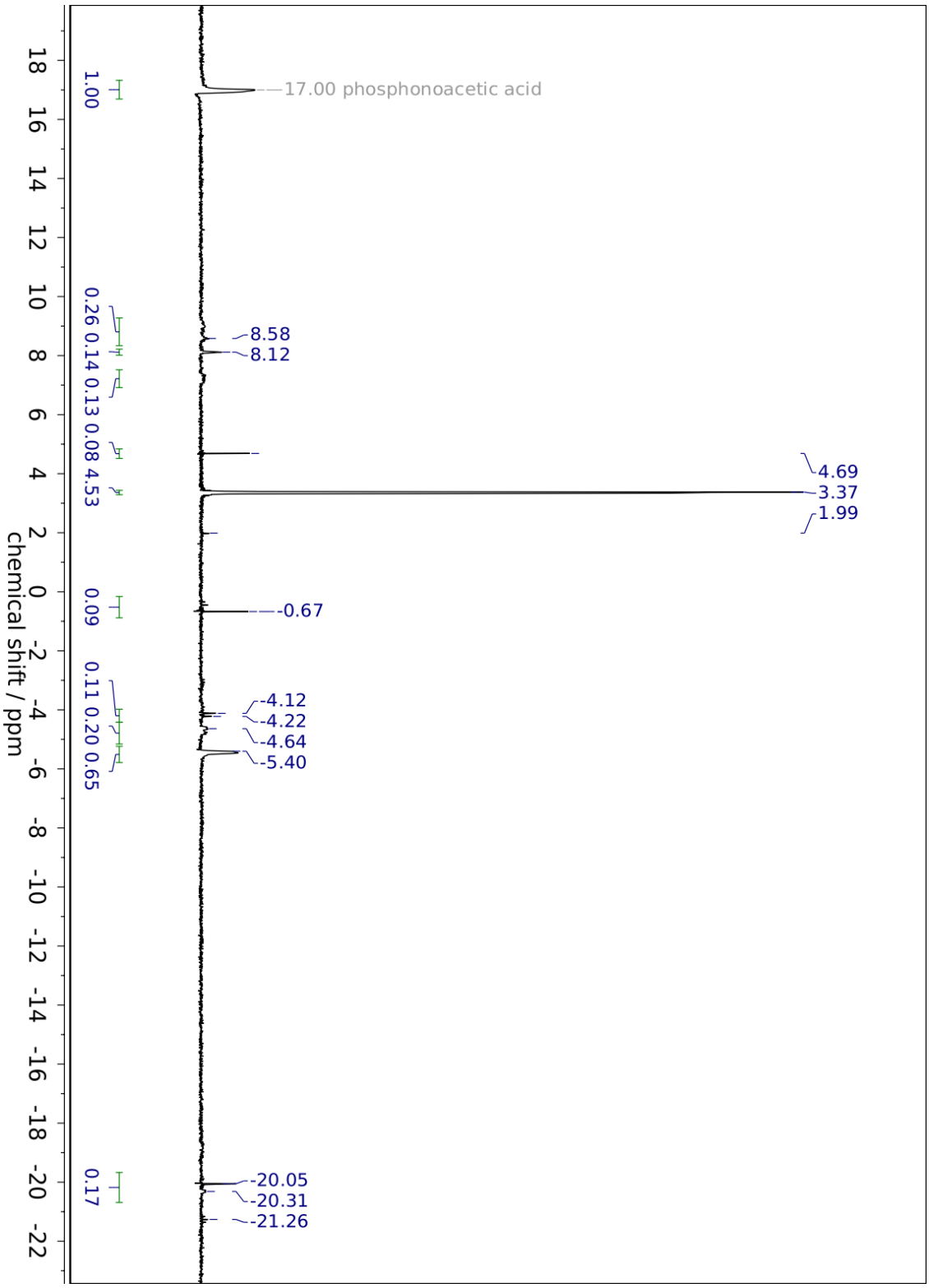

Figure 2-24. Representative quantitative ^{31}P NMR spectrum. Integrals normalized to phosphonoacetic acid internal standard at +17 ppm.

Meanwhile, Q_{total} is determined from the current integral $\int_0^t i_{\text{total}} dt$, which for a galvanostatic experiment is merely $i_{\text{applied}} t$. Putting these values together, we have:

$$\text{FE}\% = \frac{N_{\text{P}} \times \frac{5\,\text{mol e}^-}{1\,\text{mol P}} \times 96\,485\,\text{C}\cdot\text{mol}^{-1}}{i_{\text{applied}} t \times \frac{m_{\text{out}}}{m_{\text{in}}}}, \tag{2.20}$$

which for the NMR spectrum depicted in **Figure 2-24** and its associated galvanostatic bulk electrolysis **Figure 2-10** gives us

$$\begin{aligned}\text{FE}\% &= \frac{1.40\,\text{mmol P} \times \frac{5\,\text{mol e}^-}{1\,\text{mol P}} \times 96\,485\,\text{C}\cdot\text{mol}^{-1}}{75\,\text{mA} \times 13\,878\,\text{s} \times \frac{170\,\text{cm}^3\cdot\text{min}^{-1}}{250\,\text{cm}^3\cdot\text{min}^{-1}}} \\ &= 94.9\%.\end{aligned}$$

2.4.3 Gas Chromatography of Gas Outflow Streams

For analysis of counter electrode outflow streams, GC analysis was performed by injection into a Multi-Gas Analyzer (#3; SRI Instruments) equipped with a thermal conductivity detector, methanizer, and flame ionization detector in series after Molsieve 13x and Hayesep D Columns. With the counter compartment gas flowrate set to 60 sccm, baseline measurements were collected by injecting gas from the counter electrode outflow stream at rest, while experimental values were collected by injecting gas from the counter electrode outflow stream while passing a fixed cathodic current of 75 mA through the working electrode (and thereby an equivalent anodic polarization through the counter electrode).

Sample	**Baselines**		**Avg**	**Experiments**		**Avg**	**Δ**
CO	0.532799	0.971986	0.7523925	272.9964	298.872	285.9342	285.1818075
CO_2	25.95813	19.27423	22.61618	7379.202	7567.924	7473.563	7450.94682
CH_4	0.687346	0.448058	0.567702	0.25598	0.142211	0.1990955	-0.3686065

Table 2.1. Raw GC data for counter compartment outflow streams at open-circuit potential (baseline values) and under polarization (experimental values). CH_4 values are used as a control.

The results, tabulated in **Table 2.1**, show a statistically significant increase in the gas

fractions of CO and CO_2 while the counter electrode is under anodic polarization. These values correspond to a counter electrode gas outflow stream that is 96.31% CO_2 and 3.69% CO, equivalent to a net electron efficiency of 3.93 electrons per atom of carbon (out of a theoretical 4 electrons per carbon for the total conversion of $C \longrightarrow CO_2$, and relative to a value of 2 electrons per carbon for the incomplete combustion $C \longrightarrow CO$ used in the thermal process.

The generation of CO may be attributable to either the partial oxidation of graphite or the comproportionation of CO_2 with carbon, $CO_2 + C \rightleftharpoons 2\,CO$, a process known as the Boudouard reaction. At a temperature of 800 °C, this equilibrium lies markedly in favor of carbon monoxide, with equilibrium gas compositions approaching 90% CO.[59–61]

2.4.4 Current-Overpotential Studies

The collection of current-overpotential data for Tafel studies (**Figure 2-18** on page 70, **Figure 2-22** on page 78, and **Figure A-13** on page 213) entailed capacitive CV collection for ECSA determination (**Section 2.4.1**), followed by chronopotentiometric reduction. ECSA experiments were performed pre- and post-experiment in both aqueous and molten-salt conditions and found not to substantially differ (see **Figure A-12** on page 212); however, due to the fixed galvanostatic currents, variation in the electrode surface areas between experiments (due to variable depth of immersion in the melt) is responsible for the slight variation in areal current density values in these plots.

2.4.4.1 Collection of Galvanostatic Tafel Data

Electrolyses were performed galvanostatically with a fixed current series of 10 µA, 30 µA, 100 µA, 300 µA, 1 mA, 3 mA, 10 mA, 30 mA, 100 mA and 300 mA with 30 second traces and 30 seconds rest periods at OCP between electrolyses; potentials were recorded as peak cathodic (most negative) voltages recorded within each galvanostatic trace. Each galvanostatic series was performed in triplicate in every experimental setup, and experimental setups themselves

were replicated between two and nine times each to account for random variations in reactor arrangement. Error bars were calculated from standard deviations of these data sets σ as 95% confidence intervals: 1.95996σ.

2.4.4.2 Determination of Overpotential

Overpotentials for phosphate reduction were determined for each melt in this study relative to E° values determined by the hollowed-electrode method described in **Section 2.2.3.2** on page 66. A hollowed electrode was immersed in each melt, taking care to ensure that no air bubbles would be trapped in the electrode hollow upon being lowered into the melt. P_4 was generated in the electrode hollow by reductive galvanostatic electrolysis at $10\,mA{\cdot}cm^{-2}$ for one minute, and E° was determined to be the minimum OCP, not counting the relaxation from the galvanostatic reduction (see **Figure 2-17b** on page 69).

2.4.4.3 Methodology for Tafel Analysis

Tafel slopes and errors were assessed by least-squares linear fit upon the 'macropolarization' reduction regime, defined as current densities $\geq 1\,mA{\cdot}cm^{-2}$, then converted to units of $mV{\cdot}dec^{-1}$.

References

[1] Ruttenberg, K. C. In *Treatise on Geochemistry (Second Edition)*; Holland, H. D., Turekian, K. K., Eds.; Elsevier: Oxford, 2014; pp 499–558.

[2] Buendía, C.; Kleidon, A.; Porporato, A. *Biogeosciences* **2010**, *7*, 2025–2038.

[3] Oelkers, E. H.; Valsami-Jones, E.; Roncal-Herrero, T. *Mineral. Mag.* **2008**, *72*, 337.

[4] Peltzer, D. A.; Wardle, D. A.; Allison, V. J.; Baisden, W. T.; Bardgett, R. D.; Chadwick, O. A.; Condron, L. M.; Parfitt, R. L.; Porder, S.; Richardson, S. J.; Turner, B. L.; Vitousek, P. M.; Walker, J.; Walker, L. R. *Ecol. Monogr.* **2010**, *80*, 509–529.

[5] Paytan, A.; McLaughlin, K. *Chem. Rev.* **2007**, *107*, 563–576.

[6] Deloitte Sustainability,; British Geological Survey,; Bureau de Recherches Géologiques et Minières,; Netherlands Organisation for Applied Scientific Research, 2017, DOI: doi:10.2873/398823.

[7] Cushman, G. T. *Guano and the Opening of the Pacific World: A Global Ecological History*; Cambridge University Press, 2013.

[8] Greenhill, R. G.; Miller, R. M. *J. Lat. Am. Stud.* **1973**, *5*, 107–131.

[9] Szpak, P.; Millaire, J.-F.; White, C. D.; Longstaffe, F. J. *J. Archaeol. Sci.* **2012**, *39*, 3721–3740.

[10] Manner, H. I.; Thaman, R. R.; Hassall, D. C. *Aust. Geogr.* **1985**, *16*, 185–195.

[11] James, J. C. *Am. Lit. Hist.* **2012**, *24*, 115–142.

[12] Geeson, M. B.; Cummins, C. C. *ACS Cent. Sci.* **2020**, *6*, 848–860.

[13] Schipper, W. *Eur. J. Inorg. Chem.* **2014**, *2014*, 1567–1571.

[14] Ohtake, H., Tsuneda, S., Eds. *Phosphorus Recovery and Recycling*; Springer Singapore, 2019.

[15] Slootweg, J. C. *Curr. Opin. Green Sustain. Chem.* **2020**, *23*, 61–66.

[16] Cordell, D.; Drangert, J.-O.; White, S. *Glob. Environ. Change* **2009**, *19*, 292–305.

[17] Walan, P.; Davidsson, S.; Johansson, S.; Höök, M. *Resour. Conserv. Recycl.* **2014**, *93*, 178–187.

[18] USGS, *Mineral Commodity Summaries 2021*; Commodity Statistics and Information, 2021; p 200.

[19] FAO, *World Fertilizer Trends and Outlook to 2022*; FAO: Rome, Italy, 2019.

[20] Roberts, T. L. *Procedia Eng.* **2014**, *83*, 52–59.

[21] Grant, C. A.; Sheppard, S. C. *Hum. Ecol. Risk Assess.* **2008**, *14*, 210–228.

[22] Lehr, J. R.; Frazier, A. W.; Smith, J. P. *J. Agric. Food Chem.* **1966**, *14*, 27–33.

[23] Witsenplein, W. Werkwijze voor de elektrolytische verwijdering van zware metalen uit fosforzuur. 1990.

[24] Greenwood, N. N.; Earnshaw, A. *Chemistry of the Elements*, 2nd ed.; Butterworth-Heinemann: Oxford ; Boston, 1997.

[25] Marini, M.; Caro, D.; Thomsen, M. *Sci. Tot. Environ.* **2020**, *745*, 140876.

[26] Hopp, V. *Submerged-arc furnace for phosphorus production* **2019**,

[27] Diskowski, H.; Hofmann, T. *Ullmann's Encyclopedia of Industrial Chemistry*, seventh ed.; Wiley-VCH, 2000.

[28] Stephenson, C. C.; Potter, R. L.; Maple, T. G.; Morrow, J. C. *The Journal of Chemical Thermodynamics* **1969**, *1*, 59–76.

[29] Dorn, F. W.; Harnisch, H. *Chem. Ing. Tech.* **1970**, *42*, 1209–1215.

[30] Ponak, C. *Adv. Mater. Lett.* **2020**, *11*, 20071535–20071535.

[31] Caton, R. D.; Freund, H. *Anal. Chem.* **1963**, *35*, 2103–2108.

[32] Vignarooban, K.; Xu, X.; Arvay, A.; Hsu, K.; Kannan, A. M. *Appl. Energy* **2015**, *146*, 383–396.

[33] Casey, E. J.; Dubois, A. R. *Can. J. Chem.* **1971**, *49*, 2733–2745.

[34] Centnerszwer,; Szper, *Bull. Intern. Acad. Polonaise* **1931**, *A*, 364.

[35] Andreeva, V. N. *Ukr. Khim. Zh.* **1955**, *21*, 569.

[36] Yocom, P. N. The Preparation of Transition Metal Phosphides by Fused Salt Electrolysis. Ph.D. thesis, University of Illinois, 1958.

[37] Delimarskii, Y. K.; Andreeva, V. N. *Zh. Neorg. Khim.* **1960**, *5*, 1800–1805.

[38] Laitinen, H. A.; Lucas, K. R. *Journal of Electroanalytical Chemistry (1959)* **1966**, *12*, 553–563.

[39] Franks, E.; Inman, D. *Journal of Electroanalytical Chemistry and Interfacial Electrochemistry* **1970**, *26*, 13–26.

[40] Franks, E.; Inman, D. *J Appl Electrochem* **1971**, *1*, 73–78.

[41] Plambeck, J. A. **1976**, 373–388.

[42] Haupin, W. E. *J. Chem. Educ.* **1983**, *60*, 279.

[43] Prasad, S. *J. Braz. Chem. Soc.* **2000**, *11*, 245–251.

[44] Frank, W. B.; Haupin, W. E.; Vogt, H.; Bruno, M.; Thonstad, J.; Dawless, R. K.; Kvande, H.; Taiwo, O. A. *Ullmann's Encyclopedia of Industrial Chemistry*; Wiley-VCH, 2009.

[45] Inzelt, G. In *Handbook of Reference Electrodes*; Inzelt, G., Lewenstam, A., Scholz, F., Eds.; Springer: Berlin, Heidelberg, 2013; pp 331–332.

[46] Seitz, A. E.; Hippauf, F.; Kremer, W.; Kaskel, S.; Scheer, M. *Nat. Commun.* **2018**, *9*, 2–7.

[47] Bockris, J. O.; Nagy, Z. *J. Chem. Educ.* **1973**, *50*, 839.

[48] Bard, A. J.; Faulkner, L. R. *Electrochemical Methods: Fundamentals and Applications*, 2nd ed.; Wiley: New York, 2000; pp 458–464.

[49] Taylor, R. J.; Humffray, A. A. *Journal of Electroanalytical Chemistry and Interfacial Electrochemistry* **1975**, *64*, 63–84.

[50] Liu, D.; Li, X.; Wei, L.; Zhang, T.; Wang, A.; Liu, C.; Prins, R. *Dalton Trans.* **2017**, *46*, 6366–6378.

[51] Chase, M. W. *J. Phys. Chem. Ref. Data, Monograph 9* **1998**, 1–1951.

[52] Cox, J. D.; Wagman, D. D.; Medvedev, V. A. **1984**, 1.

[53] Irving, R. J.; McKerrell, H. *Trans. Faraday Soc.* **1967**, *63*, 2913–2916.

[54] Ashcroft, S. J.; Keen, E.; Mortimer, C. T. *Trans. Faraday Soc.* **1969**, *65*, 2851–2855.

[55] Rard, J. A.; Wolery, T. J. *J Solution Chem* **2007**, *36*, 1585–1599.

[56] Vieillard, P.; Tardy, Y. In *Phosphate Minerals*; Nriagu, J. O., Moore, P. B., Eds.; Springer: Berlin, Heidelberg, 1984; pp 171–198.

[57] Yoon, Y.; Yan, B.; Surendranath, Y. *J. Am. Chem. Soc.* **2018**, *140*, 2397–2400.

[58] Korzeniewski, C.; Conway, B. E. *Proceedings of the Symposium on the Electrochemical Double Layer*; Electrochemical Society Proceedings; The Electrochemical Society, 1997; Vol. 97; pp 349–350.

[59] Chen, P.; Zhang, H. B.; Lin, G. D.; Hong, Q.; Tsai, K. R. *Carbon* **1997**, *35*, 1495–1501.

[60] Wiberg, E.; Holleman, A. F.; Wiberg, N. *Inorganic Chemistry*; Academic Press, 2001.

[61] Basu, P. In *Biomass Gasification, Pyrolysis and Torrefaction (Third Edition)*; Basu, P., Ed.; Academic Press, 2018; pp 211–262.

[62] Bewick, A. *Electrochim. Acta* **1968**, *13*, 825–830.

[63] Bezold, D.; Dürr, T.; Singh, J.; Jessen, H. J. *Chem. – Eur. J.* **2020**, *26*, 2298–2308.

[64] Britz, D. *J. Electroanal. Chem. Interf. Electrochem.* **1978**, *88*, 309–352.

[65] Caldwell, A. H.; Lai, E.; Gmitter, A. J.; Allanore, A. *Electrochim. Acta* **2016**, *219*, 178–186.

[66] Cummins, C. C. *Daedalus* **2014**, *143*, 9–20.

[67] Elgrishi, N.; Rountree, K. J.; McCarthy, B. D.; Rountree, E. S.; Eisenhart, T. T.; Dempsey, J. L. *J. Chem. Educ.* **2018**, *95*, 197–206.

[68] Engels, K. R.; Nieuwhof, A.; Spijkerman, J. B. J. Removal of Cadmium from Phosphoric Acid-Containing Solutions. 1990.

[69] Fang, Y.-H.; Liu, Z.-P. *ACS Catal.* **2014**, *4*, 4364–4376.

[70] Geeson, M. B.; Cummins, C. C. *Science* **2018**,

[71] Gomes, H. I.; Dias-Ferreira, C.; Ottosen, L. M.; Ribeiro, A. B. *Chemosphere* **2015**, *131*, 157–163.

[72] Greenfield, S.; Clift, M. *Analytical Chemistry of the Condensed Phosphates*; Pergamon: Oxford, 1975.

[73] Hurst, T. L. In *Phosphorus and Its Compounds, Vol. II*; van Wazer, J. R., Ed.; Interscience: New York, 1961; Chapter 18, pp 1149–1219.

[74] Ijije, H. V.; Lawrence, R. C.; Siambun, N. J.; Jeong, S. M.; Jewell, D. A.; Hu, D.; Chen, G. Z. *Faraday Discuss.* **2014**, *172*, 105–116.

[75] Li, Z.; Yu, J.-W.; Neretnieks, I. *Environ. Sci. Technol.* **1998**, *32*, 394–397.

[76] Mabbott, G. A. *J. Chem. Educ.* **1983**, *60*, 697.

[77] Minh, D. P.; Ramaroson, J.; Nzihou, A.; Sharrock, P. *Ind. Eng. Chem. Res.* **2012**, *51*, 3851–3854.

[78] Mohamady, S.; Taylor, S. D. *Org. Lett.* **2013**, *15*, 2612–2615.

[79] Nicholson, R. S.; Shain, I. *Anal. Chem.* **1965**, *37*, 178–190.

[80] Piro, N. A.; Figueroa, J. S.; McKellar, J. T.; Cummins, C. C. *Science* **2006**, *313*, 1276–1279.

[81] Ren, J.; Lau, J.; Lefler, M.; Licht, S. *J. Phys. Chem. C* **2015**, *119*, 23342–23349.

[82] Roberts, T. L. *Procedia Eng.* **2014**, *83*, 52–59.

[83] Shepard, S. M.; Cummins, C. C. *J. Am. Chem. Soc.* **2019**, *141*, 1852–1856.

[84] Souilah, O.; Akretche, D. E.; Cameselle, C. *Electrochim. Acta* **2012**, *86*, 138–141.

[85] Thilo, E.; Schülke, U. *Angew. Chem. Int. Ed.* **1963**, *2*, 742–742.

[86] Tofan, D.; Cummins, C. C. *Angew. Chem. Int. Ed.* **2010**, *49*, 7516–7518.

[87] van Wazer, J. R. *Phosphorus and Its Compounds, Vol. I*; 1958; pp 717–800.

[88] Vanýsek, P. *Handbook of Chemistry and Physics: 93rd Edition*; Chemical Rubber Company, 2012; pp 5–80.

[89] Velian, A.; Nava, M.; Temprado, M.; Zhou, Y.; Field, R. W.; Cummins, C. C. *J Am Chem Soc* **2014**, *136*, 13586–13589.

[90] Wang, L.-P.; Tofan, D.; Chen, J.; Voorhis, T. V.; Cummins, C. C. *RSC Adv.* **2013**, *3*, 23166–23171.

[91] Weil, E. D. In *Flame - Retardant Polymeric Materials: Volume 2*; Lewin, M., Atlas, S. M., Pearce, E. M., Eds.; Springer US: Boston, MA, 1978; pp 103–131.

[92] Wendt, H.; Vogt, H.; Kreysa, G.; Kolb, D. M.; Engelmann, G. E.; Ziegler, J. C.; Goldacker, H.; Jüttner, K.; Galla, U.; Schmieder, H.; Steckhan, E. *Ullmann's Encyclopedia of Industrial Chemistry*, seventh ed.; Wiley-VCH, 2003.

[93] Wu, H.; Ji, D.; Li, L.; Yuan, D.; Zhu, Y.; Wang, B.; Zhang, Z.; Licht, S. *Adv. Mater. Technol.* **2016**, *1*, 1600092.

Chapter 3

High-Pressure Catalysts for Electrochemical Reduction of Nitrogen to Ammonia

Contents

3.1 Introduction

Ammonia (NH_3) is a key ingredient in fertilizers, making its supply critical to global food security. Most of the world's ammonia supply, well over 100 million tons per year, is produced by the legacy Haber-Bosch process (HBP), which applies high temperatures and pressures to effect the conversion of nitrogen and hydrogen gases to ammonia. While efficient, this legacy process is extraordinarily capital-intensive, requiring multiple purifiers, separators, and reformers, making point-of-use production of ammonia via HBP virtually impossible. Moreover, hydrogen for the process is produced by steam reforming of natural gas, leading to an enormous carbon footprint. N_2 reduction via the electrochemical nitrogen reduction reaction (NRR) simultaneously addresses the twin issues of carbon cost and process complexity of HBP, allowing both for integration with existing renewable technology and presenting the possibility of decentralized, distributed fertilizer production directly in fields where needed. In addition to providing a sustainable alternative to the incumbent fossil fuel-dependent HBP, such cells would have great application in developing regions without access to legacy ammonia production infrastructure. Clearly, global food security, particularly in the developing world, could be enabled via the development of such low-carbon, distributed technologies for the production of fertilizer in the form of ammonia at the point of use.

3.1.1 The Global Role of Nitrogen

Nitrogen is, by virtually any metric, the only plant macronutrient of greater importance than phosphorus. While phosphorus is necessary to (for example) produce the ribose-phosphate backbone of nucleic acids, nitrogen is not only found in all nucleotides but is further ubiquitous in every amino acid that constitute any protein a cell may require, on top of its inclusion in molecules like the crucial chromophore chlorophyll. Like phosphorus, nitrogen is frequently a growth-limiting nutrient for many plants; however, while the bioavailability of phosphorus is frequently constrained by its environmental scarcity, this certainly cannot be said of ni-

trogen, which comprises 78% of Earth's atmosphere. Rather, the limiting hurdle of nitrogen bioavailability is the cleavage of the normally-inert N≡N triple-bond, among the strongest chemical linkages broken in any biogeochemical cycle. Although the overall energetics of the reduction of nitrogen to form ammonia are actually thermodynamically downhill, with a standard enthalpy change (ΔH°) of $-45.3\,\mathrm{kJ{\cdot}mol^{-1}}$ NH_3, the activation energy (E_a) that must be overcome to effect this transformation is substantial (estimated E_a $400\,\mathrm{kJ{\cdot}mol^{-1}}$).

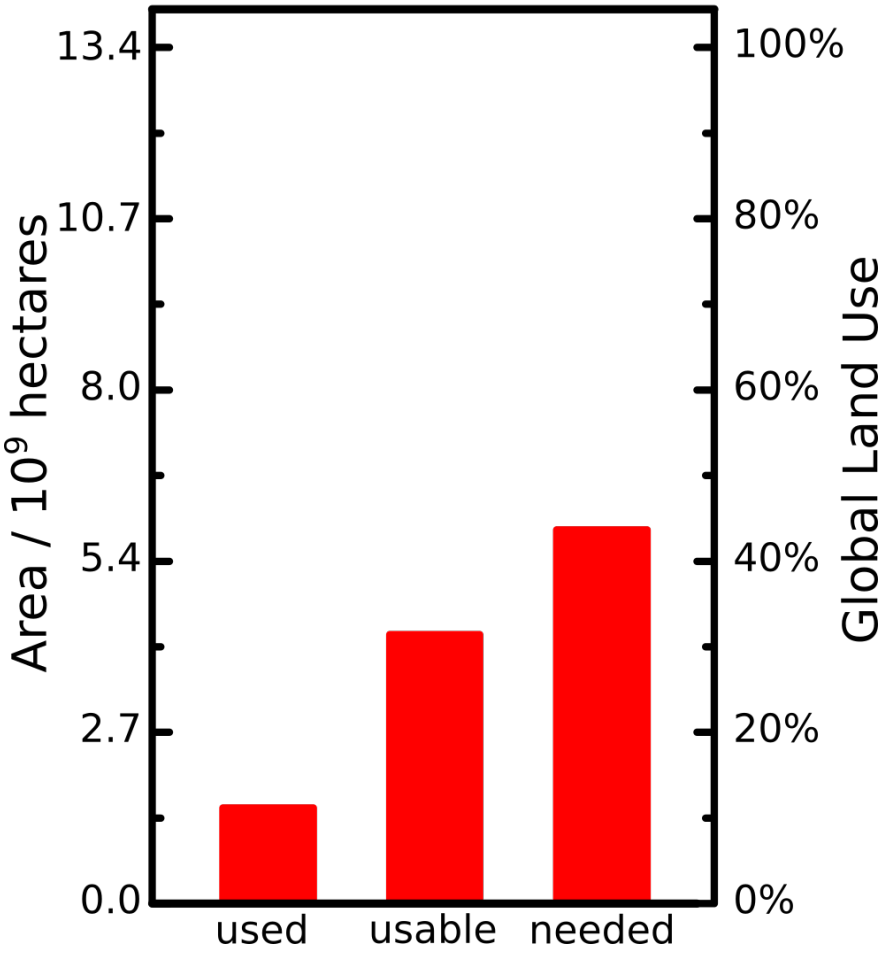

Figure 3-1. From left to right: current global land area usage for agriculture; total arable land area on Earth; land area needed to feed current human population at 1900-era (pre-artificial fertilizer) crop productivity rates.

Every year, hundreds of megatons of artificial fertilizers are produced across the globe. The generation of these artificial fertilizers is essential for supporting a global population nearing 8 billion people, as many high yield nutritious crops are dependent on the nutrients

in these fertilizers to mitigate the degradation of agriculturally useable soil. By some estimates, this artificial fertilization is responsible for feeding over 3 billion people around the globe.[1] Indeed, as depicted in **Figure 3-1**, there does not exist enough arable land on Earth to feed the current human population without the use of artificial fertilizers; only about 31% of Earth's landmass is considered suitable as cropland, while at pre-artificial fertilizer cropland fertility rates (*c.* 1900), upwards of 44% of all land on Earth would be required to feed 8 billion people. It is understandable, then, why the development of such synthetic fertilizers has been heralded as "the detonator of the population explosion" and "the most important invention of the 20th century".[2, 3] Through this innovation, the human population has boomed by nearly an order of magnitude since the turn of the century, well beyond any 'natural' carrying capacity for our planet.[4, 5]

3.1.2 Industrial Methods for Processing Nitrogen

The management of bioavailable nitrogen for crop fertilization is older than human civilization, predating written history by several millennia. The practice of crop rotation has existed nearly as long as agriculture; farmers from Mesopotamia to Ancient China to Imperial Rome quite literally reaped the benefits of annual crop variation, including soil aeration and management of weeds and pests. In particular, the alternation of energy-dense, soil-depleting cereal crops with taprooted, soil-enriching legumes has been known since prehistory.[6–8] What the ancient farmers of Sumer or the Indus Valley could not have possibly comprehended was the crucial role of symbiotic *Rhizobia* bacteria within the root nodules of leguminous plants, absorbing atmospheric nitrogen and returning it to the soil as ammonia. These nitrogen-fixating microorganisms are members of the *diazotrophs*, the only known living creatures capable of effecting the activation of N_2.

That is, until 1775, when Joseph Priestley related for the first time in the Western scientific literature the acidification of 'phlogisticated air' (dinitrogen gas) by electric sparks.[9] Subsequently, Henry Cavendish demonstrated that this phenomenon was not due to the for-

mation of 'fixed air' (carbon dioxide) as Priestley presumed, but what we now know as nitric and nitrous acids.[10–12] A little over a century later, this process was commercialized for the first time, using an electric arc to effect the synthesis of artificial nitrogenous fertilizers from air at an industrial scale.[i]

3.1.2.1 The Birkeland-Eyde Process

Kristian Birkeland and Sam Eyde began development of an industrial reactor for electric-arc nitrogen fixation in 1903 in central Norway. By passing a 50 Hz alternating current at potentials as high as 5000 V, an electric arc would be generated that was subsequently drawn into a disc of high-temperature plasma by a separate electromagnet (**Figure 3-2**). Air forced through this aperture would react to form nitric oxide (**Equation 3.1**), and through a mixture of further oxidation and disproportionation in water, would produce nitric acid suitable for purification and concentration by fractional distillation (**Equation 3.2**). The net effect of this reaction was the reaction of atmospheric concentrations of nitrogen and oxygen with water to produce nitric acid (**Equation 3.3**), from which any number of commercially valuable nitrates could be easily synthesized.[14–16]

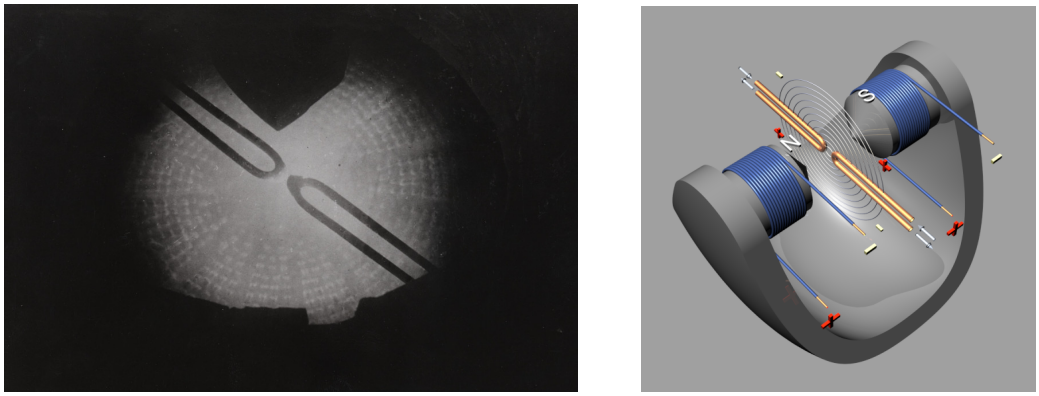

(a) **(b)**

Figure 3-2. (a) Photo of copper electrodes for electric arc generation for the Birkeland-Eyde process (BEP). **(b)** Diagram of reactor layout for Birkeland-Eyde plasma disc production.[17]

[i] Nature herself, of course, has been fixing nitrogen to NO_x by electric arc for billions of years. Approximately 14.4 Mt of nitrogen dioxide are generated in the atmosphere by lightning strikes each year.[13]

$$\mathrm{N_2 + O_2 \longrightarrow 2\,NO} \tag{3.1}$$

$$\mathrm{2\,NO + O_2 \longrightarrow 2\,NO_2}$$

$$\mathrm{3\,NO_2 + H_2O \longrightarrow 2\,HNO_3 + NO}$$

$$\mathrm{4\,NO + 3\,O_2 + 2\,H_2O \longrightarrow 4\,HNO_3} \tag{3.2}$$

$$\mathrm{2\,N_2 + 5\,O_2 + 2\,H_2O \longrightarrow 4\,HNO_3} \tag{3.3}$$

This reaction was presumed to occur thermally at the intense temperatures of the electric arc, estimated at 3500 °C.[17] Even at the time, however, some workers speculated on the possibility of direct electrochemical activation of the N≡N bond.[18] Unfortunately for Birkeland and Eyde, the high power demand of their process[ii] – approximately 15 $\mathrm{MW{\cdot}h{\cdot}t^{-1}}$ of $\mathrm{HNO_3}$ – rendered it incapable of competing with more-economical processes, and the BEP was phased out of use by the early 1920s.

3.1.2.2 The Frank-Caro Process

Contemporaneous with the BEP but more commercially successful was the Frank-Caro process (FCP), also called as the cyanamide process after its terminal product. In 1893, Henri Moissan, a pioneer in carbide chemistry, related the synthesis of calcium carbide from lime (**Equation 3.4**), upon which Adolph Frank and Nikodem Caro subsequently demonstrated in 1895 the absorption of nitrogen gas to form calcium cyanamide ($\mathrm{CaCN_2}$) at elevated tem-

[ii] Norway was a deliberate choice by Birkeland and Eyde for this exact reason; their reactors were built in conjunction with (large for the time) hydroelectric power facilities enabled by the favorable Norwegian geography. The irony is not lost on this author that among the first implementations of industrial-scale nitrogen fixation was a zero-carbon electrocatalytic process powered solely by renewable energy.

peratures (**Equation 3.5**). [19, 20]

$$\mathrm{CaO} + 3\,\mathrm{C} \longrightarrow \mathrm{CaC_2} + \mathrm{CO} \tag{3.4}$$

$$\mathrm{CaC_2} + \mathrm{N_2} \longrightarrow \mathrm{CaCN_2} + \mathrm{C} \tag{3.5}$$

$$\mathrm{CaCN_2} + 3\,\mathrm{H_2O} \longrightarrow 2\,\mathrm{NH_3} + \mathrm{CaCO_3} \tag{3.6}$$

$$\mathrm{CaO} + \mathrm{N_2} + 2\,\mathrm{C} + 3\,\mathrm{H_2O} \longrightarrow 2\,\mathrm{NH_3} + \mathrm{CO} + \mathrm{CaCO_3}$$

Even though both the formation of the carbide and the cyanamide demanded temperatures of reaction exceeding 1000 °C, requiring the use of an arc furnace, the fact that the produced $\mathrm{CaCN_2}$ could be applied directly to fields as a nitrogenous fertilizer reduced the need for further processing relative to the BEP. When applied in this manner, the cyanamide would hydrolyse to produce bioavailable ammonia in a stoichiometry related by **Equation 3.6**. At an total power demand of about $12\,\mathrm{MW{\cdot}h{\cdot}t^{-1}}$ of $\mathrm{CaCN_2}$, calcium cyanamide produced by the FCP was the most common nitrogenous fertilizer for several decades, with production peaking in 1945 (even though by this point it had long been obsoleted by the Haber and Ostwald processes, *vide infra*).[21–24]

3.1.2.3 The Ostwald Process

$$4\,\mathrm{NH_3} + 5\,\mathrm{O_2} \longrightarrow 4\,\mathrm{NO} + 6\,\mathrm{H_2O} \tag{3.7}$$

$$4\,\mathrm{NO} + 3\,\mathrm{O_2} + 2\,\mathrm{H_2O} \longrightarrow 4\,\mathrm{HNO_3} \tag{3.2}$$

$$\mathrm{NH_3} + 2\,\mathrm{O_2} \longrightarrow \mathrm{H_2O} + \mathrm{HNO_3} \tag{3.8}$$

Although the Haber and Ostwald processes are inextricably intertwined in the modern age, the latter actually predates the former by nearly a decade. Wilhelm Ostwald detailed

in a 1902 patent that, passed over a heated metal mesh of platinum, palladium, rhodium, or iridium, ammonia and oxygen react to form nitric oxide and water (**Equation 3.7**). This reaction is promoted by temperatures around 600 °C and reactor pressures up to approximately 10 atmospheres. This nitric oxide can then be subsequently taken to nitric acid by the same combination of oxidation and disproportionation reactions seen in **Equation 3.2**. The Ostwald process remains the primary synthetic route to nitric acid today (**Equation 3.8**), and coupled with the Bosch-Meiser process constitute the principal pathways for nitrogenous fertilizer generation.[25, 26]

3.1.2.4 The Bosch-Meiser Process

$$2\,NH_3 + CO_2 \longrightarrow [NH_4]^+[H_2NCOO]^- \tag{3.9}$$

$$[NH_4]^+[H_2NCOO]^- \longrightarrow CO(NH_2)_2 + H_2O \tag{3.10}$$

$$2\,NH_3 + CO_2 \longrightarrow CO(NH_2)_2 + H_2O \tag{3.11}$$

The Bosch-Meiser process (BMP) was a substantial contributor in the obsoleting of the FCP, due primarily to the substantially greater nitrogen content per mass of urea relative to calcium cyanamide. In this process, ammonia is first reacted with carbon dioxide at high temperature and pressure to form ammonium carbamate (**Equation 3.9**), which then slowly decomposes to form urea and water (**Equation 3.10**). Although the theoretical route from ammonia to urea via ammonium carbamate had been theorized since the early 1880s, it was not until the Haber process provided an industrial-scale route to ammonia that

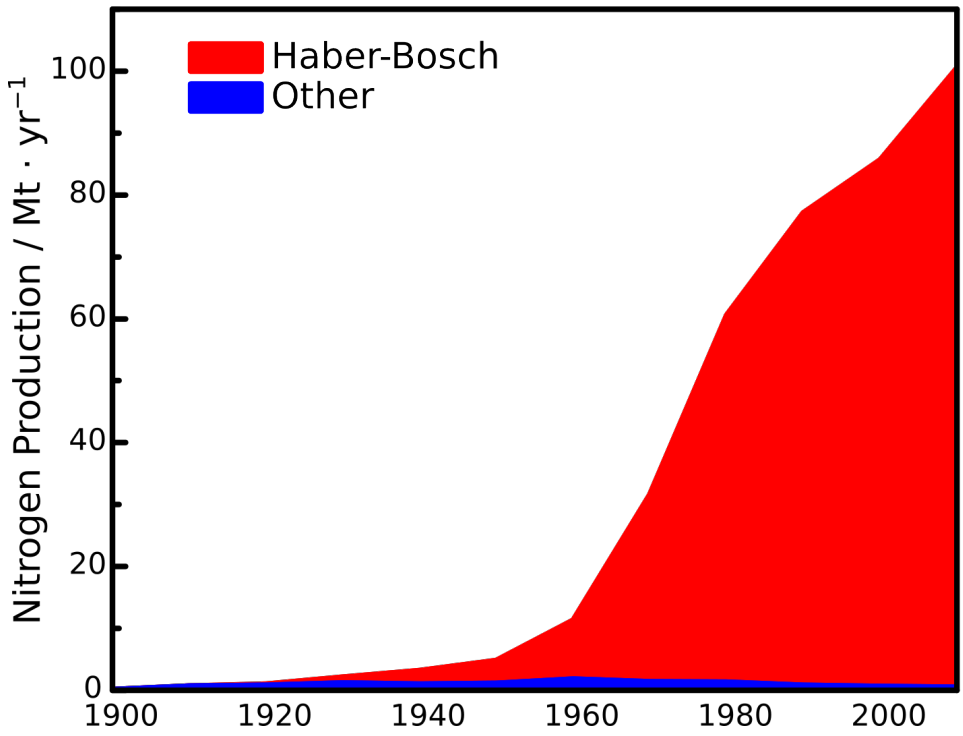

Figure 3-3. Annual global production of nitrogenous products by synthesis method.

the development of a complementary process for urea manufacture was developed.[iii] First patented in 1922, the BMP is still widely used today, effecting the conversion of carbon dioxide to urea at temperatures of about 200 °C and pressures of up to 300 atmospheres.[27–29]

3.1.2.5 The Haber-Bosch Process

Of course, all of the aforementioned processes have long been overshadowed by the Haber-Bosch process (HBP), in which N_2 and H_2 gases interact directly to form NH_3 (**Equation 3.12**), a reaction Fritz Haber first reported in his 1905 book.[30] By 1909, he empirically demonstrated the viability of the process, his lab-scale apparatus capable of generating over a kilogram of ammonia per day. By 1913, the German chemical corporation BASF had purchased

[iii] It is interesting to note that the 1:2 CO_2:NH_3 reactant stoichiometry of the BMP is actually *greater* than the 3:8 product stoichiometry of the full SMR-coupled HBP (**Equation 3.15** on page 104). As a result, coupled ammonia-urea plants consume *more* CO_2 via urea formation than is generated by the necessary methane reforming, thereby creating the appearance of carbon-negative fertilizer production. However, this phenomenon is illusory, as the fertilizing action of urea is its decomposition to form ammonium, which must necessarily release CO_2 equivalents; any semblance of a negative carbon footprint is therefore the result of outsourcing the site of CO_2 emissions from the factory to the field.

the patent and, thanks to the work of Carl Bosch, completed work on the very first HBP chemical plant, capable of producing nearly $6\,\mathrm{kt{\cdot}yr^{-1}}$ of pure anhydrous ammonia. One century later, annual ammonia production by the Haber-Bosch process was 138 Mt.[1, 31]

$$\mathrm{N_2 + 3\,H_2 \longrightarrow 2\,NH_3} \tag{3.12}$$

$$\mathrm{CH_4 + H_2O \longrightarrow CO + 3\,H_2} \tag{3.13}$$

$$\mathrm{CO + H_2O \longrightarrow CO_2 + H_2} \tag{3.14}$$

$$\mathrm{4\,N_2 + 3\,CH_4 + 6\,H_2O \longrightarrow 3\,CO_2 + 8\,NH_3} \tag{3.15}$$

Like most hydrogen gas around the world, H_2 for this process is produced primarily through steam methane reforming (SMR), in which high pressure steam and methane are flowed over a porous nickel catalyst to produce H_2 and CO (**Equation 3.13**). Additional hydrogen for the system, as well as the removal of catalyst-poisoning carbon monoxide, is further accomplished by the water-gas shift (WGS) reaction, in which steam and carbon monoxide further react over a copper or iron oxide catalyst to produce carbon dioxide and hydrogen gas (**Equation 3.14**).[32]

As pictured in **Figure 3.1**, practical implementation of the HBP is therefore limited by numerous infrastructural overheads into the reactor design, including multiple reformers, reactors, and separators. The reliance on natural gas as the hydrogen source is responsible for over half of the upkeep cost of ammonia production, while the logistic complexity evinced by coupled steam reforming prevents small-scale or distributed ammonia synthesis using Haber-type reaction schemes. In order to maintain catalyst activity and maximize ammonia yield, optimized HBP plants must incorporate multiple reactors for steam methane reforming, water-gas shift, desulfurization, and methanation, as well as separation columns, gas compressors, and heat-transfer agents to modulate temperature swings of nearly 1000 °C. As depicted in **Figure 3-4**, gas compression and refrigeration comprise the primary ener-

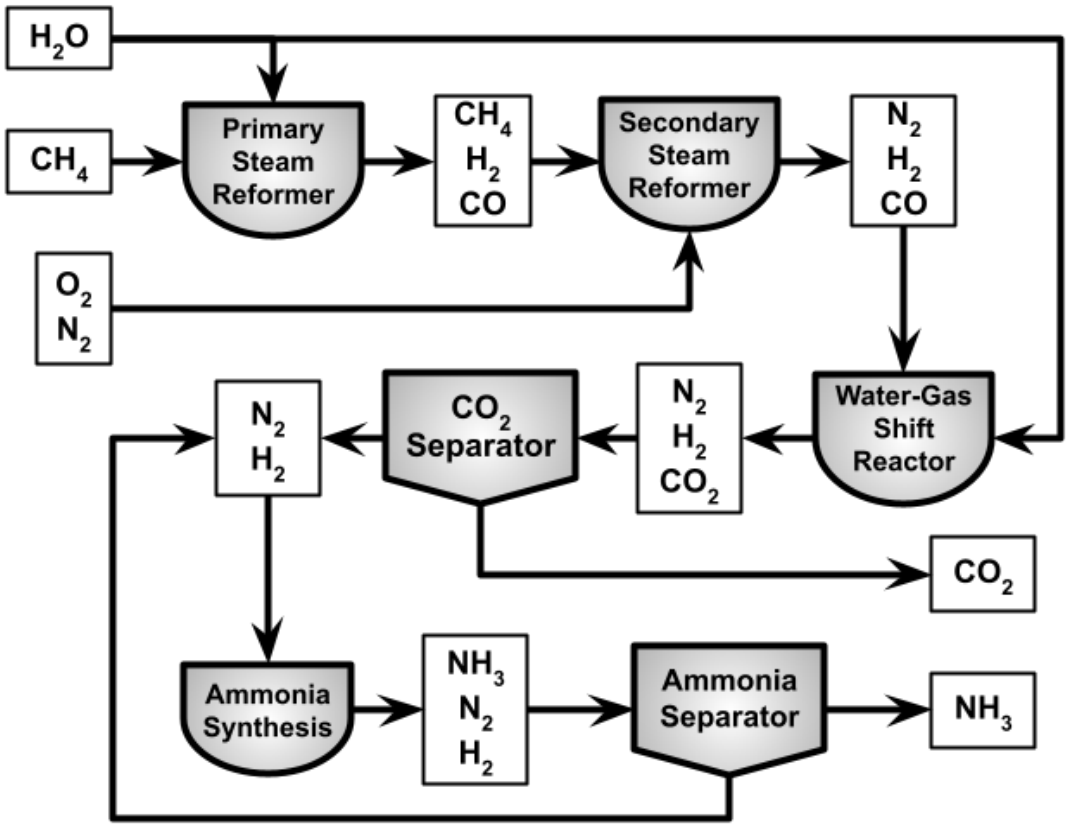

Scheme 3.1. Simplified process flow scheme of a typical steam reformer-coupled Haber-Bosch plant. Not pictured: methanation, desulfurization, secondary water-gas shift reactors.

getic costs of the Haber-Bosch process.[33–35]

After a century of improvements in reactor design and catalyst structure, the Haber-Bosch process is highly optimized, with a typical single-pass conversion efficiency of approximately 15%, with overall multi-pass process yields of up to 97% achievable with respect to nitrogen. These yields are achieved by reaction at high temperatures (around 500 °C) and pressures (around 20 MPa, though individual plants have been designed over a wide range of temperatures and pressures. Overall energy demand is approximately 7.8 $MW{\cdot}h{\cdot}t^{-1}$ of NH_3 for a typical iron oxide 'Mittasch' catalyst, which is preferred over marginally more-optimal ruthenium oxide catalysts (7.6 $MW{\cdot}h{\cdot}t^{-1}$ of NH_3) due to the substantial expense of ruthenium relative to iron. These energy efficiencies represent a catalytic system operating near the calculated limit of energy efficiency for ammonia synthesis by this process, estimated at 5.8 $MW{\cdot}h{\cdot}t^{-1}$ of NH_3, suggesting a fundamental limit on further optimization of this process. [35, 36]

All told, the need for large centralized HBP plants as the primary source of ammonia adversely affects the accessibility and widespread distribution of artificial fertilizer to remote areas of the world. Consequently, the cost for fertilization in remote and impoverished regions of the world is significantly higher, with farmers in inland Africa paying twice the amount for fertilizer compared to farmers in Europe. Furthermore, the uncertainty in fertilizer access due to unreliable ammonia distribution in remote and impoverished parts of the world often leads to preemptive over-fertilization of the soil, which is damaging to the ecosystem, human health, and the broader climate.[3, 37, 38] Moreover, the reliance on SMR for generation of H_2 produces an average of 1.87 tons of CO_2 per ton of NH_3 synthesized, making the process a substantial contributor to anthropogenic carbon emissions. The HBP by itself accounts for about 1-2% of energy and 5% of natural gas consumption worldwide, at the cost of 1.6% of all global anthropogenic CO_2 emissions.[39–41]

Collectively, these harms constitute a growing demand to develop new methods of ammonia synthesis capable of addressing three fundamentally interlinked problems: the harsh conditions of operation, which demand expensive and complex pressure- and temperature-

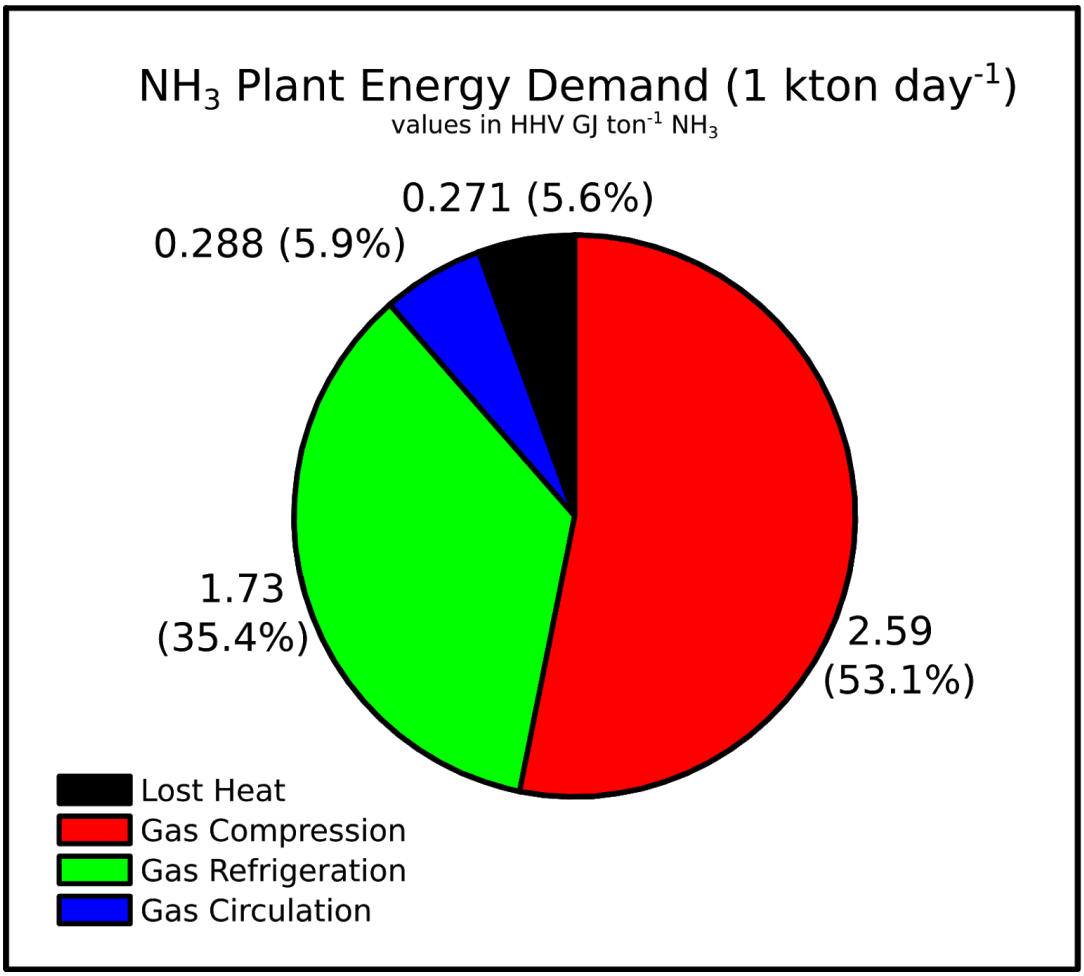

Figure 3-4. Energy demand of a typical moderate-sized SMR-coupled HBP ammonia plant. Energetic values are reported in GJ·t^{-1} of ammonia with respect to the higher heating value (HHV) of natural gas.

resistant systems; the use of natural gas as a source for atomic hydrogen, which produces substantial associated infrastructural complexity in addition to adding a substantial carbon footprint to the system; and the lack of profitable scalability for the legacy process, resulting in a centralization of ammonia production plants that increasingly fails to meet the growing food security needs of the developing world.

3.1.3 Electrochemical Nitrogen Reduction

In light of the extreme conditions of reaction demanded by all the preceding industrial nitrogen fixation processes, the action of the humble *Rhizobia* bacteria is all the more awe-inspiring. Where the HBP requires hundreds of atmospheres of pressure, the FCP demands an incredibly reactive artificial reductant, and the BEP relies upon a sustained plasma field, the humble diazotroph has been breaking the N≡N bond at atmospheric pressure and temperature for billions of years.[42] This feat is accomplished through the action of nitrogenase enzymes, of which there are three primary variations depending on the structure of the protein cofactor: a molybdenum-iron nitrogenase (MoFe) system, a vanadium-iron nitrogenase (VFe) system, and an iron-iron nitrogenase (FeFe) system.

3.1.3.1 Analogy to Biological Nitrogen Fixation

While the precise reduction mechanism and stoichiometry varies depending on the precise class of nitrogenase involved (the MoFe[43] and FeFe[44] cofactors both evince the stoichiometry in **Equation 3.16**, while the VFe[45] is observed to follow the stoichiometry in **Equation 3.17**), all nitrogenase enzymes in net effect the conversion of N_2 to NH_3 with a side reduction of H^+ to H_2, driven energetically by the cleavage of adenosine triphosphate (ATP) to adenosine diphosphate (ADP) and inorganic phosphate (P_i):

$$N_2 + 8\,H^+ + 8\,e^- + 16\,\mathrm{MgATP} \longrightarrow 2\,NH_3 + H_2 + 16\,\mathrm{MgADP} + 16\,P_i \tag{3.16}$$

$$N_2 + 14\,H^+ + 12\,e^- + 40\,\mathrm{MgATP} \longrightarrow 2\,{NH_4}^+ + 3\,H_2 + 40\,\mathrm{MgADP} + 40\,P_i \tag{3.17}$$

A common theme that separates the action of these enzymes from the industrial processes detailed in **Section 3.1.2** is that where the HBP and FCP[iv] split the N≡N bond thermally,[48] the action of nitrogenase is functionally electrochemical – incrementally directing protons and electrons to the N_2 molecules to be reduced.

3.1.3.2 Half-Reactions for Electrochemical Nitrogen Reduction

Electrochemical nitrogen reduction provides a promising alternative as a modular, scalable source for zero-carbon on-site NH_3 generation. Nitrogen could be converted directly to ammonia at the cathode of an electrochemical cell, with electrons potentially sourced from the oxidation of H_2O to O_2 (**Figure 3.2**) – effectively synthesizing ammonia directly from humid air, a carbon-neutral process predicted to be about 20% more energy-efficient than HBP in the theoretical limit of efficiency.[48–50] Without the need for steam reforming, such a cell could be coupled to renewable energy sources to directly fertilize cropland. For a sufficiently selective electrocatalyst system, a typical NH_3 usage rate of $100\,\mathrm{kg{\cdot}ha^{-1}{\cdot}yr^{-1}}$ would equate to approximately $145\,\mathrm{W{\cdot}ha^{-1}}$ – about the output of a $5\,\mathrm{m^2}$ solar cell or a residential-scale wind turbine per hectare.[51, 52]

In principle, the overall ammonia synthesis reaction $N_2 + 3\,H_2 \longrightarrow 2\,NH_3$ can be split into two half-reactions: a 2-electron hydrogen oxidation reaction (HOR) (**Equation 3.18**) and a 6-electron nitrogen reduction reaction (NRR) (**Equation 3.19**). Despite the favorable thermodynamics of the latter reduction reaction, **Figure 3-5** highlights the extreme potentials needed to access the necessary partially-reduced NRR intermediates – the electrochemical equivalent of a high E_a barrier despite favorable ΔG°.

$$H_2 \longrightarrow 2\,H^+ + 2\,e^- \qquad E^\circ = +0.000\ \mathrm{V} \tag{3.18}$$

$$N_2 + 6\,H^+ + 6\,e^- \longrightarrow 2\,NH_3 \qquad E^\circ = +0.092\ \mathrm{V} \tag{3.19}$$

[iv] Given the conditions of reaction, it is also likely that the action of the BEP is *also* fundamentally thermal in nature – though there remains substantial ambiguity about the precise mechanism.[18, 46, 47]

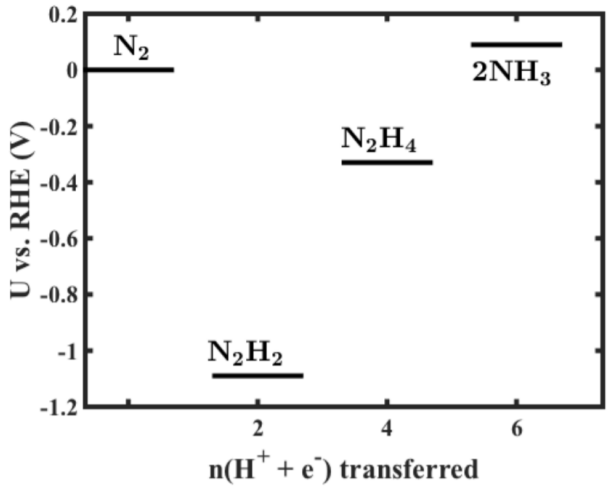

Figure 3-5. Frost diagram for reduction of elemental nitrogen to ammonia.

As with all electrochemical systems, splitting this reaction into half-reactions enables the substitution of either the anodic or cathodic reactivity. In particular, the former hydrogen oxidation reaction may be readily substituted for the oxygen evolution reaction (OER) (**Equation 3.20**), thereby sourcing the required protons and electrons from water and eliminating the need for a hydrogen feedstock (**Figure 3.2**):

$$2\,H_2O \longrightarrow 4\,H^+ + 4\,e^- + O_2 \qquad\qquad E^\circ = +1.230\ V \tag{3.20}$$

However, artificial nitrogen reduction by purely electrochemical means has yet to achieve this feat with any sort of comparable selectivity; the mechanistic profile of gathering six protons and six electrons for nitrogen reduction is rendered nontrivial by the fact that the required protons and electrons can freely combine at the electrode surface to form H_2 gas. This process, hydrogen evolution reaction (HER) (**Equation 3.21**), is the inverse of the HOR, and an extremely kinetically facile reaction which occurs in the same potential window as NRR.

$$2\,H^+ + 2\,e^- \longrightarrow H_2 \qquad\qquad E^\circ = +0.000\ V \tag{3.21}$$

This lack of selectivity for NRR over HER is generally considered to be a primary bottle-

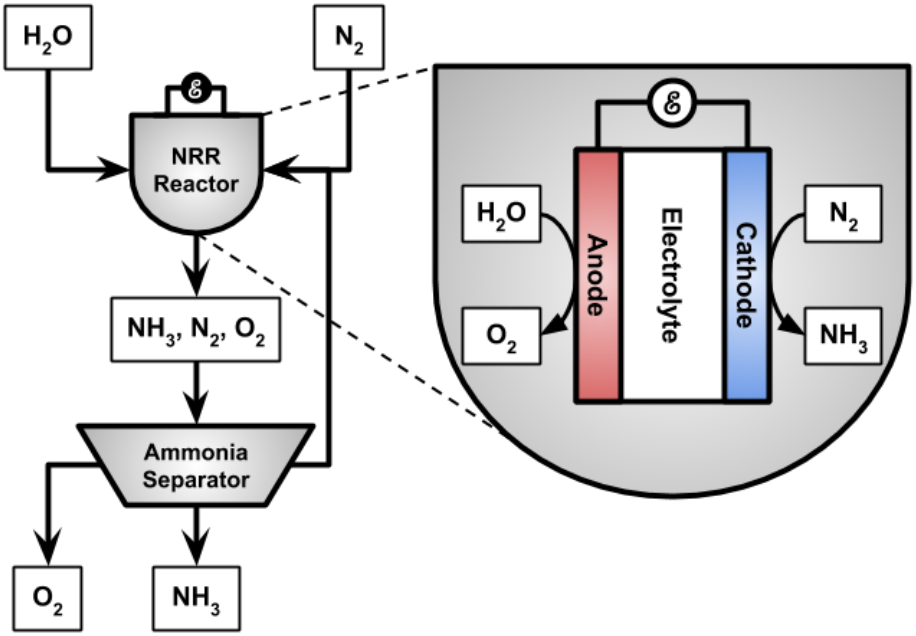

Scheme 3.2. Scheme for electrochemically coupled hydrogen oxidation reaction/nitrogen reduction reaction system.

neck towards efficient nitrogen reduction electrocatalysis in virtually all reported nitrogen reduction systems: Faradaic efficiencies rarely exceed 1% for aqueous systems, and seldom for extended time periods or in the absence of highly forcing conditions.[53–55]

3.1.3.3 Strategies for Selective Electrochemical Nitrogen Reduction

For the past several decades, the development of nitrogen-fixation electrocatalysts have struggled to balance the selectivity for NRR over HER with the need for the produced systems to operate under mild conditions in order to achieve scalable operability. Herein we present a selection of electrochemical nitrogen reduction reports, roughly categorized by their conditions of reaction, including their catalyst systems, reaction conditions, and reported selectivities and yields.

Within the field of nitrogen reduction electrocatalysis, catalyst performance is assessed primarily through two metrics: Faradaic efficiency (FE%) and surface-normalized ammonia

Cathode	Electrolyte	T[v]	P[vi]	FE%[vii]	r_{NH_3}[viii]	η[ix]	Source
Ru	2 M aq. KOH	20	1	0.92	0.09	0.26	[56]
Fe NPs on CNTs	Nafion	20	1	0.03	0.00	1.57	[57]
Pt	Nafion	25	1	2	3.20	0.39	[58]
ZnS	1 M aq. KOH	25	1	0.96	5.65	1.19	[59]
NiS	1 M aq. KOH	25	1	0.85	3.87	1.19	[59]
CdS	1 M aq. KOH	25	1	0.74	4.14	1.19	[59]
ZnSe	1 M aq. KOH	25	1	1.29	6.45	1.19	[59]
TiB_2	1 M aq. KOH	25	1	1.11	6.12	1.19	[59]
VN nanosheets	0.1 M aq. HCl	25	1	2.25	0.08	1.3	[60]
Fe/FTO	$[P_{6,6,6,14}]^+[eFAP]^-$	25	1	60	0.00	0.99	[61]
Stainless Steel	$[C_2mpyr]^+[eFAP]^-$	25	1	35	0.02	0.99	[61]
Au clusters on TiO_2	0.1 M aq. HCl	25	1	8	0.11	0.39	[62]
Mo	0.01 M aq. H_2SO_4	25	1	0.72	0.01	0.58	[63]
Au nanorods	0.1 M aq. KOH	25	1	4	0.03	0.39	[64]
N-Carbon	0.05 M aq. H_2SO_4	25	1	1.3	0.23	0.83	[65]
Pd/C	0.05 M aq. H_2SO_4	25	1	0.04	0.01	0.24	[66]
Pd/C	0.1 M aq. PBS	25	1	2.35	0.02	0.24	[66]
Pd/C	0.1 M aq. NaOH	25	1	0.09	0.01	0.24	[66]
Au/C	0.1 M aq. PBS	25	1	1.18	0.00	0.24	[66]
Pt/C	0.1 M aq. PBS	25	1	0.19	0.00	0.24	[66]
Rh	0.1 M aq. KOH	25	1	0.7	0.13	0.39	[67]
N-doped carbon	0.05 M aq. H_2SO_4	25	1	1.4	2.60	1.09	[65]
Ir	Polymer gel	60	1	0.108	0.87	1.3	[68]
γ-CD	0.1 M KCl	60	1	0.03	0.01	0.4	[69, 70]
$SmFe_{0.7}Cu_{0.3-x}Ni_xO_3$	Nafion / H_2 gas	80	1	90.4	11.00	2.11	[71]
$Sm_{1.5}Sr_{0.5}NiO_4$	Nafion / H_2 gas	80	1	-	10.3	2.5	[72]
Fe-MOF	Nafion	80	1	1.4	1.90	0.31	[73]

Table 3.1. Selected catalyst systems for nitrogen reduction under mild or ambient conditions.

yield. These two metrics exist in rough opposition to each other; while the former is a measure of the selectivity of electrons for NRR over parasitic HER, the latter is an absolute measurement of the quantity of ammonia being produced per unit time. Hence, while a low-overpotential setup may be relatively selective for nitrogen reduction over hydrogen evolution, the small reaction driving force may result in a lower ammonia yield than a system with a higher overpotential, which may produce more ammonia per second (albeit less selectively).

Nitrogen Reduction under Ambient Conditions Nitrogen reduction under ambient conditions is widely considered to be a 'holy grail' of catalysis. As previously alluded, it is no small feat to split the durable N≡N bond in the absence of high temperatures to enable thermal cleavage or high pressures to provide an entropic driving force. As demonstrated in **Table 3.1**, selective NRR catalysis under ambient conditions is highly challenging, especially in aqueous or other protic environments in which parasitic HER is competitive. Especially noteworthy are the exceptions to this trend: the comparatively high FE%s observed in the protic ionic liquids (PILs) trihexyl(tetradecyl) phosphonium ($[P_{6,6,6,14}]^+$)tris(pentafluoroethyl) trifluorophosphate ($[eFAP]^-$) and N-ethyl-N-methylpyrrolidinium ($[C_2mpyr]^+$)$[eFAP]^-$, designed to support high N_2 solubility while limiting proton content that supports parasitic HER. While this produces impressive Faradaic activities of up to 60%, the absolute rate of NH_3 generation is very low (possibly limited by low proton concentration), and the exotic nature of the electrolyte may limit the practical economic implementation of PIL-based NRR systems.[61, 74]

The samarium-doped ceria (SDC) systems $SmFe_{0.7}Cu_{0.3-x}Ni_xO_3$ and $Sm_{1.5}Sr_{0.5}NiO_4$ comprise another apparent set of outliers, as they claim NRR current densities and selectivities nearly two orders of magnitude better than competing reports. However, this is not an apples-to-apples comparison. Rather than performing electrochemical nitrogen reduction in protic solvents, these results are achieved by performing reduction on a perovskite electrode upon a solid electrolyte through the use of H_2 gas as a proton source to mitigate parasitic HER, which renders such a system reliant upon external methods for generating hydrogen, such as SMR.[71, 72]

High-Temperature Nitrogen Reduction As evidenced by **Table 3.2**, the reduction of nitrogen to ammonia at high temperatures is a thriving field of research, and a multitude

[v] Reaction temperature, °C
[vi] Reaction pressure, bar
[vii] Faradaic efficiency for NRR
[viii] Rate of NH_3 generation, $nmol \cdot s^{-1} \cdot cm^{-2}$
[ix] Reaction overpotential, volts

Cathode	Electrolyte	T	P	FE%	r_{NH_3}	η	Source
Ni	nano-Fe_3O_4 in NaOH/KOH	200	1	35	2.42	0.15	[75]
Ni mesh	nano-Fe_3O_4 in NaOH/KOH	200	1	14.17	4.41	1.9	[76]
Ru	CsH_2PO_4/SiP_2O_7	220	1	0.12	0.163	0.4	[77]
Pt/C	$CsH_5(PO_4)_2/SiO_2$	220	1	2.1	0.2	0.25	[78]
Ni foil	1 M $LiClO_4$/PC	220	1	49.93	1.88	3.2	[79]
$Ru/Cs^+/MgO$	CsH_2PO_4/SiP_2O_7	250	1	3.5	0.77	0.26	[80]
stainless steel mesh	Fe_2O_3/C in 1:1 [Na:K]OH	250	1	4.89	8.27	0.35	[81]
stainless steel mesh	Fe_2O_3/C in 1:1 [Na:K]OH	250	1	13.67	5.11	0.05	[81]
9.9:5 wt:wt% $Cs:Ru/SrZrO_3$	N/A	270	1	154.11	113	2.27	[82]
porous Ni	[Li/K/Cs]Cl + 0.5 mol% Li_3N	300	1	23	19.1	1.58	[83]
$Pr_{0.6}Ba_{0.4}Fe_{0.8}Cu_{0.2}O_3$	$[Li/Na/K]_2CO_3$	400	1	5	0.183	0.41	[84]
porous Ni	[Li/K/Cs]Cl + 0.5 mol% Li_3N	400	1	72	3.33	0.66	[85]
Fe_2O_3	BCZYZ	400	1	2.33	2.9	1.61	[86]
Pd-modified iron oxide	BCZYZ	450	1	1.64	3.96	1.63	[86]
Ru-modified iron oxide	BCZYZ	500	1	1.05	2.66	0.75	[86]
$La_{0.8}Cs_{0.2}Fe_{0.8}Ni_{0.2}O_3$	$Ce_{0.8}Gd_{0.2}O_2$ - $[Li/Na/K]_2CO_3$	400	1	0.33	0.123	0.41	[87]
$CoFe_2O_4$ – GDCO	GDCO - $[Li/Na/K]_2CO_3$	400	1	0.17	0.0649	0.61	[88]
$La_{0.6}Sr_{0.4}Fe_{0.8}Cu_{0.2}O_{3-\delta}$ – GDCO	GDCO - $[Li/Na/K]_2CO_3$	400	1	0.1	0.05	0.41	[89]
Fe_3Mo_3N–Ag	$LiAlO_2$ carbonate	425	1	1.84	0.188	1.07	[90]
$La_{0.6}Sr_{0.4}Fe_{0.8}Cu_{0.2}O_{3-\delta}Ce_{0.8}Sm_{0.2}O_{2-\delta}$	SDC-$[Li/Na/K]_2CO_3$	450	1	-	5.39	0.8	[91]
steel	LiCl-KCl/LiOH-LiCl	450	1	85	1570	7	[92]
Fe	strontia-zirconia-yttria	450	1	326.96	0.497	1.23	[93]
Ag-Pd	$BaCe_{0.9}Ca_{0.1}O_{3-\delta}$	480	1	50	2.69	-	[94]
Ag-Pd	$BaCe_{0.7}Zr_{0.2}Sm_{0.1}O_{3-\delta}$	500	1	50	2.67	-	[95]
Ni-cermet	$BaCe_{0.9}Y_{0.1}O_{3-\delta}$	500	1	0.63	0.336	0.85	[96]
Ni–$BaCe_{0.9}Y_{0.1}O_{3-\delta}$	$BaCe_{0.9}Y_{0.1}O_{3-\delta}$	500	1	0.63	0.261	0.5	[96]
Ru-doped $La_xSr_{1-x}TiO_3$	$BaCe_{0.9}Y_{0.1}O_3$	500	1	0	0.004	0.5	[97]
Co_3Mo_3N–Ag	K-β"-Al_2O_3	500	1	270.55	0.98	1.25	[98]
Ag-Pd	$La_{1.9}Ca_{0.1}Zr_2O_{7-\delta}$	520	1	80	1.76	1.2	[99]
Ag-Pd	$La_{1.95}Ca_{0.05}Zr_2O_{7-\delta}$	520	1	1	2	0.95	[100]
Ag-Pd	$Ce_{0.8}Y_{0.2}O_{1.9}$ - [Ca:K][PO_4]	650	1	50	9.5	1.2	[100]
$Ba_{0.5}Sr_{0.5}Co_{0.8}Fe_{0.2}O_{3-\delta}$	$BaCe_{0.85}Y_{0.15}O_{3-\delta}$	530	1	60	4.1	0.66	[101]
Ag-Pd	$BaCe_{0.9}Dy_{0.1}O_{3-\delta}$	530	1	52	3.5	-	[102]
Ru-Ag/MgO	$ScCe_{0.95}Yb_{0.05}O_{3-\delta}$	550	1	0.5	0.0003	2.16	[103]
$ScCe_{0.95}Yb_{0.05}O_{3-\delta}$	$ScCe_{0.95}Yb_{0.05}O_{3-\delta}$	550	1	0.5	0.00015	2.16	[103]
Pd	$ScCe_{0.95}Yb_{0.05}O_{3-\alpha}$	570	1	78	4.5	0.43	[104]
Ni–$BaCe_{0.2}Zr_{0.7}Y_{0.1}O_{2.9}$	$BaCe_{0.2}Zr_{0.7}Y_{0.1}O_{2.9}$	600	1	0.06	2.9	0.38	[105]

Table 3.2. Selected high-temperature and molten-salt catalyst systems for nitrogen reduction.

Cathode	Electrolyte	T	P	FE%	r_{NH_3}	η	Source
Ni	nano-Fe_3O_4 in 1:1 molten [Na:K]OH	250	25	35	2.42	0.7	[75]
Fe	0.2 M $LiClO_4$ + EtOH + THF	25	50	57.7	3.98	4.84	[106]
Ti	0.2 M $LiClO_4$ + EtOH + THF	25	50	50.9	3.52	4.84	[106]
Mo	0.2 M $LiClO_4$ + EtOH + THF	25	50	49.2	3.4	4.84	[106]
Ni	0.2 M $LiClO_4$ + EtOH + THF	25	50	46.3	3.2	4.84	[106]
Cu	0.2 M $LiClO_4$ + EtOH + THF	25	50	42.4	2.93	4.84	[106]
Cu	0.2 M $LiClO_4$ + MeOH + THF	25	50	4.5	0.312	4.84	[106]
polyaniline	0.1 M $LiClO_4$ + MeOH + H_2SO_4	25	50	16	3.2	0.12	[107]

Table 3.3. Selected high-pressure catalyst systems for nitrogen reduction.

of perovskites, ceramics, pyrochlores, cermets, and other inorganic materials have been assessed for nitrogen reduction activity. Like the aforementioned SDC systems, many of these materials act upon a mixed N_2/H_2 gas inflow stream through a solid electrolyte (with the same caveats detailed above), and coupled with the high temperature of reaction this is responsible for one of the apparent anomalies in this table: the number of systems which report FE%s above 100%.[82, 93, 98] This phenomenon is attributable to a phenomenon known as electrochemical promotion of catalysis (EPOC) or non-Faradaic electrochemical modification of catalytic activity (NEMCA), in which electrochemical polarization increases the rate of non-faradaic reactivity – in this case, the HBP-like thermal cleavage and fixation of N_2. While not strictly performing NRR, such systems may prove invaluable routes to milder and more selective variations upon existing HBP methodologies for converting N_2 and H_2 into ammonia.

High-Pressure Nitrogen Reduction Compared to the preceding tables, the list of high-pressure catalyst systems for nitrogen reduction (**Table 3.3**) is far more scant, an observation that may be partially attributable to the experimental difficulties associated with electrochemistry at high pressures.[108] Unlike the list of high-temperature materials, all of the listed reports under these conditions utilize a protic hydrogen source (i.e., not H_2 gas), and must therefore contend with parasitic hydrogen evolution. Despite this, Faradaic efficiencies and ammonia generation rates for these few reported high-pressure electrocatalysts are substantially higher than ambient-pressure systems, a phenomenon that is attributed in part to

Cathode	Electrolyte	T	P	FE%	r_{NH_3}	η	Source
Ni foil	1 M $LiClO_4$/PC	220	1	49.93	1.88	0.544	[79]
porous Ni	[Li/K/Cs]Cl + 0.5 mol% Li_3N	300	1	23	19.1	1.58	[83]
$Pr_{0.6}Ba_{0.4}Fe_{0.8}Cu_{0.2}O_3$	$[Li/Na/K]_2CO_3$	400	1	5	0.183	0.41	[84]
porous Ni	[Li/K/Cs]Cl + 0.5 mol% Li_3N	400	1	72	3.33	0.66	[85]
$La_{0.8}Cs_{0.2}Fe_{0.8}Ni_{0.2}O_3$	$Ce_{0.8}Gd_{0.2}O_2$ - $[Li/Na/K]_2CO_3$	400	1	0.33	0.123	0.41	[87]
$CoFe_2O_4$ – GDCO	GDCO - $[Li/Na/K]_2CO_3$	400	1	0.17	0.0649	0.61	[88]
$La_{0.6}Sr_{0.4}Fe_{0.8}Cu_{0.2}O_{3-\delta}$ – GDCO	GDCO - $[Li/Na/K]_2CO_3$	400	1	0.1	0.05	0.41	[89]
Fe_3Mo_3N-Ag composite	$LiAlO_2$-carbonate composite	425	1	1.84	0.19	0.054	[90]
stainless steel foil	LiCl-KCl/LiOH-LiCl	450	1	85	15.70	3.4	[92]
Mo foil	0.2 M $LiClO_4$ + EtOH + THF	25	1	3.1	0.21	0.062	[109]
Mo foil	0.2 M $LiClO_4$ + EtOH + THF	25	50	49.2	3.4	4.84	[106]
Ti foil	0.2 M $LiClO_4$ + EtOH + THF	25	1	8.2	0.56	0.164	[109]
Ti foil	0.2 M $LiClO_4$ + EtOH + THF	25	50	50.9	3.52	4.84	[106]
Fe foil	0.2 M $LiClO_4$ + EtOH + THF	25	1	6	0.41	0.12	[109]
Fe foil	0.2 M $LiClO_4$ + EtOH + THF	25	50	57.7	3.98	4.84	[106]
Ag foil	0.2 M $LiClO_4$ + EtOH + THF	25	1	8.4	0.58	0.168	[109]
Ni foil	0.2 M $LiClO_4$ + EtOH + THF	25	1	6.5	0.45	0.13	[109]
Ni foil	0.2 M $LiClO_4$ + EtOH + THF	25	50	46.3	3.2	4.84	[106]
Co foil	0.2 M $LiClO_4$ + EtOH + THF	25	1	6.1	0.42	0.122	[109]
Zn foil	0.2 M $LiClO_4$ + MeOH + THF	25	1	4.5	0.34	0.09	[109]
Cu foil	0.2 M $LiClO_4$ + EtOH + THF	25	50	42.4	2.93	4.84	[106]
Cu foil	0.2 M $LiClO_4$ + MeOH + THF	25	50	4.5	0.312	4.84	[106]
PEBCD	0.5 M Li_2SO_4	25	1	2.91	0.01	0.002	[110]
Ag-Au coated by ZIF	THF+$LiCF_3SO_3$	25	1	16	0.01	0.0021	[111]
polyaniline	0.1 M $LiClO_4$ + MeOH + H_2SO_4	25	50	16	3.2	0.12	[107]
Pt foil	Li_2SO_4	80	1	0.83	0.94	0.2712	[112]

Table 3.4. Selected lithium-mediated catalyst systems for nitrogen reduction.

increased N_2 solubility in the electrolyte.

Lithium-Mediated Nitrogen Reduction Separate from the discussion of reaction conditions, lithium-mediated electrolysis is a strategy for effecting the net conversion of N_2 to NH_3 that warrants specific discussion. As an orthogonal metric for system efficacy to reaction temperature or pressure, the associated **Table 3.4** of lithium-mediated nitrogen reduction systems contains several duplicate entries from **Tables 3.1**, **3.2**, and **3.3**.

This reaction strategy exploits the unique[x] property of lithium metal to react directly with N_2 gas under mild conditions to produce lithium nitride (**Equation 3.22**). This nitride may then be hydrolysed to produce lithium hydroxide, in the process liberating ammonia

[x] Some other elements, such as calcium and magnesium, are capable of forming nitrides upon combustion under a pure nitrogen atmosphere, though this is not a mild process.

(**Equation 3.23**).

$$6\,\mathrm{Li} + \mathrm{N_2} \longrightarrow 2\,\mathrm{Li_3N} \tag{3.22}$$

$$2\,\mathrm{Li_3N} + 6\,\mathrm{H_2O} \longrightarrow 6\,\mathrm{LiOH} + 2\,\mathrm{NH_3} \tag{3.23}$$

Leveraging this unique reactivity to cleave the N≡N bond, then, is simply the matter of electrochemically turning over LiOH to Li metal (**Equation 3.24**). This electrochemical reaction consists of the cathodic reduction of lithium ions to lithium (**Equation 3.25**) and the anodic oxidation of hydroxide ions to water and oxygen (**Equation 3.26**), functionally an oxygen evolution reaction.

$$6\,\mathrm{LiOH} \longrightarrow 6\,\mathrm{Li} + 3\,\mathrm{H_2O} + \frac{3}{2}\,\mathrm{O_2} \tag{3.24}$$

$$6\,\mathrm{Li^+} + 6\,\mathrm{e^-} \longrightarrow 6\,\mathrm{Li} \tag{3.25}$$

$$6\,\mathrm{OH^-} \longrightarrow 3\,\mathrm{H_2O} + \frac{3}{2}\,\mathrm{O_2} + 6\,\mathrm{e^-} \tag{3.26}$$

In net, this lithium-mediated system effects the conversion of dinitrogen and water to ammonia and oxygen (**Equation 3.27**).

$$\mathrm{N_2} + 3\,\mathrm{H_2O} \longrightarrow 2\,\mathrm{NH_3} + \frac{3}{2}\,\mathrm{O_2} \tag{3.27}$$

For these reasons, this system is highly attractive as a method for achieving high NRR selectivities, as the aprotic reduction of lithium ions to lithium metal can be physically separated from the nonfaradaic production of ammonia, thereby limiting the risks of parasitic hydrogen evolution, as evidenced by the numerous reports in **Table 3.4**. However, a drawback of this approach is the high potential necessary to effect the reduction of lithium ions to lithium metal (**Equation 3.25**), in accordance with its standard reduction potential of $-3.0401\,\mathrm{V}$ vs. standard hydrogen electrode (SHE). Thermodynamically, this makes sense; lithium must indeed be a highly reducing metal to effect the cleavage of the N≡N bond un-

der ambient conditions. However, the end result is that the potential necessary for effective lithium-mediated nitrogen reduction electrocatalysis is substantially higher than the thermodynamic potential for N_2 reduction to NH_3, which (as previously mentioned), is actually slightly *downhill* at 0.092 V vs. SHE. This phenomenon is well-reflected in **Table 3.4**, where the reported systems with highest FE%s and ammonia conversion rates are also the systems running at the highest overpotentials.

With widespread implementation of electrochemical NRR systems largely gated by reaction selectivities, the key to improving ammonia synthesis via electrochemical NRR is through the development of reaction-selective electrochemical systems that promote NRR whilst simultaneously disfavouring HER. However, on a more fundamental level, the key factor influencing the disproportionate favouring of HER over NRR is the ease with which hydrogen binds to the electrode surface compared to dinitrogen. As such, improvement of nitrogen binding whilst inhibiting hydrogen binding to the electrode surface is anticipated to improve selectivity of NRR over HER. Taken collectively, these literature reports contextualize our approach to developing novel catalyst systems for electrochemical nitrogen reduction under comparatively mild conditions. As nitrogen binding must necessarily occur before any electrochemical NRR step in a protic medium, it must therefore be either pre-rate-limiting or rate-limiting, which implies that increased concentration of nitrogen in the electrolyte must necessarily increase the rate of NRR and therefore the selectivity for NRR over HER (as nitrogen pressure will not factor into the rate of HER).

For this reason, we chose to investigate the effects of increased nitrogen pressure on common base metal electrocatalyst activity for NRR, a relatively unexplored field of research. In addition to promoting selective NRR, these high pressures enable greater absolute ammonia production rates. Given the ubiquity of ambient NH_3 and its propensity to bind to metal surfaces, even comparatively sensitive methods for ammonia quantification (see **Appendix B** on page 225) are limited by the rate at which NRR electrocatalysts generate ammonia signals beyond the level of ambient noise. By increasing absolute ammonia produc-

tion rates beyond a few nmol·s^{-1}·cm^{-2}, high applied pressures of N_2 help alleviate this issue and enable practical assessment and screening of catalysts with a rapidity that is infeasible at ambient pressures.[113]

3.2 Results and Discussion

While a variety of factors may dictate the selectivity for NRR over HER in any given catalytic system, N_2 binding is a necessary step for any successful NRR mechanism. As this binding process is expected to be largely potential-independent (due to the nonpolar nature of the N_2 molecule), modulation of the N_2 partial pressure presents the most plausible chemical handle for tuning NRR selectivity by driving N_2 adsorption. Herein, we use a custom-built electrochemical pressure reactor (**Section 3.4.1** on page 139) to explicate the electroreduction of N_2 to NH_3 at elevated nitrogen pressures on copper metal, copper nitride, and vanadium nitride electrodes. In particular, we observe nitrogen reduction on Cu_3N at low overpotentials and peak Faradaic efficiencies an order of magnitude higher than reported aqueous systems.

3.2.1 Copper Metal for Nitrogen Reduction Electrocatalysis

We began by investigating copper metal electrodes, which preliminary bulk electrolysis (BE) data suggested might be active for ammonia production at elevated N_2 pressures. As pictured in **Figure 3-6**, copper electrodes under nitrogen pressure evinced higher voltammetric currents than under argon pressure. Moreover, as seen in **Figure 3-7**, when these reactor headspaces were bubbled through sulfuric acid, a characteristic[xi] ^{1}H NMR signal for NH_4^+ was observed only in the simultaneous presence of applied N_2 pressure and applied potential. These results motivated a more detailed study on the nature and activity of the electrocatalytic species, utilizing time-resolved analytical measurements to investigate the mechanism of reaction.

[xi] This 1:1:1 NMR triplet is the result of proton coupling to the $S = 1$ ^{14}N nucleus, and is thereby distinct from a 'typical' 1:2:1 NMR triplet.

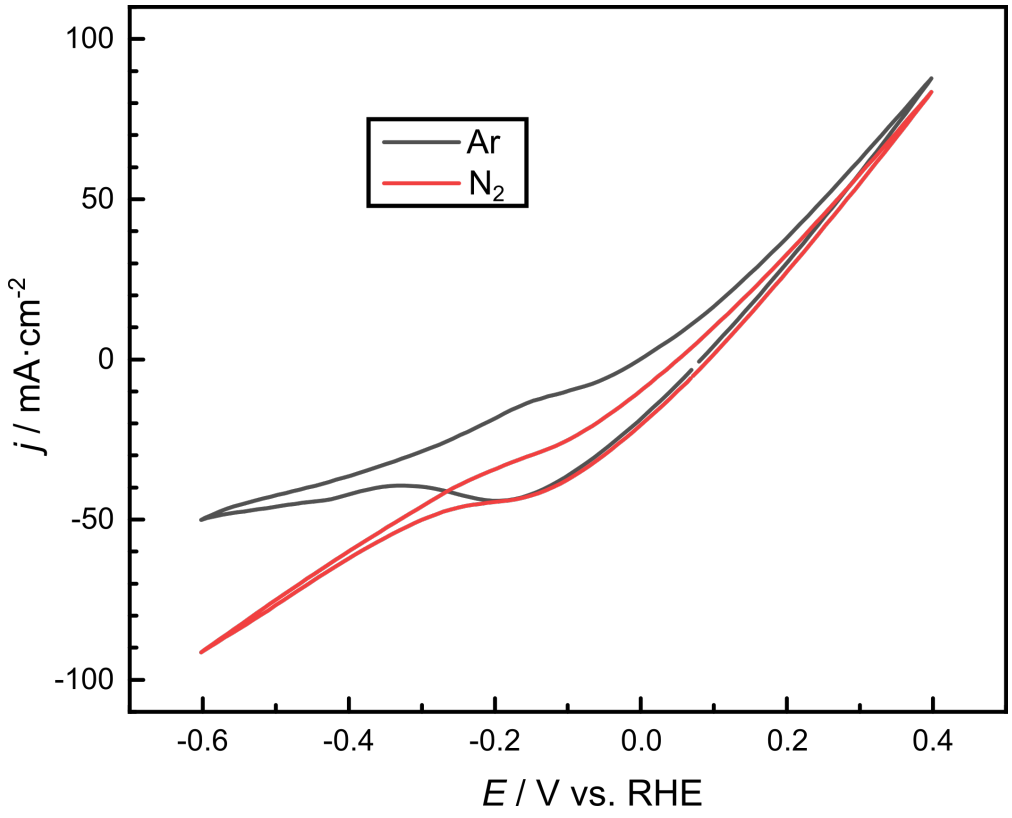

Figure 3-6. Cyclic voltammograms of copper foam electrodes under 1000 psi Ar (black) and N_2 (red), at a scanrate of $100\,mV{\cdot}s^{-1}$.

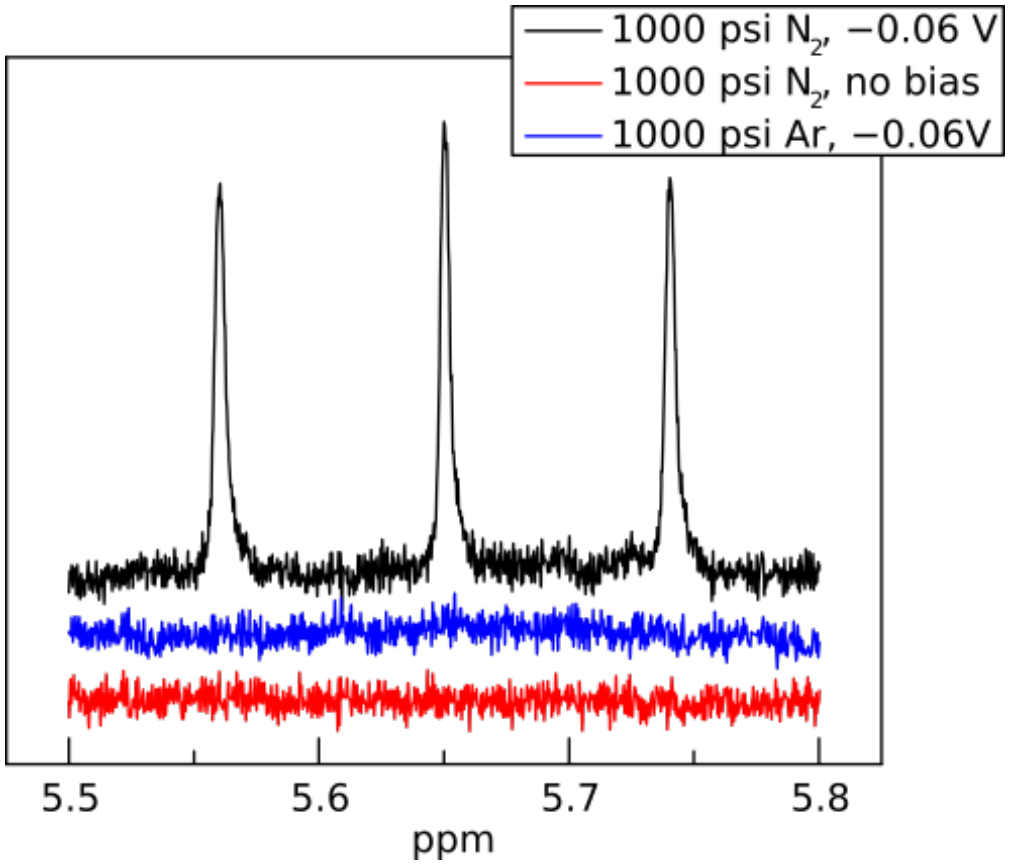

Figure 3-7. ^{1}H NMR spectra of reactor headspaces bubbled through concentrated H_2SO_4, with Cu foam electrodes in 1 M aq. KOH pressurized to 1000 psi N_2 for 8 hours.

The aggregate ammonia yields in **Figure 3-10a** exhibited a roughly linear pressure dependence, as pictured in **Figure 3-8a**. As expected, in the absence of N_2 (1000 pound-force per square inch (psi) Ar), no ammonia is generated, but at 15 psi of N_2 (about 1 bar), aggregate ammonia production was not higher at the 95% confidence level. At 1000 psi of nitrogen, this value rises to over 1 µmol NH_3 produced, well above the control case. Moreover, the apparent FE% of ammonia production (**Figure 3-8b**) also increased at higher N_2 partial pressures, peaking at almost 7% at 1000 psi of nitrogen, potentially indicative of increased selectivity for NRR over HER.

Plotting the faradaic efficiency of ammonia production as a function of potential, as seen in **Figure 3-9**, showed that selectivity for nitrogen reduction as a function of potential exhibited onset behavior negative of RHE. At +0.14 V against RHE, the faradaic efficiency is within error of zero percent; however, at 0.04 V, observed faradaic efficiency increased slightly to about 1%, a value that, although marginal, was significantly different from zero at the 95% confidence level. At −0.06 V, observed faradaic efficiency was 6.8%, as seen above, and at −0.16 V, faradaic efficiency increased even further to a peak of 12.2%. At even more negative potentials, however, both faradaic efficiency of NRR and absolute aggregate ammonia yield decrease at −0.26 V. The overall potential dependence of ammonia production appeared to indicate an onset potential somewhere between 0.14 V and 0.04 V, with selectivity over HER reaching a maximum at −0.16 V and more-reducing potentials inducing a decline in faradaic efficiency for ammonia production.

These results demonstrated the potential for N_2 pressure modulation to enhance NRR activity to high faradaic efficiencies or low overpotentials. Our plot of faradaic efficiency of ammonia production as a function of potential (**Figure 3-9**) displayed onset behavior that is consistent with a low overpotential near the thermodynamic Nernst potential for nitrogen reduction. Using the Nernst equation (**Equation 2.8**) and the standard-state reduction potential of NRR from **Equation 3.28**, we determine that at a partial pressure of 1000 psi of N_2 (about 69 bar) the equilibrium potential for nitrogen reduction falls to about 0.07 V

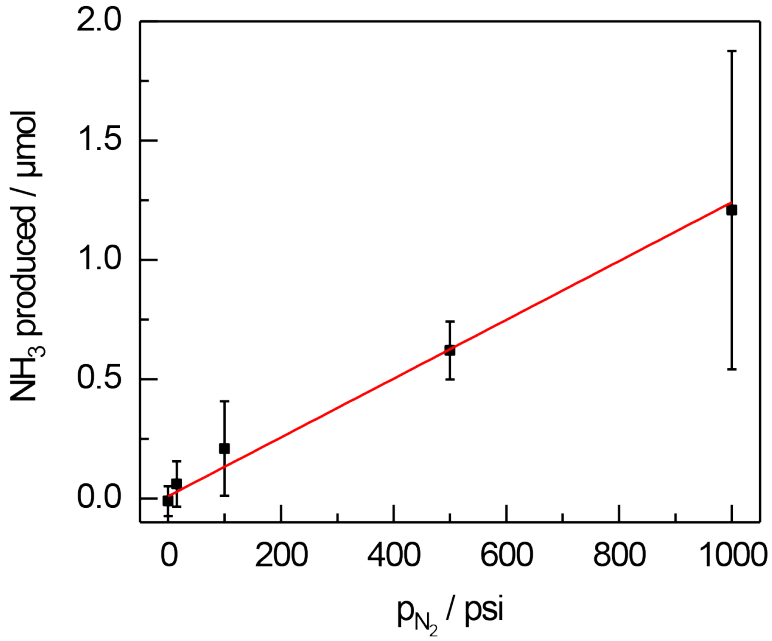

(a)

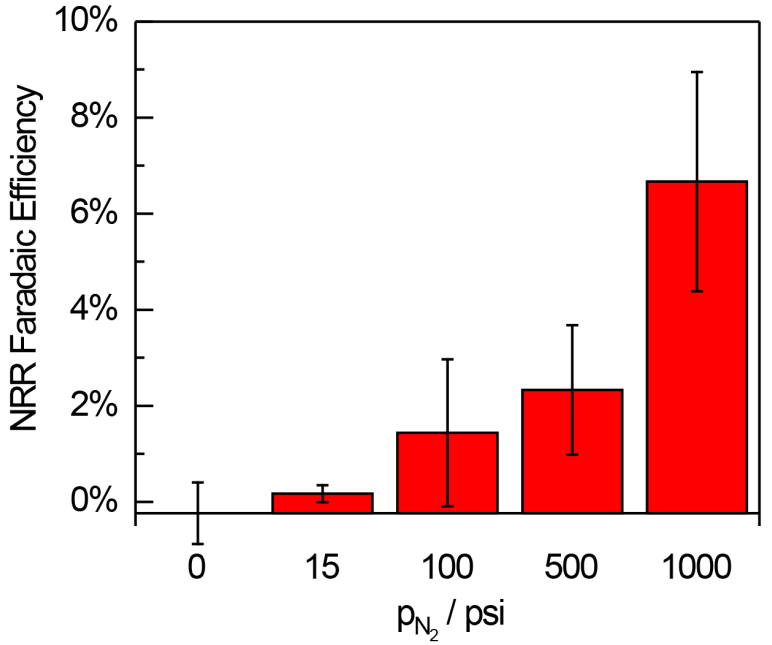

(b)

Figure 3-8. Pressure dependence of aggregate NH_3 molar yields of a Cu foam electrode in 1M KOH at 25 °C, at an applied bias of -0.065 V vs. RHE and N_2 partial pressures of 0, 15, 100, 500, and 1000 psi (1000 psi total pressure, remainder argon). **(a)** Aggregate NH_3 yield as a function of N_2 partial pressure. **(b)** Peak faradaic efficiency of ammonia production as a function of N_2 partial pressure.

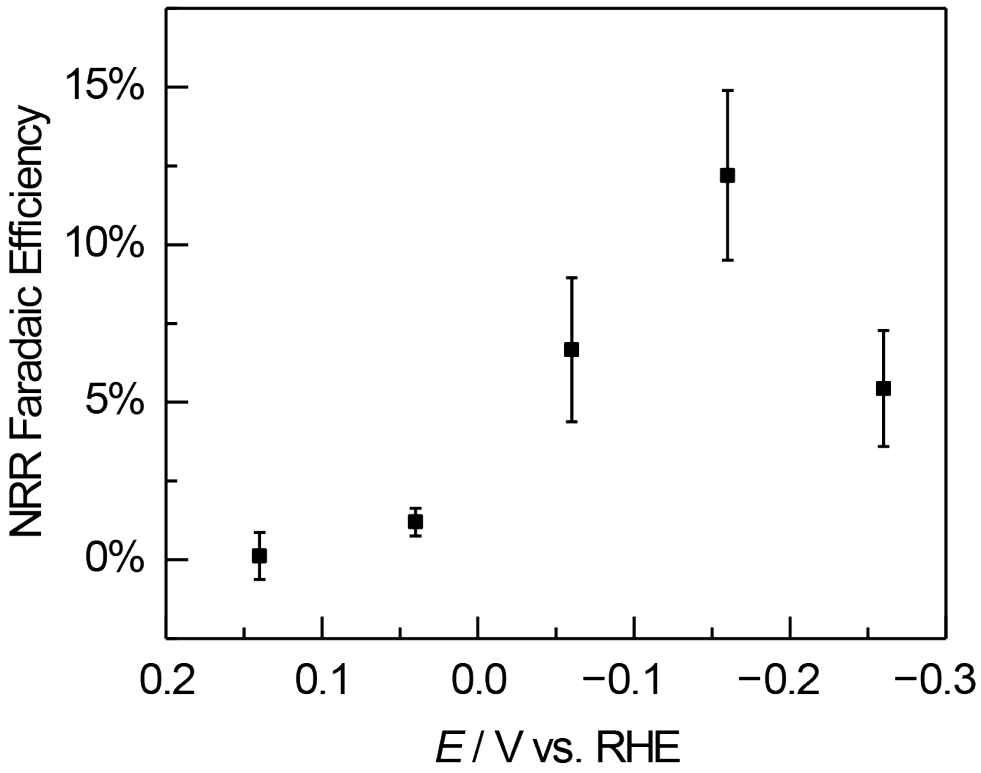

Figure 3-9. Peak faradaic efficiency for ammonia formation as a function of applied potential for a Cu foam electrode in 1M KOH at 25 °C, at a total pressure of 1000 psi N_2 and applied biases of +0.14, +0.04, -0.06, -0.16, and -0.26 V vs. RHE. Error bars represent 95% confidence intervals computed from a set of three independent measurements.

versus RHE from its standard-state value of 0.09 V. This value correlated with data, which showed no NH_3 generated at 0.14 V, an underpotential of about 60 mV. Trace (though still statistically significant) quantities of ammonia were detected at 0.04 V, at an overpotential of about 30 mV. At more reducing potentials, ammonia was detected in increasing selectivity, peaking at a maximum faradaic efficiency of 12.2% at −0.16 V, before declining at −0.26 V.

$$\Delta G^{\ominus} = -nFE^{\circ} \tag{2.7}$$

$$E^{\circ} = -\frac{\Delta G^{\ominus}}{nF}$$

$$E = E^{\circ} + \frac{RT}{nF}\ln Q \tag{2.8}$$

$$E = -\frac{\Delta G^{\ominus}}{nF} + \frac{RT}{nF}\ln Q$$

$$E = E^{\circ} + \frac{RT}{nF}\ln\left[\frac{(p_{NH_3})^2}{(p_{N_2})\,(p_{H_2})^3}\right] \tag{3.28}$$

$$E = E^{\circ} - \frac{RT}{nF}\ln 69$$

$$E = 0.092\text{ V} - 0.014\text{ V} = 0.074\text{ V}$$

In concert with this, our data also suggested that increased nitrogen partial pressure accelerated the rate of nitrogen reduction. The observed increase in faradaic efficiency at increased N_2 partial pressures, as seen in **Figure 3-8b**, indicated that the higher NH_3 yields observed were a plausible result of increased selectivity for NRR over HER, rather than an artifact of higher quantities of charged past, consistent with our supposition that dissolved N_2 is involved prior to or as part of the rate-limiting step of reaction.

However, contraindicating these data were the fact that ammonia production was observed only in the initial stages of electrolysis, with no ammonia generated following the first 15-20 minutes of applied potential, as seen in **Figure 3-10**. An inhibition process appeared to occur at roughly the same rate irrespective of N_2 concentration **(Figure 3-10a)** or electrochemical bias **(Figure 3-10b)**. However, the rate of ammonia production within the initial 15 minute window varied with applied potential and N_2 partial pressure, resulting

in differing levels of aggregate NH_3 production by the time that electrogeneration ceased.

On one hand, this vindicated our experimental approach, as elevated N_2 partial pressures were in fact be necessary for investigation of NRR on this surface; both aggregate ammonia yield and NRR FE% at 1 bar of N_2 were within a margin of error of the pure argon control. Attempts to characterize nitrogen reduction on this surface at atmospheric pressure may have been stymied by this inhibition process before ammonia concentrations were able to build to detectable levels.

We first began to characterize this phenomenon while attempting to collect current-overpotential relations, as depicted in **Figure 3-11**. Rather than displaying a traditional Tafel relation, stepped chronoamperometry data evinced a sustained bulk electrolytic process for the first 15-20 minutes of reaction. This timeframe coincided with a period of high Faradaic efficiency for ammonia generation, while following this period observed binned FE% values approximated zero (**Figure 3-12**).

Our initial hypothesis for this consistent phenomenon was catalyst electropoisoning: that trace metal ion impurities present in our electrolyte were poisoning our catalyst by deposition onto the copper surface, a phenomenon our group had previously observed on copper, silver, and gold CO_2 reduction electrocatalysts.[114]. The mechanism of inhibition appeared Faradaic, as loss of activity occured consistently 15 minutes after electrolysis began, regardless of how long the reaction mixture was allowed to equilibrate before potential was applied. The corresponding decline in absolute NH_3 yield at highly cathodic potentials (seen in **Figure 3-10b**) corroborated this hypothesis, as charge passed more quickly at more reducing potentials may have resulted in more rapid catalyst electropoisoning and lower total yield. It was independent of N_2 partial pressure, as 15 minutes of electrolysis under 1000 psi of argon nevertheless deactivated the electrode such that it was incapable of generating ammonia once the argon atmosphere is replaced with a nitrogen atmosphere. Finally, our pre-experiment electropolishing procedure (detailed on page 141) was capable of restoring electrodes that had been deactivated.

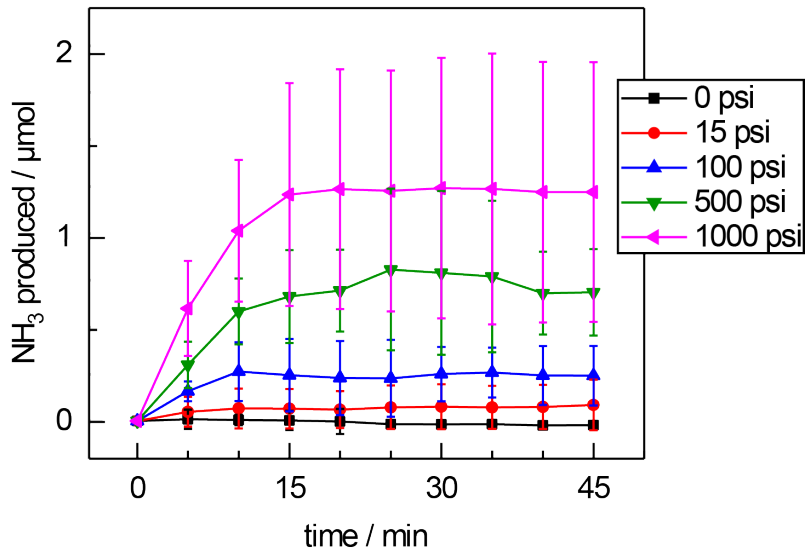

(a)

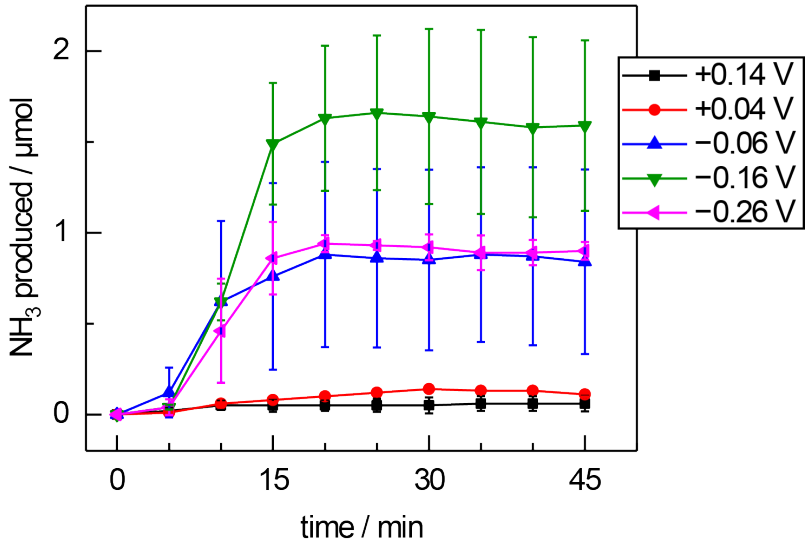

(b)

Figure 3-10. Time-resolved potentiostatic electrolyses of a Cu foam electrode in 1M KOH at 25 °C. Error bars represent 95% confidence intervals computed from a set of three independent measurements. **(a)** Ammonia production as a function of time, at an applied bias of -0.065 V vs. RHE and N_2 partial pressures of 0, 15, 100, 500, and 1000 psi (1000 psi total pressure, remainder argon). **(b)** Ammonia production as a function of time, at a total pressure of 1000 psi N_2 and applied biases of +0.14, +0.04, -0.06, -0.16, and -0.26 V vs. RHE.

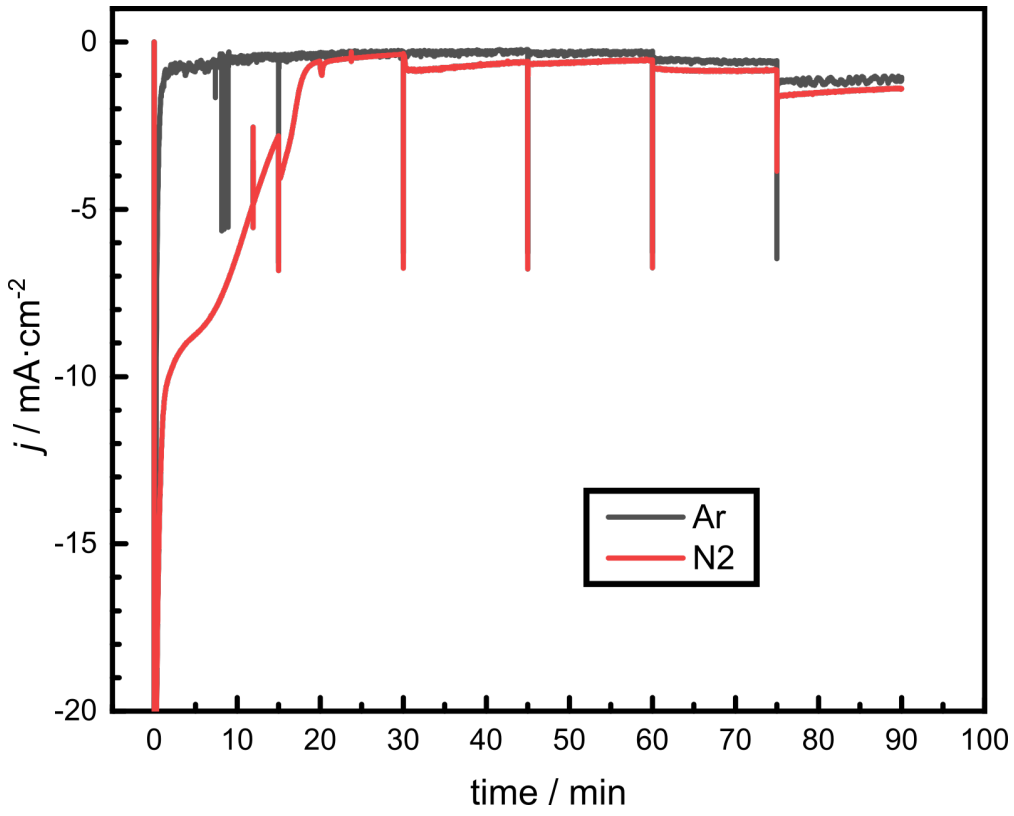

Figure 3-11. Stepped chronoamperometry of copper foil electrodes under 1000 psi Ar (black) and N_2 (red), starting at $-200\,\text{mV}$ and decreasing by $50\,\text{mV}$ every 15 minutes.

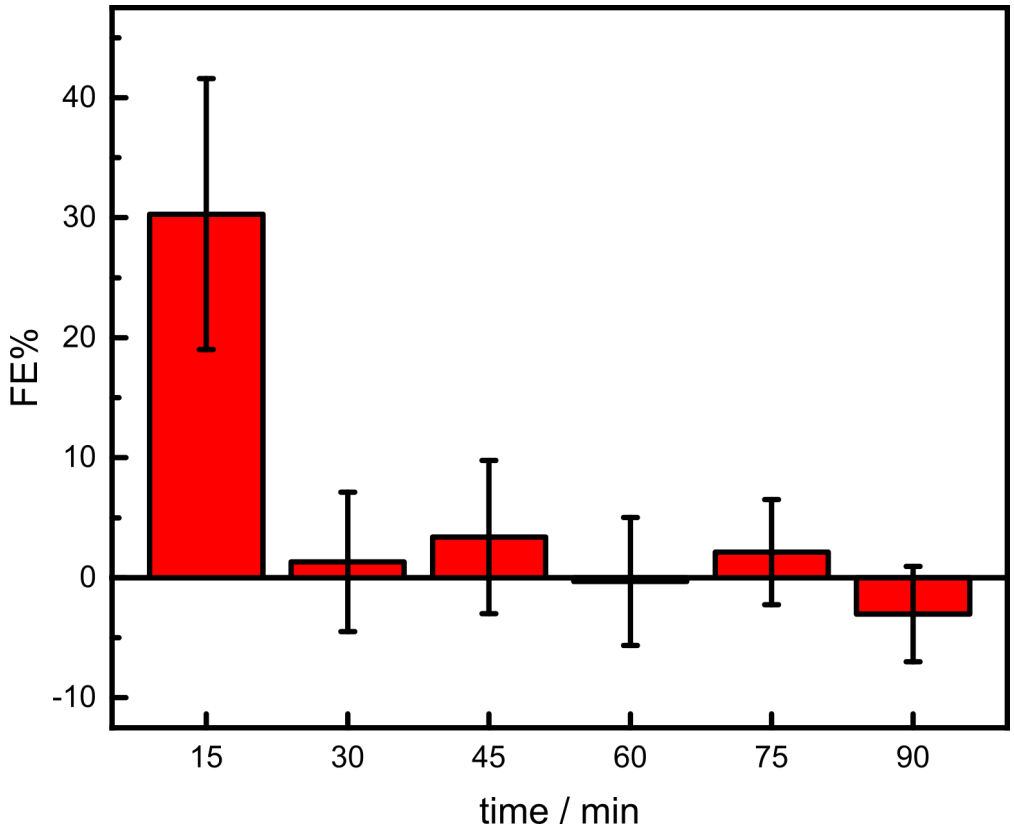

Figure 3-12. Faradaic efficiency of nitrogen reduction on copper foam electrode as a function of time, in 15-minute bins. Data collected from chronoamperometric electrolysis at −200 mV vs. RHE and quantified by colorimetry using Nessler method. Error bars represent 95% confidence intervals.

However, if this is were the case, we would expect precomplexation of impurity metal ions to suppress metal deposition and allow for sustained catalytic activity, as previously observed by our group using 'Chelex' ion chelating resin beads for carbon dioxide reduction catalysis,[114–116] a phenomenon we did not observe. Rather, we found that the pressurization of copper electrodes in aqueous electrolytes with N_2 gas produced transient NRR activity even when reactor headspaces were subsequently purged and replaced with argon. This suggested to us the possibility of a pressure-driven formation of nitride species on the electrode surface, a hypothesis that led us to assess the viability of copper nitride electrodes for NRR electrocatalysis.

3.2.2 Copper Nitride for Nitrogen Reduction Electrocatalysis

Copper nitride electrodes were synthesized by nitridation of copper electrodes (**Section 3.4.4** on page 142) and characterized by x-ray photoelectron spectroscopy (XPS) (**Appendix B.4** on page 241). As shown in **Figure 3-13**, these electrodes are active for ammonia electrosynthesis only under positive N_2 pressure and applied current. Under these conditions (bulk electrolysis in 1 M aqueous KOH solution at $-200\,\text{mV}$ vs. RHE for one hour at 1000 psi N_2), we observe peak Faradaic efficiencies of 14% and ammonia generation rates of $1.67\,\text{nmol}\cdot\text{cm}^{-2}\cdot\text{s}^{-1}$ at an overpotential of 270 mV, values which compare favorably to literature reports as listed in **Table 3.3** on page 115, especially when considering that these values are obtained in an aqueous system.

As shown in **Figure 3-14**, these nitride electrodes are competent for electrogeneration of ammonia; however, in aqueous environment, hydrolysis of Cu_3N to $Cu(OH)_2$ and NH_3 occurs even under Ar pressure and in the absence of applied current. For this reason, ammonia yields must be considered relative to the rate of nonfaradaic copper nitride hydrolysis, as detailed in **Appendix B.2.2** on page 235. Within the timespan in which the electrode creates ammonia electrochemically at a rate of $1.67\,\text{nmol}\cdot\text{cm}^{-2}\cdot\text{s}^{-1}$, ammonia is generated hydrolytically at a rate of $0.247\,\text{nmol}\cdot\text{cm}^{-2}\cdot\text{s}^{-1}$, suggesting that the rate of Faradaic nitrogen

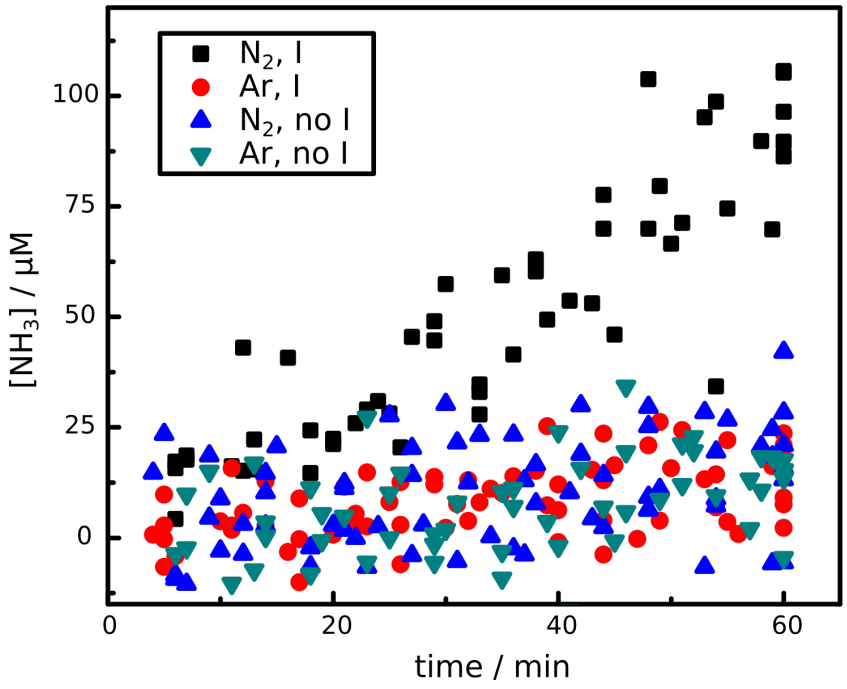

(a)

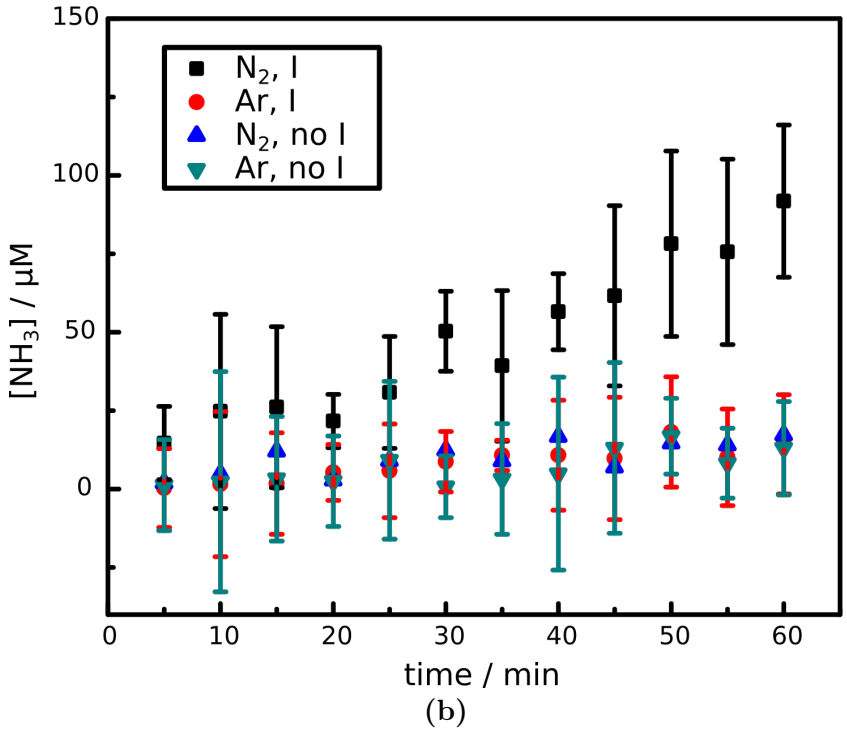

(b)

Figure 3-13. Ammonia generation on copper nitride electrode in 60 mL 1 M aq. KOH solution and quantified by colorimetry using phenate method. Conditions are either 1000 psi N_2 gas or 1000 psi Ar gas, under either open-circuit potential or under applied chronoamperometric electrolysis at −200 mV vs. RHE. **(a)** Scatterplot of NH_3 yield by individual timepoints. **(b)** Points binned in 5-minute increments; error bars represent 95% confidence intervals.

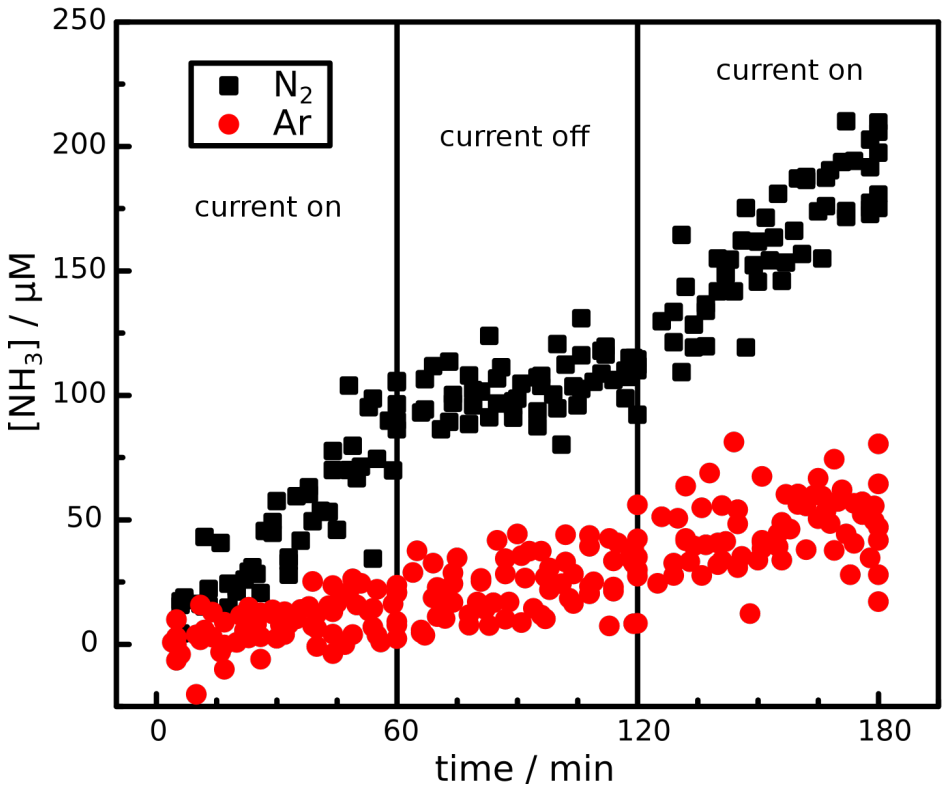

Figure 3-14. Ammonia generation of copper nitride foam electrodes in 60 mL 1 M aq. KOH solution pressurized to either 1000 psi N_2 (black) or 1000 psi Ar (red) and quantified by Nessler method. The first 60 minutes are under chronoamperometric electrolysis at −200 mV vs. RHE, the next 60 minutes are at open-circuit potential, and the final 60 minutes are also under chronoamperometric electrolysis at −200 mV vs. RHE.

fixation attributable to NRR is closer to 1.42 $\text{nmol}\cdot\text{cm}^{-2}\cdot\text{s}^{-1}$.

While this hydrolysis presumably limits the application of these electrodes for prolonged ammonia generation under aqueous conditions, extended BE experiments nevertheless evince substantial (albeit highly variable) yields of NH_3 at timescales as long as 72 hours, as seen in **Figure 3-15**. Faradaic efficiencies for these electrolyses work out to 5.37%, corresponding to an average areal ammonia generation rate of approximately 0.758 $\text{nmol}\cdot\text{cm}^{-2}\cdot\text{s}^{-1}$.

Furthermore, as seen in **Figure 3-16**, the rate of ammonia electrosynthesis on this electrode also correlates with the partial pressure of N_2, such that the selectivity for NRR over HER at ambient pressure is unlikely to produce statistically significant generation of ammonia relative to the rate of copper nitride hydrolysis.

Due to the ubiquity of adventitious ammonia and its proclivity to bind to metallic sur-

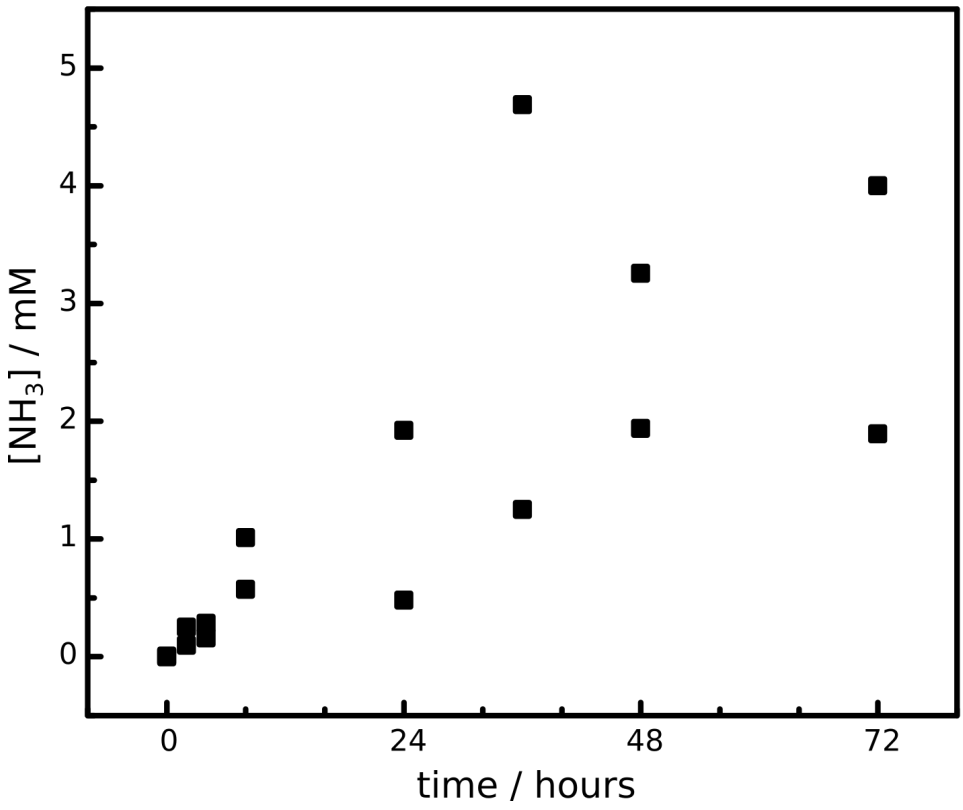

Figure 3-15. Bulk electrolysis of copper nitride electrode foam electrodes under chronoamperometric electrolysis at −200 mV vs. RHE for up to 72 hours in 60 mL 1 M aq. KOH solution pressurized to either 1000 psi N_2 and quantified by Nessler method.

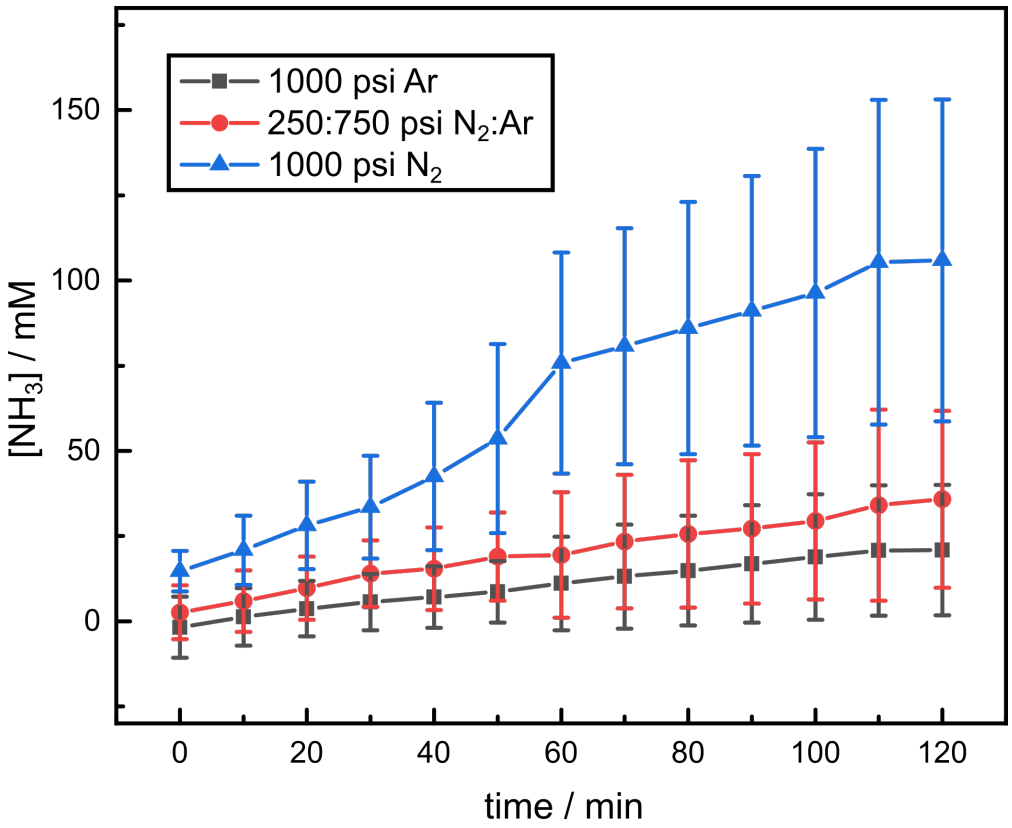

Figure 3-16. Pressure dependence of ammonia generation on copper nitride electrode. Data collected from chronoamperometric electrolysis at −200 mV vs. RHE in 60 mL 1 M aq. KOH solution and quantified by colorimetry using Nessler method. Error bars represent 95% confidence intervals.

faces, even these numerous control experiments do not by themselves constitute truly iron-clad evidence for the reduction of molecular N_2 to NH_3. The quantities of ammonia that are produced in a typical NRR experiment, on the order of µmols, may also be attributable to contamination from ammonia found in air, in ion-exchange membranes, or even in human breath. Moreover, labile nitrogenous impurities in an N_2 gas input stream, such as nitrates or nitrites, may be reduced to ammonia by applied electrochemical potential, thereby creating a situation whereby an apparent NRR electrocatalyst may appear to generate ammonia only under applied potential and N_2 flow, despite being incapable of actually effecting cleavage of the N≡N bond. These convoluting factors constitute a major hurdle for reproducibility in the field, as many reports of NRR electrocatalysis determined solely by colorimetric or spectroscopic studies have been unable to be replicated under more rigorous experimental conditions. In this regard, $^{15}N_2$ isotope labeling studies are generally considered to be a 'gold-standard' experiment for demonstrating nitrogen fixation, although the contamination of $^{15}N_2$ gas stocks with ^{15}N-labeled ammonium and nitrogen oxide impurities means even this methodology is not without flaws.[113, 117, 118]

The difficulty and expense of performing an isotope labeling study are exacerbated for high-pressure systems, as in addition to the inordinate cost of the $^{15}N_2$ feedstock (currently US$457.00 for 500 mL of gas at STP), the high pressure of reaction means not only that more $^{15}N_2$ is required than at STP, but also that $^{15}N_2$ stocks are not available in lecture bottles at sufficient pressures to run an experiment in pure $^{15}N_2$ without the use of a separate gas compressor; the previously-mentioned 500 mL tank comes as a 25 mL lecture bottle at a pressure of 275 pound-force per square inch gauge (psig).

As reducing the overall reaction pressure would reduce the selectivity towards NRR, we opted instead to create an isotopically enriched reactor headspace by combining $^{15}N_2$ and $^{14}N_2$ to a total reactor pressure of 1000 psi, at a rough $^{15}N_2$:$^{14}N_2$ ratio of 11.5:88.5. We conducted electrolysis on this inflow stream under typical reaction conditions (potentiostatically at −200 mV vs. RHE for 4 hours in 60 mL 1 M aq. KOH solution using a Cu_3N foam) and

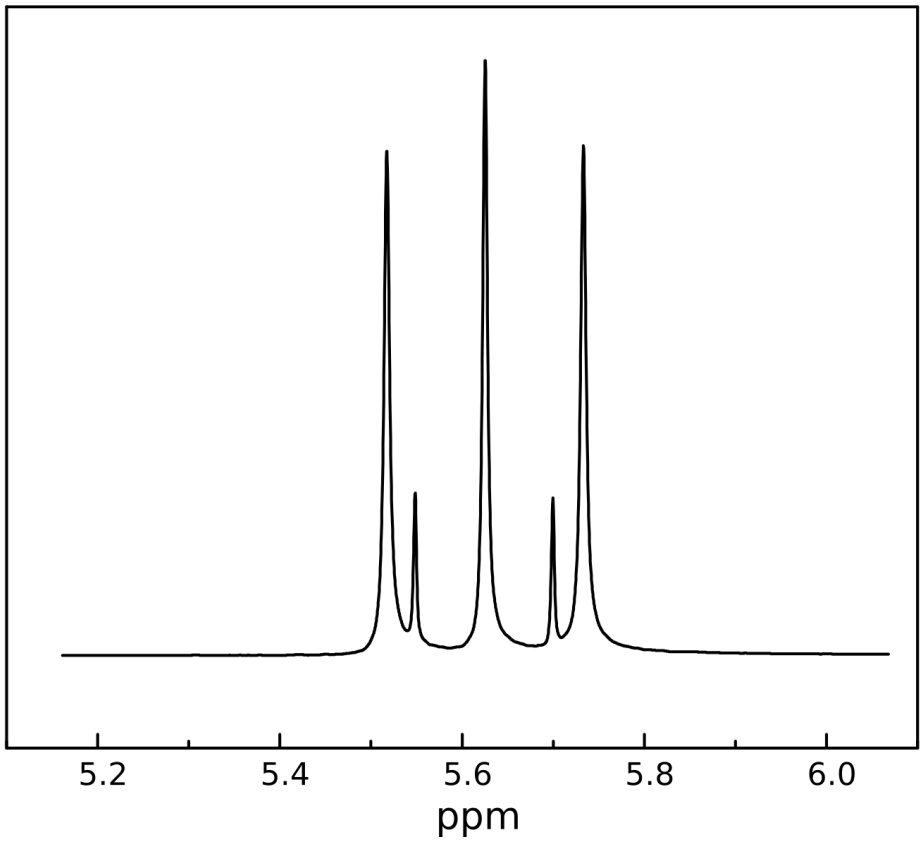

Figure 3-17. ^{1}H NMR of reactor headspace bubbled through concentrated H_2SO_4 following electrolysis. Reactor was pressurized with 115 psi $^{15}N_2$ and 885 psi $^{14}N_2$, for a total pressure of 1000 psi. Bulk electrolysis was performed potentiostatically at −200 mV vs. RHE for 4 hours in 60 mL 1 M aq. KOH solution using a Cu_3N foam. The ratio of peak area for the $^{15}NH_4^+$ doublet to the total area is 9.4%, out of an expected value of 11.5%.

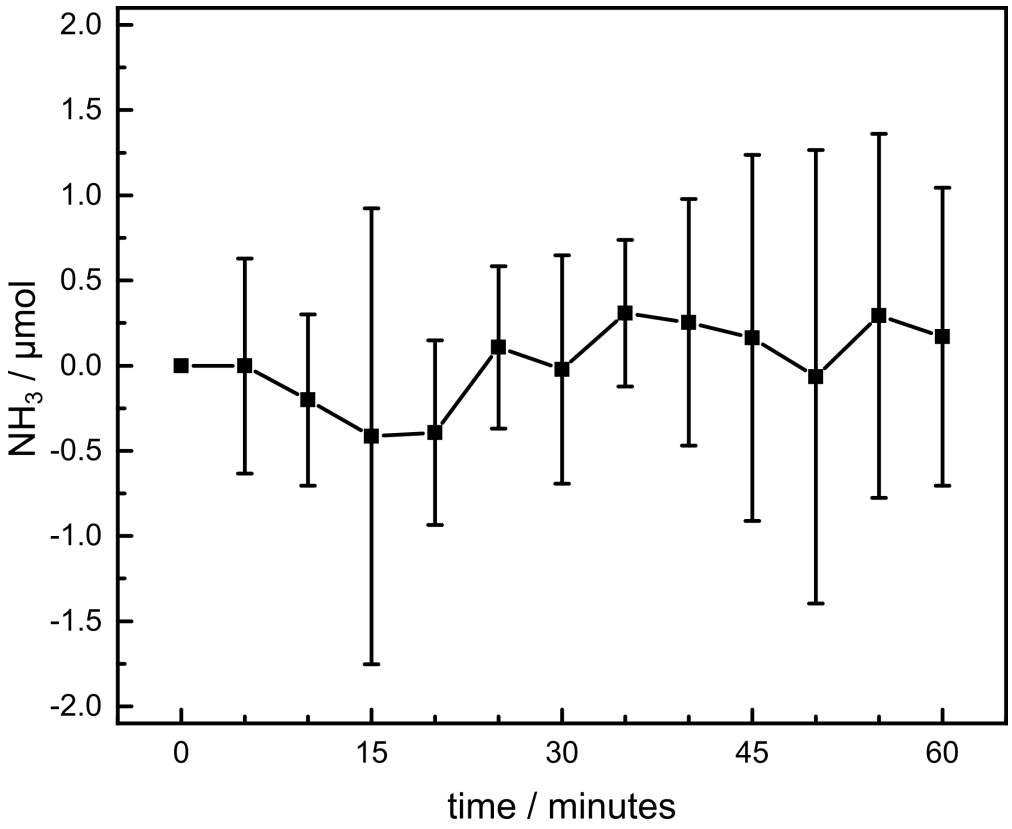

Figure 3-18. NRR activity of vanadium nitride nanoparticles electrodes in 60 mL 1 M aq. KOH solution pressurized to 1000 psi N_2 under chronoamperometric electrolysis at −200 mV vs. RHE and quantified by Nessler method. Error bars represent 95% confidence intervals computed from a set of three independent measurements.

bubbled the headspace through concentrated H_2SO_4, intermittently sonicating the reactor to desolvate dissolved ammonia. Taking a ^{1}H NMR spectrum (**Figure 3-17**), we observe in addition to the typical $^{14}NH_4^+$ 1:1:1 triplet a smaller, inset 1:1 doublet, corresponding to a $^{15}NH_4^+$ signal, the doublet splitting due to the $S = \frac{1}{2}$ nuclear spin of the ^{15}N nucleus. The ratio of peak area for this $^{15}NH_4^+$ doublet to the peak area for the $^{14}NH_4^+$ triplet is 9.4:90.6, comparing favorably to our expected value of 11.5%.

3.2.3 Vanadium Nitride for Nitrogen Reduction Electrocatalysis

While testing copper nitride electrodes, we also assessed the NRR activity of vanadium nitride electrodes at elevated N_2 pressures, inspired by a report of catalytic activity of VN nanosheets for NRR.[60, 119]

We did not observe statistically significant NH_3 formation under our conditions of reaction (**Figure 3-18**), which (to draw analogy to our Cu_3N system) were at 1000 psi of N_2 and 25 °C in 1 M aq. KOH. However, these conditions vary substantially to the reported literature conditions of 85 °C and an electrolyte of 1 M H_2SO_4, and it is conceivable that this is responsible for our lack of observed ammonia generation in this system.

3.3 Concluding Remarks

Utilizing high-pressure electrochemistry to amplify the rate of nitrogen reduction allows us to investigate the fundamental mechanistics that govern electrocatalytic ammonia generation at a high level of time resolution. Though electrochemistry at high pressures itself represents a novel approach from the existing electrochemical nitrogen reduction literature, this project seeks moreover to utilize the additional mechanistic handle afforded by high-pressure electrochemistry to more rigorously understand the kinetics of nitrogen reduction on heterogeneous metal surfaces, so as to enable the development of next-generation NRR electrocatalysts. Although electrochemical nitrogen reduction is a mature field with decades of ongoing literature, it is often plagued by poor replicability and low rates of NRR selectivity and yield.[120–140]

The application of N_2 pressure as a driving force for NRR selectivity over HER is a promising yet underutilized technique for enhancing ammonia yield and Faradaic efficiency. In this work, a high-pressure electrochemical setup was used to investigate the pressure and potential dependence of nitrogen reduction electrocatalysis in aqueous alkaline electrolyte. At a partial pressure of 1000 psi N_2, successful nitrogen reduction to ammonia was observed at low overpotentials (as small as 30 mV) and at high faradaic efficiencies (as high as 14.4% at 240 mV overpotential), a figure which is over an order of magnitude higher than reported nitrogen reduction electrocatalysts in aqueous media. These high faradaic efficiencies can be attributed to increased selectivity for NRR over parasitic HER, induced by elevated

nitrogen solubility at high N_2 partial pressures. These results demonstrate that copper nitride electrodes in particular may function as selective NRR electrocatalysts at elevated pressures of N_2, although practical use may be limited by nonfaradaic electrode hydrolysis.

3.4 Experimental Details

3.4.1 Cell Design and Layout

In order to evaluate the kinetics of this electrochemical reaction, it was necessary to develop a high-throughput method for sampling the cell electrolyte, a deceptively difficult task to perform in a sealed high-pressure reactor. To this end, a stainless steel 160 mL Parr Reactor Model No. 4774 General Purpose Vessel adapted with a high-pressure electrochemical feedthrough gland ([TG-24T(KN)-A4-G] by Conax Technologies) was modified with a 1/8" polyether ether ketone (PEEK) tube (pressure rated up to 6,000 psi) epoxied through a Swagelok SS-ORS2-A needle valve for use as sampling port to allow for aliquots of electrolyte to be extracted from the cell without depressurizing or interrupting electrochemical measurements, as pictured in **Figure 3-19**. To minimize the possibility of gas sorption to or reaction with the metal interior of the cell, the reactor was coated in a perfluoroalkoxy alkane (PFA) polymer by Donwell Company, Inc.

3.4.2 Electrochemical Methods

All measurements were taken at room temperature (25 °C) using a Gamry REF 600 potentiostat and a three-electrode electrochemical setup, with 1 M aqueous KOH as an electrolyte. The working electrode varied, and current densities were normalized against ECSA using the capacitive method detailed in **Section 2.4.1** on page 81. The reference electrode was a leakless Ag/AgCl cell in 3.4 M NaCl electrolyte (ET072-1 from eDAQ, Inc.) and the counter electrode was a Pt mesh separated from the solution by a porous glass frit. Potentials collected against this Ag/AgCl reference electrode were converted to potentials against RHE using

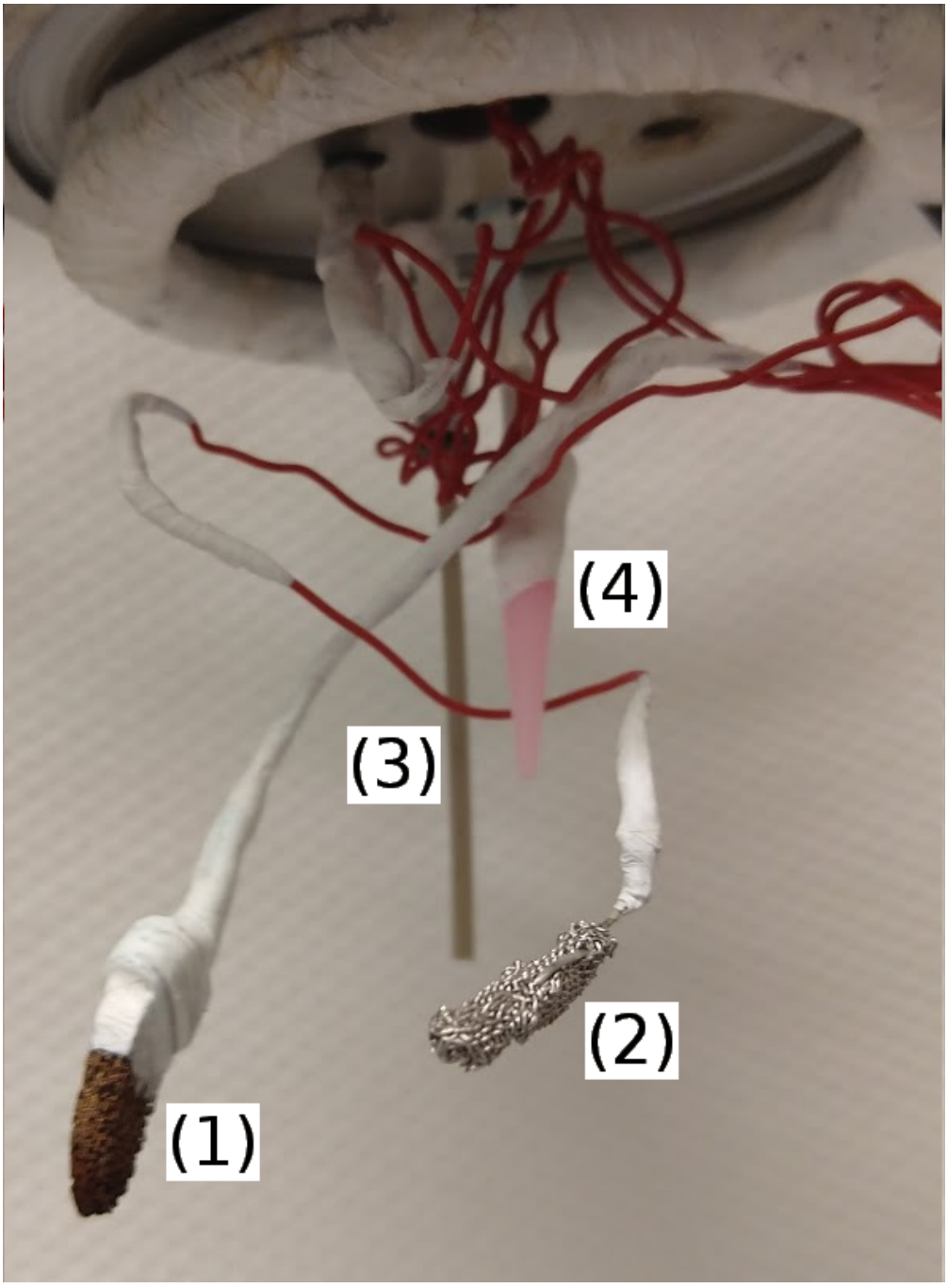

Figure 3-19. The pressure reactor head, with electrochemical feedthrough and electrodes. **(1)** Copper foam working electrode. **(2)** Platinum mesh counter electrode. **(3)** Leakless Ag/AgCl reference electrode. **(4)** PEEK siphon tube.

Equation 3.29; unless otherwise specified, all potentials listed are referenced against RHE.

$$E_{\mathrm{RHE}} = E_{\mathrm{Ag/AgCl}} + 0.205\ \mathrm{V} + (\mathrm{pH} \times 0.0591\ \mathrm{V}) \tag{3.29}$$

For experiments on copper metal, the working electrode was electropolished between experiments in a two-electrode setup for 3 minutes at +0.30 V against a copper foil counter electrode in *ortho*-phosphoric acid (99.99% pure trace metals basis, 345245 from Sigma-Aldrich), followed by sonication in MilliQ water (Millipore Type 1, 18 MΩ-cm resistivity) for 5 minutes. The counter electrode was also sonicated and rinsed with MilliQ, followed by cleaning in a butane flame, while the reference electrode was rinsed with MilliQ and the tip left to soak. Prior to use, glassware was soaked in aqua regia and, along with all cell components, rinsed with MilliQ water and dried in an oven at 150 °C for two hours.

3.4.3 Analytical Methods

Ammonia produced by the system was quantified through a variety of spectroscopic and colorimetric methods. Ammonia was first unambiguously identified by slowly bubbling the post-experiment reactor headspace through a flask of concentrated sulfuric acid, allowing for detection of the characteristic ^{1}H NMR signal, a 1:1:1 triplet induced by coupling to the spin-1 ^{14}N nucleus . Though this approach proved diagnostic for positive ammonia formation, the high aqueous solubility of NH_3 ($k_H^{\circ} \approx 60 \frac{\mathrm{mol}}{\mathrm{kg \cdot bar}}$)[141] meant that alternative quantification techniques were necessary to accurately calculate yield and selectivity.

For this purpose, a variety of colorimetric methods were evaluated: the Nessler method, the phenate method, and the salicylate method, as detailed in **Appendix B.1** on page 225.[142] Though all of these methods were found to be in agreement, the Nessler method was ultimately chosen as the primary method for quantification, owing to its rapid rate of color development. Towards this purpose, electrolyte timepoints of approximately 1 mL were dispensed by a teflon siphon tube (**Section 3.4.1**) and immediately quantified by colorimetric

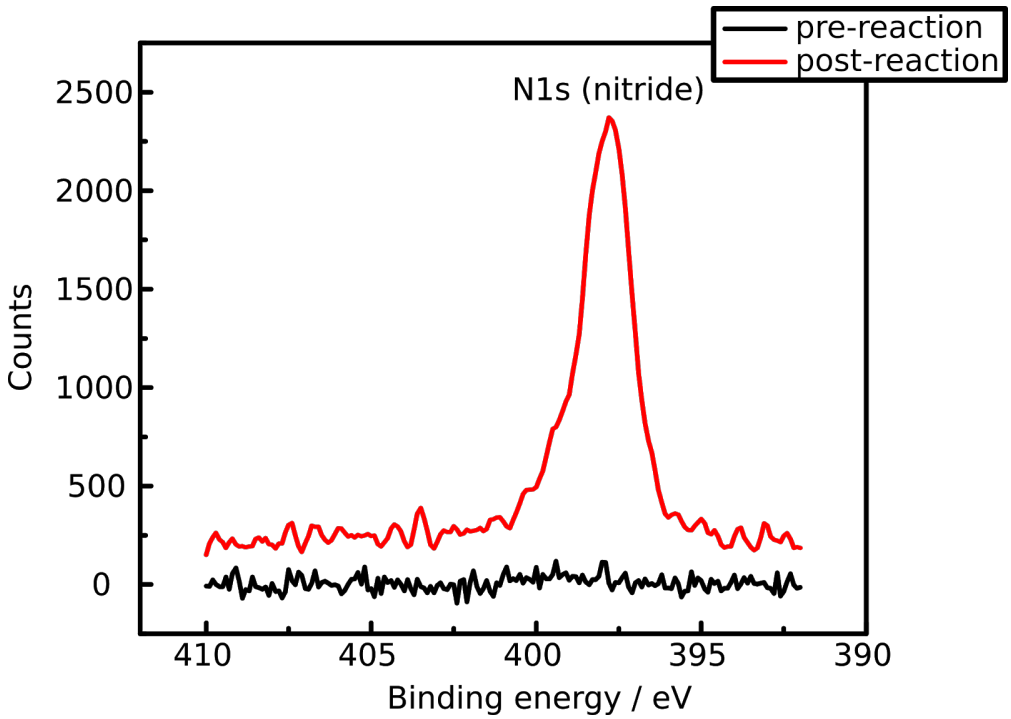

Figure 3-20. Characteristic N(1s) XPS spectrum of nitride, as collected on copper metal pre- and post-nitridation by sodium amide prep (**Section 3.4.4.1**).

methods to minimize the effects of adventitious ambient ammonia. Experiments were reproduced in triplicate, and 95% confidence intervals were calculated as 1.95996 times the standard error of the mean.

3.4.4 Synthesis and Characterization of Metal Nitrides

Nitridation syntheses have been reported by a variety of methodologies, from thin-film synthesis by magnetron sputtering[143, 144] to atomic-layer deposition[145] to the impressively named 'exploding wire technique'.[146] For the purposes of this work, we focus on three methodologies: nitridation by solid-state reaction of metal oxides with sodium amide,[147], nitridation by ammonia flow at elevated temperatures[148, 149], and nitridation by calcination with urea.[150] Samples were characterized pre- and post-reaction by XPS, with an eye towards the characteristic N(1s) nitride peak at 398 eV (**Figure 3-20**); full XPS spectra can be found in **Appendix B.4** on page 241.

3.4.4.1 Solid-State Synthesis of Cu_3N from Sodium Amide

Cu_3N Foam A 63% porous lost carbonate sintering (LCS) copper foam (CU003804 from Goodfellow USA) was baked in air at 340 °C for 8 hours to form a copper oxide layer. The foam was then brought into a nitrogen glovebox and covered in 30 g sodium amide (98%, Sigma-Aldrich) in a cylindrical heavy-wall PTFE-screw-capped glass pressure vessel and heated for 72 hours at 170 °C. The vessel was then removed from the glovebox and the sodium amide carefully quenched by sequential addition of 0.1 M acetic acid in isopropanol, 0.1 M acetic acid in ethanol, and finally 0.1 M aqueous acetic acid.

Cu_3N Foil A 1.0 mm-thick copper foil (99.999% trace metals basis, Sigma-Aldrich) was baked in air at 340 °C for 8 hours to form a copper oxide layer. The foil was then brought into a nitrogen glovebox and covered in 15 g sodium amide (98%, Sigma-Aldrich) in a cylindrical heavy-wall PTFE-screw capped glass pressure vessel and heated for 72 hours at 170 °C. The vessel was then removed from the glovebox and the sodium amide carefully quenched by sequential addition of 0.1 M acetic acid in isopropanol, 0.1 M acetic acid in ethanol, and finally 0.1 M aqueous acetic acid.

Cu_3N Powder 150 mg of copper(II) oxide powder (99.99% trace metals basis, Sigma-Aldrich) and 3.0 g sodium amide (98%, Sigma-Aldrich) were mixed in a nitrogen-filled glovebox and heated for 72 hours at 170 °C. The mixture was then removed from the glovebox and the sodium amide carefully quenched by addition of 0.1 M acetic acid in ethanol, yielding 93.5 mg of reddish-brown, fine coppery powder (72.6% yield)

3.4.4.2 Synthesis of Cu_3N Under NH_3 Flow

Both copper foils and foams were electropolished in a two-electrode setup for 3 minutes at +0.30 V against a copper foil counter electrode in *ortho*-phosphoric acid (99.99% pure trace metals basis, 345245 from Sigma-Aldrich), followed by sonication in MilliQ water (Millipore

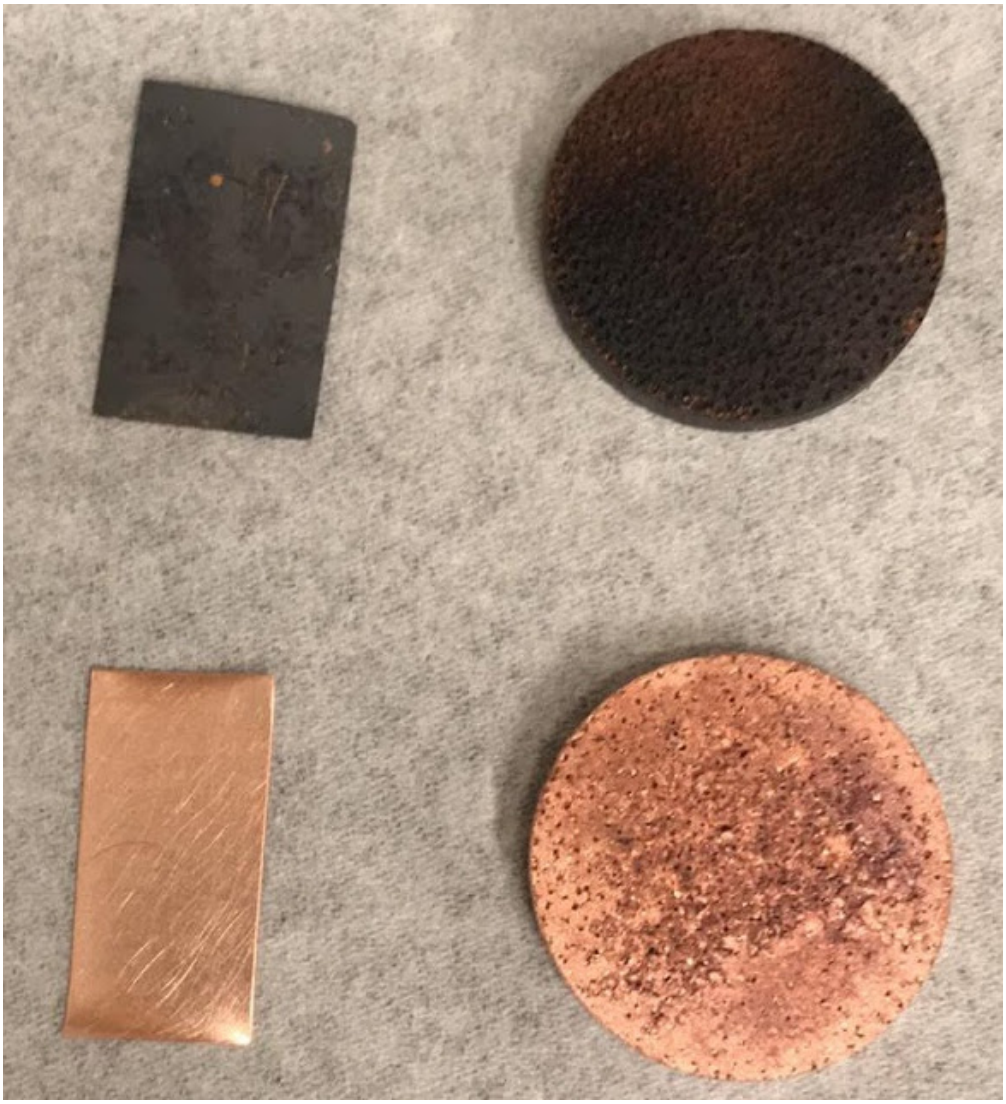

Figure 3-21. (top) Copper foil and foam nitridated by sodium amide prep. **(bottom)** Copper foil and foam nitridated by flowing-ammonia prep.

Type 1, 18 MΩ-cm resistivity) for 5 minutes, dried in air, and finally nitridated in a sealed furnace at 400 °C under gaseous NH_3 flow for 12 hours.

3.4.4.3 Solid-State Synthesis of VN from Sodium Amide

VN Powder 18.2 mg of vanadium(V) oxide powder (99.95% trace metals basis, Sigma-Aldrich) and 3.0 g sodium amide (98%, Sigma-Aldrich) were mixed in a nitrogen-filled glovebox and heated for 72 hours at 190 °C. The mixture was then removed from the glovebox and the sodium amide carefully quenched by addition of 0.1 M acetic acid in ethanol, yield-

ing 6.2 mg of eggshell-white powder (94.5% yield).

VN Foil A 1.0 mm-thick copper foil (99.8% trace metals basis, Alfa Aesar) was baked in air at 700 °C for 8 hours to form a vanadium oxide layer. The foil was then brought into a nitrogen glovebox and covered in 15 g sodium amide (98%, Sigma-Aldrich) in a cylindrical heavy-wall PTFE-screw capped glass pressure vessel and heated for 72 hours at 170 °C. The vessel was then removed from the glovebox and the sodium amide carefully quenched by sequential addition of 0.1 M acetic acid in isopropanol, 0.1 M acetic acid in ethanol, and finally 0.1 M aqueous acetic acid.

3.4.4.4 Synthesis of VN Nanoparticles from Urea

VN Powder 1.0 g vanadium oxytrichloride (99%, Sigma-Aldrich) and 1.04 g urea (≥99%, Fisher Scientific) were mixed well in 2 g ethanol, which was then spread onto an alumina boat and heated in a furnace under N_2 flow at 800 °C for 3 hours.

Electrodeposition on Carbon Felt 10 µg of vanadium nitride powder, as synthesized by the urea-glass method above, was dissolved in 450 µL milliQ water, 450 µL isopropyl alcohol, and 100 µL Nafion™ solution (LIQUion-1105-1100 EW, 5 wt%, FuelCellStore) to create an ink which was spray-dried on a carbon felt to an approximate loading of 0.5 mg·cm^{-2}.

References

[1] Smil, V. *Enriching the Earth: Fritz Haber, Carl Bosch, and the Transformation of World Food Production*; MIT Press, 2004.

[2] Smil, V. *Nature* **1999**, *400*, 415–415.

[3] Medford, A. J.; Hatzell, M. C. *ACS Catal.* **2017**, *7*, 2624–2643.

[4] Smil, V. *World Agriculture* **2011**, *2*, 9–13.

[5] Foster, S. L.; Bakovic, S. I. P.; Duda, R. D.; Maheshwari, S.; Milton, R. D.; Minteer, S. D.; Janik, M. J.; Renner, J. N.; Greenlee, L. F. *Nat. Catal.* **2018**, *1*, 490–500.

[6] Tariq, M.; Ali, H.; Hussain, N.; Nasim, W.; Mubeen, M.; Ahmad, S.; Hasanuzzaman, M. In *Agronomic Crops: Volume 1: Production Technologies*; Hasanuzzaman, M., Ed.; Springer: Singapore, 2019; pp 545–559.

[7] Fu, X.; JingYing, Z.; YongJun, J.; Lu, S.; JianFeng, Z.; Wei, Y.; Zhuang, B.; Nan, N.; Ying, Q. *Acta Pratacult. Sin.* **2011**, *20*, 245–255.

[8] White, K. D. *Agric. Hist.* **1970**, *44*, 281–290.

[9] Priestley, J.; Johnson, J.; Adams, J.; John Adams Library (Boston Public Library) BRL, *Experiments and Observations on Different Kinds of Air / by Joseph Priestly, LL.D.F.R.S*; Joseph Johnson: London, 1775.

[10] Cavendish, H. *Philos. Trans. R. Soc. Lond.* **1784**, *74*, 119–153.

[11] Cavendish, H. *Philos. Trans. R. Soc. Lond.* **1785**, *75*, 372–384.

[12] Cavendish, H. *Philos. Trans. R. Soc. Lond.* **1788**, *78*, 261–276.

[13] Hill, R. D.; Rinker, R. G.; Wilson, H. D. *J. Atmos. Sci.* **1980**, *37*, 179–192.

[14] Eyde, H. S. *J. Roy. Soc. Arts* **1909**, *57*, 568–576.

[15] Perkin, F. M. *Nature* **1906**, *74*, 444–446.

[16] Birkeland, K. *Trans. Faraday Soc.* **1906**, *2*, 98–116.

[17] Knox, J. *The Fixation of Atmospheric Nitrogen*; Gurney & Jackson, 1914.

[18] Lepel, F. V. *Ber. Dtsch. Chem. Ges.* **1903**, *36*, 1251–1258.

[19] Moissan, H. *C. R. Acad. Sci.* **1897**, *125*, 839–844.

[20] Caro, N. *Angew. Chem.* **1906**, *19*, 1569–1581.

[21] Beschraenkter, H. C. Verfahren zur Durchführung der chemischen Reaktion zwischen Stickstoff und Karbiden. 1910.

[22] Kastens, M. L.; McBurney, W. G. *Ind. Eng. Chem.* **1951**, *43*, 1020–1033.

[23] Eschenmoser, W. *Chim. Int. J. Chem* **1997**, *51*, 259–269.

[24] Travis, A. S. In *The Synthetic Nitrogen Industry in World War I: Its Emergence and Expansion*; S. Travis, A., Ed.; SpringerBriefs in Molecular Science; Springer International Publishing: Cham, 2015; pp 17–72.

[25] Ostwald, W. Improvements in the Manufacture of Nitric Acid and Nitrogen Oxides. 1902.

[26] Ostwald, W. Improvements in and Relating to the Manufacture of Nitric Acid and Oxides of Nitrogen. 1903.

[27] Fenton, H. J. H. *J. Chem. Soc., Trans.* **1882**, *41*, 262–263.

[28] Bosch, C.; Meiser, W. Process of Manufacturing Urea. 1922.

[29] Maxwell, G. R., Ed. *Synthetic Nitrogen Products: A Practical Guide to the Products and Processes*; Springer US: Boston, MA, 2004; pp 267–284.

[30] Haber, F. *Thermodynamik technischer Gasreaktionen: Sieben Vorlesungen*; R. Oldenburg, 1905.

[31] Haber, F. *Reson* **1920**, *7*, 86–94.

[32] Häussinger, P.; Lohmüller, R.; Watson, A. M. *Hydrogen, 2. Production*; Ullmann's Encyclopedia of Industrial Chemistry; Wiley-VCH, 2011.

[33] Appl, M. *Ammonia, 1. Introduction*; Ullmann's Encyclopedia of Industrial Chemistry; Wiley-VCH, 2011.

[34] Appl, M. *Ammonia, 2. Production Processes*; Ullmann's Encyclopedia of Industrial Chemistry; Wiley-VCH, 2011.

[35] Appl, M. *Ammonia, 3. Production Plants*; Ullmann's Encyclopedia of Industrial Chemistry; Wiley-VCH, 2011.

[36] Mittasch, A. *Berichte Dtsch. Chem. Ges. B Ser.* **1926**, *59*, 13–36.

[37] Gilbert, N. *Nat. News* **2012**, *483*, 525.

[38] Chen, G.-F.; Ren, S.; Zhang, L.; Cheng, H.; Luo, Y.; Zhu, K.; Ding, L.-X.; Wang, H. *Small Methods* **2019**, *3*, 1800337.

[39] Erisman, J. W.; Sutton, M. A.; Galloway, J.; Klimont, Z.; Winiwarter, W. *Nat. Geosci.* **2008**, *1*, 636–639.

[40] Rouwenhorst, K. H. R.; Krzywda, P. M.; Benes, N. E.; Mul, G.; Lefferts, L. *Ammonia, 4. Green Ammonia Production*; Ullmann's Encyclopedia of Industrial Chemistry; Wiley-VCH, 2020.

[41] Zapp, K.-H.; Wostbrock, K.-H.; Schäfer, M.; Sato, K.; Seiter, H.; Zwick, W.; Creutziger, R.; Leiter, H. *Ammonium Compounds*; Ullmann's Encyclopedia of Industrial Chemistry; Wiley-VCH, 2000.

[42] Mus, F.; Colman, D. R.; Peters, J. W.; Boyd, E. S. *Free Radic. Biol. Med.* **2019**, *140*, 250–259.

[43] Hoffman, B. M.; Lukoyanov, D.; Yang, Z.-Y.; Dean, D. R.; Seefeldt, L. C. *Chem Rev* **2014**, *114*, 4041–4062.

[44] Harris, D. F.; Lukoyanov, D. A.; Shaw, S.; Compton, P.; Tokmina-Lukaszewska, M.; Bothner, B.; Kelleher, N.; Dean, D. R.; Hoffman, B. M.; Seefeldt, L. C. *Biochemistry* **2018**, *57*, 701–710.

[45] Sippel, D.; Einsle, O. *Nat Chem Biol* **2017**, *13*, 956–960.

[46] Maira, N.; Remy, A.; Roy, N. C.; Pattyn, C.; Reniers, F. *Meet. Abstr.* **2020**, *MA2020-01*, 1126.

[47] Rouwenhorst, K. H. R.; Jardali, F.; Bogaerts, A.; Lefferts, L. *Energy Environ. Sci.* **2021**,

[48] Vojvodic, A.; Medford, A. J.; Studt, F.; Abild-Pedersen, F.; Khan, T. S.; Bligaard, T.; Nørskov, J. K. *Chem. Phys. Lett.* **2014**, *598*, 108–112.

[49] Honkala, K.; Hellman, A.; Remediakis, I. N.; Logadottir, A.; Carlsson, A.; Dahl, S.; Christensen, C. H.; Nørskov, J. K. *Science* **2005**, *307*, 555–558.

[50] Lindley, B. M.; Appel, A. M.; Krogh-Jespersen, K.; Mayer, J. M.; Miller, A. J. M. *ACS Energy Lett.* **2016**, *1*, 698–704.

[51] Soloveichik, G. *Nat. Catal.* **2019**, *2*, 377–380.

[52] Martín, A. J.; Shinagawa, T.; Pérez-Ramírez, J. *Chem* **2019**, *5*, 263–283.

[53] van der Ham, C. J. M.; Koper, M. T. M.; Hetterscheid, D. G. H. *Chem. Soc. Rev.* **2014**, *43*, 5183–5191.

[54] Singh, A. R.; Rohr, B. A.; Schwalbe, J. A.; Cargnello, M.; Chan, K.; Jaramillo, T. F.; Chorkendorff, I.; Nørskov, J. K. *ACS Catal.* **2017**, *7*, 706–709.

[55] Skúlason, E.; Bligaard, T.; Gudmundsdóttir, S.; Studt, F.; Rossmeisl, J.; Abild-Pedersen, F.; Vegge, T.; Jónsson, H.; K. Nørskov, J. *Phys. Chem. Chem. Phys.* **2012**, *14*, 1235–1245.

[56] Kordali, V.; Kyriacou, G.; Lambrou, C. *Chem. Commun.* **2000**, *0*, 1673–1674.

[57] Chen, S.; Perathoner, S.; Ampelli, C.; Mebrahtu, C.; Su, D.; Centi, G. *Angew. Chem. Int. Ed.* **2017**, *56*, 2699–2703.

[58] Lan, R.; Irvine, J. T. S.; Tao, S. *Sci. Rep.* **2013**, *3*, 1145.

[59] Furuya, N.; Yoshiba, H. *J. Electroanal. Chem. Interf. Electrochem.* **1990**, *291*, 269–272.

[60] Zhang, R.; Zhang, Y.; Ren, X.; Cui, G.; Asiri, A. M.; Zheng, B.; Sun, X. *ACS Sust. Chem. Eng.* **2018**, *6*, 9545–9549.

[61] Zhou, F.; Miguel Azofra, L.; Ali, M.; Kar, M.; N. Simonov, A.; McDonnell-Worth, C.; Sun, C.; Zhang, X.; R. MacFarlane, D. *Energy Environ. Sci.* **2017**, *10*, 2516–2520.

[62] Shi, M.-M.; Bao, D.; Wulan, B.-R.; Li, Y.-H.; Zhang, Y.-F.; Yan, J.-M.; Jiang, Q. *Adv. Mater.* **2017**, *29*, 1606550.

[63] Yang, D.; Chen, T.; Wang, Z. *J. Mater. Chem. A* **2017**, *5*, 18967–18971.

[64] Di, B.; Qi, Z.; Fan-Lu, M.; Hai-Xia, Z.; Miao-Miao, S.; Yu, Z.; Jun-Min, Y.; Qing, J.; Xin-Bo, Z. *Adv. Mater.* **2016**, *29*, 1604799.

[65] Liu, Y.; Su, Y.; Quan, X.; Fan, X.; Chen, S.; Yu, H.; Zhao, H.; Zhang, Y.; Zhao, J. *ACS Catal.* **2018**, *8*, 1186–1191.

[66] Wang, Z.; Li, Y.; Yu, H.; Xu, Y.; Xue, H.; Li, X.; Wang, H.; Wang, L. *ChemSusChem* **2018**, *11*, 3480–3485.

[67] Liu, H.-M.; Han, S.-H.; Zhao, Y.; Zhu, Y.-Y.; Tian, X.-L.; Zeng, J.-H.; Jiang, J.-X.; Xia, B. Y.; Chen, Y. *J. Mater. Chem. A* **2018**, *6*, 3211–3217.

[68] Sheets, B. L.; Botte, G. G. *Chem. Commun.* **2018**,

[69] Pospíšil, L.; Bulíčková, J.; Hromadová, M.; Gál, M.; Civiš, S.; Cihelka, J.; Tarábek, J. *Chem. Commun.* **2007**, *0*, 2270–2272.

[70] Pospíšil, L.; Hromadová, M.; Gál, M.; Bulíčková, J.; Sokolová, R.; Fanelli, N. *Electrochimica Acta* **2008**, *53*, 7445–7450.

[71] Xu, G.; Liu, R.; Wang, J. *Sci. Chin. Ser. B Chem.* **2009**, *52*, 1171–1175.

[72] Xu, G.; Liu, R. *Chin. J. Chem.* **2010**, *28*, 139–142.

[73] Zhao, X.; Yin, F.; Liu, N.; Li, G.; Fan, T.; Chen, B. *J. Mater. Sci.* **2017**, *52*, 10175–10185.

[74] Kang, C. S. M.; Zhang, X.; MacFarlane, D. R. *J. Phys. Chem. C* **2018**, *122*, 24550–24558.

[75] Licht, S.; Cui, B.; Wang, B.; Li, F.-F.; Lau, J.; Liu, S. *Science* **2014**, *345*, 637–640.

[76] Bicer, Y.; Dincer, I. *Int. J. Energy Res.* **2017**, *41*, 1987–2000.

[77] Kishira, S.; Qing, G.; Suzu, S.; Kikuchi, R.; Takagaki, A.; Oyama, S. T. *Int. J. Hydrog. Energy* **2017**, *42*, 26843–26854.

[78] Qing, G.; Kikuchi, R.; Kishira, S.; Takagaki, A.; Sugawara, T.; Oyama, S. T. *J. Electrochem. Soc.* **2016**, *163*, E282–E287.

[79] Kim, K.; Lee, S. J.; Kim, D.-Y.; Yoo, C.-Y.; Choi, J. W.; Kim, J.-N.; Woo, Y.; Yoon, H. C.; Han, J.-I. *ChemSusChem* **2018**, *11*, 120–124.

[80] Imamura, K.; Matsuyama, M.; Kubota, J. *ChemistrySelect* **2017**, *2*, 11100–11103.

[81] Cui, B.; Zhang, J.; Liu, S.; Liu, X.; Xiang, W.; Liu, L.; Xin, H.; Lefler, M. J.; Licht, S. *Green Chem.* **2017**, *19*, 298–304.

[82] Manabe, R.; Nakatsubo, H.; Gondo, A.; Murakami, K.; Ogo, S.; Tsuneki, H.; Ikeda, M.; Ishikawa, A.; Nakai, H.; Sekine, Y. *Chem. Sci.* **2017**, *8*, 5434–5439.

[83] Murakami, T.; Nohira, T.; Goto, T.; Ogata, Y. H.; Ito, Y. *Electrochim. Acta* **2005**, *50*, 5423–5426.

[84] Lan, R.; Alkhazmi, K. A.; Amar, I. A.; Tao, S. *Applied Catalysis B, Environmental* **2014**, *152-153*, 212–217.

[85] Murakami, T.; Nishikiori, T.; Nohira, T.; Ito, Y. *J. Am. Chem. Soc.* **2003**, *125*, 334–335.

[86] Klinsrisuka, S.; Irvine, J. T. S. *Catal. Today* **2017**, *286*, 41–50.

[87] Lan, R.; Alkhazmi, K. A.; Amar, I. A.; Tao, S. *Electrochim. Acta* **2014**, *123*, 582–587.

[88] Amar, I. A.; Petit, C. T.; Lan, R.; Mann, G.; Skabara, P. J.; Tao, S. *INT J HYDROGEN ENERGY* **2014**, *39*, 4322–4330.

[89] Amar, I. A.; Petit, C. T. G.; Lan, R.; Mann, G.; Tao, S. *RSC Adv.* **2014**, *4*, 18749–18754.

[90] Amar, I. A.; Lan, R.; Petit, C. T.; Tao, S. *Int. J. Electrochem. Sci.* **2015**, *10*, 3757–3766.

[91] Amar, I. A.; Petit, C. T. G.; Zhang, L.; Lan, R.; Skabara, P. J.; Tao, S. *Solid State Ionics* **2011**, *201*, 94–100.

[92] McEnaney, J. M.; Singh, A. R.; Schwalbe, J. A.; Kibsgaard, J.; Lin, J. C.; Cargnello, M.; Jaramillo, T. F.; Nørskov, J. K. *Energy Environ. Sci.* **2017**, *10*, 1621–1630.

[93] Ouzounidou, M.; Skodra, A.; Kokkofitis, C.; Stoukides, M. *Solid State Ionics* **2007**, *178*, 153–159.

[94] Liu, J.; Li, Y.; Wang, W.; Wang, H.; Zhang, F.; Ma, G. *J Mater Sci* **2010**, *45*, 5860–5864.

[95] Wang, X.; Yin, J.; Xu, J.; Wang, H.; Ma, G. *Chin. J. Chem* **2011**, *29*, 1114–1118.

[96] Shimoda, N.; Kobayashi, Y.; Kimura, Y.; Nakagawa, G.; Satokawa, S. *J. Ceram. Soc. Jpn.* **2017**, *125*, 252–256.

[97] Kosaka, F.; Noda, N.; Nakamura, T.; Otomo, J. *J Mater Sci* **2017**, *52*, 2825–2835.

[98] Díez-Ramírez, J.; Kyriakou, V.; Garagounis, I.; Vourros, A.; Vasileiou, E.; Sánchez, P.; Dorado, F.; Stoukides, M. *ACS Sustainable Chem. Eng.* **2017**, *5*, 8844–8851.

[99] Xie, Y.-H.; Wang, J.-D.; Liu, R.-Q.; Su, X.-T.; Sun, Z.-P.; Li, Z.-J. *Solid State Ionics* **2004**, *168*, 117–121.

[100] Wang, J.; Yahong, X.; Zhengfang, Z.; Ruiquan, L.; Zhijie, L. *Mater. Res. Bull.* **2005**, *40*, 1294–1302.

[101] Wang, W. B.; Cao, X. B.; Gao, W. J.; Zhang, F.; Wang, H. T.; Ma, G. L. *J. Membr. Sci.* **2010**, *1-2*, 397–403.

[102] Wang, W.; Liu, J.; Li, Y.; Wang, H.; Zhang, F.; Ma, G. *Solid State Ionics* **2010**, *181*, 667–671.

[103] Skodra, A.; Stoukides, M. *Solid State Ionics* **2009**, *180*, 1332–1336.

[104] Marnellos, G.; Stoukides, M. *Science* **1998**, *282*, 98–100.

[105] Vasileiou, E.; Kyriakou, V.; Garagounis, I.; Vourros, A.; Stoukides, M. *Solid State Ionics* **2015**, *275*, 110–116.

[106] Tsuneto, A.; Kudo, A.; Sakata, T. *J. Electroanal. Chem.* **1994**, *367*, 183–188.

[107] Köleli, F.; Röpke, T. *Applied Catalysis B: Environmental* **2006**, *62*, 306–310.

[108] Giovanelli, D.; Lawrence, N. S.; Compton, R. G. *Electroanalysis* **2004**, *16*, 789–810.

[109] Tsuneto, A.; Kudo, A.; Sakata, T. *Chem. Lett.* **1993**, *22*, 851–854.

[110] Chen, Z.; Zhao, J.; Yin, L.; Chen, Z. *J. Mater. Chem. A* **2019**, *7*, 13284–13292.

[111] Lee, H. K.; Koh, C. S. L.; Lee, Y. H.; Liu, C.; Phang, I. Y.; Han, X.; Tsung, C.-K.; Ling, X. Y. *Sci. Adv.* **2018**, *4*, eaar3208.

[112] Lan, R.; Tao, S. *RSC Adv.* **2013**, *3*, 18016–18021.

[113] Greenlee, L. F.; Renner, J. N.; Foster, S. L. *ACS Catal.* **2018**, *8*, 7820–7827.

[114] Wuttig, A.; Surendranath, Y. *ACS Catal.* **2015**, *5*, 4479–4484.

[115] Wuttig, A.; Yaguchi, M.; Motobayashi, K.; Osawa, M.; Surendranath, Y. *PNAS* **2016**,

[116] Hall, A. S.; Yoon, Y.; Wuttig, A.; Surendranath, Y. *J. Am. Chem. Soc.* **2015**, *137*, 14834–14837.

[117] Andersen, S. Z. et al. *Nature* **2019**, *570*, 504–508.

[118] Dabundo, R.; Lehmann, M. F.; Treibergs, L.; Tobias, C. R.; Altabet, M. A.; Moisander, P. H.; Granger, J. *PLOS ONE* **2014**, *9*, e110335.

[119] Yang, X.; Nash, J.; Anibal, J.; Dunwell, M.; Kattel, S.; Stavitski, E.; Attenkofer, K.; Chen, J. G.; Yan, Y.; Xu, B. *J. Am. Chem. Soc.* **2018**, *140*, 13387–13391.

[120] Aika, K.-i.; Hori, H.; Ozaki, A. *J. Catal.* **1972**, *27*, 424–431.

[121] Aika, K.-i.; Takano, T.; Murata, S. *J. Catal.* **1992**, *136*, 126–140.

[122] Giddey, S.; Badwal, S. P. S.; Kulkarni, A. *Int. J. Hydrog. Energy* **2013**, *38*, 14576–14594.

[123] Guo, X.; Du, H.; Qu, F.; Li, J. *J. Mater. Chem. A* **2019**, *7*, 3531–3543.

[124] Han, J.; Liu, Z.; Ma, Y.; Cui, G.; Xie, F.; Wang, F.; Wu, Y.; Gao, S.; Xu, Y.; Sun, X. *Nano Energy* **2018**, *52*, 264–270.

[125] Hu, L.; Khaniya, A.; Wang, J.; Chen, G.; Kaden, W. E.; Feng, X. *ACS Catal.* **2018**, *8*, 9312–9319.

[126] Kitano, M.; Inoue, Y.; Yamazaki, Y.; Hayashi, F.; Kanbara, S.; Matsuishi, S.; Yokoyama, T.; Kim, S.-W.; Hara, M.; Hosono, H. *Nat. Chem.* **2012**, *4*, 934–940.

[127] Köleli, F.; Kayan, D. B. *J. Electroanal. Chem.* **2010**, *638*, 119–122.

[128] Li, L.; Tang, C.; Xia, B.; Jin, H.; Zheng, Y.; Qiao, S.-Z. *ACS Catal.* **2019**, *9*, 2902–2908.

[129] Liu, X.; Wang, Z.; Zhao, J.; Zhao, J.; Liu, Y. *Appl. Surf. Sci.* **2019**, *487*, 833–839.

[130] Nazemi, M.; El-Sayed, M. A. *J. Phys. Chem. Lett.* **2018**, *9*, 5160–5166.

[131] Pickett, C. J.; Talarmin, J. *Nature* **1985**, *317*, 652–653.

[132] Shipman, M. A.; Symes, M. D. *Catal. Today* **2017**, *286*, 57–68.

[133] Song, P.; Wang, H.; Kang, L.; Ran, B.; Song, H.; Wang, R. *Chem. Commun.* **2019**, *55*, 687–690.

[134] Suryanto, B. H. R.; Du, H.-L.; Wang, D.; Chen, J.; Simonov, A. N.; MacFarlane, D. R. *Nat. Catal.* **2019**, *2*, 290.

[135] Wang, D.; Azofra, L. M.; Harb, M.; Cavallo, L.; Zhang, X.; Suryanto, B. H. R.; MacFarlane, D. R. *ChemSusChem* **2018**, *11*, 3416–3422.

[136] Wang, J.; Yu, L.; Hu, L.; Chen, G.; Xin, H.; Feng, X. *Nat. Commun.* **2018**, *9*, 1795.

[137] Yin, F.; Lin, X.; He, X.; Chen, B.; Li, G.; Yin, H. *Materials Letters* **2019**, *248*, 109–113.

[138] Zhang, L.; Zhao, W.; Zhang, W.; Chen, J.; Hu, Z. *Nano Res.* **2019**, *12*, 1181–1186.

[139] Zhang, L.; Ding, L.-X.; Chen, G.-F.; Yang, X.; Wang, H. *Angew. Chem. Int. Ed.* **2019**, *131*, 2638–2642.

[140] Zhang, Y.; Du, H.; Ma, Y.; Ji, L.; Guo, H.; Tian, Z.; Chen, H.; Huang, H.; Cui, G.; Asiri, A. M.; Qu, F.; Chen, L.; Sun, X. *Nano Res.* **2019**, *12*, 919–924.

[141] Sander, R.; Linstrom, P. J.; Mallard, W. G. *Henry's Law Constants*; NIST Standard Reference Database 69; National Institute of Standards and Technology: Gaithersburg MD, 20899.

[142] Molins-Legua, C.; Meseguer-Lloret, S.; Moliner-Martinez, Y.; Campíns-Falcó, P. *Trends Anal. Chem.* **2006**, *25*, 282–290.

[143] Wang, J.; Chen, J. T.; Yuan, X. M.; Wu, Z. G.; Miao, B. B.; Yan, P. X. *J. Cryst. Growth* **2006**, *286*, 407–412.

[144] Ji, A. L.; Huang, R.; Du, Y.; Li, C. R.; Wang, Y. Q.; Cao, Z. X. *J. Cryst. Growth* **2006**, *295*, 79–83.

[145] Törndahl, T.; Ottosson, M.; Carlsson, J.-O. *J. Electrochem. Soc.* **2006**, *153*, C146.

[146] Joncich, M. J.; Vaughn, J. W.; Knutsen, B. F. *Can. J. Chem.* **1966**, *44*, 137–142.

[147] Miura, A.; Takei, T.; Kumada, N. *J. Asian Ceram. Soc.* **2014**, *2*, 326–328.

[148] Baiker, A.; Maciejewski, M. *J. Chem. Soc. Faraday Trans. 1 Phys. Chem. Condens. Phases* **1984**, *80*, 2331–2341.

[149] Mishra, P. P.; Theerthagiri, J.; Panda, R. N. *Adsorption Science & Technology* **2014**, *32*, 465–474.

[150] Giordano, C.; Erpen, C.; Yao, W.; Milke, B.; Antonietti, M. *Chem. Mater.* **2009**, *21*, 5136–5144.

[151] Abbasfard, H.; Ghanbari, M.; Ghasemi, A.; Ghahraman, G.; Jokar, S. M.; Rahimpour, M. R. *Appl. Therm. Eng.* **2014**, *67*, 223–229.

[152] Anderson, J. S.; Rittle, J.; Peters, J. C. *Nature* **2013**, *501*, 84–87.

[153] Arashiba, K.; Kinoshita, E.; Kuriyama, S.; Eizawa, A.; Nakajima, K.; Tanaka, H.; Yoshizawa, K.; Nishibayashi, Y. *J. Am. Chem. Soc.* **2015**, *137*, 5666–5669.

[154] Back, S.; Jung, Y. *Phys. Chem. Chem. Phys.* **2016**, *18*, 9161–9166.

[155] Battino, R.; Rettich, T. R.; Tominaga, T. *J. Phys. Chem. Ref. Data* **1984**, *13*, 563–600.

[156] Boisen, A.; Dahl, S.; Nørskov, J. K.; Christensen, C. H. *J. Catal.* **2005**, *230*, 309–312.

[157] Bratsch, S. G. *J. Phys. Chem. Ref. Data* **1989**, *18*, 1–21.

[158] Cao, Y.; Gao, Y.; Zhou, H.; Chen, X.; Hu, H.; Deng, S.; Zhong, X.; Zhuang, G.; Wang, J. *Adv. Theory Simul.* **2018**, *1*, 1800018.

[159] Chen, G.; Ding, L.; Luo, R.; Wang, H. *Meet. Abstr.* **2019**, *MA2019-01*, 1674–1674.

[160] Chen, S.; Perathoner, S.; Ampelli, C.; Centi, G. In *Studies in Surface Science and Catalysis*; Albonetti, S., Perathoner, S., Quadrelli, E. A., Eds.; Horizons in Sustainable Industrial Chemistry and Catalysis; Elsevier, 2019; Vol. 178; pp 31–46.

[161] Choi, C.; Back, S.; Kim, N.-Y.; Lim, J.; Kim, Y.-H.; Jung, Y. *ACS Catal.* **2018**, *8*, 7517–7525.

[162] Creighton, H. J. M. *Journal of the Franklin Institute* **1919**, *187*, 705–735.

[163] Dahl, S.; Logadottir, A.; Jacobsen, C. J. H.; Nørskov, J. K. *Appl. Catal. A* **2001**, *222*, 19–29.

[164] Garagounis, I.; Kyriakou, V.; Skodra, A.; Vasileiou, E.; Stoukides, M. *Front. Energy Res.* **2014**, *2*.

[165] Gross, S. A.; Avens, H. J.; Banducci, A. M.; Sahmel, J.; Panko, J. M.; Tvermoes, B. E. *J. Air Waste Manag. Assoc.* **2013**, *63*, 424–432.

[166] Hao, Y.-C. et al. *Nat. Catal.* **2019**, *2*, 448.

[167] Hong, J.; Prawer, S.; Murphy, A. B. *IEEE Trans. Plasma Sci.* **2014**, *42*, 2338–2339.

[168] Hu, B.; Hu, M.; Seefeldt, L.; Liu, T. L. *ACS Energy Lett.* **2019**, *4*, 1053–1054.

[169] Jennings, J. R. *Catalytic Ammonia Synthesis: Fundamentals and Practice*; Springer US : Imprint : Springer: Boston, MA, 1991.

[170] Kim, K.; Yoo, C.-Y.; Kim, J.-N.; Yoon, H. C.; Han, J.-I. *J. Electrochem. Soc.* **2016**, *163*, F1523–F1526.

[171] Kim, K.; Lee, N.; Yoo, C.-Y.; Kim, J.-N.; Yoon, H. C.; Han, J.-I. *J. Electrochem. Soc.* **2016**, *163*, F610.

[172] Kirova-Yordanova, Z. *Energy* **2011**, *36*, 3733–3744.

[173] Kyriakou, V.; Garagounis, I.; Vasileiou, E.; Vourros, A.; Stoukides, M. *Catal. Today* **2017**, *286*, 2–13.

[174] Lan, R.; Irvine, J. T. S.; Tao, S. *International Journal of Hydrogen Energy* **2012**, *37*, 1482–1494.

[175] Laplaza, C. E.; Johnson, A. R.; Cummins, C. C. *J. Am. Chem. Soc.* **1996**, *118*, 709–710.

[176] Laplaza, C. E.; Johnson, M. J. A.; Peters, J. C.; Odom, A. L.; Kim, E.; Cummins, C. C.; George, G. N.; Pickering, I. J. *J. Am. Chem. Soc.* **1996**, *118*, 8623–8638.

[177] Lazouski, N.; Schiffer, Z. J.; Williams, K.; Manthiram, K. *Joule* **2019**, *3*, 1127–1139.

[178] Lazouski, N.; Manthiram, K. *Trends in Chemistry* **2019**, *1*, 141–142.

[179] Li, Y.; Kong, Y.; Hou, Y.; Yang, B.; Li, Z.; Lei, L.; Wen, Z. *ACS Sust. Chem. Eng.* **2019**, *7*, 8853–8859.

[180] Lipman, T.; Shah, N. *Ammonia as an Alternative Energy Storage Medium for Hydrogen Fuel Cells: Scientific and Technical Review for Near-Term Stationary Power Demonstration Projects, Final Report*; 2007.

[181] Liu, H.; Wei, L.; Liu, F.; Pei, Z.; Shi, J.; Wang, Z.-j.; He, D.; Chen, Y. *ACS Catal.* **2019**, 5245–5267.

[182] Liu, C.; Li, Q.; Zhang, J.; Jin, Y.; MacFarlane, D. R.; Sun, C. *J. Mater. Chem. A* **2019**, *7*, 4771–4776.

[183] Liu, A.; Yang, Y.; Ren, X.; Zhao, Q.; Gao, M.; Guan, W.; Meng, F.; Gao, L.; Yang, Q.; Liang, X.; Ma, T. *ChemSusChem* **2020**, *13*, 3766–3788.

[184] Luo, Y.; Chen, G.-F.; Ding, L.; Chen, X.; Ding, L.-X.; Wang, H. *Joule* **2019**, *3*, 279–289.

[185] Maheshwari, S.; Janik, M. J. *Joule* **2019**, *3*, 915–916.

[186] Manjunatha, R.; Schechter, A. *Electrochem. Commun.* **2018**, *90*, 96–100.

[187] Manjunatha, R.; Karajić, A.; Goldstein, V.; Schechter, A. *ACS Appl. Mater. Interf.* **2019**, *11*, 7981–7989.

[188] Mao, C.; Wang, J.; Zou, Y.; Li, H.; Zhan, G.; Li, J.; Zhao, J.; Zhang, L. *Green Chem.* **2019**,

[189] Nazemi, M.; Panikkanvalappil, S. R.; El-Sayed, M. A. *Nano Energy* **2018**, *49*, 316–323.

[190] Nazemi, M.; El-Sayed, M. A. *J Phys Chem A* **2019**,

[191] Pang, F.; Wang, Z.; Zhang, K.; He, J.; Zhang, W.; Guo, C.; Ding, Y. *Nano Energy* **2019**, *58*, 834–841.

[192] Patil, B. S.; Hessel, V.; Seefeldt, L. C.; Dean, D. R.; Hoffman, B. M.; Cook, B. J.; Murray, L. J. *Nitrogen Fixation*; Ullmann's Encyclopedia of Industrial Chemistry; Wiley-VCH, 2017.

[193] Pérez-Ramírez, J.; Kapteijn, F.; Schöffel, K.; Moulijn, J. A. *Appl. Catal. B* **2003**, *44*, 117–151.

[194] Pérez-Ramírez, J.; Vigeland, B. *Angew. Chem. Int. Ed.* **2005**, *44*, 1112–1115.

[195] Pérez-Ramírez, J.; Vigeland, B. *Catal. Today* **2005**, *105*, 436–442.

[196] Pfromm, P. H. *J. Renew. Sustain. Energy* **2017**, *9*, 034702.

[197] Pool, J. A.; Lobkovsky, E.; Chirik, P. J. *Nature* **2004**, *427*, 527–530.

[198] Rayment, T.; Schlögl, R.; Thomas, J. M.; Ertl, G. *Nature* **1985**, *315*, 311–313.

[199] Rostamikia, G.; Maheshwari, S.; Janik, M. J. *Catal. Sci. Technol.* **2019**, *9*, 174–181.

[200] Shi, L.; Li, Q.; Ling, C.; Zhang, Y.; Ouyang, Y.; Bai, X.; Wang, J. *J. Mater. Chem. A* **2019**, *7*, 4865–4871.

[201] Somorjai, G. A.; Materer, N. *Top Catal* **1994**, *1*, 215–231.

[202] Stoltze, P.; Nørskov, J. K. *Phys. Rev. Lett.* **1985**, *55*, 2502–2505.

[203] Strait, R.; Nagvekar, M. **2010**, 1–5.

[204] Studt, F.; Tuczek, F. *Angew. Chem. Int. Ed.* **2005**, *44*, 5639–5642.

[205] Suttmiller, D.; Foster, S. L.; Bakovic, S. I. P.; Loney, C.; Maheshwari, S.; Janik, M. J.; Renner, J.; Greenlee, L. F. *Meet. Abstr.* **2018**, *MA2018-01*, 2002–2002.

[206] Tao, H.; Choi, C.; Ding, L.-X.; Jiang, Z.; Han, Z.; Jia, M.; Fan, Q.; Gao, Y.; Wang, H.; Robertson, A. W.; Hong, S.; Jung, Y.; Liu, S.; Sun, Z. *Chem* **2019**, *5*, 204–214.

[207] Timur, K.; E., S. M.; Anatoliy, S.; Malte, B.; Robert, S. *Angew. Chem. Int. Ed.* **2013**, *52*, 12723–12726.

[208] Vanýsek, P. *CRC Handbook of Chemistry and Physics*; CRC Press, 2011; Vol. 5; pp 80–81.

[209] Wan, Y.; Xu, J.; Lv, R. *Mater. Today* **2019**,

[210] Wang, X.-G.; Zhang, Q.; Zhang, X.; Wang, C.; Xie, Z.; Zhou, Z. *Small Methods* **2018**, *0*, 1800334.

[211] Xie, H.; Wang, H.; Geng, Q.; Xing, Z.; Wang, W.; Chen, J.; Ji, L.; Chang, L.; Wang, Z.; Mao, J. *Inorg. Chem.* **2019**, *58*, 5423–5427.

[212] Yandulov, D. V.; Schrock, R. R. *Science* **2003**, *301*, 76–78.

[213] Yu, H.; Wang, Z.; Yang, D.; Qian, X.; Xu, Y.; Li, X.; Wang, H.; Wang, L. *J. Mater. Chem. A* **2019**, *7*, 12526–12531.

[214] Zhang, Y.; Qiu, W.; Ma, Y.; Luo, Y.; Tian, Z.; Cui, G.; Xie, F.; Chen, L.; Li, T.; Sun, X. *ACS Catal.* **2018**, *8*, 8540–8544.

Chapter 4

An Industrial Process Flow Scheme for Efficient Product Separation of Electrochemically Functionalized Methane

Contents

4.1 Introduction

Every year, 30 billion dollars of natural gas are wastefully burned around the globe in a process known as methane flaring, generating 400 million tons of CO_2 for no economic benefit. 90% of this flaring occurs at remote oil production sites, primarily because the comparatively high costs of gas liquefaction and transport render it cost-ineffective to capture and bring to market. Catalytic processes to effect the conversion of methane to liquid fuels could allow for the recovery of much of this wasted energy; however, existing gas-to-liquid (GTL) technologies are neither efficient nor scalable enough for cost-effective industrial application. Though indirect conversion processes through steam reforming are highly optimized, they operate at high temperatures and pressures (over 1000 °C and 100 bar) that require substantial infrastructure that cannot be productively deployed to the remote locations where flaring occurs. Electrochemical methane functionalization systems have shown promise as a mild alternative to incumbent GTL processes; however, the separation of partially-oxidized methane liquid fuels into a continuous product stream has proven challenging, and has historically hindered successful commercialization of these catalysts. Herein, we detail a novel process scheme for electrochemical methane GTL conversion, leveraging a previously unreported reactivity of functionalized methane to effect mild and efficient product separation with potential routes for upconversion to higher hydrocarbons, without the need for energetically demanding dilution or distillation processes.

4.1.1 Global Need for Methane Valorization

Natural gas is a fossil hydrocarbon mixture composed primarily of methane (CH_4). Frequently co-occurring in oil deposits as associated petroleum gas (APG), natural gas was considered for centuries to be an unwanted byproduct of the petroleum extraction process, and was either vented into the atmosphere or burned off onsite,[i] a process known as gas flaring.[3]

[i] Burning off natural gas for no practical use is environmentally preferable to releasing it into the atmosphere, as the capacity for methane to contribute to global warming by increased radiative forcing is, per kilogram, between 1 and 2 orders of magnitude greater than carbon dioxide.[1, 2]

Over time, petroleum corporations developed methodologies to realize the value of this energy source – building pipelines to nearby consumer markets, or using high pressure to generate compressed natural gas (CNG) or low temperature to produce liquified natural gas (LNG) that is suitable for transport and commodofication over larger distances. Unfortunately, the construction of pipelines is only viable for wellheads near population centers, while compression to CNG or liquefaction to LNG are both energy-intensive processes that reduce the actualizable profit of the natural gas. As discussed below, chemical routes to valorizing these natural gas feedstocks are also energetically and infrastructurally intensive, limiting their profitability to large plants and militating in particular the capture and utilization of coproduced APGs in remote locations, such as offshore oil rigs or wellheads in sparsely populated areas.

This problem was exacerbated by the predominately American "shale gas revolution" in the early 2000s, in which novel techniques such as horizontal drilling and hydraulic fracturing ('fracking') opened access to methane-rich shale gas formations previously thought to be economically inviable.[ii] The resulting supply glut, coupled with tumbling prices for renewable energy sources, sharply curtailed the price of natural gas, and with it the profitability of bringing APG to market.[13–15] It is this economic context that informs the record-breaking quantities of natural gas currently being flared around the world, to the tune of over 150 billion m^3/yr – the resulting carbon footprint comprising about 1% of all anthropogenic CO_2 emissions.[16] The proportion of flared natural gas has, as of 2020, spiked to levels not seen since 1970, with over 10% of all APG being flared at the site of production.[17–19] On top of this, deliberate or inadvertant release of natural gas by the oil & gas industry contributes a substantial proportion of all anthropogenic methane emissions, to the tune of some $75\,Mt{\cdot}yr^{-1}$, a figure which represents some 25% of all anthropogenic methane emis-

[ii] U.S. shale gas production increased by over an order of magnitude from 2000 to 2010 as the country, formerly the largest importer of natural gas, became completely self-sufficient and overtook Russia to become the world's leading producer of natural gas. While the reduced carbon content of methane relative to heavier hydrocarbon fuels such as oil or coal meant the shale-gas boom coincided with a net decrease in American carbon emissions, the techniques associated with the boom (particularly hydraulic fracturing) remain highly controversial due to their well-documented environmental implications, particularly groundwater contamination.[4–12]

sions. [20, 21] Clearly, novel routes towards the cost-effective valorization of this wasted fuel stream, capable of scaling to modestly sized wellheads, are desperately needed to mitigate this wasteful practice and realize this unfulfilled market.

4.1.2 Incumbent Routes for Methane Gas-to-Liquid Conversion

While numerous chemical pathways have been proposed for effecting the conversion of methane to liquid fuels, all GTL methodologies that are currently employed at industrial scale rely upon the intermediate conversion of CH_4 to H_2 and CO via steam methane reforming (SMR) (**Equation 3.13** on page 104). The water-gas shift (WGS) reaction (**Equation 3.14** on page 104) is also used to carefully tune the ratio of H_2 and CO to produce a mixture of hydrogen and carbon monoxide gases, known as *syngas*, that can then be further reacted to form heavier liquid hydrocarbons via a variety of reaction trajectories.

$$CH_4 + H_2O \longrightarrow CO + 3\,H_2 \tag{3.13}$$

$$CO + H_2O \longrightarrow CO_2 + H_2 \tag{3.14}$$

However, as previously discussed in **Chapter 3**, the nontrivial conditions of these reactions, including temperatures up to 1100 °C and outlet pressures of up to 100 bar, contribute substantially to the infrastructural requirements for reaction, limiting the scalability of legacy GTL processes.

4.1.2.1 The Fischer-Tropsch Process

First discovered in 1925, the Fischer-Tropsch process (FTP) is today among the most ubiquitous reactions for C1 upconversion, and comprises a set of chemical reactions capable of converting syngas into liquid hydrocarbons, as depicted in **Equation 4.1**.

$$(2n{+}1)\,H_2 + n\,CO \longrightarrow C_nH_{2n+2} + n\,H_2O \tag{4.1}$$

Typical values for n in the FTP range from 10 to 20; the process primarily produces straight-chain alkanes, although small quantities of olefins, alcohols, and other hydrocarbons or oxyhydrocarbons may be produced. The conditions for reaction may range from 150 °C to 300 °C and 1 bar to 50 bar, depending on the specific layout and desired reaction inputs and outputs. The selected catalyst determines the favorable H_2:CO ratio and the general distribution of hydrocarbon products; commonly used catalysts include cobalt, iron, and ruthenium.[iii] For the purposes of methane GTL conversion, cobalt is typically used, as its optimal H_2:CO ratio of about 1.9–2.1 is higher than other catalysts and therefore better-suited for a hydrogen-rich SMR-based syngas stream.[23–25]

Industrial Fischer-Tropsch plants for methane GTL and/or coal liquefaction are common and have been built since the 1950s in countries from South Africa to Malaysia to Uzbekistan to Qatar. Currently, the largest methane GTL plant in the world is the Pearl GTL plant in Ras Laffan, Qatar, operated jointly by Shell and Qatar Petroleum. Since reaching full capacity in 2012, Pearl GTL is capable of transforming 45 million m^3/d of natural gas into oil equivalents and petroleum liquids, a conversion achieved over cobalt catalysts at a temperature of about 230 °C.[26]

4.1.2.2 The Mobil Methanol-to-Gasoline Process

Although the FTP is by far the premier reaction for methane GTL conversion, other routes do exist, such as the Mobil methanol-to-gasoline (MTG) process, developed in 1978.

$$2\,H_2 + CO \longrightarrow CH_3OH \tag{4.2}$$

$$2\,CH_3OH \longrightarrow CH_3OCH_3 + H_2O \tag{4.3}$$

$$\frac{n}{2}\,CH_3OCH_3 \longrightarrow C_nH_{2n} + \frac{n}{2}\,H_2O \tag{4.4}$$

[iii] Nickel catalysts are technically usable for Fischer-Tropsch chemistry, but they are highly selective for methane formation $CO + 3\,H_2 \longrightarrow CH_4 + H_2O$. This reaction is known as *methanation* and is a valuable industrial process in its own right – though it can essentially be thought of as a subset of Fischer-Tropsch reactivity. However, for the purposes of converting methane into liquid fuels, the generation of methane as a terminal product is obviously not ideal.[22] *See also:* footnote *iv* on page 193.

In this process, syngas from methane reforming is converted into methanol (**Equation 4.2**), a reaction that takes place over copper and zinc oxide catalysts at temperatures of about 250 °C and pressures of 50 bar to 100 bar. This methanol is then dehydrated to dimethyl ether (DME) over an amorphous alumina catalyst (**Equation 4.3**). Finally, further dehydration occurs of DME to light olefins (n from 2 to 11), which then oligomerize and combine via various reaction mechanisms into a distribution of paraffins, naphthenes, aromatics, and other hydrocarbons that comprises synthetic gasoline. This last reaction, **Equation 4.4**, can be catalyzed by a variety of zeolitic materials, such as ZSM-5 or SAPO-34.[27–34]

Although not operated nearly as widely as the FTP, the Mobil MTG process has in the past been successfully commercialized for GTL conversion, at the Synfuel gas-to-gasoline complex that began production in 1986 in Motunui, New Zealand. Upon commissioning, this complex was capable of converting approximately 4.5 million m^3/d of natural gas into synthetic gasoline, a figure which increased to about 8 million m^3/d over the plant's lifetime. Despite this, falling oil prices rendered the MTG process uneconomical by the late 90s, and production of synthetic petroleum at the Synfuel site ceased in April 1999.[35, 36] Iterations of the MTG process are still used for coal liquefaction in regions such as Jincheng, China; however, application of this process for methane GTL is no longer practiced industrially.

4.1.3 Electrochemical Methane Functionalization

The financial inviability of these legacy industrial routes for methane GTL conversion, especially at small scales, is fundamentally inextricable from the use of syngas as a chemical intermediate. Due to their intense conditions of reaction, the need for SMR and WGS reactors imposes nontrivial infrastructural overheads onto these indirect pathways for transforming methane into liquid fuels – values that bear out in reality, as capital costs are responsible for over 60% of all expenses associated with indirect methane-to-methanol conversion by syngas processes.[37]. The development of direct routes for effecting the conversion of methane to functionalized methyl products – essentially a subset of C-H activation chemistry – would

thereby have enormous promise in accessing mild routes for methane gas-to-liquid conversion. Moreover, the spatial separation of reductive and oxidative half-reactions enabled by an electrochemical approach has additional benefits, such as preventing water generated via oxygen reduction reaction (ORR) at the cathode from diluting the anolyte of the methane oxidation reaction (MOR) half-reaction. This reduces catalyst inhibition that invariably occurs in single-cell systems, while increasing the efficacy of product separations. [38, 39]

4.1.3.1 Analogy to Biological Methane Oxidation

As is frequently the case (see **Section 3.1.3.1** on page 108), Nature herself long ago designed systems to effect this transformation efficiently and selectively. The enzyme methane monooxygenase (MMO), native to a group of bacteria called the *methanotrophs*, effects the conversion of methane to methanol (**Equation 4.5**):

$$CH_4 + O_2 + NAD(P)H + H^+ \longrightarrow CH_3OH + NAD(P)^+ + H_2O. \tag{4.5}$$

Like nitrogenase, the action of MMO is fundamentally electrochemical. Applying driving force from the cleavage of NAD(P)H, MMO induces the reduction of O_2; one oxygen atom is inserted into a C-H bond of methane (formally a 2-electron oxidation relative to carbon), while the other oxygen atom is reduced to water – formally a 2-electron reduction.[40–42]

4.1.3.2 Electrocatalysts for Methane Functionalization

Reported Homogeneous Catalysts A variety of homogeneous systems have been observed to effect the activation of the C-H bond of methane – in fact, a large proportion of all electrophilic high-valent transition metal, main-group, or rare-earth cations are capable of effecting this functionalization process, such as Au^{III}, Pb^{IV}, Tl^{III}, Ce^{IV}, or I^{I}. To assess the viability of these ions as catalysts (here generically cat_{ox}), these systems can be further subcategorized by a handful of important diagnostic criteria. The redox process of methane oxi-

dation must necessarily evince a net reduction at the high-valent cation $cat_{ox} \longrightarrow cat_{red}$. By itself, this constitutes a (highly atom-uneconomical) stoichiometric methane activation process. In order to turn this system into a viable catalyst, a separate terminal oxidizing agent is necessary to turn over the reduced catalytic species back to the active high-valent cat_{ox}.[43]

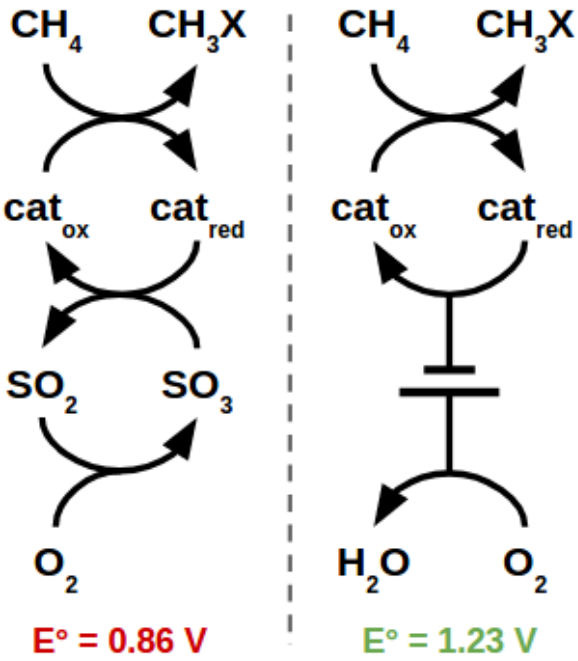

Scheme 4.1. Generic catalytic scheme for methane functionalization as mediated by an SO_2/SO_3 redox couple **(left)** or electrochemically via cathodic oxygen reduction reaction **(right)**.

For a process seeking to effect the bulk oxidation of methane, it is clear that the only economical terminal oxidant for this process is molecular oxygen from air (**Equation 4.6**).

$$CH_4 + \frac{1}{2}\,O_2 \longrightarrow CH_3OH \tag{4.6}$$

Fundamentally, this means that the oxidative regeneration of the catalyst $cat_{red} \longrightarrow cat_{ox}$ is limited by the reduction potential of the oxygen reduction reaction (ORR) that takes O_2 to H_2O – nominally 1.23 V. In practice, this potential is further constrained due the promiscuous redox chemistry of dioxygen, which reacts indiscriminately with many potential catalyst

systems. As a result, many reported systems for O_2-regenerable methane functionalization make heavy use of redox mediators such as SO_3, which are then regenerated by combustion in air (**Scheme 4.1**). However, this has the effect of further curtailing the feasible redox potential of the cat_{ox}/cat_{red} cycle to that of the SO_3/SO_2 redox couple, a mere 0.86 V. This renders many high-valent ions unregenerable by a terminal O_2 oxidant, limiting their application as methane functionalization electrocatalysts. An electrochemical system may replace this redox mediator using the spatial separation of half-reactions that is inherent to most electrochemical engineering; by this method, not only can the full 1.23 V of oxygen reduction be harnessed to turn over methane functionalization catalysts, but even greater potentials may be accessed by applying an electromotive driving force to make up the deficit voltage (assuming, of course, that the energetic cost of that driving force is justified by the electrogenerated species). As the energetic barrier to methane functionalization correlates inversely with the electrophilicity of the high-valent activated catalyst species cat_{ox}, this is quite possibly a desirable process; the more oxidized the high-valent species is, the more difficult it is to regenerate from the low-valent species cat_{red} via traditional chemical redox agents.

The Role of Product Protection Having established that many high-valent cations are capable of cleaving the C—H bond, it is perhaps more meaningful to query how this transformation might be accomplished selectively. The challenge with methane oxidation is less frequently initiating an oxidation than it is preventing overoxidation. This makes sense on an intuitive level; it is trivial to burn CH_4 to CO_2, but partially combusting methane to methanol would be an impressive feat, indeed! Examining the relative C—H bond dissociation energies (BDEs) of methane and methanol reveals the problem: while the BDE of methane is 105 $kcal \cdot mol^{-1}$, the BDE of methanol is significantly reduced, at 96 $kcal \cdot mol^{-1}$. In a certain sense, this may be considered a consequence of the substitution of a hydrogen atom with an electron-rich hydroxyl group, thereby activating the remaining C—H bonds in methanol to further oxidative attack.

Within the methane functionalization literature, the predominate strategy for circumventing the propensity for overoxidation is 'product protection', by which partially-oxidized species such as methanol are converted to relatively deactivated species. For example, by performing methane functionalization in concentrated sulfuric acid, methyl equivalents can be transformed from methanol into methylsulfonic acid (MSA) or sulfate esters like methyl bisulfate (MBS). Relative to methanol, the sulfonyl linkages in these compounds are significantly less electron-donating in character, and as a result the estimated C—H BDEs of these compounds are closer to that of methane than methanol (calculated BDE for MBS: $107\,\mathrm{kcal{\cdot}mol^{-1}}$; calculated BDE for MSA: $104\,\mathrm{kcal{\cdot}mol^{-1}}$)[44]. More concretely, these 'protected' methyl equivalents exhibit substantially elevated barriers to oxidation compared to both methane and methanol, allowing the accumulation of functionalized methyl equivalents in the reaction media in their protected forms.[45] Although some exceptional systems are capable of partial methane oxidation directly to methanol without overoxidation of unprotected methyl products,[46, 47] the large majority of reported catalysts for methane functionalization are performed in oxidizing acidic media such as sulfuric or trifluoroacetic acid, as any methanol generated under these conditions will rapidly esterify to a protected form.[48–51]

Active Electrocatalysts for Methane Functionalization With this context, our group has previously assessed the electrochemical activity of several high-valent transition-metal and main-group ions to assess their potential for electrocatalytic methane functionalization activity in concentrated sulfuric acid media. Several elements, including cobalt (**Figure 4-1**), palladium, silver, and iodine, were found to be catalytically active for the generation of MBS and/or MSA under positive methane pressure and applied electrochemical potential. Other elements, such as nickel, rhodium, iridium, and thallium, did not display electrochemical activity and consequently did not evince catalytic methane functionalization. Finally, some metal species, such as copper, lead, and platinum, did not readily solubilize in the reaction medium sufficiently to allow for assessment of their electrocatalytic properties.

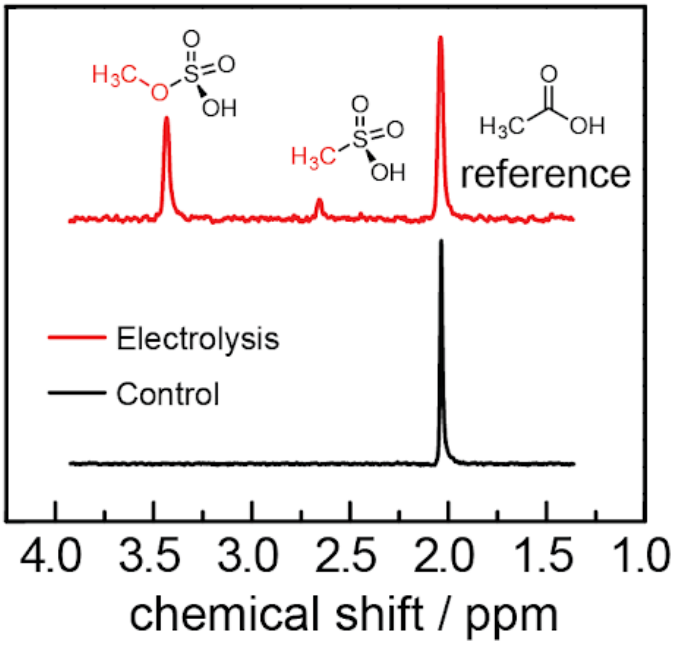

Figure 4-1. ^{1}H NMR of H_2SO_4 electrolyte following bulk electrolysis of $CoSO_4$ under 500 psi methane pressure, showing generation of protected methyl products MSA and MBS.

In particular, we note the electrocatalytic activity of $PdSO_4$, which our group has previously shown to be competent for the generation of MSA and MBS via a novel electrogenerated $Pd_2^{III,III}$ dimer,[52–54], and the activity of $PtCl_4^{2-}$ which (being the 'Shilov catalyst' alluded to previously[46, 47]) is capable of selectively producing unprotected methanol without substantial overoxidation.[55]

4.2 Results and Discussion

Having established the ability for numerous methane functionalization catalysts to be turned over electrochemically, we sought to model the viability of various closed process schemes at reasonable industrial scales. We chose to assess the efficacy of our processes at a methane inflow of 1 million m^3/d, a representative figure for a modestly sized wellhead and one that is substantially smaller than the modern GTL systems discussed in **Section 4.1.2**. Calculations were performed in Aspen Plus® v.8.4; full process flow diagrams, associated stream

tables, and general simulation assumptions can be found in **Appendix C** on page 289.

4.2.1 Process Modeling for Methyl Bisulfate Hydrolysis

In the first system we modeled (**Figure 4-2**), methane is oxidized to MBS electrochemically. Because we are not modeling the efficacy of the MOR process, and we wish to determine the limit of efficiency for methanol generation in this system, the efficiency of this process is imposed artificially at 90% conversion of methane to MBS, 5% overoxidation to CO_2, and 5% flowthrough of unconverted CH_4. The mixture of concentrated sulfuric acid and methyl bisulfate leaving this reactor is then reacted with a large excess of water in order to hydrolyse the methyl bisulfate to methanol. This methanol is then distilled off from the aqueous H_2SO_4 medium, which must then be reconcentrated up to be returned to the electrochemical reactor. At a methane inflow of 1 million m^3/d, this process generates some $630\,t{\cdot}d^{-1}$ of MeOH, a value which represents approximately 29% yield of methanol per methane molecule in the feedstock.

This low conversion efficiency is attributable in large part to the unfavorability hydrolysis of MBS to MeOH (**Equation 4.7**), both in a kinetic and thermodynamic sense. At 25 °C, the forward rate constant k for this hydrolysis is $2{\times}10^{-11}\ s^{-1}$, a value which corresponds to a reaction half-life $t_{1/2} = 1100\,yr$. What's more, due to the high $\Delta H^{\ddagger} = 134\,kJ{\cdot}mol^{-1}$ and comparatively minute $\Delta S^{\ddagger} = 0.0267\,J{\cdot}mol^{-1}{\cdot}K^{-1}$, it is challenging to increase the driving force for this hydrolysis by merely increasing the temperature.[56]

$$CH_3OSO_3H + H_2O \longrightarrow H_2SO_4 + CH_3OH \tag{4.7}$$

As a result of this sluggish hydrolysis, a substantial excess of water is needed to sufficiently favor the hydrolysis reaction. This drastically increases the energetic demand of the methanol and H_2SO_4 distillation columns, which reach a net power demand of approximately 126 MW, with the column for the intensely hygroscopic sulfuric acid in particular responsible for nearly

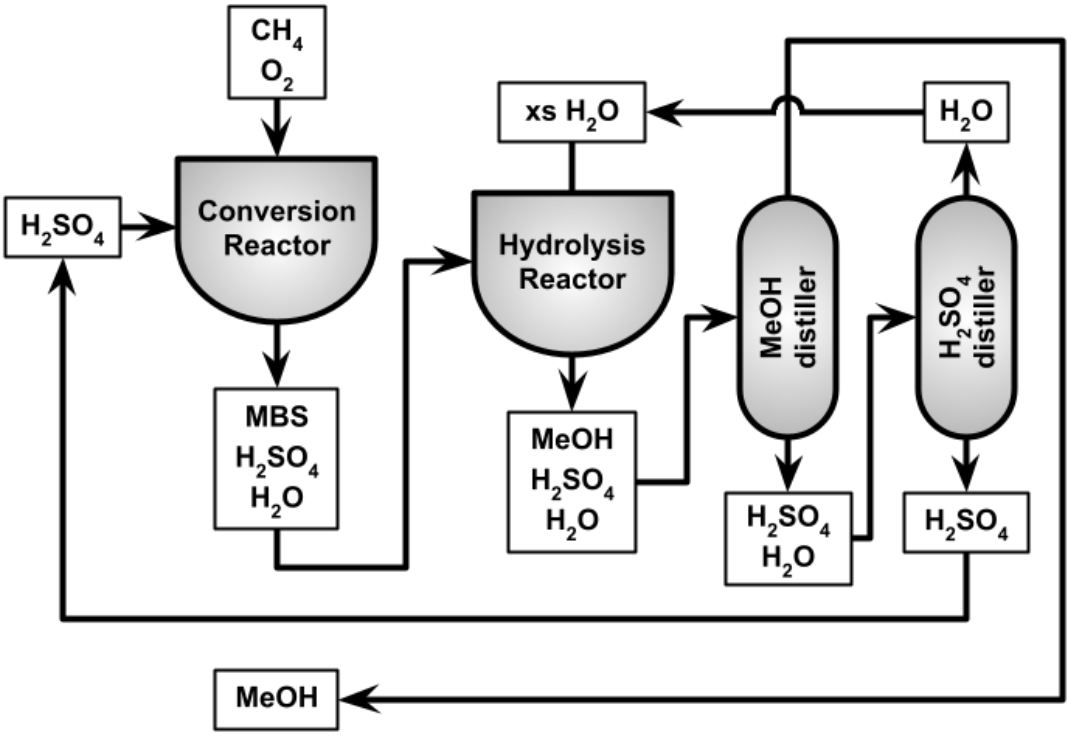

Figure 4-2. Process-flow diagram for methane gas-to-liquid conversion by electrochemical functionalization to methyl bisulfate and subsequent hydrolysis to methanol.

80% of this value at 99 MW. As the heating value of 1 million m^3/d CH_4 only comes to 443 MW, this means that even with an optimum methane electrofunctionalization catalyst, 28.4% of our methane input stream must be burned right off the bat in order to run the sulfuric acid and methanol distillation columns.

4.2.2 Methyl Halides for Functionalized Methane Separations

This inefficiency, rooted not in an inadequate catalyst but an intractable product separations framework, motivated our desire to develop alternative methodologies for liberating methyl equivalents from a reaction medium. Like its two-carbon brother dimethyl sulfate (DMS), MBS is a competent methylating agent under the right reaction conditions. If methyl bisulfate could be induced to transfer its methyl equivalent into a volatilizable form, such as a methyl halide ($CH_3OSO_3H + HX \longrightarrow H_2SO_4 + CH_3X$), perhaps product separations might be accomplished without significant dilution of the hygroscopic sulfuric acid

medium. To this end, we focused our efforts on the reaction of HCl with MBS to produce MeCl (**Equation 4.8**), which is among the most volatile methyl halides, with a boiling point of -24.2 °C.[iv]

$$CH_3OSO_3H + HCl \longrightarrow H_2SO_4 + CH_3Cl \tag{4.8}$$

4.2.2.1 Methyl Chloride Synthesis

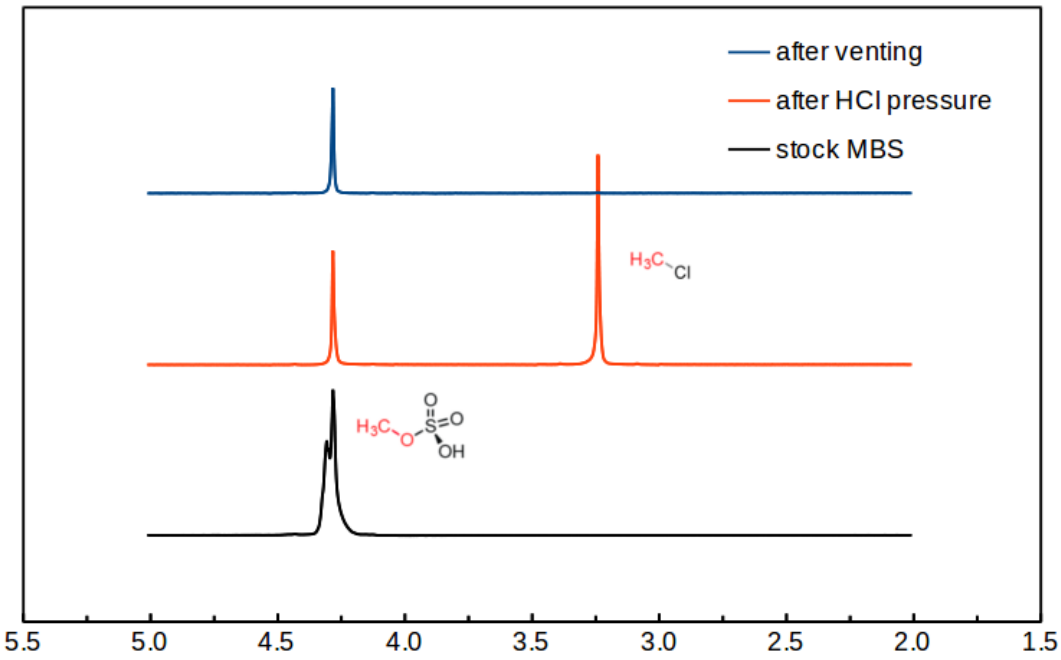

Figure 4-3. (bottom) ^{1}H NMR spectra in concentrated H_2SO_4 of MBS and DMS, **(middle)** formation of MeCl following exposure to HCl gas, and **(top)** desolvation of MeCl after mild heating.

As depicted in **Figure 4-3**, this proves indeed to be a viable reactivity in a sulfuric acid medium. Under even autogenous HCl pressure in a sealed J. Young NMR tube, a distinct MeCl signal is observed by ^{1}H NMR. By pressurizing to up to 50 psi of hydrogen chloride gas, up to 70% single-pass conversion for MBS to MeCl can be achieved at room temperature. Substantial desolvation of MeCl can be achieved by simply waiting at room temperature,

[iv] Only methyl fluoride, BP -78.4 °C, is more volatile than methyl chloride. We rejected studies that would entail pressurization with hydrogen fluoride gas, for reasons that are hopefully obvious. *See also:* footnote *iv* on page 193.

and >99% extraction from the reaction medium can be achieved by brief heating at 100 °C for 15 minutes.

4.2.2.2 Stability of Methane Functionalization Catalysts

It is worth noting that some homogeneous catalysts for methane functionalization (in particular, palladium), are unstable to HCl exposure, precipitating polymeric $PdCl_2$. While this is not a problem if these species can be heterogenized, as a methyl chloride reactor can be separated from the methane functionalization reactor, it poses a problem for a purely homogeneous system. While this precludes the use of the $Pd_2^{III,III}$ methane functionalization electrocatalyst previously described by our group,[53, 54] other homogeneous catalyst systems proved robust to HCl pressure. The 'Periana-Catalytica' system, $[Pt(bpym)Cl_2]$,[49] was found to be stable to HCl (**Figure C-3** on page 292), and I_2^+[48] was also found to retain catalytic activity following HCl pressure (**Figure C-2** on page 291), though the partial generation of methyl iodide may convolute the separations process in this case.

4.2.2.3 Hydrolysis to Methanol

As methyl chloride is a gas and contains a Cl atom that must remain within any closed chemical system without a chlorine input stream, further conversion of MeCl is necessary following separation. There are multiple possible routes for generation of a terminal liquid product from methyl chloride. The most obvious is hydrolysis to methanol and hydrochloric acid, both of which must be subsequently distilled to produce pure methanol and hydrogen chloride gas, respectively. Fortunately, estimates of the hydrolysis of methyl chloride (**Equation 4.9**) suggest it is several orders of magnitude more tractable than that of methyl bisulfate hydrolysis.

$$CH_3Cl + H_2O \longrightarrow CH_3OH + HCl \tag{4.9}$$

Unfortunately, that does not mean the reaction is facile. At 25 °C, the forward rate constant k for this hydrolysis is $2\times10^{-8}\ \mathrm{s}^{-1}$, a value which corresponds to a reaction half-life $t_{1/2} = 1\,\mathrm{yr}$. The value of $\Delta H\ddagger = 38.8\,\mathrm{kJ{\cdot}mol^{-1}}$ is substantially smaller than in the MBS hydrolysis case, and the much greater entropic contribution $\Delta S\ddagger = 9.79\,\mathrm{J{\cdot}mol^{-1}{\cdot}K^{-1}}$ means temperature effects will be more substantial for this reaction. While this makes the MeCl hydrolysis route drastically favorable to the MBS hydrolysis route overall, the existence of a constant-boiling azeotrope that must be broken at 108.6 °C and 20:80% HCl:H_2O will greatly increase the power demand of the hydrogen chloride distillation column[57–62]

4.2.2.4 Upconversion to Higher-Carbon Products

Instead of introducing water into the system, it is also possible to simply upconvert methyl halides to liquid hydrocarbons, a reactivity highly analogous to the upgrading of DME to synthetic gasoline in the Mobil MTG process (**Section 4.1.2.2** on page 162) However, instead of converting DME to light olefins with the release of water (**Equation 4.4**), the reaction of methyl chloride will instead release HCl gas (**Equation 4.10**). Because water is not produced, this increases the ease of the separations process, since there is no distillation necessary.

$$n\,\mathrm{CH_3Cl} \longrightarrow \mathrm{C}_n\mathrm{H}_{2n} + n\,\mathrm{HCl} \tag{4.10}$$

Numerous zeolitic catalysts are known to effect this conversion to light olefins (n from 2 to 4), including H-ZSM-5,[63, 64], Mg-ZSM-5,[65], H-ZSM-22,[66], and H-SAPO-34.[67–71]. The conditions of reaction range from 350 °C to 500 °C, and conversion rates are up to 96%, with up to 80% selectivity for ethylene,[72–75] propylene,[76–79] and butylene,[80–84] all of which can be subsequently oligomerized to liquid hydrocarbon fuels such as 1-octene. As such, instead of the net reaction of methane and oxygen to form methanol (**Equation 4.6**), a

representative overall reaction for this process might be **Equation 4.11**.

$$8\,CH_4 + 4\,O_2 \longrightarrow C_8H_{16} + 8\,H_2O \tag{4.11}$$

4.2.3 Process Scheme for Methyl Halide-Based Functionalization

Having described these two systems – hydrolysis and upgrading – for valorizing separated methyl chloride, we then proceeded to model both for the same 1 million m^3/d methane wellhead described in **Section 4.2.1**. As before, calculations were performed in Aspen Plus® v.8.4, and full process flow diagrams, associated stream tables, and general simulation assumptions can be found in **Appendix C** on page 289.

4.2.3.1 Flow Scheme for Hydrolysis to Methanol

In the hydrolytic process (**Figure 4-4**), methane and oxygen are reacted to form MBS. Unlike the previous system, however, the efficiency of the MOR reactor is not artificially imposed at 90% but at a more realistic 59% conversion of methane to MBS, with 41% of methane unconverted and passing through the system, necessitating multiple passes. This MBS solution is then brought into a separate MeCl reactor where it is reacted with HCl to produce volatile MeCl, which is brought into a separate hydrolysis reactor for production of methanol.

Because the hygroscopic H_2SO_4 is not massively diluted by a process of MBS hydrolysis, the power demand of the sulfuric acid distillation column is drastically reduced from the 99 MW of the MBS hydrolytic process to 21 MW here. Moreover, the increased facility of MeCl hydrolysis relative to MBS hydrolysis means the methanol distillation column is less dilute, and hence requires only 14 MW instead of 27 MW as in the MBS hydrolytic route. Unfortunately, the addition of the hydrogen chloride loop means an additional distillation column, and 31 MW are required in order to break the HCl:H_2O azeotrope. This comes to a total power demand of 66 MW – nearly half that of the MBS hydrolytic route, and meaning

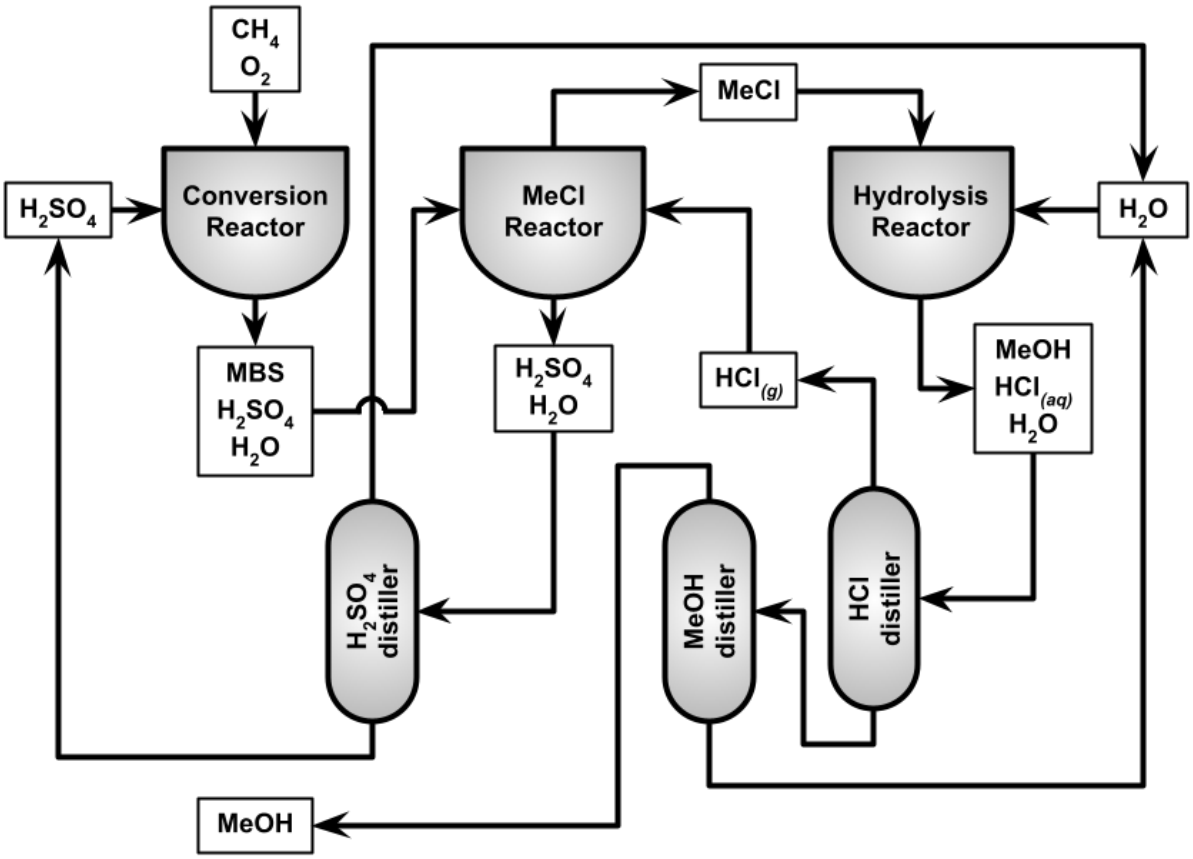

Figure 4-4. Process-flow diagram for methane gas-to-liquid conversion by electrochemical functionalization to methyl bisulfate, conversion to methyl chloride, and hydrolysis to methanol.

only 14.9% of the incoming methane feed is required to power the burners for this process, and allowing an accordingly greater rate of methanol production at over $800\,\mathrm{t{\cdot}d^{-1}}$.

4.2.3.2 Flow Scheme for Upgrading to Olefins

The first two steps of the methyl chloride upgrading process (**Figure 4-5**) are identical to the hydrolytic process, but instead of hydrolysing the evolved MeCl, they are oligomerized over zeolites to produce olefins and liberate HCl gas. For the purposes of this model, all olefin products were assumed to be C8 products, but variation from C6-C10 was not observed to substantially alter the system energetics. Because of the overall lack of distillation columns, only the 21 MW sulfuric acid column is required in this system. This means that only 4.7% of incoming methane is necessary to power the burners for this reaction, and as such the

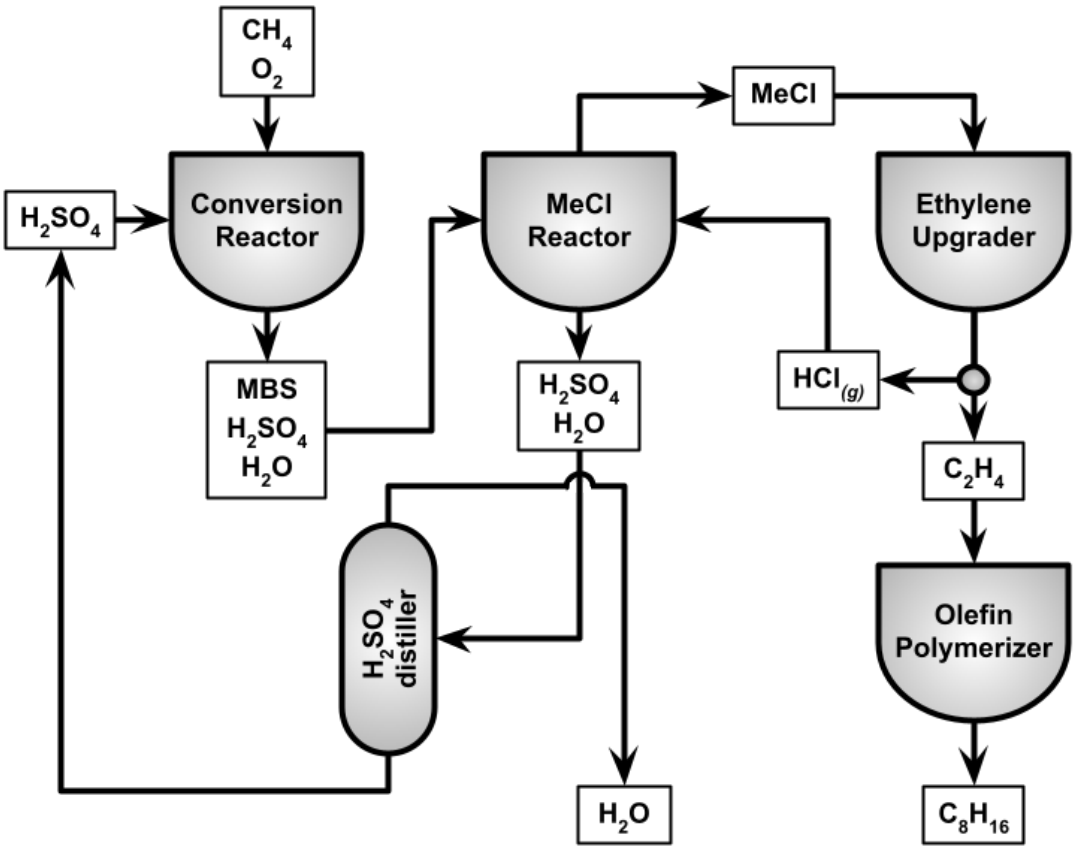

Figure 4-5. Process-flow diagram for methane gas-to-liquid conversion by electrochemical functionalization to methyl bisulfate, conversion to methyl chloride, and upgrading to olefins like 1-octene.

conversion efficiency of this system is higher than any of the two previous systems, producing $1260\,\mathrm{t{\cdot}d^{-1}}$ of olefins. As seen in **Table 4.1**, because the per-carbon energy density of 1-octene is slightly lower than that of methanol, the overall energy efficiency of this process is slightly lower than expected relative to the drastically improved carbon atom efficiency. Nevertheless, this process is in nearly all ways the most efficient of the models studied in this report.

4.2.3.3 Comparison of Power Efficiency

A comparison of the overall distillative energy demands of the three process detailed in this report can be seen in **Figure 4-6**. **Table 4.1** further details the efficiencies of these process schemes, in terms of distillative power demand, methane inflow fraction needed for burners,

	MBS Hydrolysis	MeCl Hydrolysis	MeCl Upconversion
Distiller Energy	126 MW	66 MW	21 MW
Burned Methane	28.4%	14.9%	4.7%
Carbon Efficiency	29%	37%	58%
Energy Efficiency	25%	33%	43%

Table 4.1. Efficiency comparison of GTL process schemes, in terms of distillative power demand, methane inflow fraction needed for burners, end-to-end carbon atom efficiency, and overall energy efficiency.

end-to-end carbon atom efficiency, and overall energy efficiency.

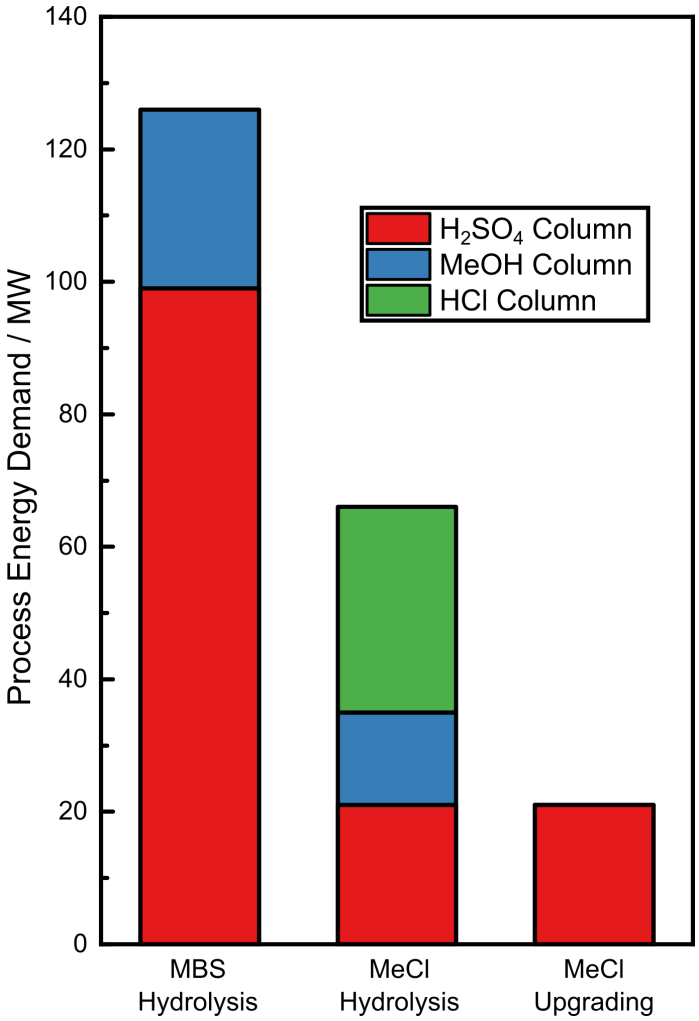

Figure 4-6. Distillative energy demands for methyl bisulfate hydrolysis, methyl chloride hydrolysis, and methyl chloride upgrading process strategies. Distillation loops include sulfuric acid reconcentration, methanol distillation, and hydrogen chloride vaporization.

4.3 Concluding Remarks

The development of novel methane GTL processes capable of deployment in remote locations at comparatively small scale has long been considered a highly valuable practical application of C—H functionalization catalysis. Electrochemical systems have in particular shown great promise in their ability to turn over known homogenous catalysts for methane functionalization, in addition to their ability to electrogenerate completely novel high-valent species for effecting this transformation. While necessary, however, the development of efficient catalysts capable of selectively achieving the partial oxidation of methane is by it-

self not sufficient for the the overall electrochemical system to efficiently carry out the desired transformation at scale. This is well-represented by our MBS hydrolysis model, where despite presupposing 90% single-pass catalyst efficiency for methane functionalization, the overall process only realizes 25% of the heating value of the incoming methane fuel stream, with only about 29% of methane molecules coming out the other end as methanol. This inefficiency stems in large part from the intractable hydrolysis thermodynamics of MBS, which demand large excesses of water that in turn induce a substantial distillative power demand, with nearly as much of the incoming methane flow stream being burned to power distillation columns as is functionalized to methanol in the first place.

In this work, we present an alternative process flow scheme for achieving product separations from an arbitrary methane functionalization system, such as the electrochemical methods previously investigated by our group. We demonstrate experimentally that methyl bisulfate, a common 'protected product' for preventing methane overoxidation, is rapidly converted to volatile methyl chloride upon exposure to hydrogen chloride gas. This process occurs rapidly at single-pass conversion rates of up to 70%, with near-total (>99%) extraction of methyl chloride from the reaction medium upon mild heating. We then further investigate and model two potential systems for transforming methyl chloride into liquid fuels: hydrolysis to methanol and zeolite-catalyzed upgrading to olefins. While the favorable hydrolysis kinetics of methyl chloride relative to methyl bisulfate render this process a modest improvement in overall carbon and energy efficiency, the minimal distillation entailed by the olefin-upgrading strategy dramatically reduces the power demand of the overall process, with only 4.7% of the incoming methane stream shunted into burners. As a result, the carbon efficiency of this process is essentially double that of the MBS hydrolysis route at 58%. These results convincingly demonstrate that innovations in product separation strategies are necessary to realize the potential of industrial electrocatalysis even at the limits of catalyst efficiency and selectivity.

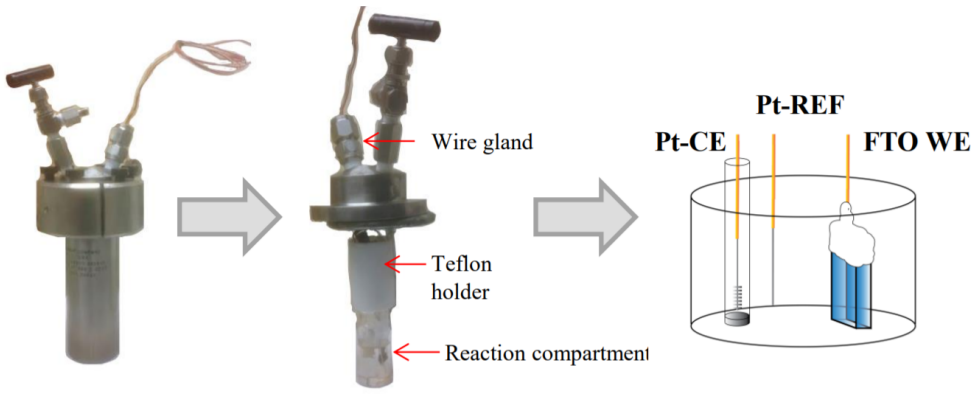

Figure 4-7. Diagram of cell for high-pressure methane functionalization chemistry. Diagram adapted from O'Reilly, M. E. *et. al.*[52]

4.4 Experimental Details

4.4.1 Cell Design and Layout

Several experiments for this project were performed in a custom-built high-pressure electrochemical reactor. This vessel was a stainless steel 80 mL Parr Reactor Model No. 4774 General Purpose Vessel adapted with a high-pressure electrochemical feedthrough gland ([TG-24T(KN)-A4-G] by Conax Technologies) (**Figure 4-7**). However, use of this vessel was retired following the conclusion of this project, as the insufficient reactor ports to install rupture discs was considered a safety hazard.

4.4.2 Synthesis of Methyl Chloride

4.4.2.1 In NMR Tube by *in situ* HCl Generator

In H_2SO_4 400 µL fuming sulfuric acid (reagent grade, 20% free SO_3 basis, Sigma-Aldrich) and 100 µL $D_2SO_4-d_2$ (96-98% in D_2O, Cambridge Isotope Laboratories) were added to a J. Young tube. 5 µL methanol (anhydrous, 99.8%, Sigma-Aldrich) and 10 µL ammonium sulfate solution (0.5318 M in H_2SO_4, ≥99.0%, Sigma-Aldrich) were added by micropipette, to form methyl bisulfate and as an internal standard for NMR, respectively. The J. Young tube was then carefully immersed in a dry ice/acetone bath for 10 minutes in order to freeze the

sulfuric acid. 100 mg sodium chloride (≥99.0%, Sigma-Aldrich) were added to the tube such that they lay on top of the frozen sulfuric acid as an autogenous HCl generator. The tube was then sealed and allowed to thaw to room temperature in an ice/water bath for two hours.

4.4.2.2 In Electrochemical Cell Under HCl Pressure

In H_2SO_4 20 mmol (640.8 mg) methanol (anhydrous, 99.8%, Sigma-Aldrich) was dissolved in 20 ml of concentrated sulfuric acid (98%, Fisher Scientific) to create a 1 M stock solution. This solution was then loaded into an electrochemical pressure reactor and pressurized to 75 psi of hydrogen chloride gas (anhydrous, ≥99%, Sigma-Aldrich) using an Aldrich® corrosive gas regulator with electroless nickel-plated body and cross purge assembly. The reactor was sealed and heated at 200 °C for 26 h before being depressurized into a bicarbonate trap. The reactor was opened (in a ventilated fume hood) and an aliquot of the reaction media was taken for NMR.

In Trifluoroacetic acid (HTFA) 10 mmol (320.4 mg) methanol (anhydrous, 99.8%, Sigma-Aldrich) was dissolved in 10 ml of trifluoroacetic acid (≥99.0%, Sigma-Aldrich) to create a 1 M stock solution. This solution was then loaded into an electrochemical pressure reactor and pressurized to 75 psi of hydrogen chloride gas (anhydrous, ≥99%, Sigma-Aldrich) using an Aldrich® corrosive gas regulator with electroless nickel-plated body and cross purge assembly. The reactor was sealed and heated at 60 °C for 24 h before being depressurized into a bicarbonate trap. The reactor was opened (in a ventilated fume hood) and an aliquot of the reaction media was taken for NMR.

4.4.2.3 With $Pt(bpym)Cl_2$

Dichloro(η-2-{2,2'-bipyrimidyl})platinum(II) [(bpym)$PtCl_2$] was synthesized by literature prep.[49] 59 µmol (25 mg) dichloro(η-2-{2,2'-bipyrimidyl})platinum(II) was dissolved in 5 mL fuming sulfuric acid (reagent grade, 20% free SO_3 basis, Sigma-Aldrich), loaded into an elec-

trochemical pressure reactor, and pressurized at 500 psi of methane gas (Airgas) and heated for 4 hours at 220 °C. The methane was vented and the cell was then pressurized to 75 psi of hydrogen chloride gas (anhydrous, ≥99%, Sigma-Aldrich) using an Aldrich® corrosive gas regulator with electroless nickel-plated body and cross purge assembly and heated for 24 h at 200 °C before being depressurized into a bicarbonate trap. The reactor was opened (in a ventilated fume hood) and an aliquot of the reaction media was taken for NMR.

4.4.2.4 With I_2

100 µmol (25.4 mg) elemental iodine (≥99.99% trace metals basis, Sigma-Aldrich) was dissolved in 5 mL fuming sulfuric acid (reagent grade, 20% free SO_3 basis, Sigma-Aldrich), loaded into an electrochemical pressure reactor, and pressurized at 500 psi of methane gas (Airgas) and heated for 6 hours at 195 °C. The methane was vented and the cell was then pressurized to 75 psi of hydrogen chloride gas (anhydrous, ≥99%, Sigma-Aldrich) using an Aldrich® corrosive gas regulator with electroless nickel-plated body and cross purge assembly and heated for 24 h at 200 °C before being depressurized into a bicarbonate trap. The reactor was opened (in a ventilated fume hood) and an aliquot of the reaction media was taken for NMR.

References

[1] Etminan, M.; Myhre, G.; Highwood, E. J.; Shine, K. P. *Geophys. Res. Lett.* **2016**, *43*, 12,614–12,623.

[2] Myhre, G. et al. *Climate Change 2013: The Physical Science Basis. Contribution of Working Group I to the Fifth Assessment Report of the Intergovernmental Panel on Climate Change*; Cambridge University Press: Cambridge, UK and New York, NY, 2013; p 82.

[3] Roeland, T. H. *Associated Petroleum Gas in Russia: Reasons for Non-Utilization*; 2010.

[4] Clough, E. *Curr. Opin. Environ. Sci. Health* **2018**, *3*, 14–18.

[5] Jackson, R. B.; Vengosh, A.; Carey, J. W.; Davies, R. J.; Darrah, T. H.; O'Sullivan, F.; Pétron, G. *Annu. Rev. Environ. Resour.* **2014**, *39*, 327–362.

[6] Evensen, D. *WIREs Water* **2016**, *3*, 575–586.

[7] Vengosh, A.; Warner, N.; Jackson, R.; Darrah, T. *Procedia Earth Planet. Sci.* **2013**, *7*, 863–866.

[8] Torres, L.; Yadav, O. P.; Khan, E. *Sci. Tot. Environ.* **2016**, *539*, 478–493.

[9] Osborn, S. G.; Vengosh, A.; Warner, N. R.; Jackson, R. B. *Proc. Nat. Acad. Sci.* **2011**, *108*, 8172–8176.

[10] Gallegos, T. J.; Varela, B. A.; Haines, S. S.; Engle, M. A. *Water Resour. Res.* **2015**, *51*, 5839–5845.

[11] Merrill, T. W.; Schizer, D. M. *Minn. L. Rev.* **2013**, *98*, 145–264.

[12] Burton, T. G.; Rifai, H. S.; Hildenbrand, Z. L.; Carlton, D. D.; Fontenot, B. E.; Schug, K. A. *Sci. Tot. Environ.* **2016**, *545-546*, 114–126.

[13] Wang, Q.; Chen, X.; Jha, A. N.; Rogers, H. *Renew. Sust. Energy Rev.* **2014**, *30*, 1–28.

[14] Middleton, R. S.; Gupta, R.; Hyman, J. D.; Viswanathan, H. S. *Appl. Energy* **2017**, *199*, 88–95.

[15] Krauss, C. Natural Gas Boom Fizzles as a U.S. Glut Sinks Profits. 2019.

[16] Elvidge, C. D.; Zhizhin, M.; Baugh, K.; Hsu, F.-C.; Ghosh, T. *Energies* **2016**, *9*, 14.

[17] Office of Oil and Natural Gas,; Office of Fossil Energy, *Natural Gas Flaring and Venting: State and Federal Regulatory Overview, Trends, and Impacts*; 2019.

[18] Tabuchi, H. Despite Their Promises, Giant Energy Companies Burn Away Vast Amounts of Natural Gas. 2019.

[19] Tabuchi, H. A Secret Recording Reveals Oil Executives' Private Views on Climate Change. 2020.

[20] IEA, Interactive Country and Regional Estimates – Methane Tracker 2020. https://www.iea.org/reports/methane-tracker-2020/interactive-country-and-regional-estimates, 2020.

[21] Alvarez, R. A. et al. *Science* **2018**, *361*, 186–188.

[22] Rönsch, S.; Schneider, J.; Matthischke, S.; Schlüter, M.; Götz, M.; Lefebvre, J.; Prabhakaran, P.; Bajohr, S. *Fuel* **2016**, *166*, 276–296.

[23] Kaneko, T.; Derbyshire, F.; Makino, E.; Gray, D.; Tamura, M. *Ullmann's Encyclopedia of Industrial Chemistry*; Wiley-VCH, 2001.

[24] de Klerk, A. *Kirk-Othmer Encyclopedia of Chemical Technology*; American Cancer Society, 2013; pp 1–20.

[25] Brownstein, A. M. In *Renewable Motor Fuels*; Brownstein, A. M., Ed.; Butterworth-Heinemann: Boston, 2015; pp 33–46.

[26] Mesters, C. *Annu. Rev. Chem. Biomol. Eng.* **2016**, *7*, 223–238.

[27] Wood, A. *Energy Res Rep* **1978**, *4:22*.

[28] Grimmer, H. R.; Thiagarajan, N.; Nitschke, E. In *Studies in Surface Science and Catalysis*; Bibby, D. M., Chang, C. D., Howe, R. F., Yurchak, S., Eds.; Methane Conversion; Elsevier, 1988; Vol. 36; pp 273–291.

[29] Wilson, S.; Barger, P. *Micropor. Mesopor. Mater.* **1999**, *29*, 117–126.

[30] Olsbye, U.; Svelle, S.; Bjørgen, M.; Beato, P.; Janssens, T. V. W.; Joensen, F.; Bordiga, S.; Lillerud, K. P. *Angew. Chem. Int. Ed.* **2012**, *51*, 5810–5831.

[31] Tian, P.; Wei, Y.; Ye, M.; Liu, Z. *ACS Catal.* **2015**, *5*, 1922–1938.

[32] Amghizar, I.; Vandewalle, L. A.; Van Geem, K. M.; Marin, G. B. *Engineering* **2017**, *3*, 171–178.

[33] Bakare, I. A.; Muraza, O.; Sanhoob, M. A.; Miyake, K.; Hirota, Y.; Yamani, Z. H.; Nishiyama, N. *Fuel* **2018**, *211*, 18–26.

[34] Khadzhiev, S. N.; Kolesnichenko, N. V.; Khivrich, E. N.; Batova, T. I. *Pet. Chem.* **2019**, *59*, 427–437.

[35] Maiden, C. J. In *Studies in Surface Science and Catalysis*; Bibby, D. M., Chang, C. D., Howe, R. F., Yurchak, S., Eds.; Methane Conversion; Elsevier, 1988; Vol. 36; pp 1–16.

[36] Hindman, M. ExxonMobil Methanol to Gasoline (MTG). 2017.

[37] Lunsford, J. *Catal. Today* **2000**, *63*, 165–174.

[38] da Silva, M. J. *Fuel. Proc. Tech.* **2016**, *145*, 42–61.

[39] Wang, B.; Albarracín-Suazo, S.; Pagán-Torres, Y.; Nikolla, E. *Catal. Today* **2017**, *285*, 147–158.

[40] Rosenzweig, A. C.; Frederick, C. A.; Lippard, S. J.; Nordlund, P. *Nature* **1993**, *366*, 537–543.

[41] Hanson, R. S.; Hanson, T. E. *Microbiol. Rev.* **1996**, *60*, 439–471.

[42] Basch, H.; Mogi, K.; Musaev, D. G.; Morokuma, K. *J. Am. Chem. Soc.* **1999**, *121*, 7249–7256.

[43] Gunsalus, N. J.; Koppaka, A.; Park, S. H.; Bischof, S. M.; Hashiguchi, B. G.; Periana, R. A. *Chem. Rev.* **2017**, *117*, 8521–8573.

[44] Hendon, C. MBS, MSA BDEs (Personal Correspondence). 2017.

[45] Ahlquist, M.; Nielsen, R. J.; Periana, R. A.; Goddard III, W. A. *J. Am. Chem. Soc.* **2009**, *131*, 17110–17115.

[46] Shilov, A. E.; Shul'pin, G. B. *Chem. Rev.* **1997**, *97*, 2879–2932.

[47] Shilov, A. E.; Shul'pin, G. B. *Activation and Catalytic Reactions of Saturated Hydrocarbons in the Presence of Metal Complexes*; Catalysis by Metal Complexes; Springer Netherlands, 2000.

[48] Periana, R.; Mirinov, O.; J. Taube, D.; Gamble, S. *Chem. Commun.* **2002**, *0*, 2376–2377.

[49] Periana, R. A.; Taube, D. J.; Gamble, S.; Taube, H.; Satoh, T.; Fujii, H. *Science* **1998**, *280*, 560–564.

[50] Hashiguchi, B. G.; Konnick, M. M.; Bischof, S. M.; Gustafson, S. J.; Devarajan, D.; Gunsalus, N.; Ess, D. H.; Periana, R. A. *Science* **2014**, *343*, 1232–1237.

[51] Stahl, S. S.; Labinger, J. A.; Bercaw, J. E. *Angew. Chem. Int. Ed.* **1998**, *37*, 2180–2192.

[52] O'Reilly, M. E.; Kim, R. S.; Oh, S.; Surendranath, Y. *ACS Cent. Sci.* **2017**, *3*, 1174–1179.

[53] Kim, R. S.; Nazemi, A.; Cundari, T. R.; Surendranath, Y. *ACS Catal.* **2020**, *10*, 14782–14792.

[54] Kim, R. S.; Wegener, E. C.; Yang, M. C.; O'Reilly, M. E.; Oh, S.; Hendon, C. H.; Miller, J. T.; Surendranath, Y. *J. Am. Chem. Soc.* **2020**, *142*, 20631–20639.

[55] Kim, R. S.; Surendranath, Y. *ACS Cent. Sci.* **2019**, *5*, 1179–1186.

[56] Wolfenden, R.; Yuan, Y. *Proc. Nat. Acad. Sci.* **2007**, *104*, 83–86.

[57] Heppolette, R. L.; Robertson, R. E.; Steacie, E. W. R. *Proc. Math. Phys. Eng. Sci.* **1959**, *252*, 273–285.

[58] Moelwyn-Hughes, E. A. *Proc. Math. Phys. Eng. Sci.* **1938**, *164*, 295–306.

[59] Aida, M.; Yamataka, H. *Comput. Theor. Chem.* **1999**, *461-462*, 417–427.

[60] Yamataka, H.; Aida, M. *Chem. Phys. Lett.* **1998**, *289*, 105–109.

[61] Aida, M.; Yamataka, H.; Dupuis, M. *Chem. Phys. Lett.* **1998**, *292*, 474–480.

[62] Lescisin, M.; Jianu, O. A.; Pope, K.; Rosen, M. A. *Int. J. Hydrog. Energy* **2020**, *45*, 26080–26089.

[63] Xu, T.; Zhang, Q.; Song, H.; Wang, Y. *J. Catal.* **2012**, *295*, 232–241.

[64] Taylor, C. E.; Noceti, R. P.; Schehl, R. R. In *Studies in Surface Science and Catalysis*; Bibby, D. M., Chang, C. D., Howe, R. F., Yurchak, S., Eds.; Methane Conversion; Elsevier, 1988; Vol. 36; pp 483–489.

[65] Sun, Y.; Campbell, S. M.; Lunsford, J. H.; Lewis, G. E.; Palke, D.; Tau, L. M. *J. Catal.* **1993**, *143*, 32–44.

[66] Kong, L.-t.; Shen, B.-x.; Zhao, J.-g.; Liu, J.-c. *Ind. Eng. Chem. Res.* **2014**, *53*, 16324–16331.

[67] Ghosh, A. K.; Khanmamedova, A.; Mier, M.; BANKE, J. Silicoaluminophosphate Catalyst for Chloromethane Conversion. 2016.

[68] Nilsen, M. H.; Svelle, S.; Aravinthan, S.; Olsbye, U. *Appl. Catal. A* **2009**, *367*, 23–31.

[69] Svelle, S.; Aravinthan, S.; Bjørgen, M.; Lillerud, K.-P.; Kolboe, S.; Dahl, I. M.; Olsbye, U. *J. Catal.* **2006**, *241*, 243–254.

[70] Noceti, R. P.; Taylor, C. E. United States Patent: 4769504 - Process for Converting Light Alkanes to Higher Hydrocarbons. 1988.

[71] Wei, Y.; Zhang, D.; Liu, Z.; Su, B.-L. *J. Catal.* **2006**, *238*, 46–57.

[72] Andrei, R. D.; Borodina, E.; Minoux, D.; Nesterenko, N.; Dath, J.-P.; Cammarano, C.; Hulea, V. *Ind. Eng. Chem. Res.* **2020**, *59*, 1746–1752.

[73] Sydora, O. L. *Organometallics* **2019**, *38*, 997–1010.

[74] Agapie, T. *Coord. Chem. Rev.* **2011**, *255*, 861–880.

[75] Malinowski, J.; Jacewicz, D.; Gawdzik, B.; Drzeżdżon, J. *Sci. Rep.* **2020**, *10*, 16578.

[76] Vernuccio, S.; Bickel, E. E.; Gounder, R.; Broadbelt, L. J. *ACS Catal.* **2019**, *9*, 8996–9008.

[77] Robert, M. Oligomerization of Propylene. 1976.

[78] Li, X.; Han, D.; Wang, H.; Liu, G.; Wang, B.; Li, Z.; Wu, J. *Fuel* **2015**, *144*, 9–14.

[79] Occelli, M. L.; Hsu, J. T.; Galaya, L. G. *J. Mol. Catal.* **1985**, *32*, 377–390.

[80] Kumar, P.; Varkolu, M.; Mailaram, S.; Kunamalla, A.; Maity, S. K. In *Polygeneration with Polystorage for Chemical and Energy Hubs*; Khalilpour, K. R., Ed.; Academic Press, 2019; pp 373–407.

[81] Tabak, S. A.; Krambeck, F. J.; Garwood, W. E. *AIChE J.* **1986**, *32*, 1526–1531.

[82] Popov, A. G.; Fedosov, D. A.; Ivanova, I. I.; Vedernikov, O. S.; Kleimenov, A. V.; Kondrashev, D. O.; Miroshkina, V. D.; Abrashenkov, P. A.; Kuznetsov, S. E. *Pet. Chem.* **2016**, *56*, 237–243.

[83] Chen, M. C.; Shao, H. Q.; Jiang, T. *Adv. Mater. Res.* **2013**, *634-638*, 659–663.

[84] Li, C.; Wang, H.; Zhu, S.-s.; Liu, G.-b.; Wu, J.-h. *J. Fuel Chem. Technol.* **2017**, *45*, 1088–1094.

[85] Gadewar, S. B.; Wyrsta, M. D.; Grosso, P.; Zhang, A.; Mcfarland, E.; Komon, Z. J. A.; Sherman, J. H. Continuous Process for Converting Natural Gas to Liquid Hydrocarbons. 2007.

[86] Liu, Z.; Huang, L.; Li, W. S.; Yang, F.; Au, C. T.; Zhou, X. P. *J. Mol. Catal. A: Chem.* **2007**, *273*, 14–20.

[87] Mat, R.; Amin, N. A. S.; Ramli, Z.; Abu Bakar, W. A. W. *J. Nat. Gas Chem.* **2006**, *15*, 259–265.

[88] Olah, G. A. *Angew. Chem. Int. Ed.* **2005**, *44*, 2636–2639.

[89] Vedernikov, A. N. *Acc. Chem. Res.* **2012**, *45*, 803–813.

[90] Waycuilis, J. J.; Turner, W. J.; Thomas, R. Processes for Converting Gaseous Alkanes to Liquid Hydrocarbons. 2009.

[91] Waycuilis, J. J. Process for Converting Gaseous Alkanes to Olefins and Liquid Hydrocarbons. 2011.

[92] Yang, H.; Tsang, S. C. E. *Appl. Petrochem. Res.* **2012**, *2*, 85–91.

Appendix A

Supplementary Information on Molten Phosphate Reduction

Contents

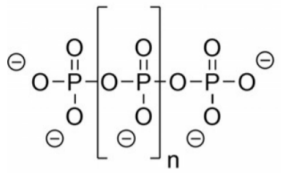

(a) Structure of a polyphosphate ion, $n \geq 0$.

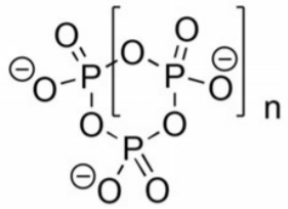

(b) Structure of a metaphosphate ion, $n \geq 1$.

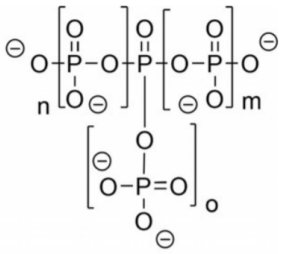

(c) Structure of an ultraphosphate ion, $m, n, o \geq 1$.

Figure A-1. Types of condensed phosphates.

A.1 Synthesis of Arbitrary Condensed Phosphate Melts

A.1.1 Composition and Structure of Molten Condensed Phosphates

Condensed phosphates are defined as phosphate salts that are dehydrated relative to free orthophosphate, possessing at least one phosphoryl anhydride linkage between adjacent phosphorus atoms. Collectively, the condensed phosphates comprise the linear polyphosphates (**Figure A-1a**), the cyclic metaphosphates (**Figure A-1b**), and the branched ultraphosphates (**Figure A-1c**)[i].

These phosphoryl anhydride linkages are crucial to describing the chemistry of the condensed phosphates, as their oxide-induced cleavage to terminal phosphates is fundamental to the 'oxide-accepting' character of condensed phosphate melts (**Scheme A.1**). This reactivity allows condensed phosphate melts to intrinsically fulfill the role performed in the thermal process by the conversion of silicon dioxide to metasilicate, which is associated with a majority of the slag formation (and associated energetic losses) of the thermal process.

Individual units in a condensed phosphate melt may be categorized into one of four types (**Figure A-2**), each of which may be associated with a different 'pure' phosphate compound or class of compounds under standard conditions. The most common is the *orthophosphate*,

[i] Though pictured here with only a single branching phosphate group connecting three linear chain phosphates, the ultraphosphates themselves comprise any condensed phosphate containing any branched moieties whatsoever. This additionally includes condensed phosphates with multiple branching phosphate groups, as well as condensed phosphates containing crosslinked ring phosphates or mixtures of ring and chain phosphates.

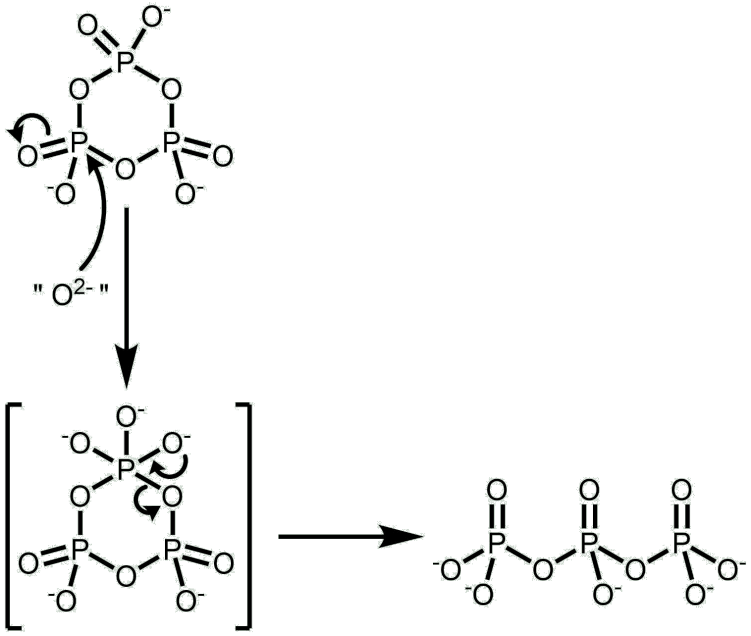

Scheme A.1. Representative mechanism for cleavage of a phosphoryl anhydride linkage by an oxide equivalent, here showing the formation of tripolyphosphate from trimetaphosphate. Note that oxide equivalents rarely exist as free O^{2-} ions, and in practice are more likely to be represented as nucleophilic polyphosphate chains.

PO_4^{3-}, so much so that it is commonly referred to as simply 'phosphate' in most elementary or non-field-specific applications. All other three classes of phosphate units fall under the category of 'condensed phosphates', being dehydrated relative to orthophosphate in that they have at least one phosphoryl anhydride linkage connecting adjacent phosphorus centers into an oligomeric or potentially even polymeric structure. Terminal phosphates have one phosphoryl anhydride linkage per phosphorus atom; the (archaic, albeit technically accurate) nomenclature for this structure is typified in the dipolyphosphate, also known as the *para-*

phosphate.[ii] Bridging phosphates have two phosphoryl anhydride linkages per phosphorus atom; cyclic *metaphosphates* consist solely of bridging phosphate groups, although they can also be found in any polyphosphate chains at least 3 phosphate units long. Finally, branching phosphates may crosslink poly- and metaphosphate chains and rings in *ultraphosphates*; although it is not technically classified as a phosphate salt owing to its neutral charge, phosphoric anhydride (P_4O_{10}) can be thought of as 'pure ultraphosphate' in that it consists solely of branching phosphate moieties, with 3 phosphoryl anhydride linkages per phosphorus atom.

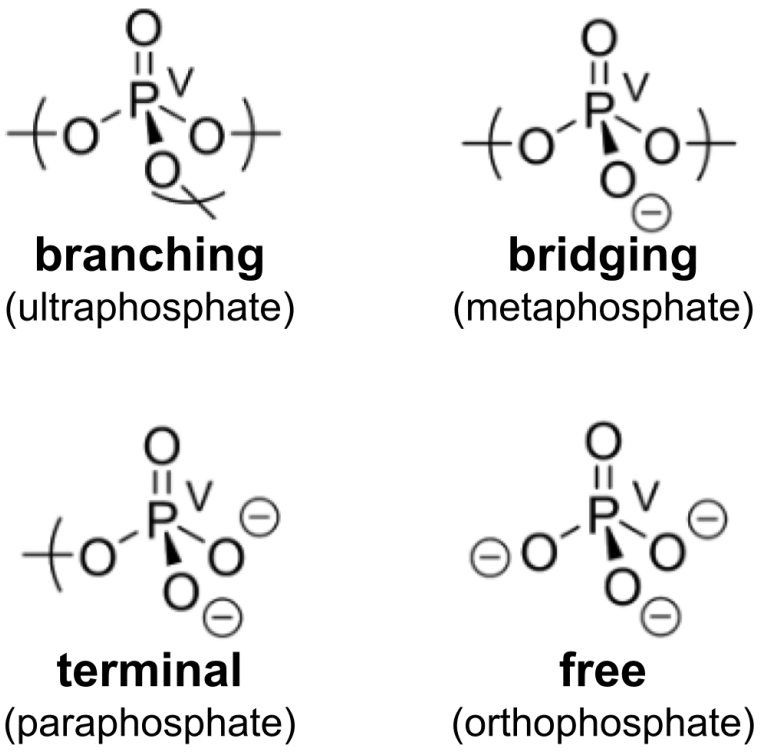

Figure A-2. Phosphorus atoms in a molten phosphate melt can be categorized as one of four types based on their number of phosphoryl anhydride linkages, between 0 and 3.

[ii] 'Paraphosphate' is considered an obsolete phraseology equivalent to 'pyrophosphate'. This is because the pyrophosphate – functionally the dipolyphosphate – is the only possible condensed phosphate consisting solely of terminal phosphate units. Hence, from a structural or spectroscopic perspective, the only phosphate species consisting purely of homogeneous units are free phosphate (the orthophosphate), ring phosphates (the metaphosphate), and dipolyphosphate (the paraphosphate). Over time, the 'paraphosphate' terminology fell out of favor, or was corrupted, in favor of 'pyrophosphate', allegedly in reference to the heating process necessary to produce the pure dipolyphosphate, even though such a dehydrative synthesis is intrinsic to the production of *any* condensed phosphate species (including all metaphosphates or higher polyphosphates). It is conceivable that, within a more descriptive and less spectroscopic understanding of phosphate nomenclature, a naming scheme with a specific prefix for the second-smallest phosphate was deemed unnecessary or confusing. Whatever the case, the terms 'orthophosphate' and 'metaphosphate' remain in common use, while the legacy of the paraphosphate is slowly being lost to time.[1]

Prefix	Structure	Anhydrides	Oxides	Formula Unit
ortho-	free	0	$1\frac{1}{2}$	PO_4^{3-}
para-	terminal	1	1	$PO_{3.5}^{2-}$
meta-	bridging	2	$\frac{1}{2}$	PO_3^{-}
ultra-	branching	3	0	$PO_{2.5}$

Table A.1. Phosphate species by the number of phosphoryl anhydride linkages per phosphorus atom and their oxide content relative to phosphoric anhydride.

Individual condensed phosphate species consist of a mixture of terminal, branching, and bridging moieties such that, by the relations detailed in **Table A.1**, all condensed phosphate ions will satisfy the relation:

$[(PO_{2.5})_u(PO_3)_m(PO_{3.5})_p]^{(m+2p)-}$,

where u is the number of branching (ultraphosphate) moieties, m is the number of bridging (metaphosphate) moieties, and p is the number of terminal (paraphosphate) moieties.[iii] For obvious reasons, free orthophosphate ions cannot be part of a condensed phosphate oligomer, as they have no phosphoryl anhydride linkages and hence are not condensed phosphates.

Within a melt, phosphate units may rapidly interconvert in a manner such that the total number of phosphoryl anhydride linkages remains constant: two paraphosphates may "disproportionate" to an orthophosphate and a metaphosphate, two metaphosphates may "disproportionate" to a paraphosphate and an ultraphosphate, an orthophosphate and a metaphosphate may "comproportionate" to two paraphosphates, a paraphosphate and an ultraphospate may "comproportionate" to two metaphosphates, or an orthophosphate and an ultraphosphate may form a paraphosphate and a metaphosphate. These reactions occur dynamically and all molten phosphate species should be considered to be in dynamic equilibrium while at temperature. As the precise distribution of condensed phosphate chains is a function of temperature, precise characterization of a melt cannot be performed by analysis of the solidified electrolyte, and future studies on the *in situ* character of the melt (perhaps

[iii] While the presence of fractional oxygen atoms for bridging and terminal phosphate groups may seem problematic at first, the nature of terminal and branching groups in a phosphate oligomer is such that the total number of bridging and terminal phosphates must always be an even number, so this is not an issue.

by high-temperature NMR) may be warranted to further elucidate the dispersion of phosphate species in the reaction media.

A.1.2 Selected Condensed Phosphate Mixtures

As seen in **Table A.2**, four selected condensed phosphate melts of varying degrees of oxide content were selected for analysis in this work, spanning a range of phosphoryl anhydride concentrations from 5.4368 $\text{mol}\cdot\text{kg}^{-1}$ to 9.8076 $\text{mol}\cdot\text{kg}^{-1}$. While the first of these melts was equivalent to a pure metaphosphate melt, the remainder were synthesized by mixing targeted mole fractions of sodium trimetaphosphate (S3MP) and sodium orthophosphate (SOP) to produce a homogenous electrolyte upon fusion. A 75:25 mol:mol mixture of S3MP:SOP (84.9:15.1 by mass) is 8.3210 $\text{mol}\cdot\text{kg}^{-1}$ in phosphoryl anhydride linkages; a 50:50 mol:mol mixture (65.1:34.9 by mass) is 6.3883 $\text{mol}\cdot\text{kg}^{-1}$, and a 40:60 mol:mol mixture (55.4:44.6 by mass) is 5.4368 $\text{mol}\cdot\text{kg}^{-1}$. Lower concentrations of phosphoryl anhydride linkages are largely inaccessible at the selected temperature of 800 °C; the next lowest polyphosphate, sodium pyrophosphate (5.4368 $\text{mol}\cdot\text{kg}^{-1}$ in phosphoryl anhydride linkages) has a melting point of 988 °C, and pure sodium orthophosphate (0 $\text{mol}\cdot\text{kg}^{-1}$) does not melt until 1583 °C.

	[anhydride]	**mol% S3MP**	**mol% SOP**
S3MP	9.8076	100%	0%
S10PP	8.3210	75%	25%
S4PP	6.3883	50%	50%
S3PP	5.4368	60%	40%

Table A.2. Condensed phosphate melts selected for study, their net anhydride content (in $\text{mol}\cdot\text{kg}^{-1}$), their homogeneous equivalent species (in terms of oxide/anhydride content), and the molar ratios of sodium trimetaphosphate (S3MP) and sodium orthophosphate (SOP) required for synthesis.

For each of these selected melts, a total mass of 60 g was measured out in the prescribed ratio of S3MP (99.9999%, anhydrous, #AA89063A1 from Alfa Aesar™) to SOP (99.9999%, anhydrous, #AC389810010 from Acros Organics™) and ground together in a mortar & pestle to ensure the system's homogeneity. This mixture was then poured into a glassy carbon

crucible for electroanalysis as described in **Section 2.2.1**.

A.2 Effects of IR Compensation on Phosphate Reduction Electroanalysis

A.2.1 Measuring Uncompensated Resistance

In any electrochemical system, the nonzero resistance of the electrolyte will induce a voltage drop between the reference electrode and the working electrode. The magnitude of this voltage drop is defined by Ohm's law: $V = IR$. Here, the voltage drop V is the product of the current I and the *uncompensated resistance (R_u)*, so-called because it is not automatically compensated for by the potentiostat.[iv] R_u may be broadly understood to be a measure of solution resistance, but it will vary depending on many factors, including but not limited to reaction temperature, electrode surface area, electrolyte composition, and the spatial orientation of electrodes within the electrochemical cell. As a result, it must be empirically determined and accounted for in every experiment, a process known as IR compensation.[2]

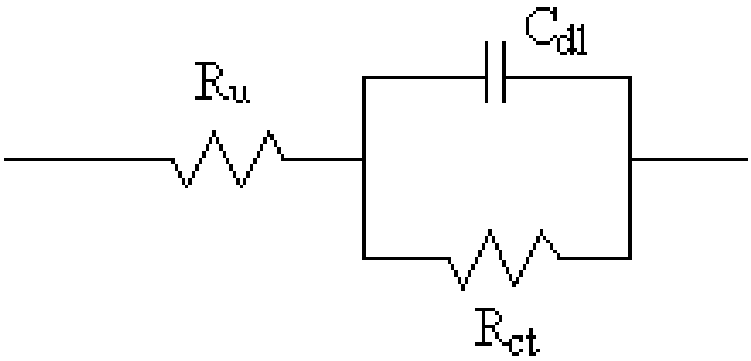

Figure A-3. Simplified Randles cell equivalent circuit of an electrochemical system. R_u is the solution resistance, equivalent to the uncompensated resistance, C_{dl} is the capacitance of the electrochemical double-layer, and R_{ct} is the charge-transfer resistance at the electrode.

There are two primary methods for assessing R_u and thereby calculating the necessary voltage to be compensated: the electrochemical impedance spectroscopy (EIS) method and

[iv] Duh!

the current interrupt (CI) method. EIS is an alternating current (AC) method that exploits the ability of high-frequency signals to pass unimpeded through capacitors; within the Randles model of the electrochemical cell (**Figure A-3**), this effectively short-circuits the charge-transfer resistance (R_{ct}) through the double-layer capacitance (C_{dl}), thereby distinguishing R_{ct} from R_u. The CI method, by comparison, is a direct current (DC) technique that utilizes the double layer's capacity to maintain charge to measure R_u; by passing a relatively large current and quickly turning off (interrupting) the current, we can induce an immediate drop in the cell voltage equal to R_u in an ideal system. For the purposes of this work, all R_u values were assessed by the CI method, passing currents of 200 mA at 50 ms intervals.

A.2.2 Methods for IR Compensation

Unfortunately, merely knowing R_u is only enough to perfectly compensate for solution potential drop in galvanostatic experiments, where the current is fixed. In these cases, the solution resistance is trivial to compensate for post-experiment, since $V_{applied} = V_{desired} + V_u$ and $V_u = i_{applied}R_u$. This presents a problem for nongalvanostatic measurements, particularly voltammetric or other potential-sweep measurements, where it is impossible to know the applied current before it is, well, applied. As a result, iterative methods are necessary to dynamically account for solution resistance; for each data point, the applied potential is modified by the IR drop of the *previous* data point: $V_{applied}[i] = V_{desired}[i] + V_u[i-1]$. This process is known as *positive-feedback IR compensation* and it is viable for dynamic correction of even fast voltammetric experiments that cannot be post-corrected, although it relies upon predetermining an R_u value that must not change over the course of the experiment.

A.2.3 IR Overcompensation

However, compensating in this manner for the solution resistance of the previous datapoint creates a potentially dangerous feedback loop. If the entirety of the R_u is compensated for in this manner, the system will enter an undamped oscillation, as the system is functionally

controlling a purely capacitive electrode. Fractional compensation is necessary to damp this oscillation, the degree of compensation being variable based on the electrochemical system itself and the experimental sampling rate. Compensation rates of 80 to 90% are typical for aqueous systems with solution resistances up to 100 Ω; higher solution resistances mean a greater fraction of IR compensation is both necessary to mitigate the increased IR drop and possible without excess oscillation entering the positive feedback loop.[2, 3]

However, as depicted in **Figure A-4**, our molten-salt reactor has the opposite problem: the high conductivity of the molten salt coupled with the small electrode spacing evinces astoundingly low R_u values around 1 Ω, which are accordingly overcompensated at even comparatively low IR compensation fractions. This IR overcompensation manifests as a steep, nearly vertical feature in reductive-scan LSVs, as even small changes or errors in R_u are iteratively magnified by positive-feedback IR compensation. The flipside of this, of course, is that with such low R_u values the IR-induced errors in potential are small except at the highest current densities. For example, at an R_u of 1 Ω, even a relatively high current of 10 mA only induces an IR drop of 10 mV, which is less than the noise from correction to our Na/Na^+ quasireference electrode. Moreover, our few high-current experiments (such as **Figure 2-10** on 61) are collected galvanostatically, in which post-reaction IR correction is trivial and dynamic compensation is unnecessary. For this reason, dynamic IR compensation is eschewed for all molten-salt voltammetric measurements in this work.

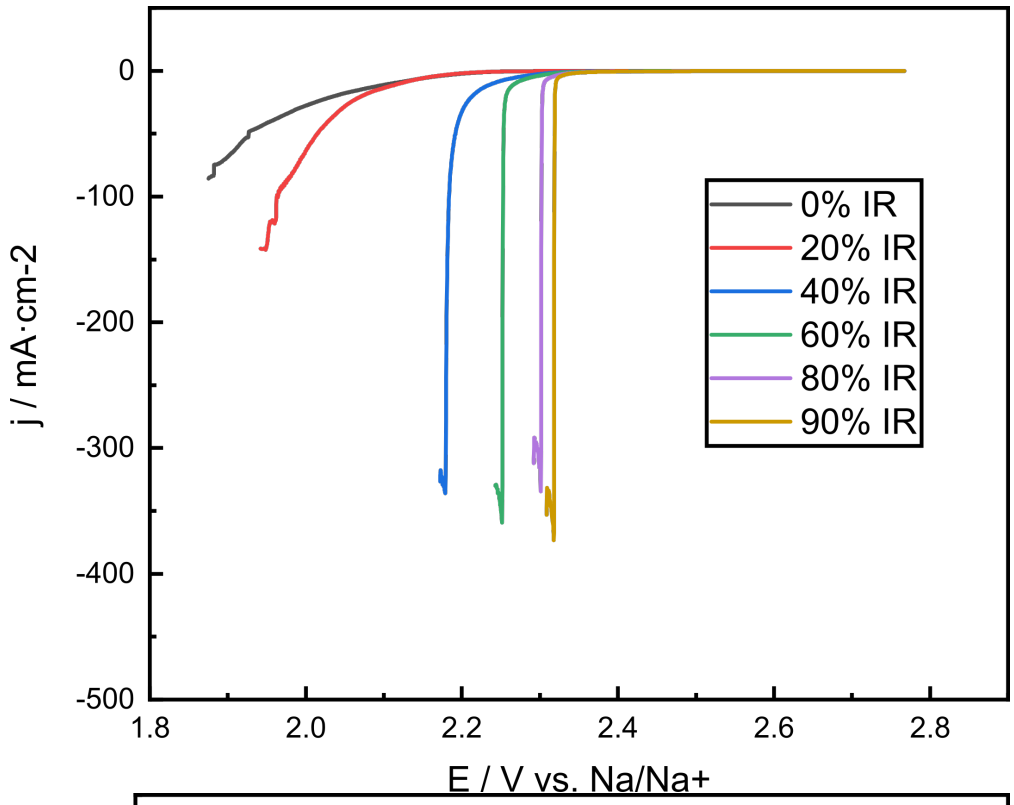
0
-100
-200
-300
-400
-500
j / mA·cm-2
1.8
2.0
2.2
2.4
2.6
2.8
E / V vs. Na/Na+
0% IR
20% IR
40% IR
60% IR
80% IR
90% IR

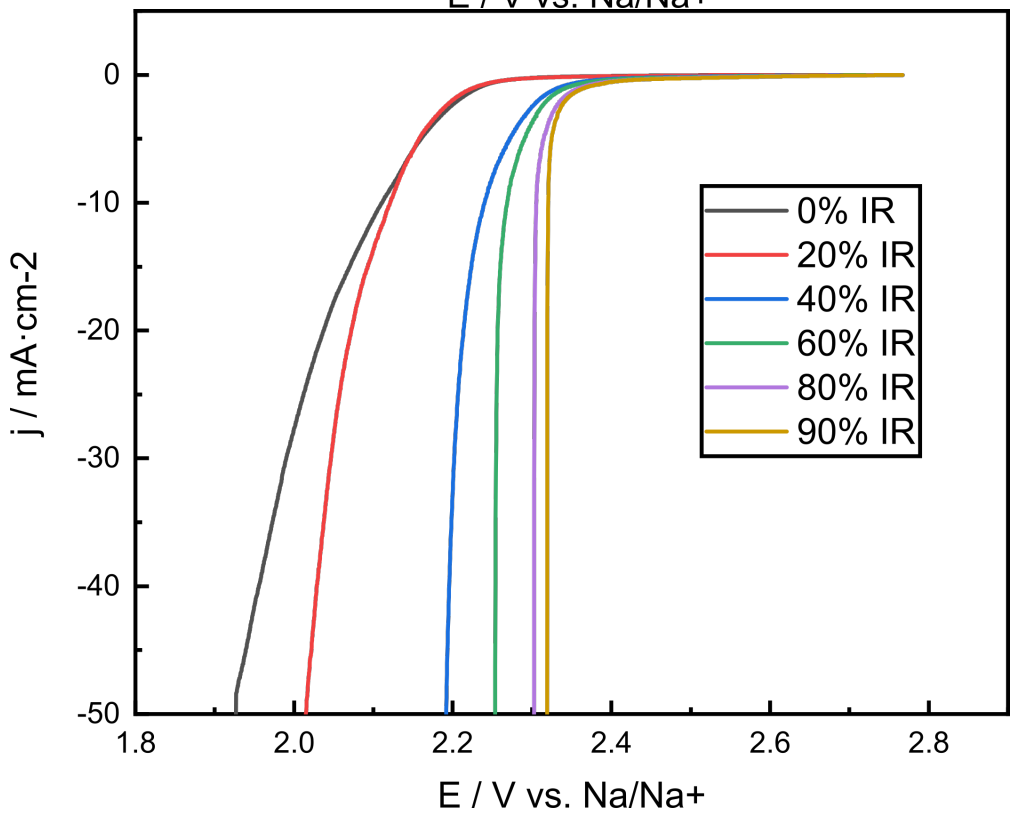
0
-10
-20
-30
-40
-50
j / mA·cm-2
1.8
2.0
2.2
2.4
2.6
2.8
E / V vs. Na/Na+
0% IR
20% IR
40% IR
60% IR
80% IR
90% IR

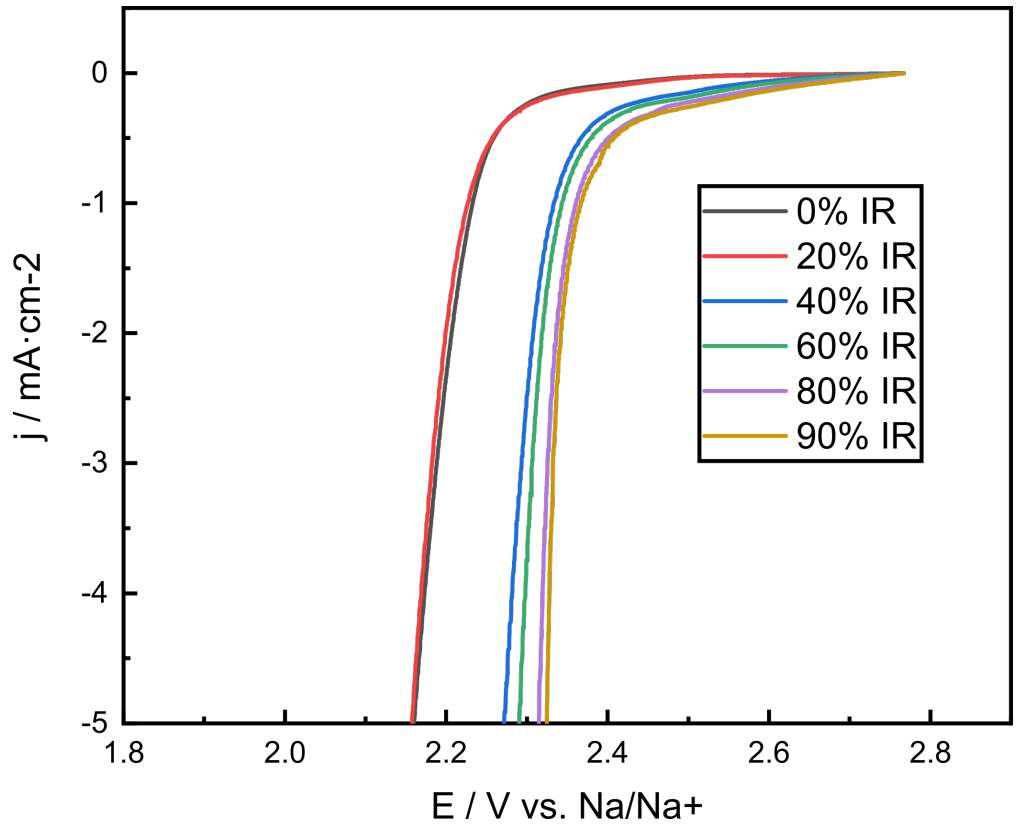

Figure A-4. Linear-sweep voltammograms of sharpened graphite electrodes at various IR compensation values, scanning reductively at $100\,\mathrm{mV{\cdot}s^{-1}}$. Note y-axis ranges of $500\,\mathrm{mA{\cdot}cm^{-2}}$, $50\,\mathrm{mA{\cdot}cm^{-2}}$ and $5\,\mathrm{mA{\cdot}cm^{-2}}$.

A.3 Synthetic Routes towards New Alkali Metaphosphate Melts

To assess the role of cation effects in the phosphate reduction process, work was initiated towards the synthesis of alkali trimetaphosphate (MTMP; M=Li, K, Cs) salts beyond the commercially-available sodium trimetaphosphate. While a viable synthetic pathway was identified towards these materials through salt metathesis from tetra-*n*-butylammonium trimetaphosphate (TBATMP), unoptimized yields for the metathesis reaction itself precluded the generation of MTMP salts in the >60 g quantities necessary for electrochemical analysis in our system (owing in part due to challenges imposed by the occluding interference of the coronavirus disease 2019 (COVID-19) pandemic). Other proposed and heretofore unexplored synthetic routes to alkali trimetaphosphate salts include the stoichiometric dehydration of alkali orthophosphate salts in a phosphoric anhydride melt. For the sake of completeness, preparative details and characterization of crude products is included in this document.

A.3.1 Synthesis and Characterization of TBATMP

A.3.1.1 Synthetic Route to TBATMP

Alkali trimetaphosphate salts were accessed through a TBATMP precursor, which was synthesized according by ion-exchange chromatography preps adapted from the literature to use glass frits instead of packed columns in order to achieve higher reaction throughput. [4, 5]

184 mL (311.10 mmol; 5eq) Dowex® 50W X8 ion exchange resin (#217514, 200 Mesh from Millipore-Sigma) was dispersed in 300 mL reagent grade water (Millipore Type 1, 18 MΩ·cm resistivity) and dispersed as a plug upon a 500 mL medium-porosity fritted glass funnel under vacuum. The plug was then rinsed ten times with MilliQ-grade water in order to remove excess H_2SO_4 moieties, until the eluent was neutral by pH test strips. The cation-exchange resin was then loaded with tetra-*n*-butylammonium (TBA) residues by flowing through 404 mL (622.2 mmol; 10 eq) tetra-*n*-butylammonium hydroxide (TBAOH) (40%

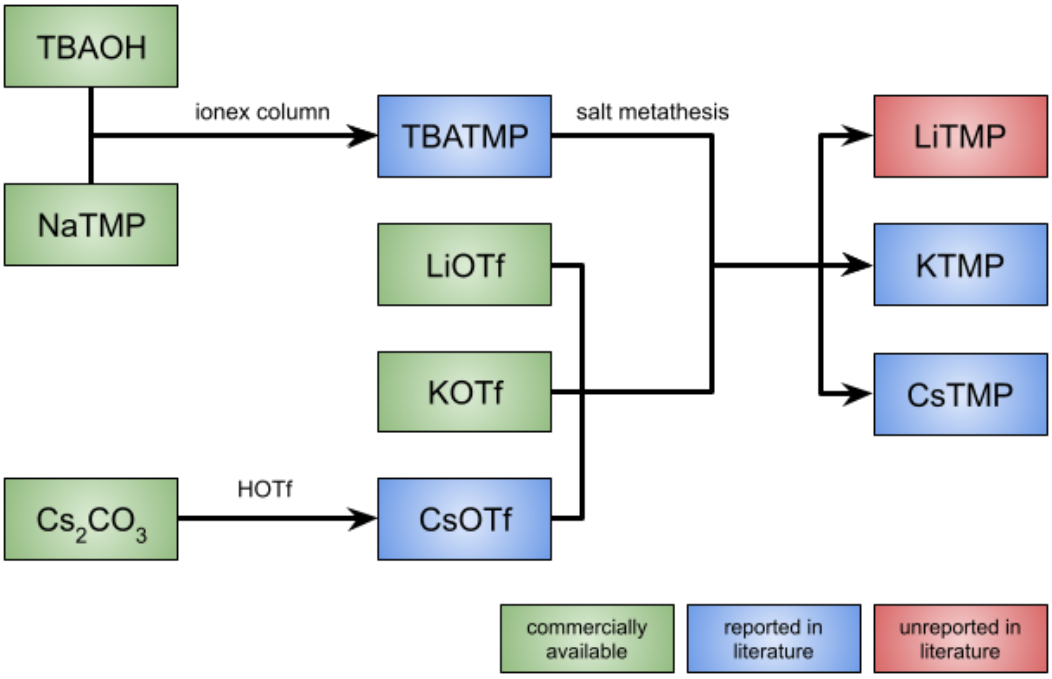

Scheme A.2. Synthetic route towards lithium, potassium, and cesium metaphosphate salts from commercially-available precursors.

w/w cation regenerant solution, #NC9390323 from Fisher Scientific®) five times, Finally, 19.03 g (62.22 mmol; 1 eq) sodium trimetaphosphate (S3MP) was dissolved in 500 mL MilliQ-grade water and passed through the plug five times. The effluent was evaporated off to a greasy solid at 60 °C under vacuum and washed with 3×50 mL of diethyl ether to produce a tacky, off-white solid which was dried overnight *in vacuo* over $CaSO_4$. The crude product was dissolved in 500 mL acetonitrile and gravity filtered under N_2 to remove unreacted S3MP; the solid was then purified under vacuum to yield 45.7 g of TBATMP product (47.4 mmol; 76.2% yield). The product was of sufficient purity for further preparation and was stored in a vacuum dessicator over $CaSO_4$.

A.3.1.2 NMR Characterization of TBATMP

All NMR spectra were recorded with Bruker AVANCE-400 spectrometers and processed using MestReNova software. Of note, spectra were collected in protic solvents MeCN$-h_3$ and

H_2O using a Norell® #NI5CCI-B coaxial NMR insert tube filled with D_2O as a lock solvent. ^1H NMR chemical shifts are given in ppm with respect to the residual solvent peak (MeCN δ2.01 ppm). 13C1H NMR shifts are given in ppm with respect to $CDCl_3$ (δ77.2 ppm) or MeCN (δ118.3 ppm, 1.3 ppm). ^{31}P NMR shifts are given with respect to a phosphonoacetic acid internal standard (δ+17.0 ppm). Coupling constants are reported as J-values in Hz.

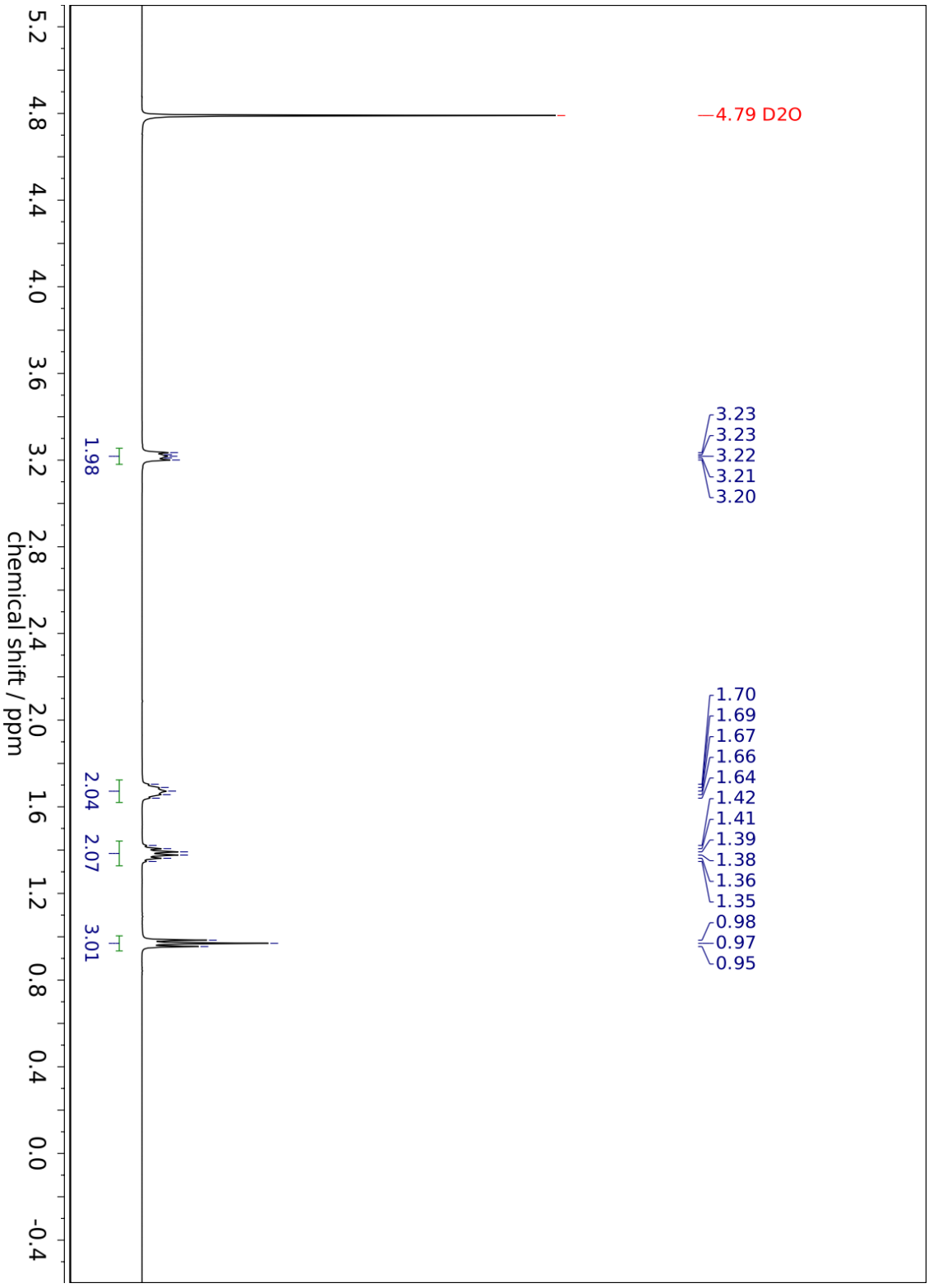

Figure A-5. ^{1}H NMR spectra of TBATMP.

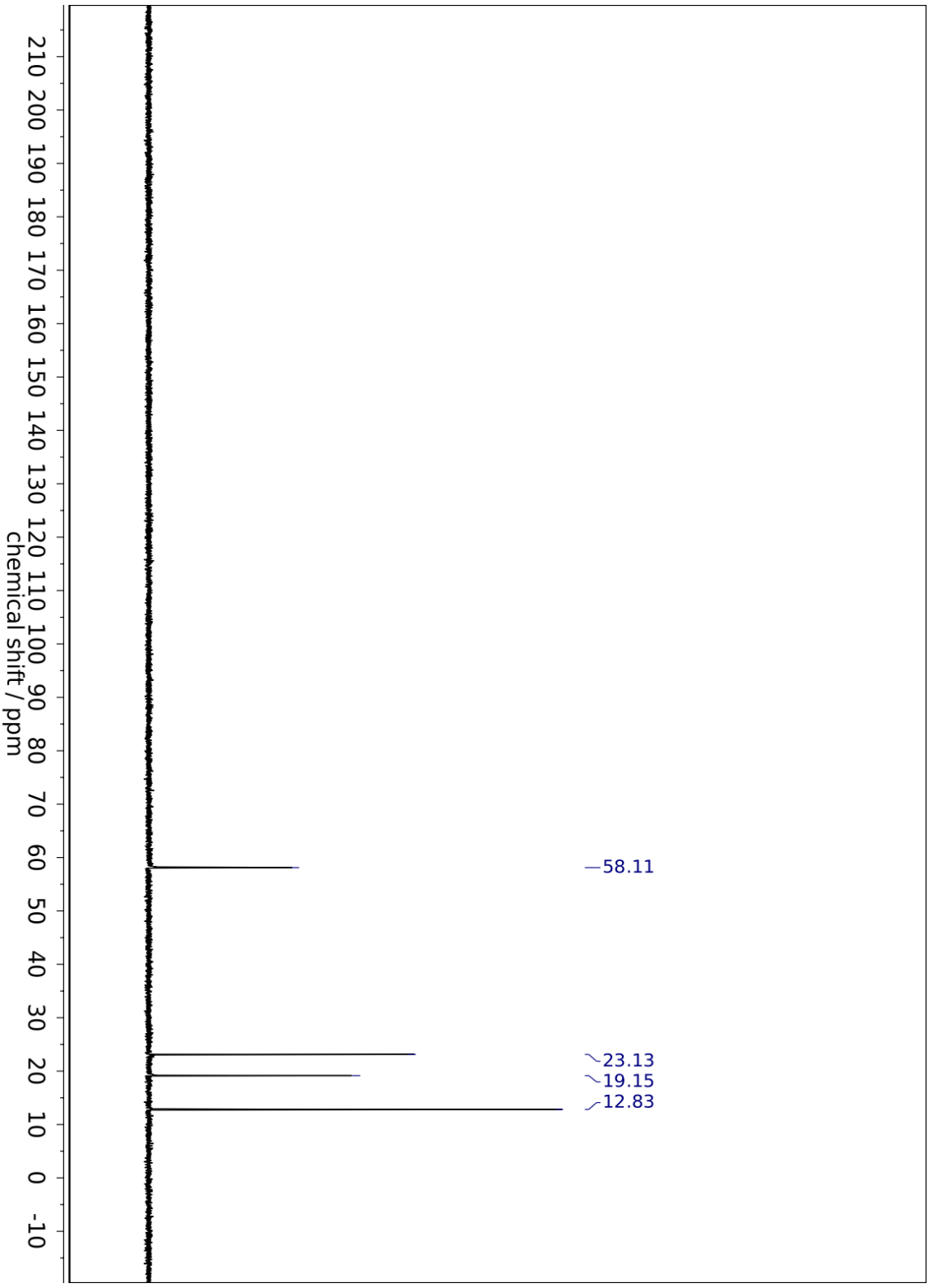

Figure A-6. ^{13}C NMR spectra of TBATMP.

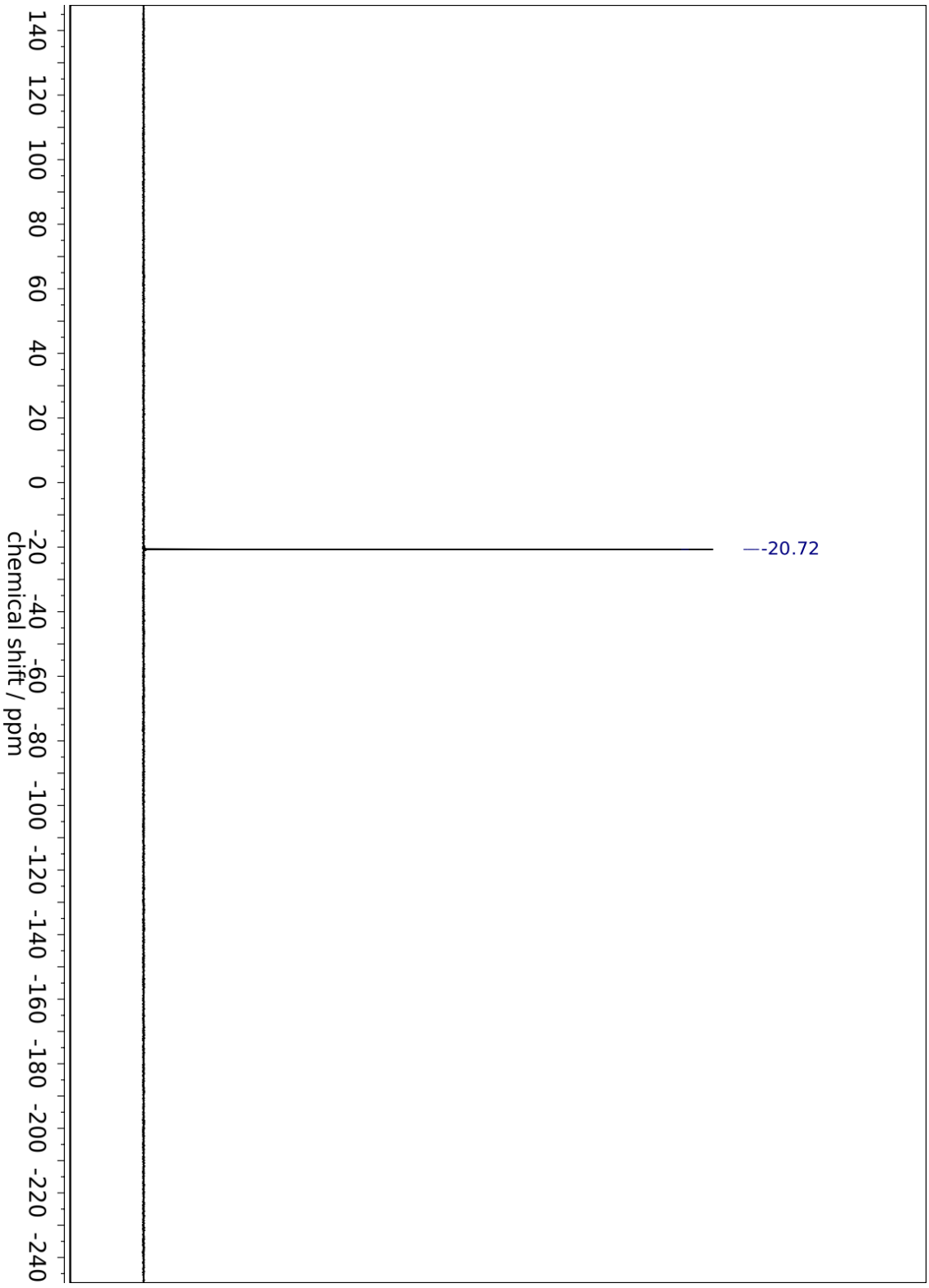

Figure A-7. ^{31}P NMR spectra of TBATMP.

A.3.2 Synthesis and Characterization of MTMP (M=Li, K, Cs)

A.3.2.1 Synthesis of CsOTf by Neutralization

To enable the necessary reactant solubilities demanded by the salt metathesis prep described below, alkali trifluoromethanesulfonate salts LiOTf, KOTf, and CsOTf were used. While the former two were commercially available in high purity, the latter salt was not; as a result, it was synthesized by the neutralization of commercially-available cesium carbonate Cs_2CO_3 (99%, #441902 from Sigma-Aldrich) with triflic acid HOTf (≥99%, #347817 from Sigma-Aldrich).

4.9086 g Cs_2CO_3 (15.065 mmol) was dissolved in 10 mL reagent-grade water in a small round-bottom flask. 2.666 mL 11.30 M HOTf (30.13 mmol; 2.1 equiv.) was added dropwise to the flask while stirring. The solvent was then removed by refluxing at 165 °C using a Claisen condenser and heated to dryness, producing 7.8921 g (27.99 mmol; 92.9% yield) of powdery white product which was stored in a calcium sulfate dessicator under vacuum.

A.3.2.2 Synthesis of MTMP by Salt Metathesis

Synthesis of LiTMP In a nitrogen glovebox, 2.003 g dry LiOTf (12.837 mmol, 1.1 equiv.) was dissolved in 40 mL of anhydrous acetonitrile (MeCN). In a separate flask, 11.26 g dry TBATMP (11.67 mmol, 1 equiv.) was dissolved in 20 mL of anhydrous MeCN. The two solutions were mixed together, precipitating a flocculent solid which was filtered off in air to produce 0.230 g (1.47 mmol, 12.6% yield) of powdery white LiTMP product.

Synthesis of KTMP In a nitrogen glovebox, 10.99 g dry KOTf (58.39 mmol, 1.1 equiv.) was dissolved in 300 mL of anhydrous MeCN. In a separate flask, 51.19 g dry TBATMP (53.08 mmol, 1 equiv.) was dissolved in 100 mL of anhydrous MeCN. The two solutions were mixed together, precipitating a flocculent solid which was filtered off in air to produce 3.132 g (8.84 mmol, 16.6% yield) of powdery off-white KTMP product.

Synthesis of CsTMP In a nitrogen glovebox, 10.1160 g dry CsOTf (35.88 mmol, 1 equiv.) was dissolved in 80 mL of anhydrous MeCN. In a separate flask, 34.596 g dry TBATMP (35.88 mmol, 1 equiv.) was dissolved in 100 mL of anhydrous MeCN. The two solutions were mixed together, precipitating a flocculent solid which was filtered off in air to produce 8.2121 g (12.92 mmol, 27.4% yield) of powdery white CsTMP product.

A.3.2.3 ^{31}P NMR Characterization of MTMP Salts

All NMR spectra were recorded with Bruker AVANCE-400 spectrometers and processed using MestReNova software. Of note, spectra were collected in protic MeCN$-h_3$ using a Norell® #NI5CCI-B coaxial NMR insert tube filled with D_2O as a lock solvent. ^{31}P NMR shifts are given with respect to a phosphonoacetic acid internal standard (δ+17.0 ppm). Coupling constants are reported as J-values in Hz.

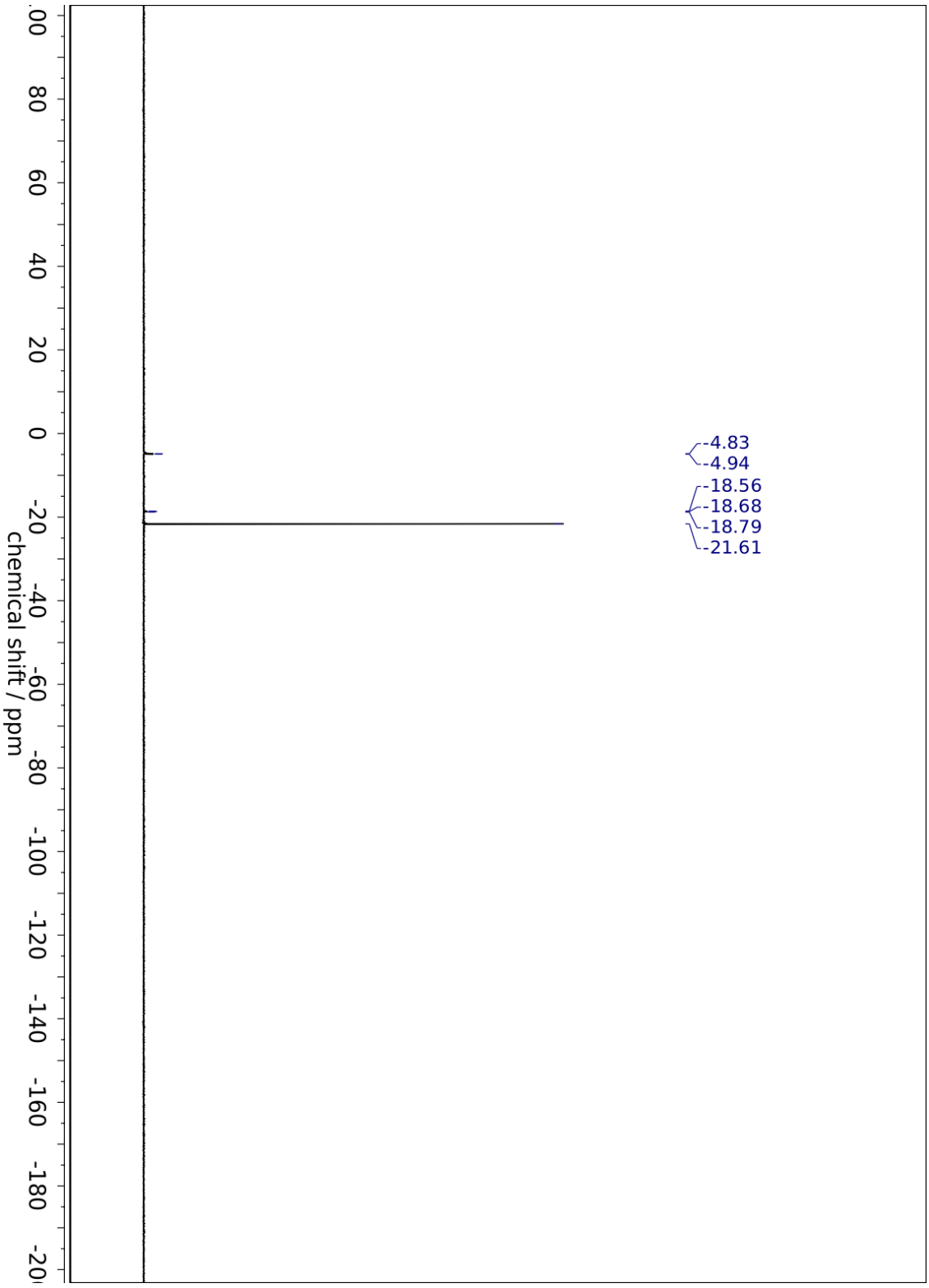

Figure A-8. ^{31}P NMR spectra of LiTMP.

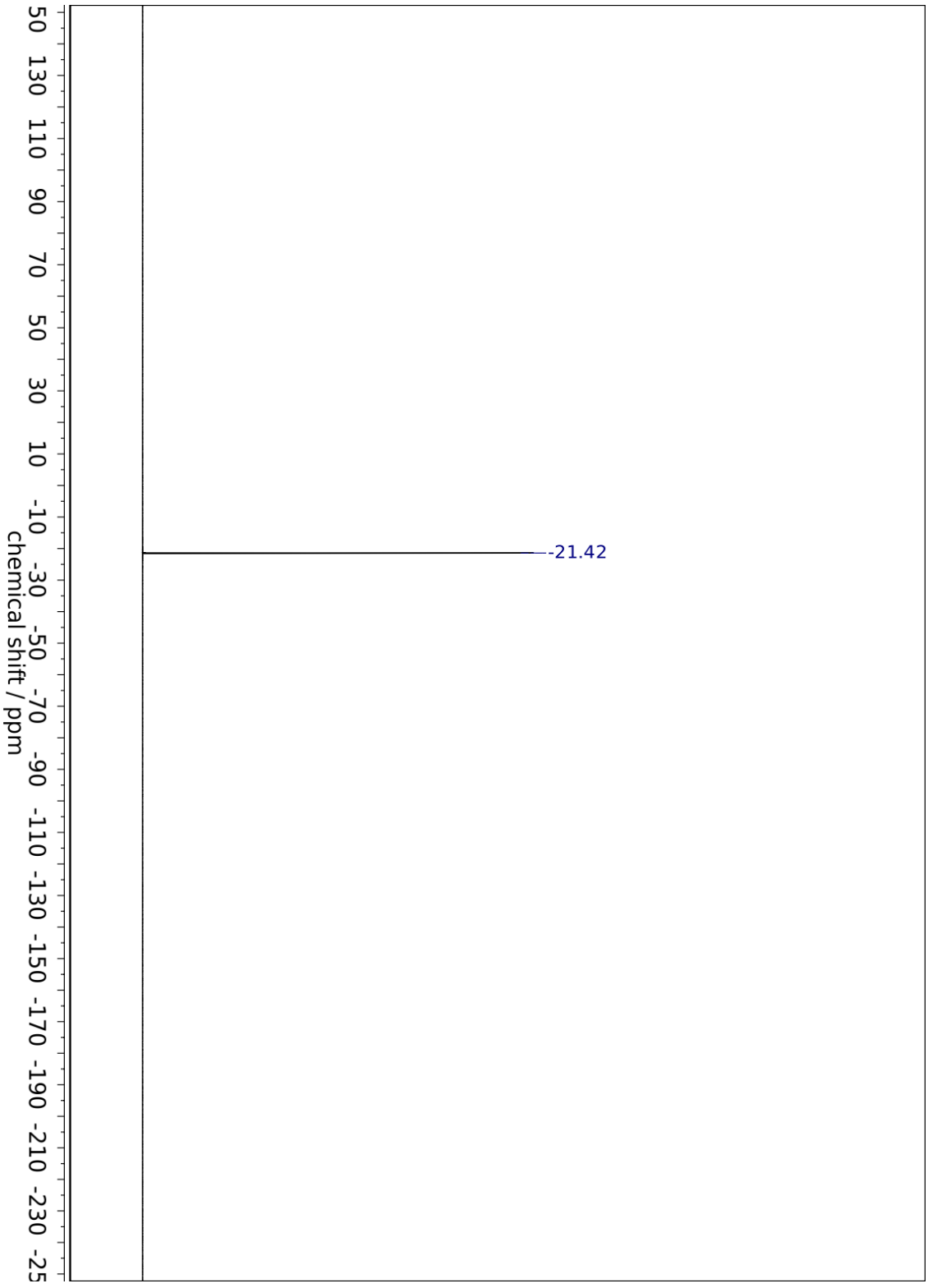

Figure A-9. ^{31}P NMR spectra of KTMP.

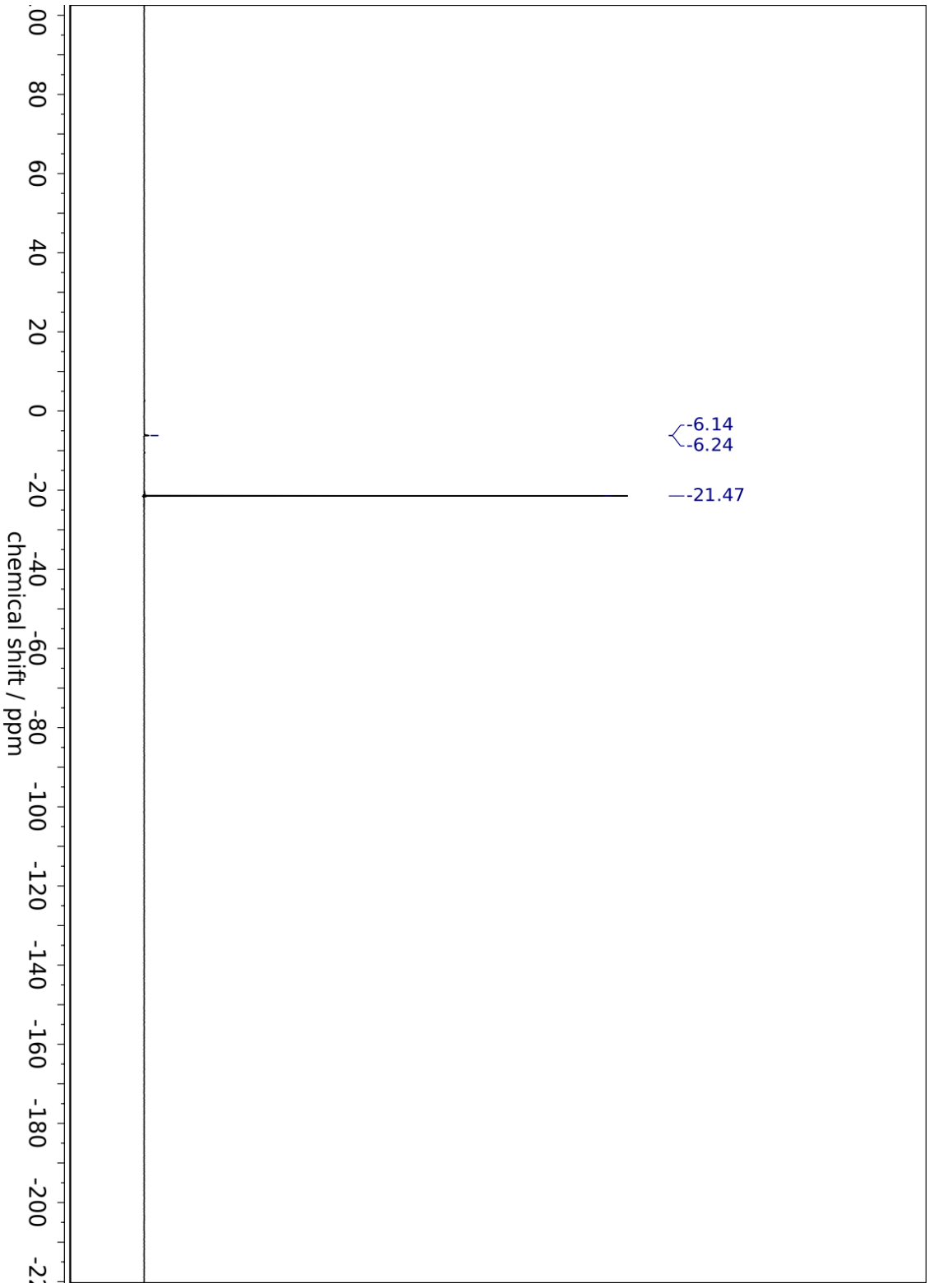

Figure A-10. ^{31}P NMR spectra of CsTMP.

A.4 Effects of Metal Plating on Graphite Electrodes for Phosphate Reduction

As an attempt to survey the catalytic activity of late transition metals towards PRR, conical graphite electrodes were electroplated with copper, silver, gold, nickel, palladium, and platinum towards the generation of chronopotentiometric current-overpotential (Tafel) plots. Electroplated graphite rods were chosen for this purpose primarily because the electrochemical reactor is designed for fixed-length rigid electrodes; a 3/16" graphite rod is necessary to ensure reactor sealing, and wires or foils appended to this rod run the risk of shorting against the glassy carbon crucible or becoming disconnected within the melt (a failure which can cost a day or more of work, as the entire reactor must be cooled, disassembled, and reassembled).

Unfortunately, these electroplated layers proved insufficiently robust to the oxidizing metaphosphate melt, which has been previously demonstrated to dissolve even noble metals.[6–8]. XPS analysis demonstrated substantial losses in the electroplated layers to the solution; as a result, the collected chronopotentiometric data essentially comprise studies of the (lack of) catalytic activity of late-transition metal ions at a graphite electrode surface in a metaphosphate melt.

A.4.1 Electroplating of Graphite Electrodes

Electroplating of Copper To 40 mL reagent-grade water was added 966.4 mg (4.0 mmol) copper (II) nitrate trihydrate ($Cu(NO_3)_2 \cdot 3\,H_2O$) in a 2-neck electrochemical cell. Copper was then plated galvanostatically at a fixed current of -10 mA for 30 minutes in a two-electrode configuration, with a conical 3/16" graphite working electrode and a 1/4" graphite rod counter/reference electrode.

Electroplating of Silver To 50 mL reagent-grade water was added 128.47 mg (0.50 mmol) silver triflate (AgOTf) and 612.2 mg (5.0 mmol) sodium perchlorate ($NaClO_4$) supporting

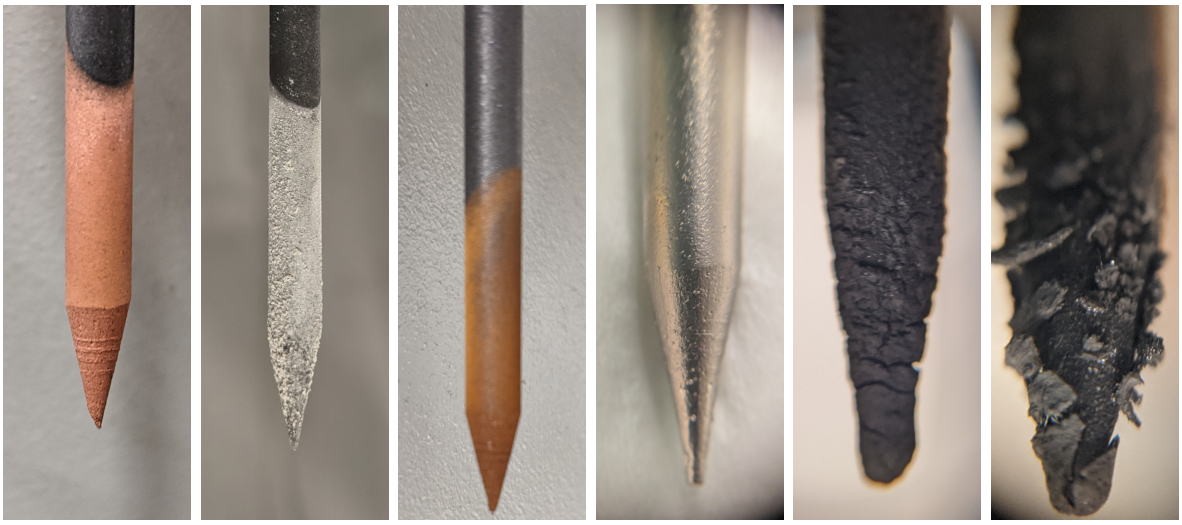

Figure A-11. Metal-electroplated graphite electrodes. From left to right: copper, silver, gold, nickel, palladium, platinum.

electrolyte in a 2-neck electrochemical cell. Silver was then plated galvanostatically at a fixed current of −10 mA for 30 minutes in a two-electrode configuration, with a conical 3/16" graphite working electrode and a 1/4" graphite rod counter/reference electrode.

Electroplating of Gold To 40 mL reagent-grade water was added 157.53 mg (0.40 mmol) chloroauric acid trihydrate ($HAuCl_4 \cdot 3\,H_2O$) and 489.76 mg (4.0 mmol) sodium perchlorate ($NaClO_4$) supporting electrolyte in a 2-neck electrochemical cell in a 2-neck electrochemical cell. Gold was then plated galvanostatically at a fixed current of −10 mA for 30 minutes in a two-electrode configuration, with a conical 3/16" graphite working electrode and a 1/4" graphite rod counter/reference electrode.

Electroplating of Nickel To 40 mL reagent-grade water was added 4.95 g (17.5 mmol) nickel (II) acetate tetrahydrate ($Ni(OAc)_2 \cdot 4\,H_2O$) in a 2-neck electrochemical cell. Nickel was then plated galvanostatically at a fixed current of −10 mA for 150 minutes in a two-electrode configuration, with a conical 3/16" graphite working electrode and a 1/4" graphite rod counter/reference electrode.

Electroplating of Palladium To 40 mL reagent-grade water was added 158.934 mg (0.40 mmol) potassium hexachloropalladate(IV) ($K_2[PdCl_6]$) and 489.76 mg (4.0 mmol) sodium perchlorate ($NaClO_4$) supporting electrolyte in a 2-neck electrochemical cell. Palladium was then plated galvanostatically at a fixed current of −25 mA for 30 minutes in a two-electrode configuration, with a conical 3/16" graphite working electrode and a 1/4" graphite rod counter/reference electrode.

Electroplating of Platinum To 40 mL reagent-grade water was added 153.12 mg (0.40 mmol) sodium tetrachloroplatinate(II) ($Na_2[PtCl_4]$) and 489.76 mg (4.0 mmol) sodium perchlorate ($NaClO_4$) supporting electrolyte in a 2-neck electrochemical cell. Platinum was then plated galvanostatically at a fixed current of −10 mA for 4 hours in a two-electrode configuration, with a conical 3/16" graphite working electrode and a 1/4" graphite rod counter/reference electrode.

A.4.2 Electroanalysis of Metal-Plated Electrodes

Once generated, these metal-plated electrodes were subjected to galvanostatic overpotential-current studies in an attempt to identify potential metal electrocatalysts for phosphate reduction. Electrochemical surface area (ECSA) measurements of the type described in **Section 2.4.1** on page 81 were used to assess electrode surface areas; an aqueous prereaction ECSA cyclic voltammetry (CV) set was taken following electroplating, another ECSA CV set was taken as soon as the electrode was immersed in the S3MP melt, a postreaction set was taken in the melt following the Tafel chronopotentiograms, and a final aqueous postreaction set was taken after the electrode was removed. Ultimately, the melt ECSAs were found to be plagued with substantially nonlinear capacitances that greatly exaggerated the calculated electrode surface areas relative to the comparatively stable aqueous surface areas, as pictured in **Figure A-12**. For this reason, aqueous ECSAs are used exclusively for area-normalizing current densities in this section.

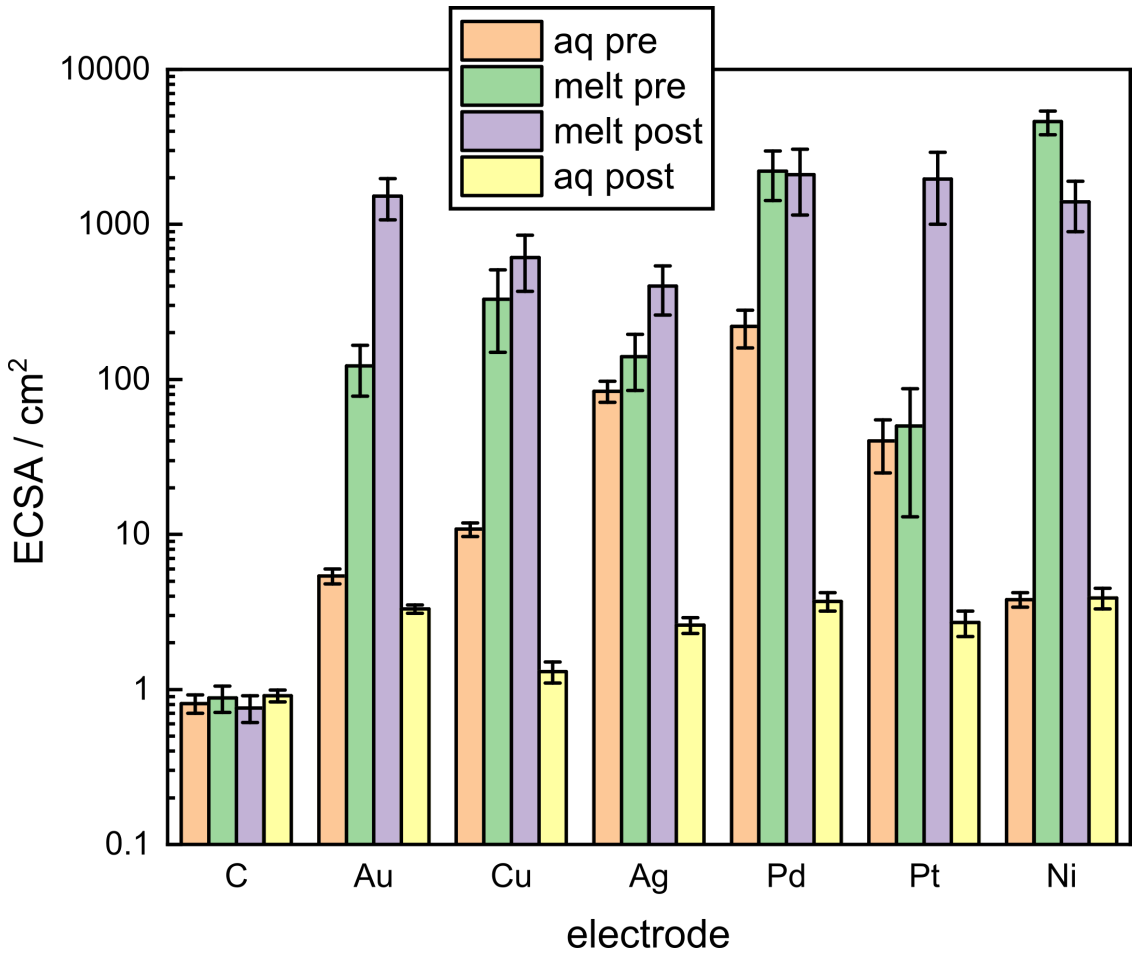

Figure A-12. Pre- and postreaction ECSA estimates for late-transition metal-electroplated graphite electrodes in both molten sodium trimetaphosphate and aqueous conditions.

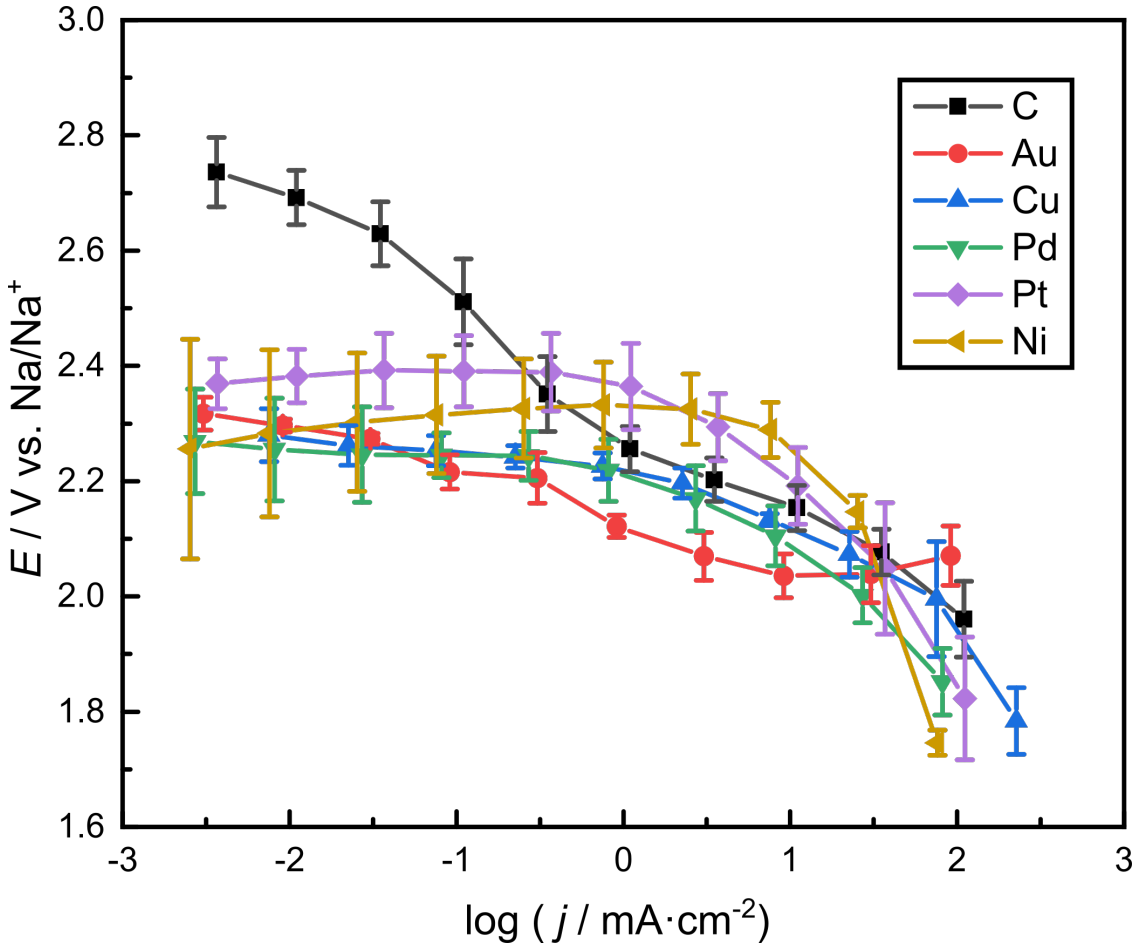

Figure A-13. Plot of phosphate reduction overpotential on selected late-transition metal-electroplated graphite electrodes as a function of current density in molten sodium trimetaphosphate

Using aqueous surface areas, we compare chronopotentiometric overpotential-current plots (**Figure A-13**) and find little statistically significant variation in catalytic activity for PRR across late-transition metal-plated electrodes. In the low-current density regime, observe that all metal-plated electrodes are broadly indistinguishable within a 95% margin of error, all at reductive overpotentials hundreds of millivolts more cathodic than bare graphite – potentially reflecting occlusion from rereduction of solubilized metal ions. In the high-current density regime, metal-plated electrodes are again broadly indistinguishable, converging upon a Tafel slope that highly resembles that of bare graphite. From this we conclude that metal-plated graphite electrodes are broadly electrochemically incompetent for metaphosphate reduction, conveying no apparent catalytic activity beyond that of unfunctionalized graphite.

A.4.3 Instability of Metal Platings on Graphite

The consistent loss in aqueous ECSA pre- and postreaction (for all metal-plated electrodes except for nickel) are highly suggestive of metal dissolution in the melt, a phenomenon we further interrogated via XPS on copper, gold, and platinum electrodes. Following the collection of current-overpotential data, we collected XPS spectra on the metal-plated graphite electrodes both at points that were immersed in the metaphosphate melt and at points that lay just above the molten salt electrolyte meniscus. The level of this meniscus was easy to determine, both due to the trace residues of metaphosphate on the electrode and the visible loss of metal plating where the electrode was immersed. By contrast, metal platings above this point remained clean and highly specular – often moreso than when freshly electroplated, presumably as amorphous oxide structures such as the palladium and platinum black coatings seen in **Figure A-11** thermally annealed to pure metal at high temperatures under N_2 flow.

M	**above melt**	**in melt**
Au	11.0%	5.1%
Pt	15.6%	1.9%
Cu	6.8%	3.0%

Table A.3. Atomic percentages of metal-plated electrodes by XPS, at points immersed in the melt and points above the melt.

While control experiments are still needed to determine the extent to which this metal loss is solely attributable to non-Faradaic dissolution, given the cathodic potentials of reaction it appears unlikely that the application of reducing potential would increase the rate of metal dissolution in the melt. Full survey spectra are included below, and the relevant atomic composition percentages are summarized in **Table A.3**, showing that in all cases metal content decreased below the surface of the electrolyte.

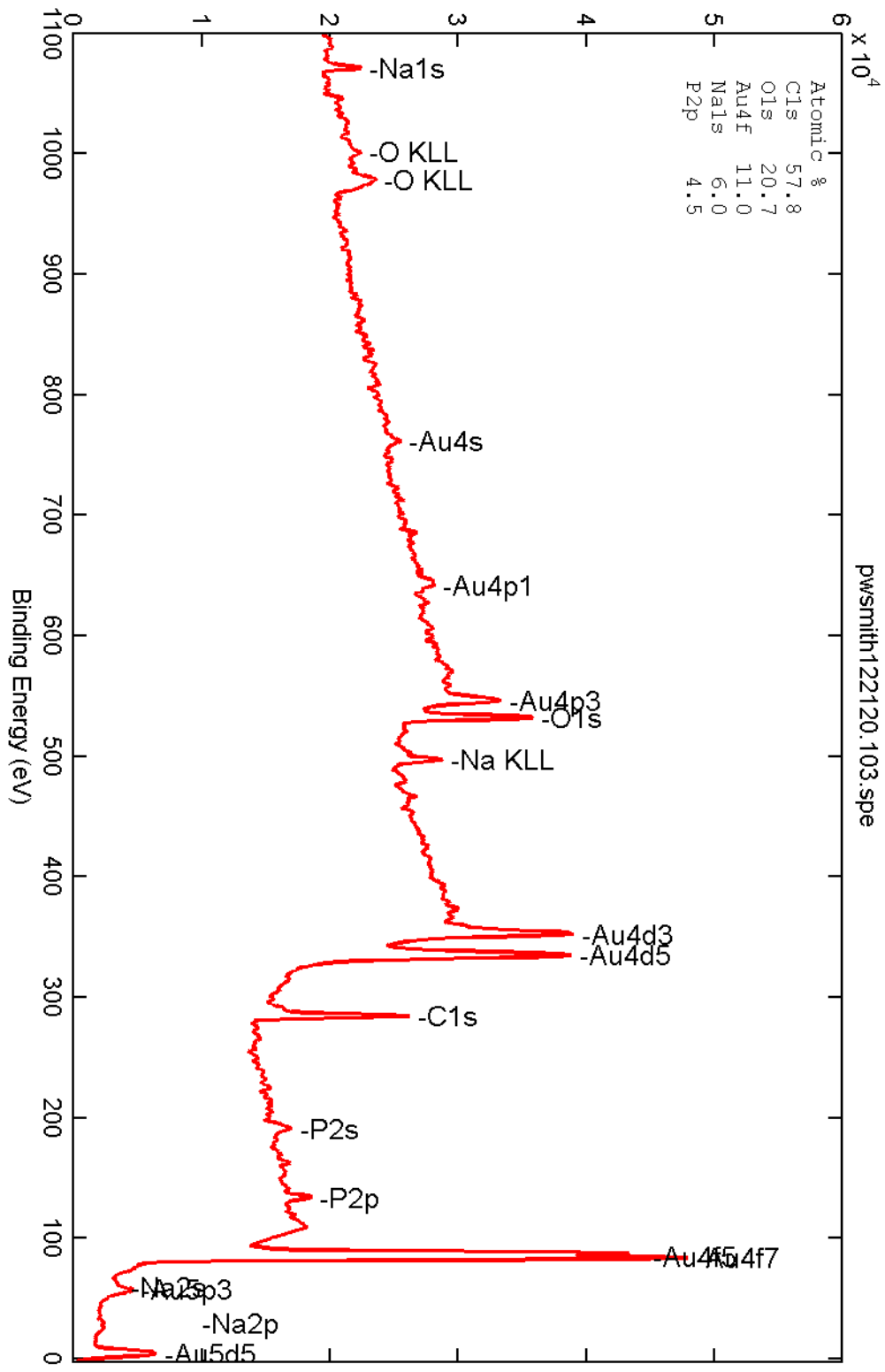

Figure A-14. Survey X-ray photoelectron spectrum of Au-plated graphite electrode at a point not immersed in sodium trimetaphosphate melt.

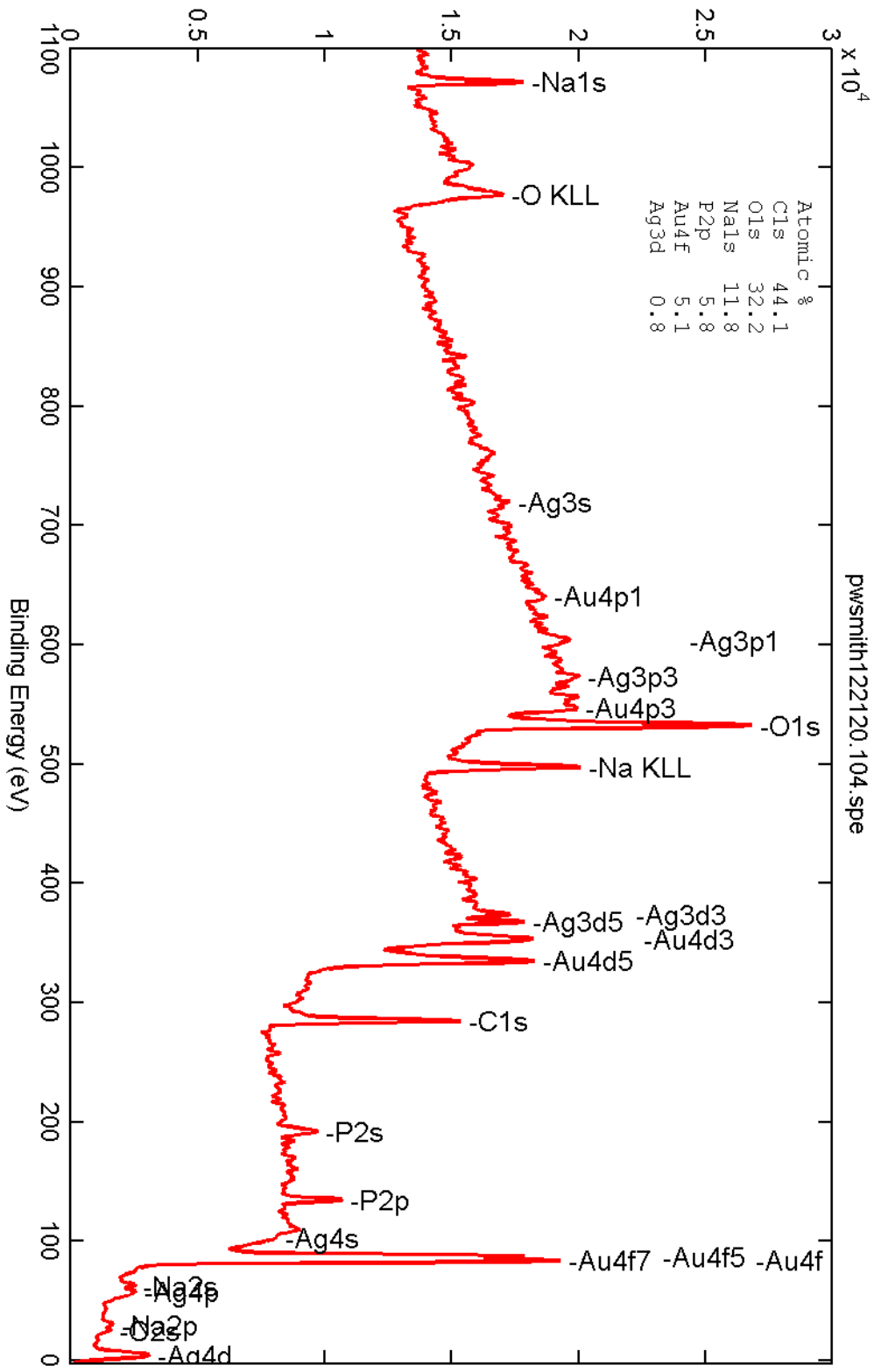

Figure A-15. Survey X-ray photoelectron spectrum of Au-plated graphite electrode in sodium trimetaphosphate melt.

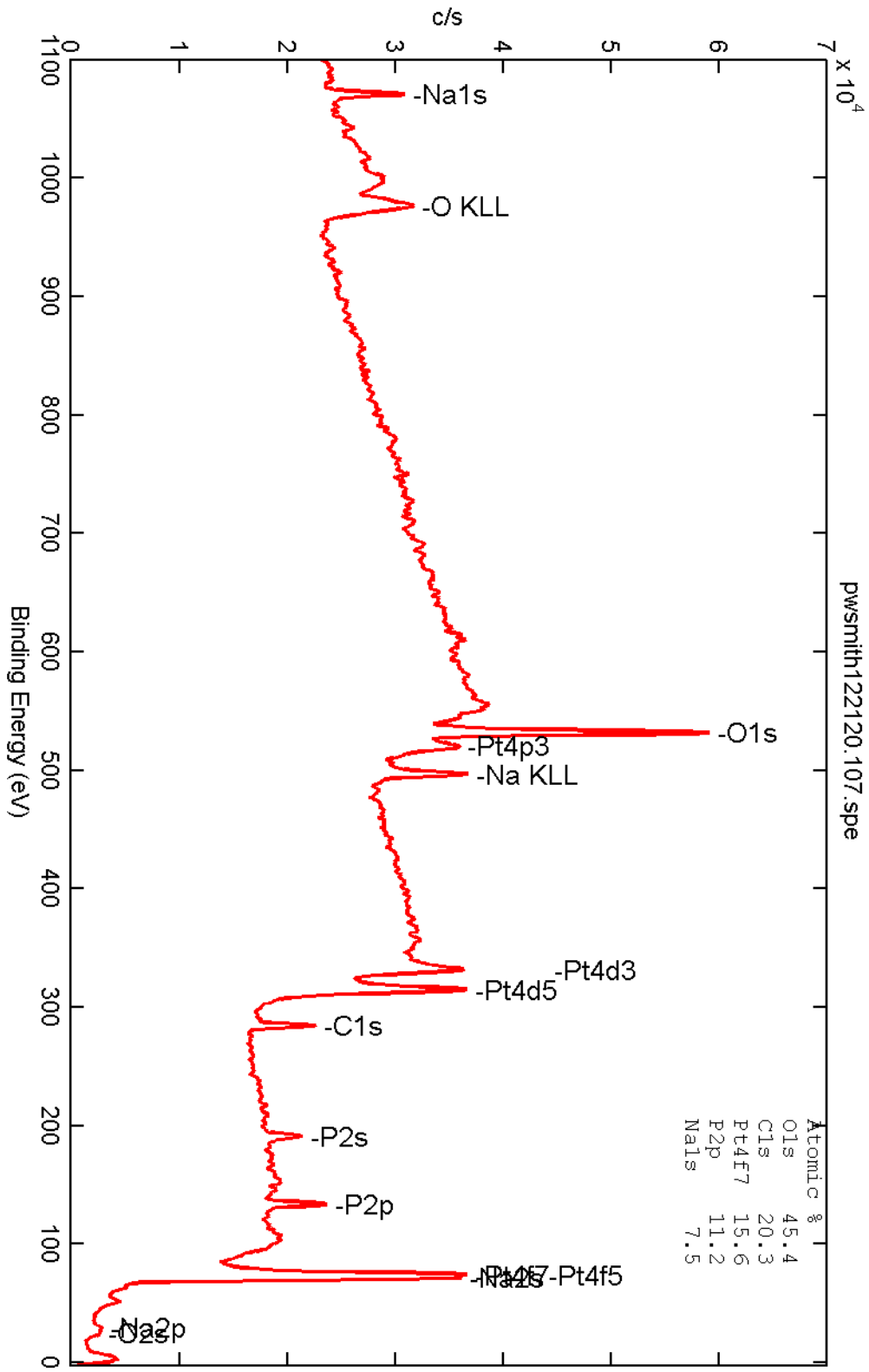

Figure A-16. Survey X-ray photoelectron spectrum of Pt-plated graphite electrode at a point not immersed in sodium trimetaphosphate melt.

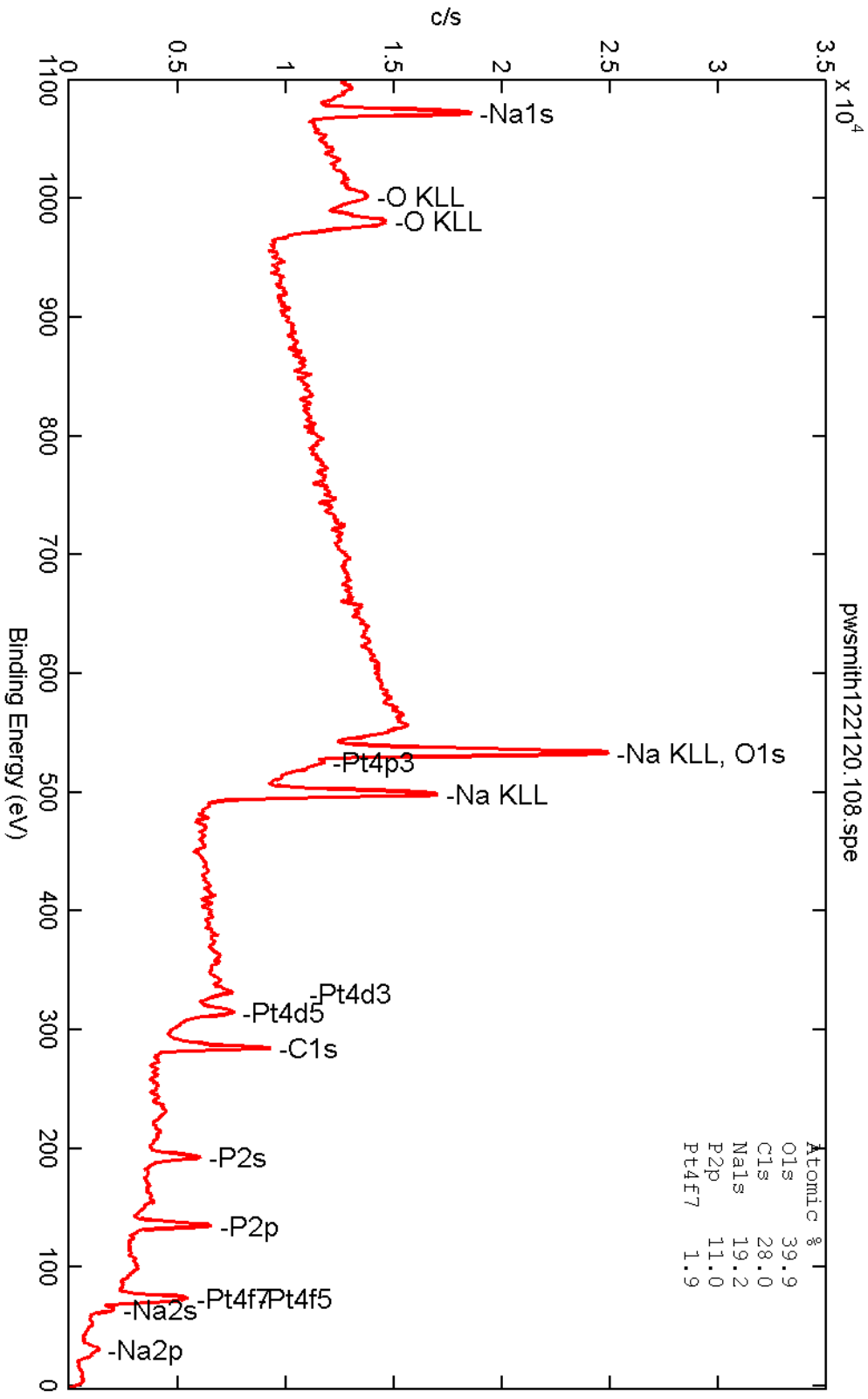

Figure A-17. Survey X-ray photoelectron spectrum of Pt-plated graphite electrode in sodium trimetaphosphate melt.

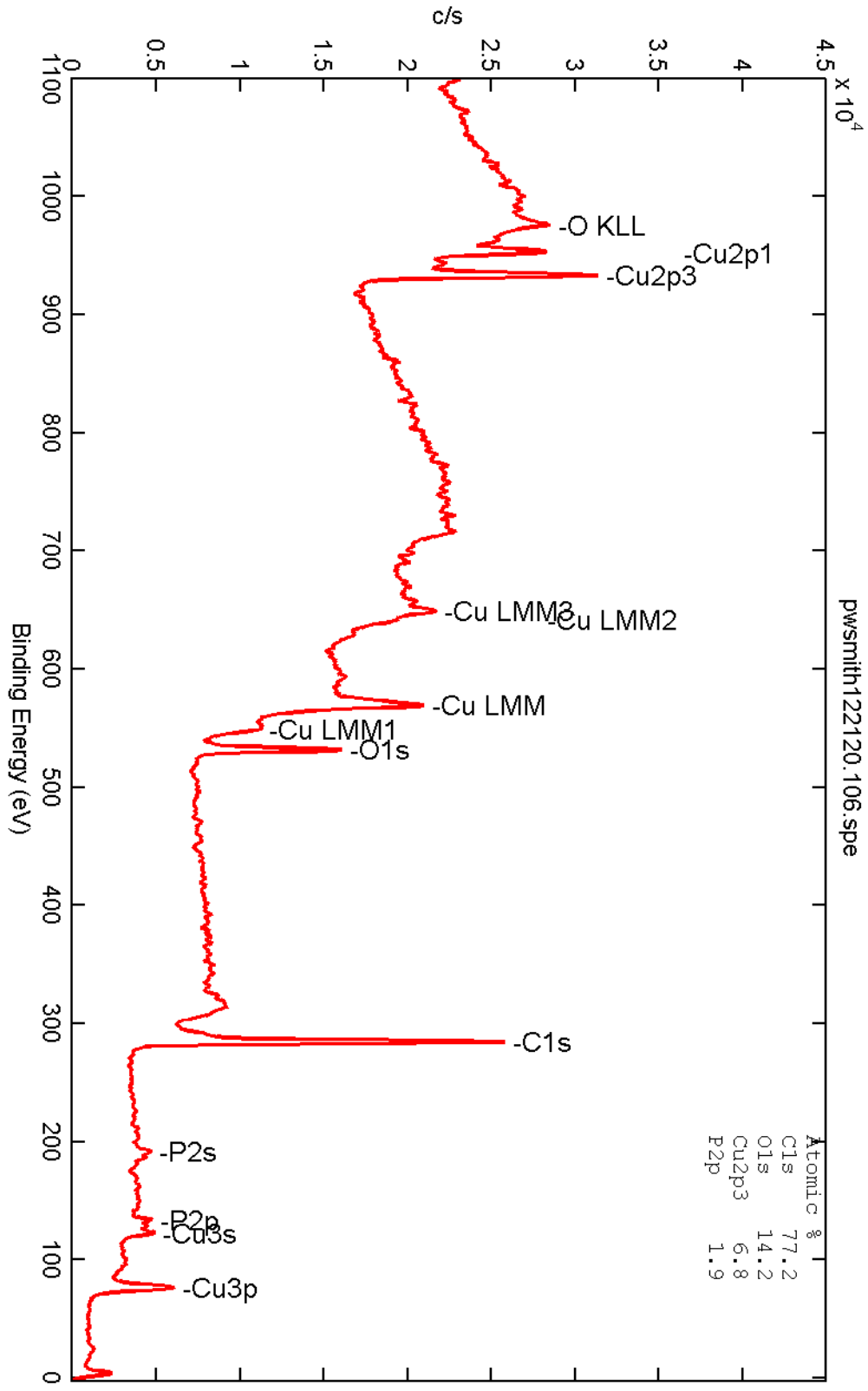

Figure A-18. Survey X-ray photoelectron spectrum of Cu-plated graphite electrode at a point not immersed in sodium trimetaphosphate melt.

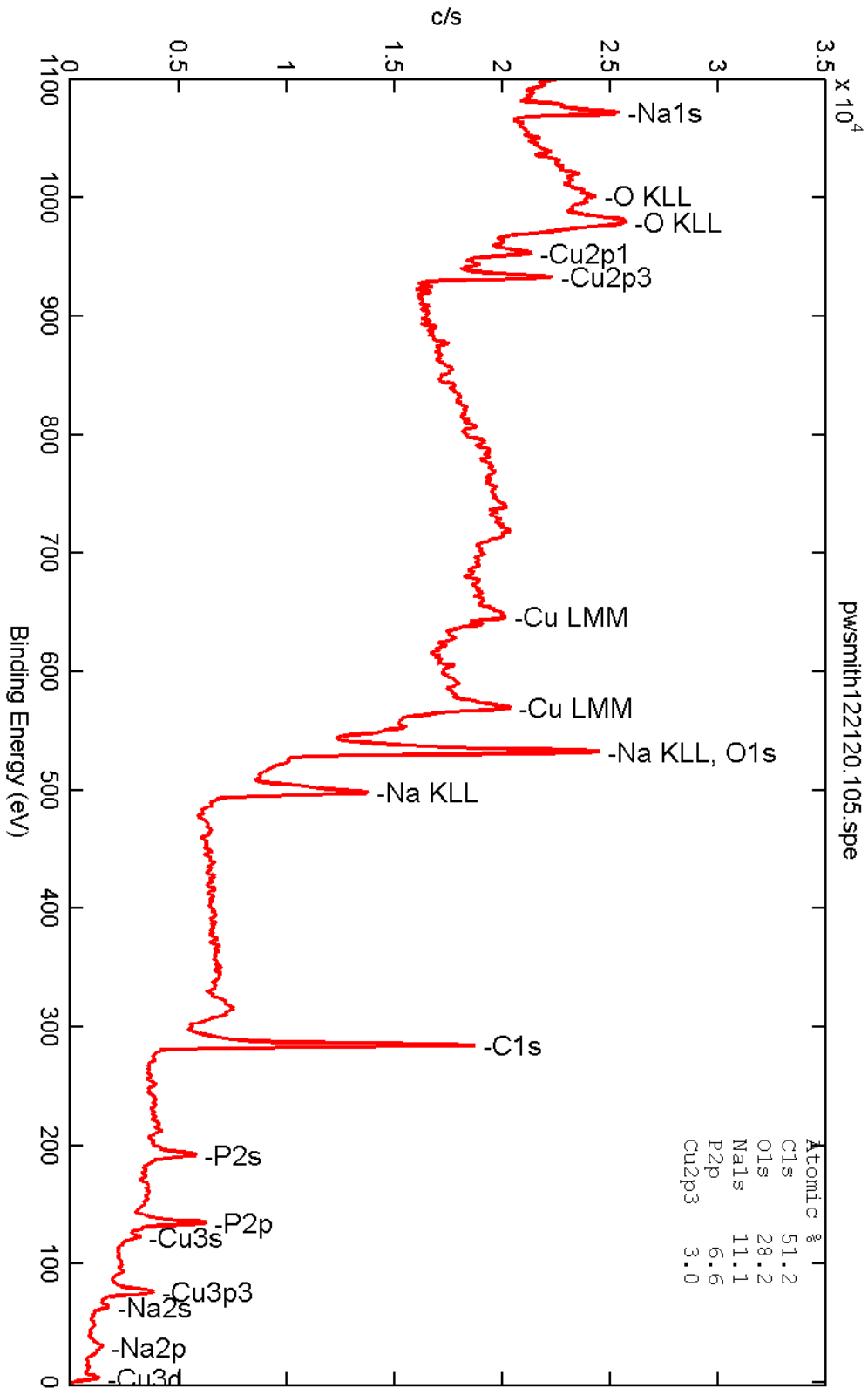

Figure A-19. Survey X-ray photoelectron spectrum of Cu-plated graphite electrode in sodium trimetaphosphate melt.

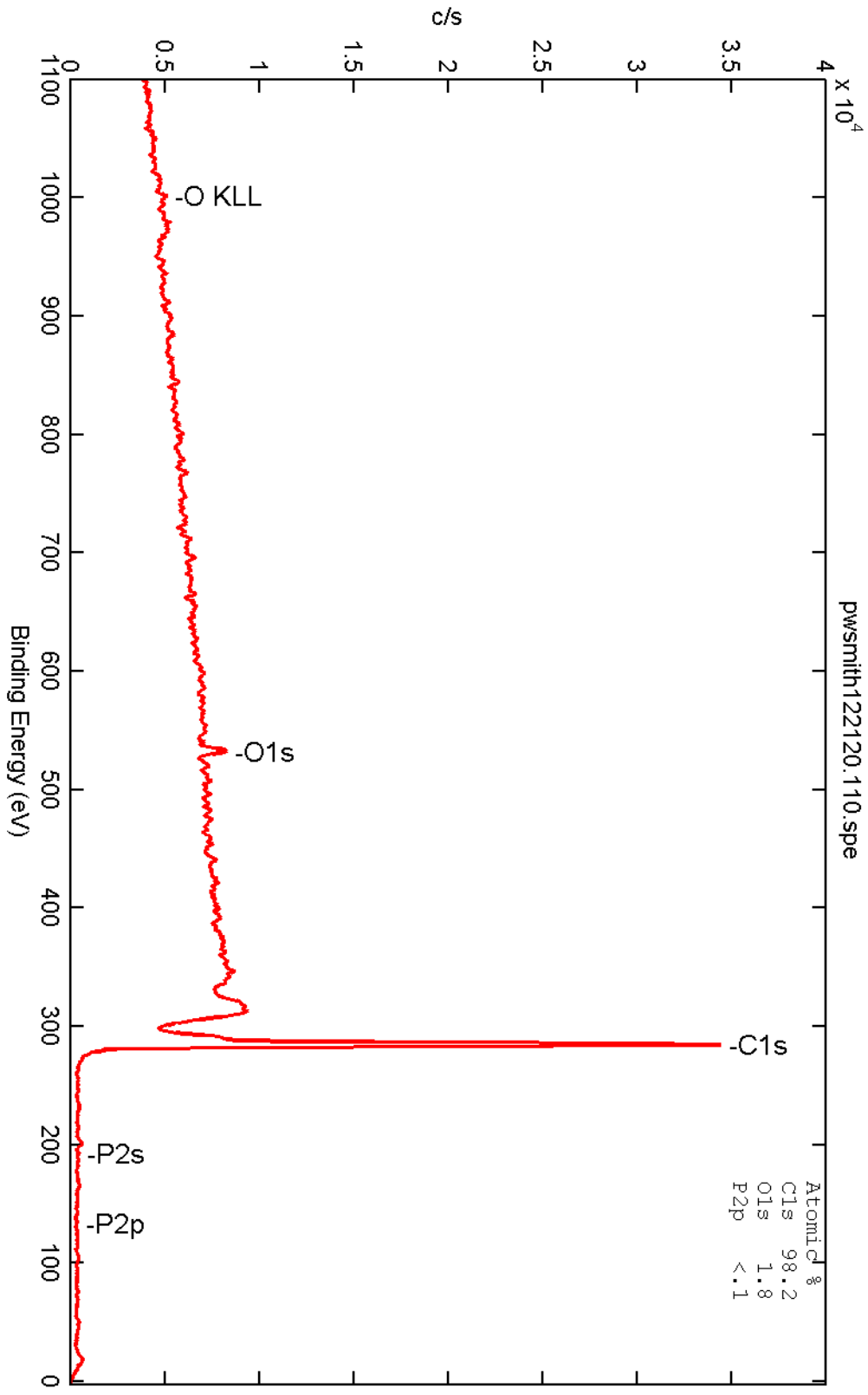

Figure A-20. Survey X-ray photoelectron spectrum of unmodified graphite electrode at a point not immersed in sodium trimetaphosphate melt.

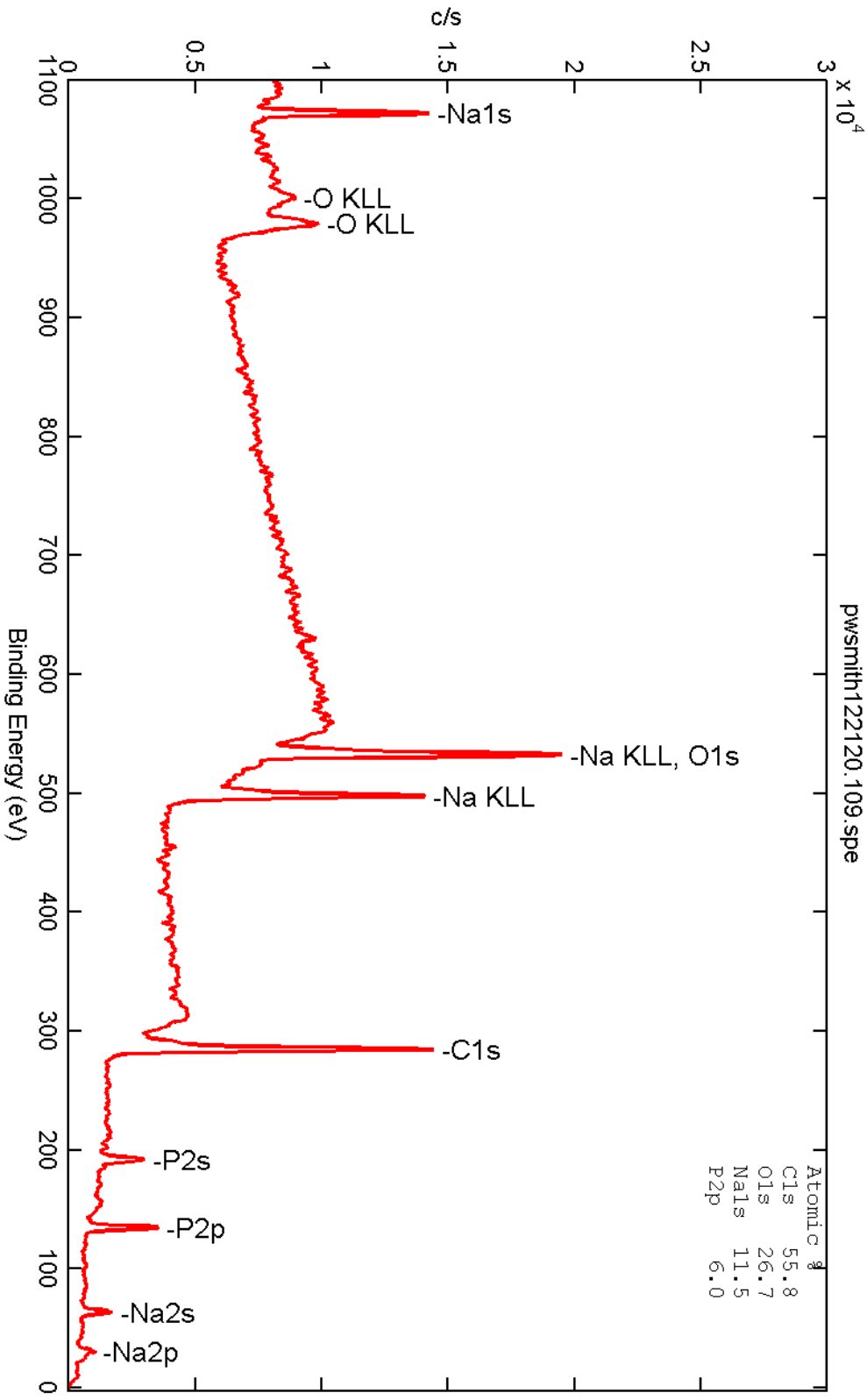

Figure A-21. Survey X-ray photoelectron spectrum of unmodified graphite electrode in sodium trimetaphosphate melt.

References

[1] Greenfield, S.; Clift, M. *Analytical Chemistry of the Condensed Phosphates*; Pergamon: Oxford, 1975.

[2] Britz, D. *J. Electroanal. Chem. Interf. Electrochem.* **1978**, *88*, 309–352.

[3] Bewick, A. *Electrochim. Acta* **1968**, *13*, 825–830.

[4] Mohamady, S.; Taylor, S. D. *Org. Lett.* **2013**, *15*, 2612–2615.

[5] Shepard, S. M.; Cummins, C. C. *J. Am. Chem. Soc.* **2019**, *141*, 1852–1856.

[6] Delimarskii, Y. K.; Andreeva, V. N. *Zh Neorg Khim* **1960**, *5*, 1800–1805.

[7] Caton, R. D.; Freund, H. *Anal. Chem.* **1963**, *35*, 2103–2108.

[8] Caldwell, A. H.; Lai, E.; Gmitter, A. J.; Allanore, A. *Electrochimica Acta* **2016**, *219*, 178–186.

Appendix B

Supplementary Information on High-Pressure Nitrogen Reduction

Contents

B.1 Colorimetric and Spectroscopic Methods for Ammonia Quantification

Several methodologies were assessed for determining the concentration of dissolved ammonia in the electrolyte of NRR cells.

B.1.1 Nessler Method

B.1.1.1 Colorimetric Methodology

To 750 µL of sample was added 25 µL of Nessler's reagent (0.09 M $K_2[HgI_4]$ in 2.5 M aq. KOH, Sigma-Aldrich) and mixed well. Color develops rapidly and the solution was let to stand for no more than 5 minutes before collecting a UV/Vis spectrum and reading absorbance at 430 nm. If the solution is let to sit for more than 20-30 minutes, a brown precipitate of $HgO \cdot Hg(NH_2)I$ may form, especially at high concentrations of ammonia; this will detract from the accuracy of the measurement and must be avoided.

B.1.1.2 Calibration Curve

A calibration series (**Figure B-1**) was constructed spanning a concentration range up to 1 mM and a calibration curve (**Figure B-3**) was constructed from absorbance values at 430 nm. The calibration curve was fitted to a linear regression by least-squares method ($r^2 = 0.999$) within the range 0 µM to 250 µM; analyte samples with ammonia concentrations greater than 250 µM were first sequentially diluted into this range before assessment by the linear fit:

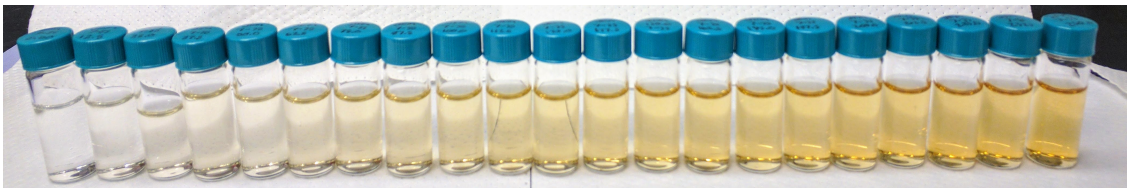

Figure B-1. Calibration series for ammonia colorimetry by Nessler method.

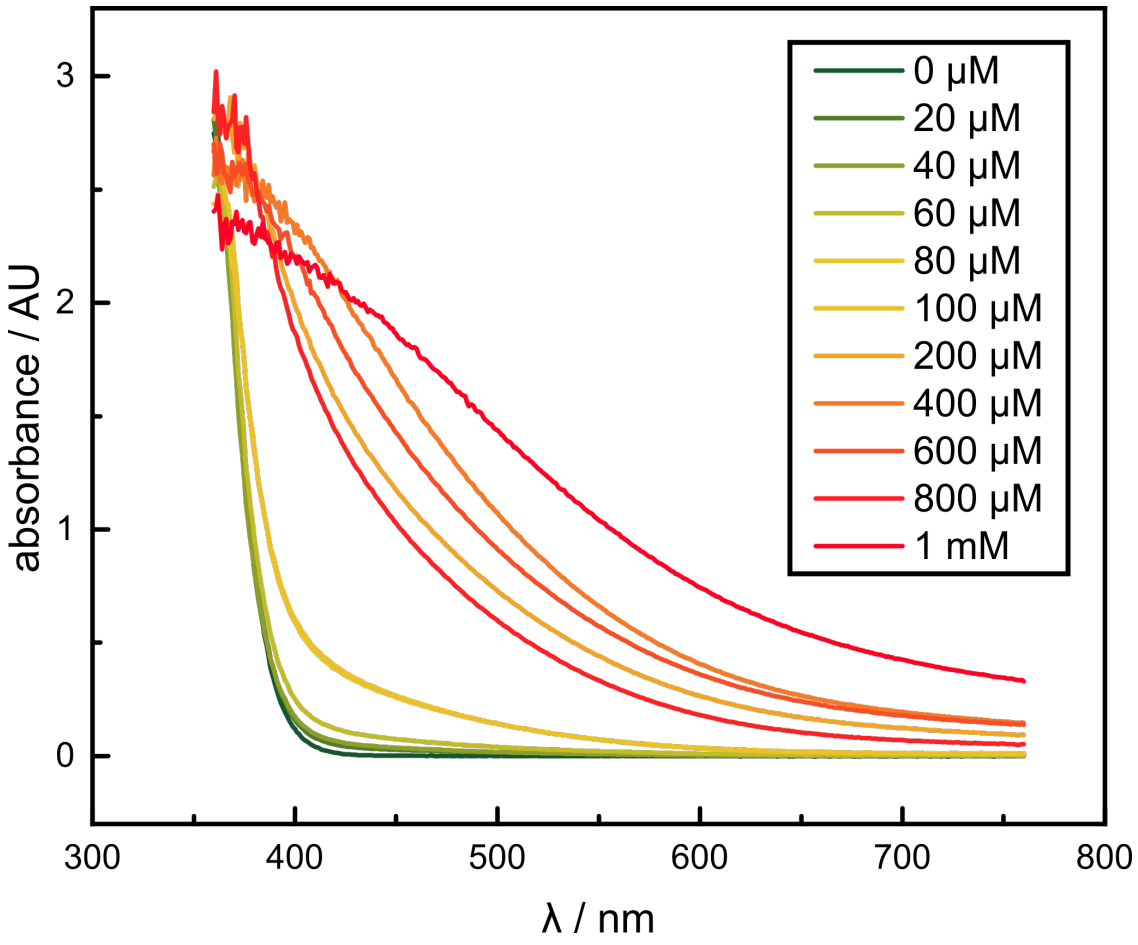

Figure B-2. Representative UV/Vis spectra for ammonia colorimetry by Nessler method.

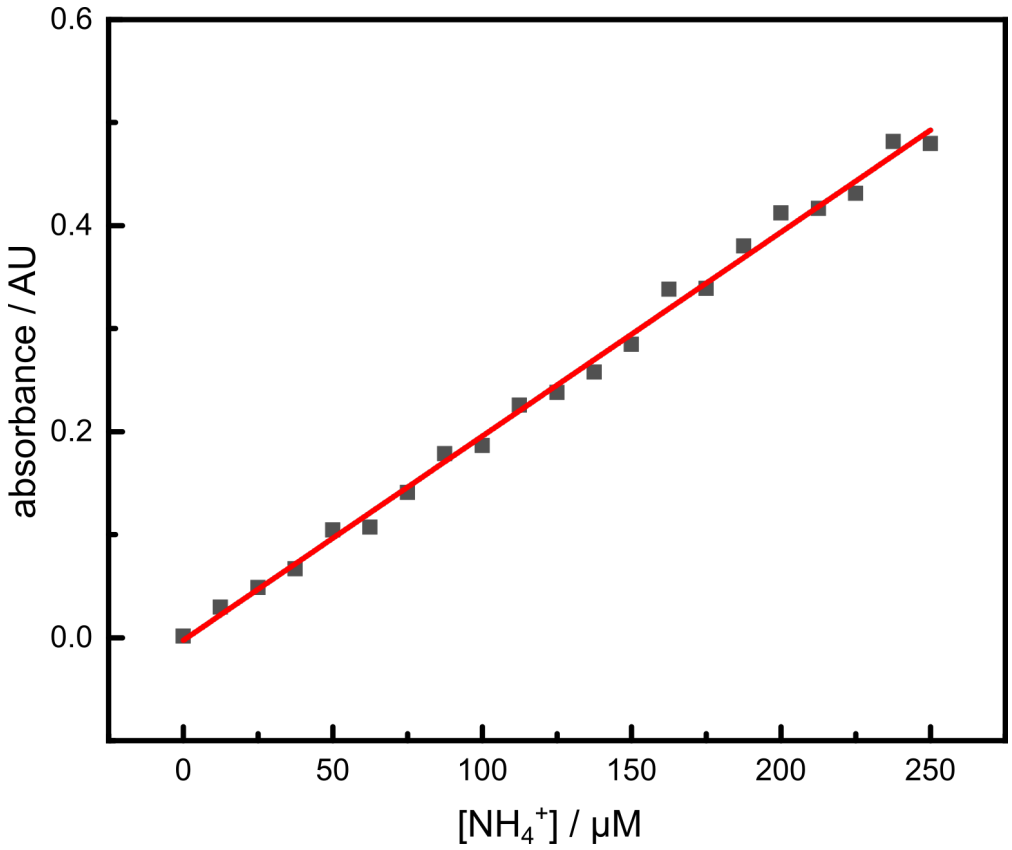

Figure B-3. Calibration curve for ammonia colorimetry by Nessler method. Pearson's $r^2 = 0.999$.

$$A = 0.0019664 \times [NH_3], \tag{B.1}$$

where A is absorbance (AU) and $[NH_3]$ is the concentration of dissolved ammonia in µM.

The sensitivity of Nessler's reagent as a spot test for ammonia was found to be approximately 100 µM, and the lower detection limit was found to be approximately 10 µM. Owing to the rapid rate of color development and the facility of the colorimetric preparation, this methodology was the primary metric utilized for assessing ammonia content of sampled timepoints in this work, although the produced solutions are not stable for extended periods and, due to their mercury content, require special disposal processes.

B.1.2 Phenate Method

B.1.2.1 Colorimetric Methodology

Reagent solutions were preprepared in the following stoichiometry:

- A citrate buffer solution was created by combining 3 g sodium citrate tribasic ($\geq$ 99.0%, Sigma-Aldrich) with 150 mg sodium hydroxide (semiconductor grade, 99.99% trace metals basis, Sigma-Aldrich) and dissolving in 15 mL distilled water.
- An oxidizing solution was created by combining 20 µL 5.25 wt% sodium hypochlorite solution (Clorox® brand bleach) with 80 µL citrate buffer solution.

Figure B-4. Calibration series for ammonia colorimetry by phenate method.

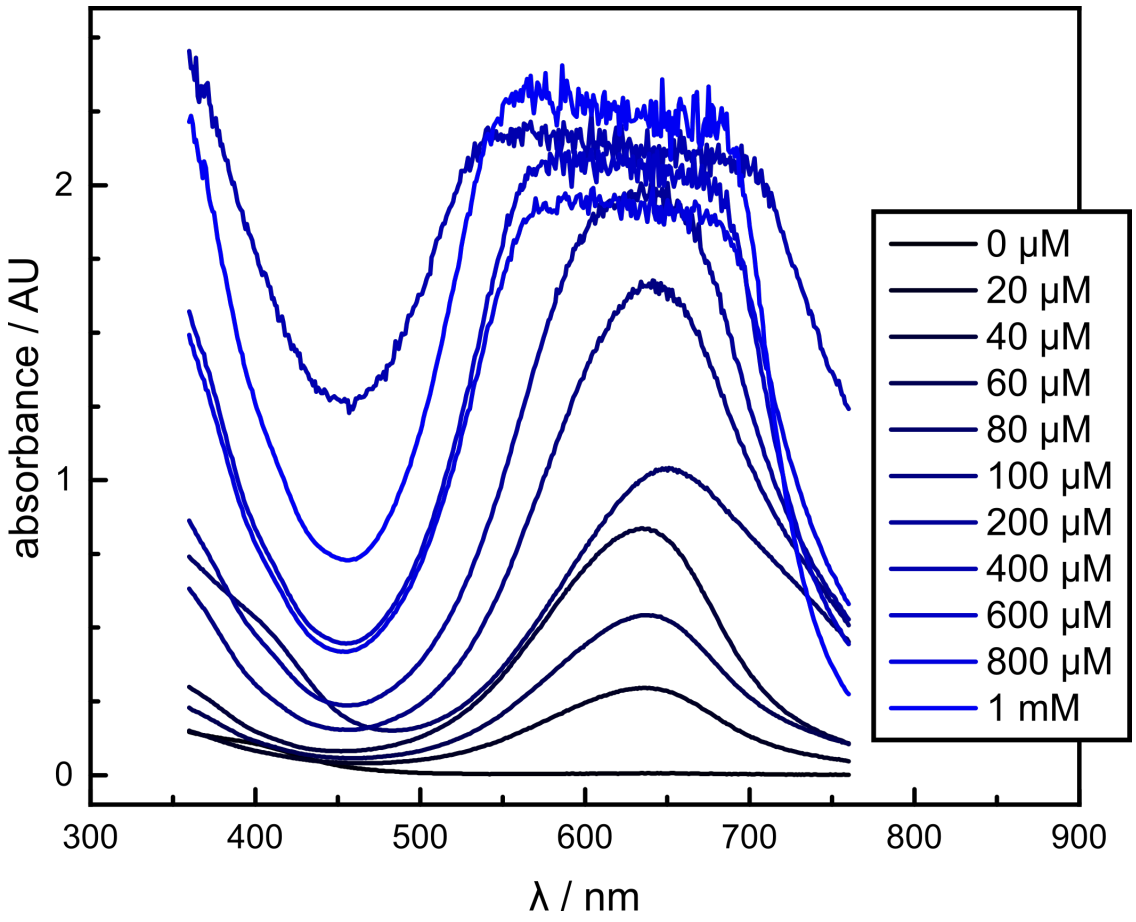

Figure B-5. Representative UV/Vis spectra for ammonia colorimetry by phenate method.

- A phenol solution was created by dissolving 1.5 g phenol (≥99.0%, Sigma-Aldrich) in 15 mL ethanol.
- A nitroprusside solution was solution was created by dissolving 75 mg sodium nitroprusside dihydrate (≥99%, puriss. p.a., Sigma-Aldrich) in 15 mL distilled water.

To 1 mL of analytical sample was added 40 µL phenol solution, 40 µL nitroprusside solution, and 100 µL oxidizing solution. The sample was mixed well and let sit in darkness for 1-3 hours before collecting a UV/Vis spectrum and reading absorbance at 630 nm.

B.1.2.2 Calibration Curve

A calibration series (**Figure B-4**) was constructed spanning a concentration range up to 1 mM and a calibration curve (**Figure B-6**) was constructed from absorbance values at

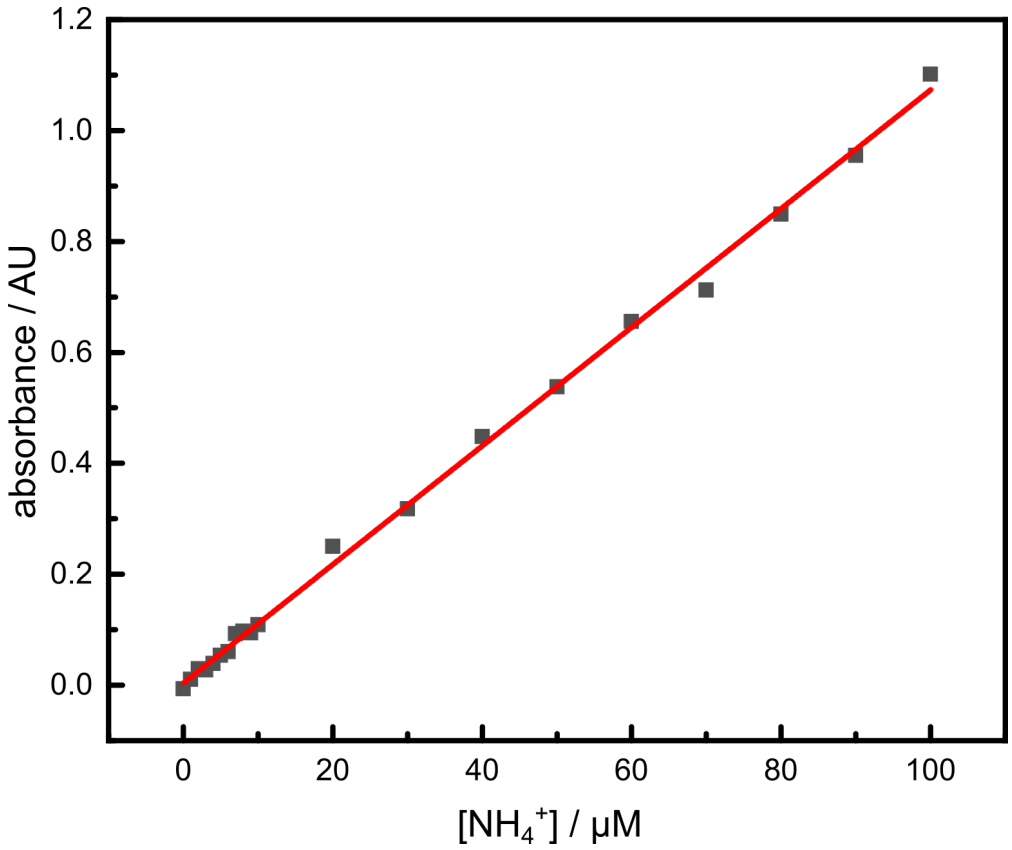

Figure B-6. Calibration curve for ammonia colorimetry by phenate method. Pearson's $r^2 = 0.999$.

630 nm. The calibration curve was fitted to a linear regression by least-squares method ($r^2 = 0.999$) within the range 0 µM to 100 µM; analyte samples with ammonia concentrations greater than 100 µM were first sequentially diluted into this range before assessment by the linear fit:

$$A = 0.0106242 \times [NH_3], \tag{B.2}$$

where A is absorbance (AU) and $[NH_3]$ is the concentration of dissolved ammonia in µM.

The lower detection limit for ammonia using the phenate method was found to be approximately 1 µM. Owing to the involved colorimetric preparation and the comparatively slow rate of color development, application of the phenate method was limited to circumstances in which the stability of the produced analyte samples, the enhanced ammonia sensitivity (about fivefold with respect to the Nessler method), or an appreciation for the sheer loveliness of the evolved deep-blue color (about a million times with respect to the ochrous Nessler method) was deemed necessary.

B.1.3 Methods for Quantitative NMR

B.1.3.1 Ammonia Capture in Sulfuric Acid

The reactor headspace was slowly sparged through a coarse glass frit immersed in 3 mL concentrated sulfuric acid in a 50 mL pear-shaped flask (**Figure B-7**). During this process, the reactor was intermittently sonicated to promote desolvation of ammonia from the electrolyte. A 500 µL aliquot of sulfuric acid was taken, to which was added 25 µL dimethylsulfoxide for use as an internal standard for quantitation.

B.1.3.2 Ammonium Quantitation by NMR

NMR spectra were recorded with Bruker AVANCE-400 spectrometers and processed using MestReNova software. Spectra were collected in protic $H_2SO_4 - h_2$ using a Norell®

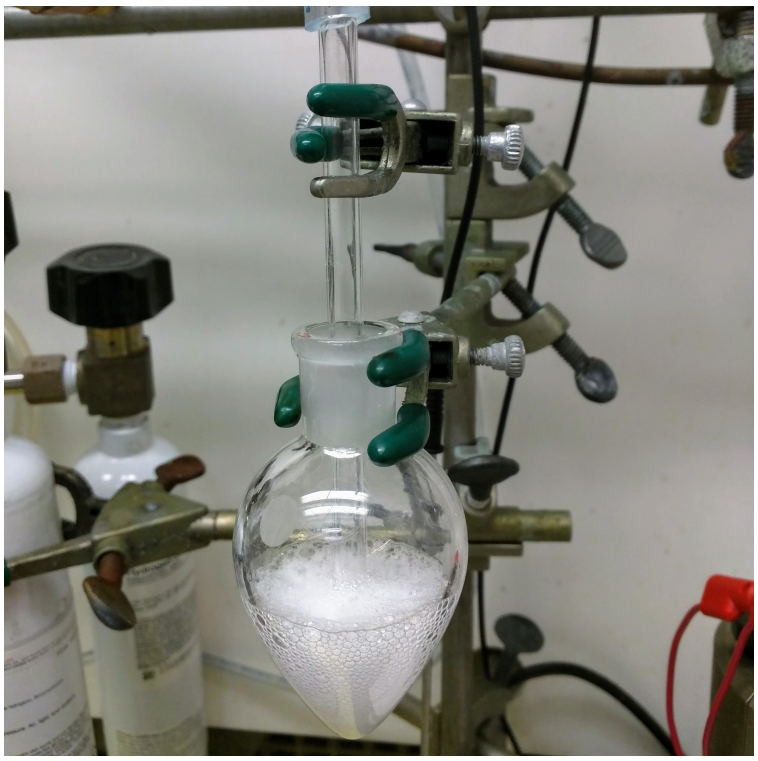

Figure B-7. Sulfuric acid sparge trap for ammonia capture and quantification by ^{1}H NMR.

#NI5CCI-B coaxial NMR insert tube filled with D_2O as a lock solvent.

This method was unable to capture a significant portion of solvated ammonia in the electrolyte solution, and the lower detection limit for ammonium of about 25 µM compared unfavorably with that of the aforementioned colorimetric preparations. For this reason, ^{1}H NMR was not utilized for ammonia quantitation purposes, though it still served an important purpose in product identification due to the characteristic 1:1:1 triplet ^{1}H NMR signal of the $^{14}NH_4^+$ ion, especially as distinguished from the isotope-labeled 1:1 double ^{1}H NMR signal of the $^{15}NH_4^+$ ion.

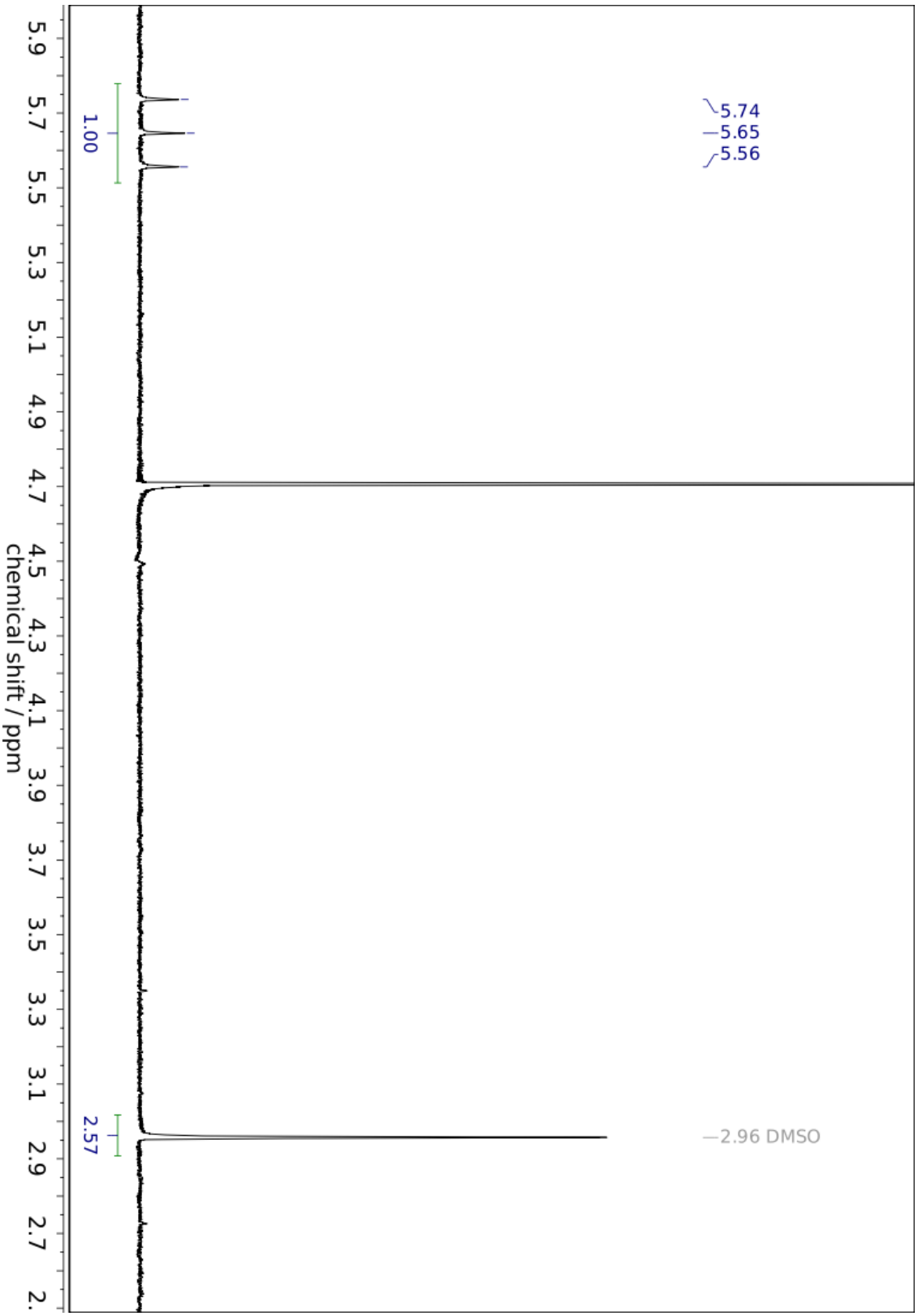

Figure B-8. Representative ^{1}H NMR spectrum of vented NH_4^+ captured in H_2SO_4 trap.

B.2 Evaluation of Copper Nitride Stability

B.2.1 Decomposition of Copper Nitride under Vacuum

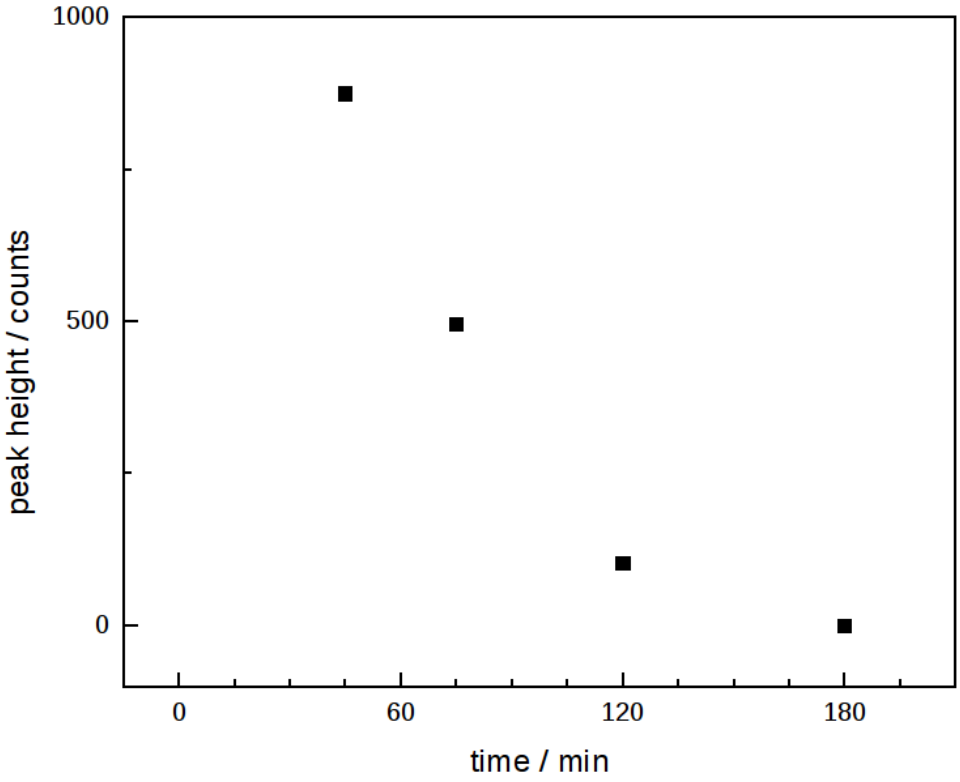

Figure B-9. Peak height of XPS nitride signal for Cu_3N foil prepared by sodium amide prep as a function of time under vacuum.

The copper nitride catalyst was found to decompose under the ultra-high vacuum ($< 1 \times 10^{-8}$ torr) conditions of the Thermo Scientific K-Alpha+ XPS instrument, limiting the utility of this measurement to identify trace nitride signals as may have been generated by NRR catalysis on copper metal.

B.2.2 Hydrolysis of Copper Nitride

Cu_3N was found to hydrolyse in aqueous conditions to produce ammonia, in accordance with the stoichiometry:

$$2\,Cu_3N + 6\,H_2O + 6\,OH^- \longrightarrow 6\,Cu(OH)_2 + 2\,NH_3 \tag{B.3}$$

In order to account for this decomposition and to deconvolute its contribution to ammonia generation during electrochemical NRR studies, Cu_3N powders were dispersed in various aqueous solutions to assess the rate of copper nitride hydrolysis.

10 mg of copper nitride as prepared by the sodium amide method (**Section 3.4.4.1** on page 143) were dispersed in either 10 mL of distilled water (pH 7) or 1 M aqueous KOH solution (pH 14). These dispersions were stirred for 72 hours at temperatures of either 25 °C, 50 °C, or 75 °C, and timepoints were intermittently taken off, strained by syringe filter, and quantitated colorimetrically by the Nessler method (**Appendix B.1.1** on page 226). The resulting plots, **Figure B-10**, demonstrate that the rate of nitride hydrolysis increases with temperature and at lower pH values; however, it is substantially lower than the observed rate of ammonia generation in our electrochemical NRR systems.

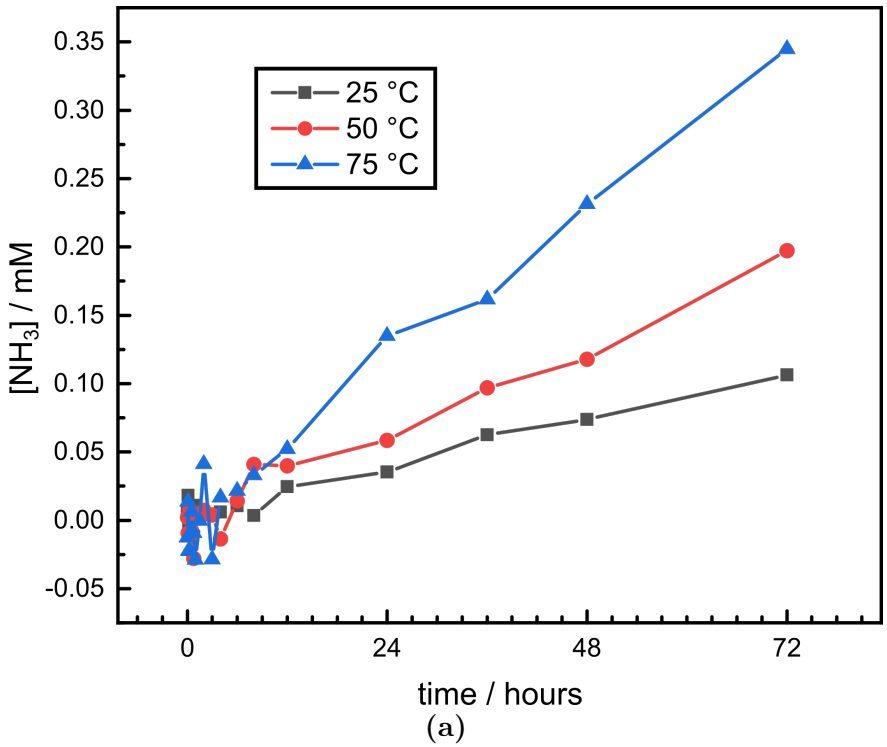

(a)

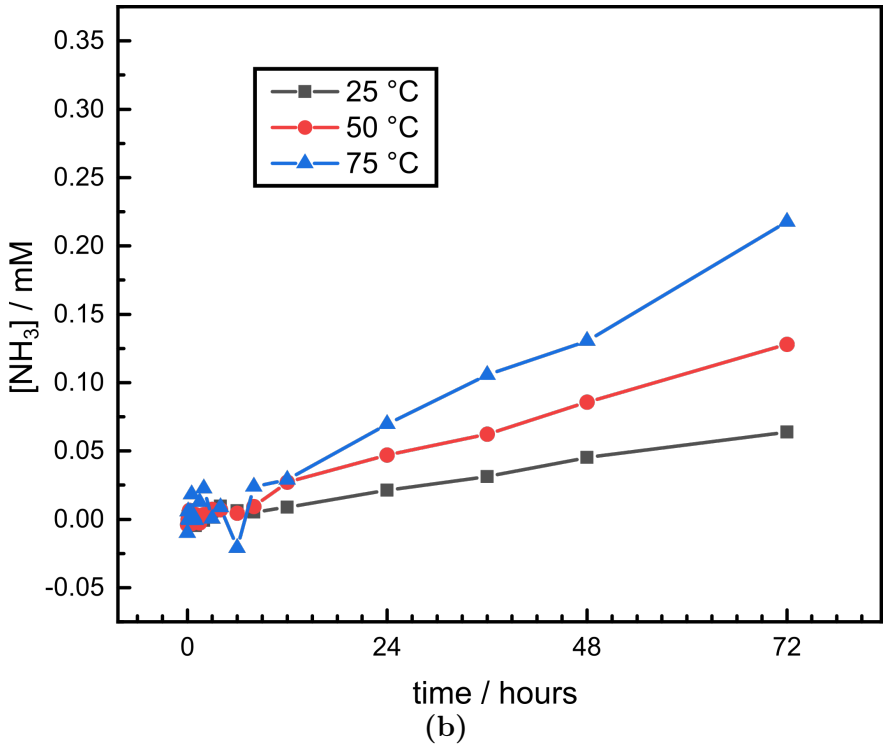

(b)

Figure B-10. Ammonia content over time (determined by Nessler method) of Cu_3N powder synthesized by sodium amide prep soaking in **(a)** distilled water and **(b)** 1 M KOH as a function of temperature.

B.3 Evaluation of Haber-Like Ammonia Formation

The possibility was considered that H_2 gas generated electrochemically by hydrogen evolution reaction might react at elevated pressures with N_2 gas, potentially on the stainless steel walls of the reaction vessel, thereby producing ammonia via a nonfaradaic Haber-like reactivity. To mitigate the potential role of the the metal interior of the cell, the reactor interior was coated in an inert PFA polymer by Donwell Company, Inc. (**Section 3.4.1** on page 139).

To assess the efficacy of this coating and the possibility of Haber-like ammonia generation, three experiments were performed.

B.3.1 Electrochemical Control Experiment

A two-electrode system was set up inside the cell, with a brand-new 63% porous LCS copper foam (CU003804 from Goodfellow USA) used as a working electrode and a platinum mesh counter electrode. The electrolyte was 60 mL 2 M aq. KOH. The cell was pressurized to 1000 psi of N_2 and a fixed current of -5000 mA (approximately -16.7 mA·cm^{-2}) was passed chronopotentiometrically for 12 hours.

Following this experiment, a total of 6.9 µmol of NH_3 were quantitated in the electrolyte medium by Nessler's colorimetric method.

B.3.2 Evolved Hydrogen Experiment

The same two-electrode system as before was set up inside the cell, although no Faradiac current was passed for this experiment. The cell was pressurized with 1000 psi N_2 and 15 psi H_2, the latter being the approximate partial pressure of hydrogen gas that would be evolved following 12 hours of electrolytic hydrogen evolution at a current of -5000 mA (216 coulombs passed). The cell was sonicated for 15 minutes to ensure mixing, then stirred for 12 hours at room temperature.

Following this experiment, a total of 0.0234 nmol of NH_3 were quantitated in the elec-

trolyte medium by the phenate colorimetric method.

B.3.3 Haber-Bosch Experiment

In this experiment, the conditions were set up to be as deliberately favorable for Haber-type reactivity as possible. The same two-electrode system as before was set up inside the cell, although no Faradiac current was passed for this experiment. The cell was pressurized with 667 psi N_2 and 333 psi H_2, a highly active ratio for industrial ammonia forming gas. The cell was sonicated for 15 minutes to ensure mixing, then stirred for 12 hours at 100 °C, to overaccount for the potential for Ohmic heating in the system.

Following this experiment, a total of 0.147 µmol of NH_3 were quantitated in the electrolyte medium by the phenate colorimetric method.

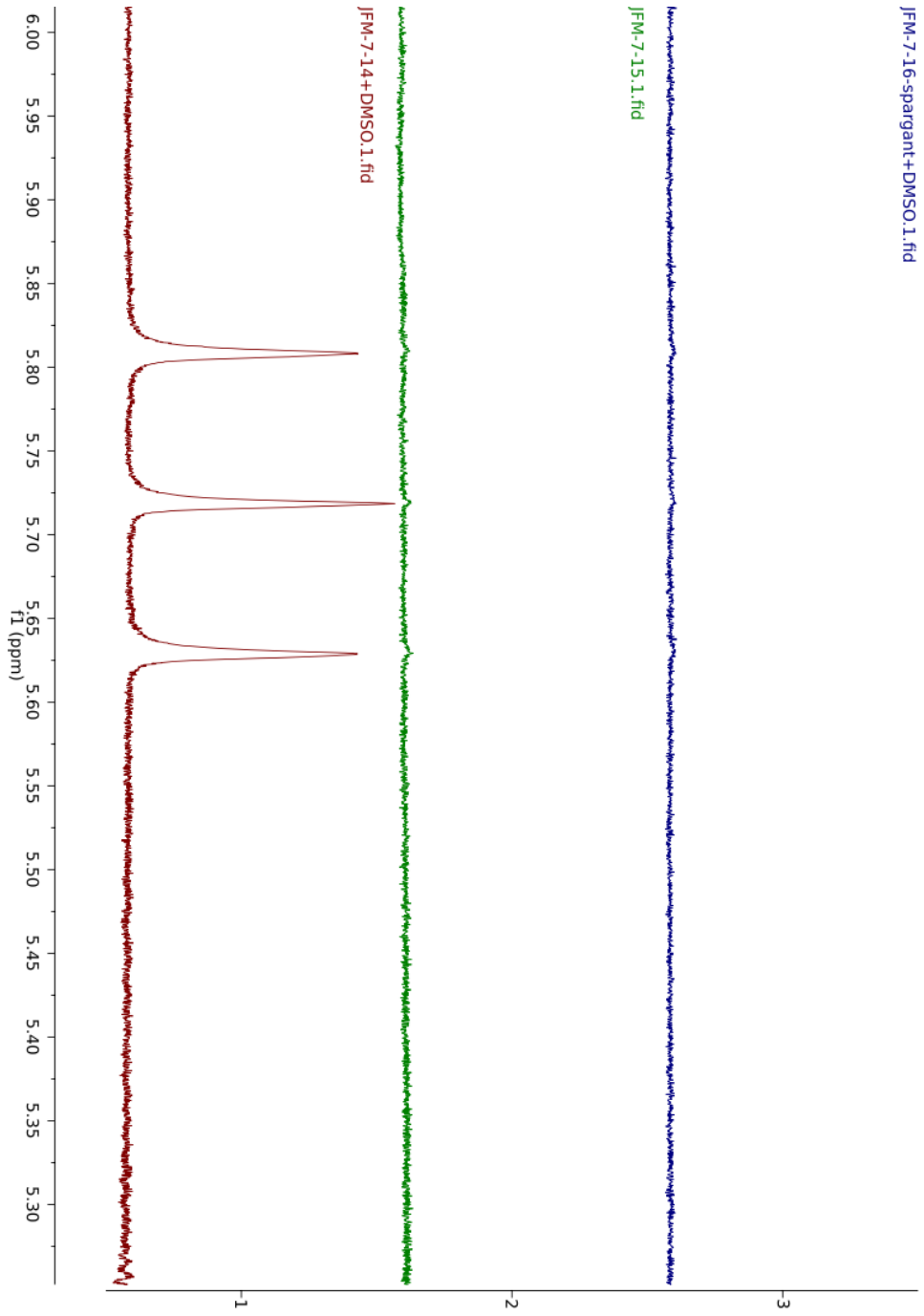

Figure B-11. ^{1}H NMR spectra of Haber formation control experiments. **(red)** Current passed potentiostatically at $-5000\,\mathrm{mA}$ for 12 hours. **(green)** No current passed, 2:1 mixture of N_2:H_2 heated at 100 °C for 12 hours. **(blue)** No current passed, 1.5% mixture of H_2 in N_2 let sit for 12 hours.

B.4 X-Ray Photoelectron Spectroscopy of NRR Electrodes

X-ray photoelectron spectroscopy data collected on Thermo Scientific K-Alpha+ XPS with Al k-αmicro-focused monochromated x-ray source (30 µm to 400 µm spot size). Argon-ion sputtering was performed by built in ion gun at 1 keV for 5-minute increments. Survey spectra are averaged over 5 spectra, elemental spectra are averaged over 50 spectra.

B.4.1 Copper Metal

B.4.1.1 Fresh Copper Electrode

Data collected on a brand-new 63% porous LCS copper foam (CU003804 from Goodfellow USA).

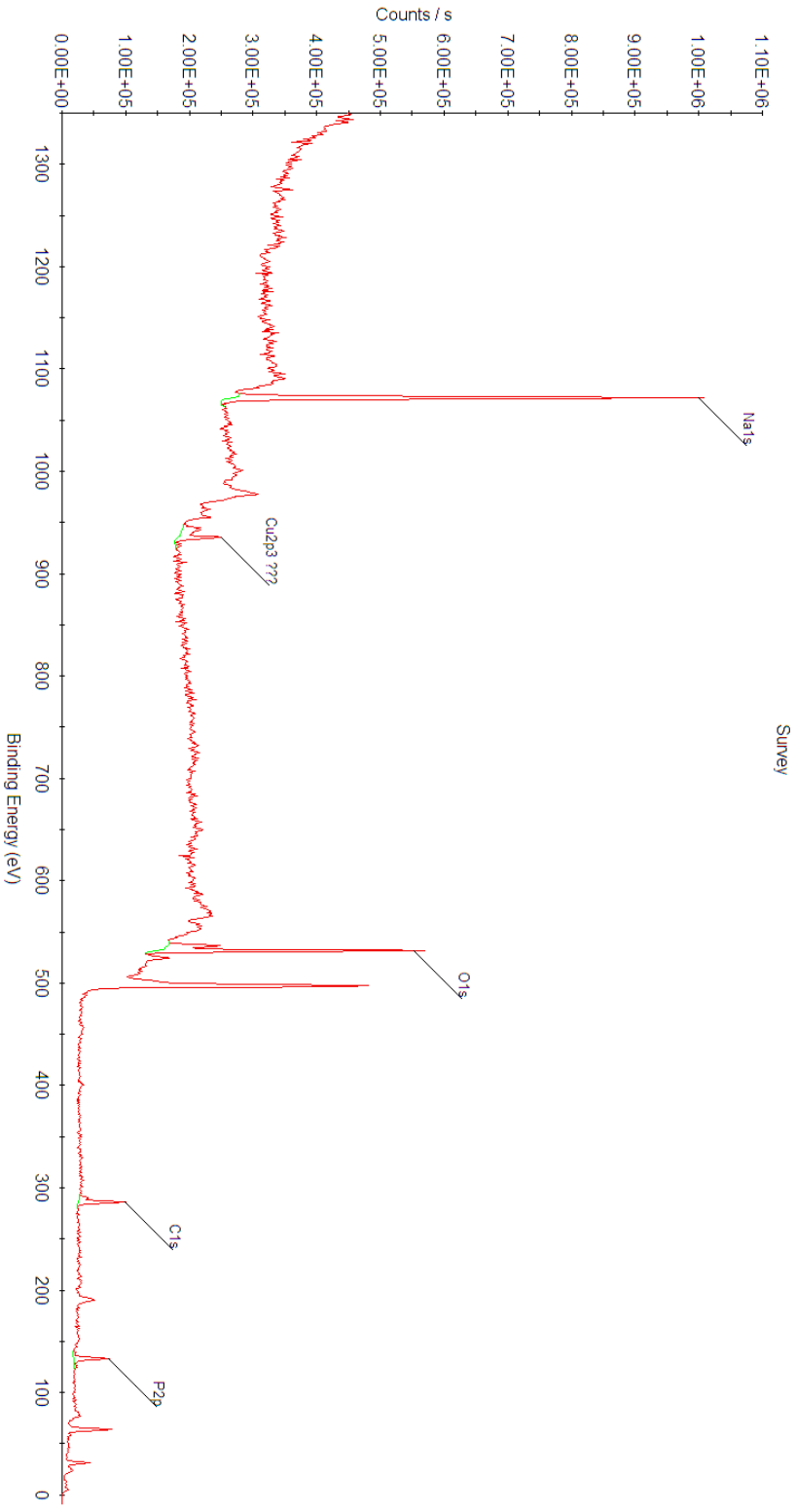

Figure B-12. Survey x-ray photoelectron spectrum of fresh Cu electrode.

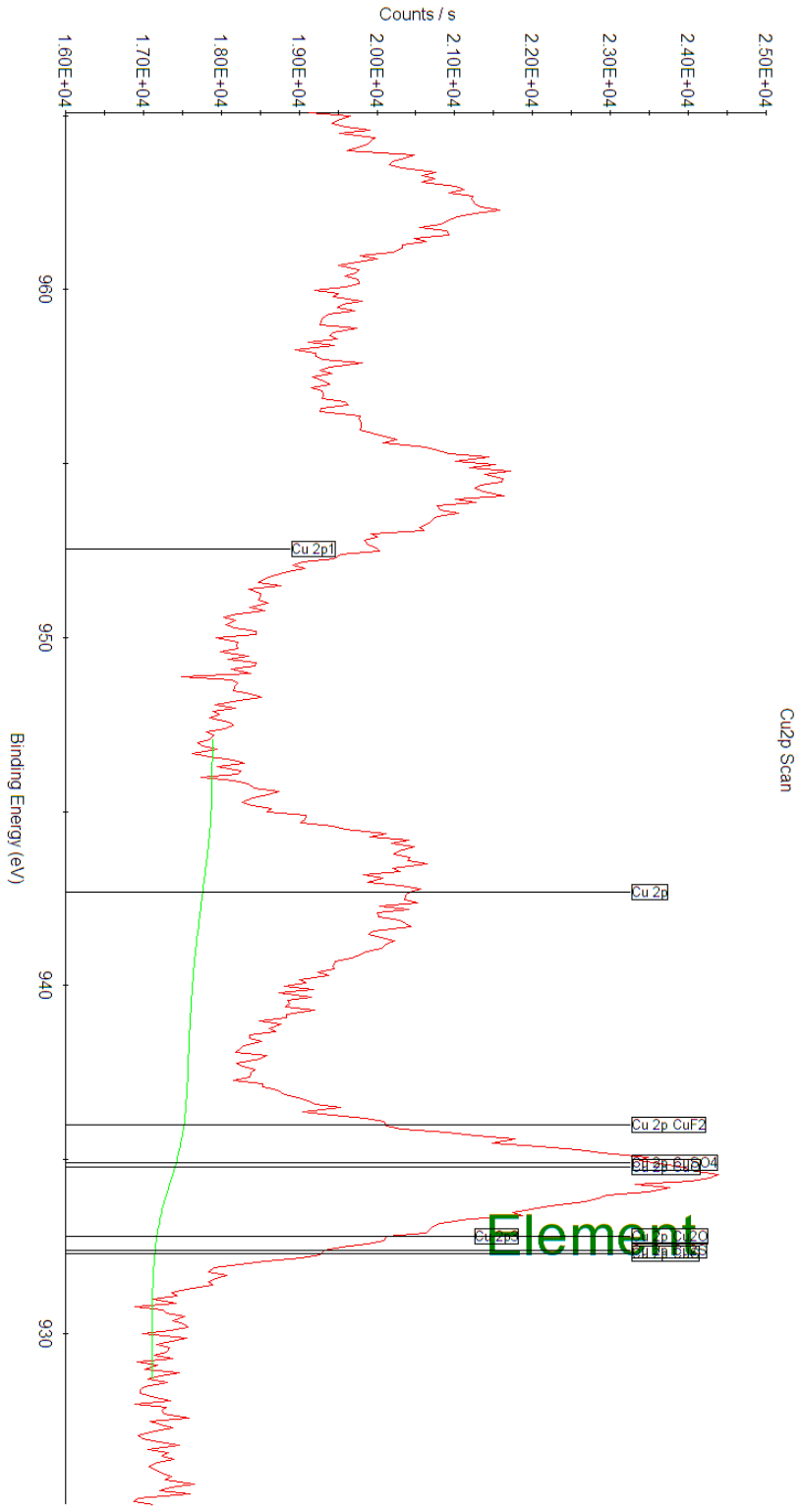

Figure B-13. Copper 2p x-ray photoelectron spectrum of fresh Cu electrode.

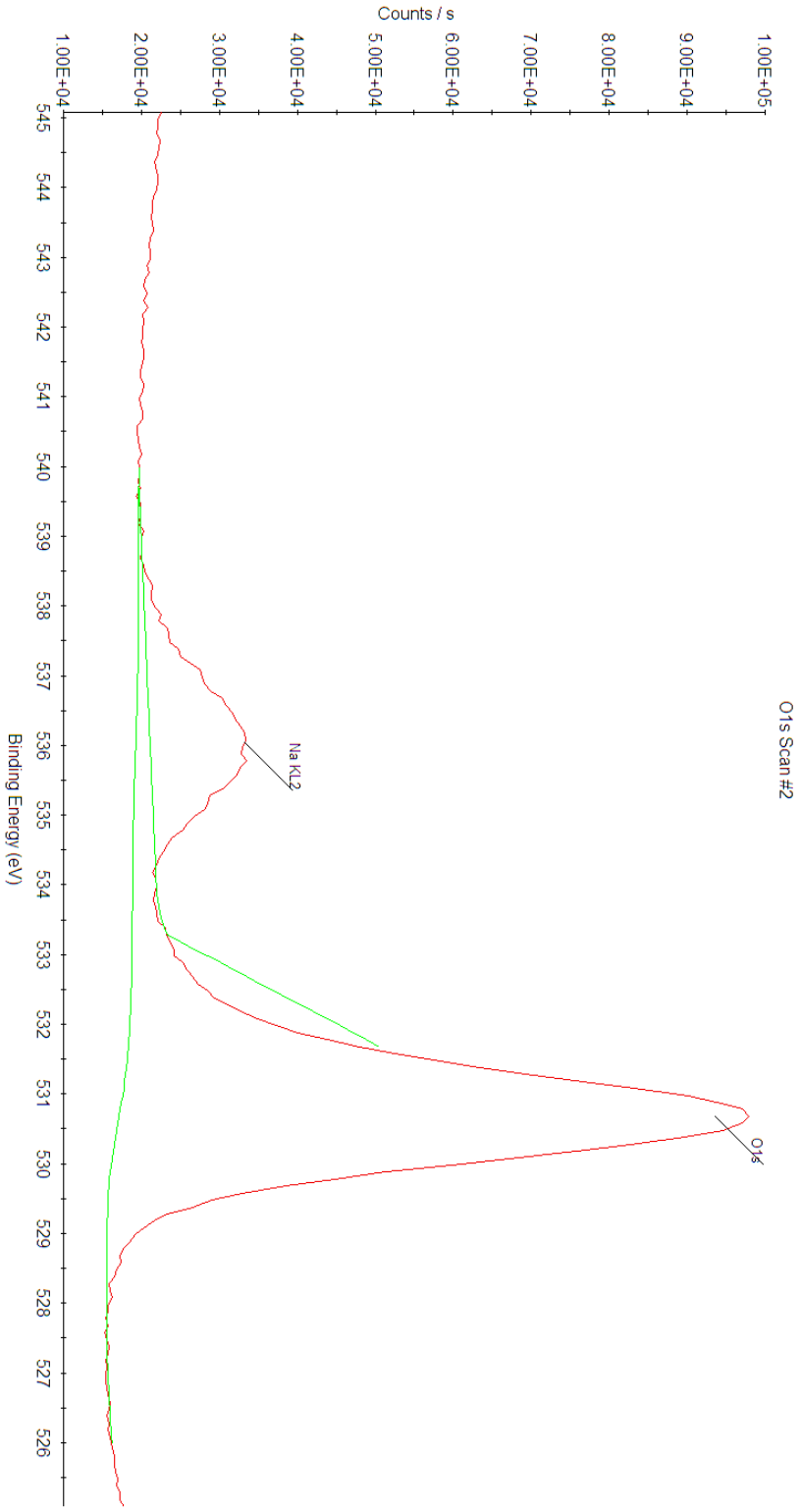

Figure B-14. Oxygen 1s x-ray photoelectron spectrum of fresh Cu electrode.

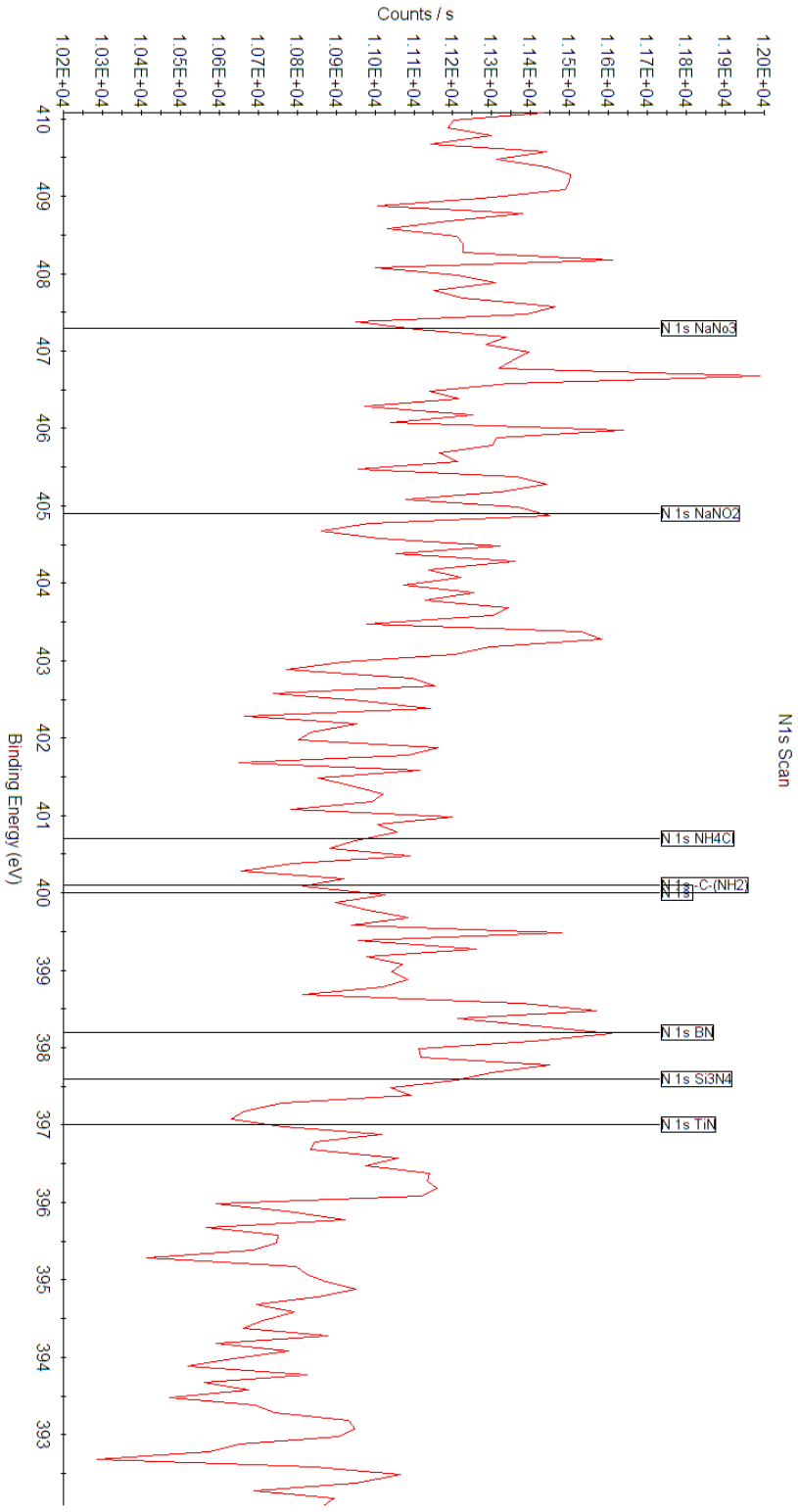

Figure B-15. Nitrogen 1s x-ray photoelectron spectrum of fresh Cu electrode.

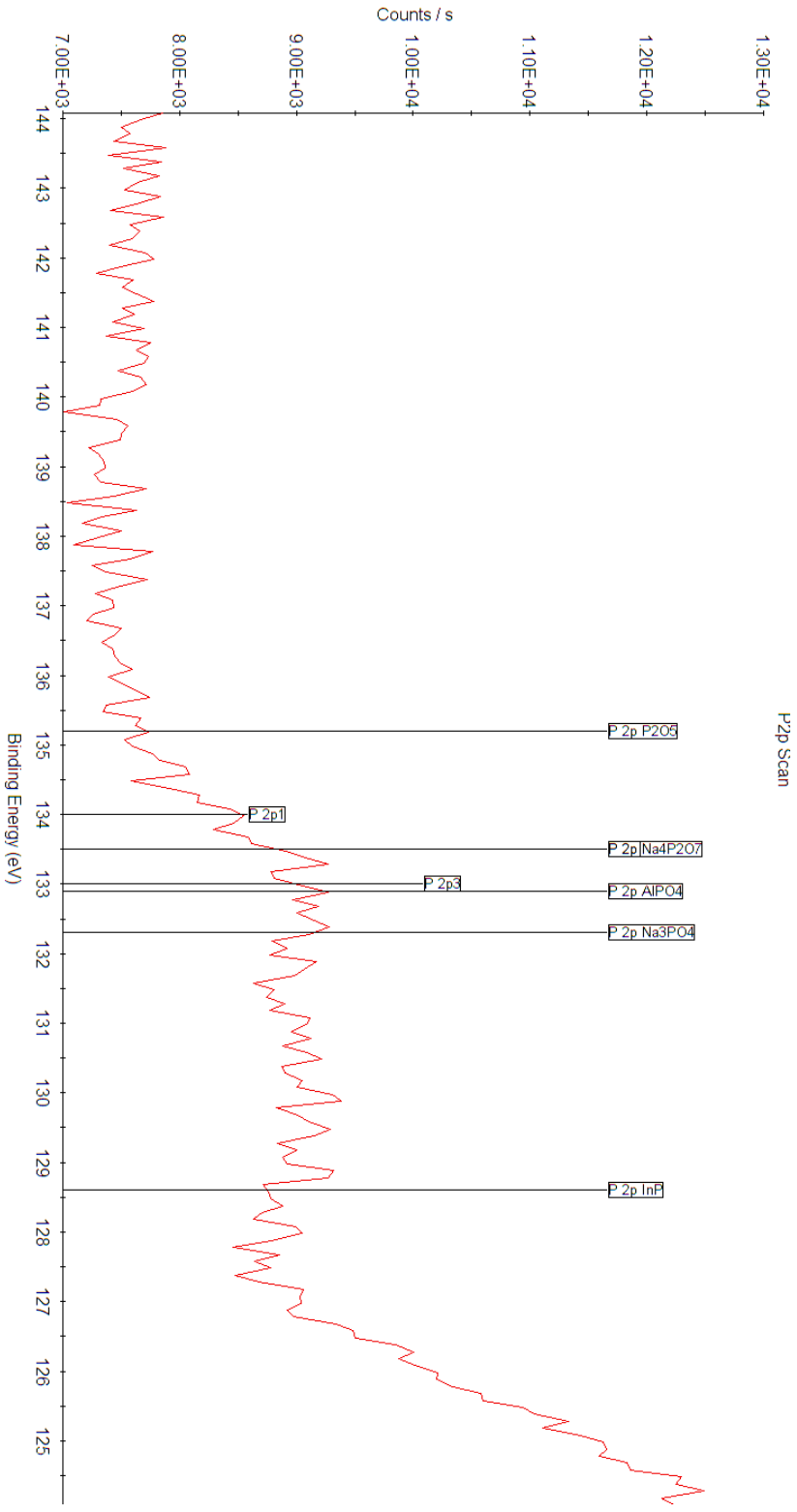

Figure B-16. Phosphorus 2p x-ray photoelectron spectrum of fresh Cu electrode.

B.4.1.2 Post-Electropolishing Copper Electrode

Copper foam from previous experiment was electropolished in a two-electrode setup at 300 mA for against a copper foil counter electrode in *ortho*-phosphoric acid (99.99% pure trace metals basis, 345245 from Sigma-Aldrich), followed by sonication in MilliQ water (Millipore Type 1, 18 MΩ-cm resistivity) for 5 minutes.

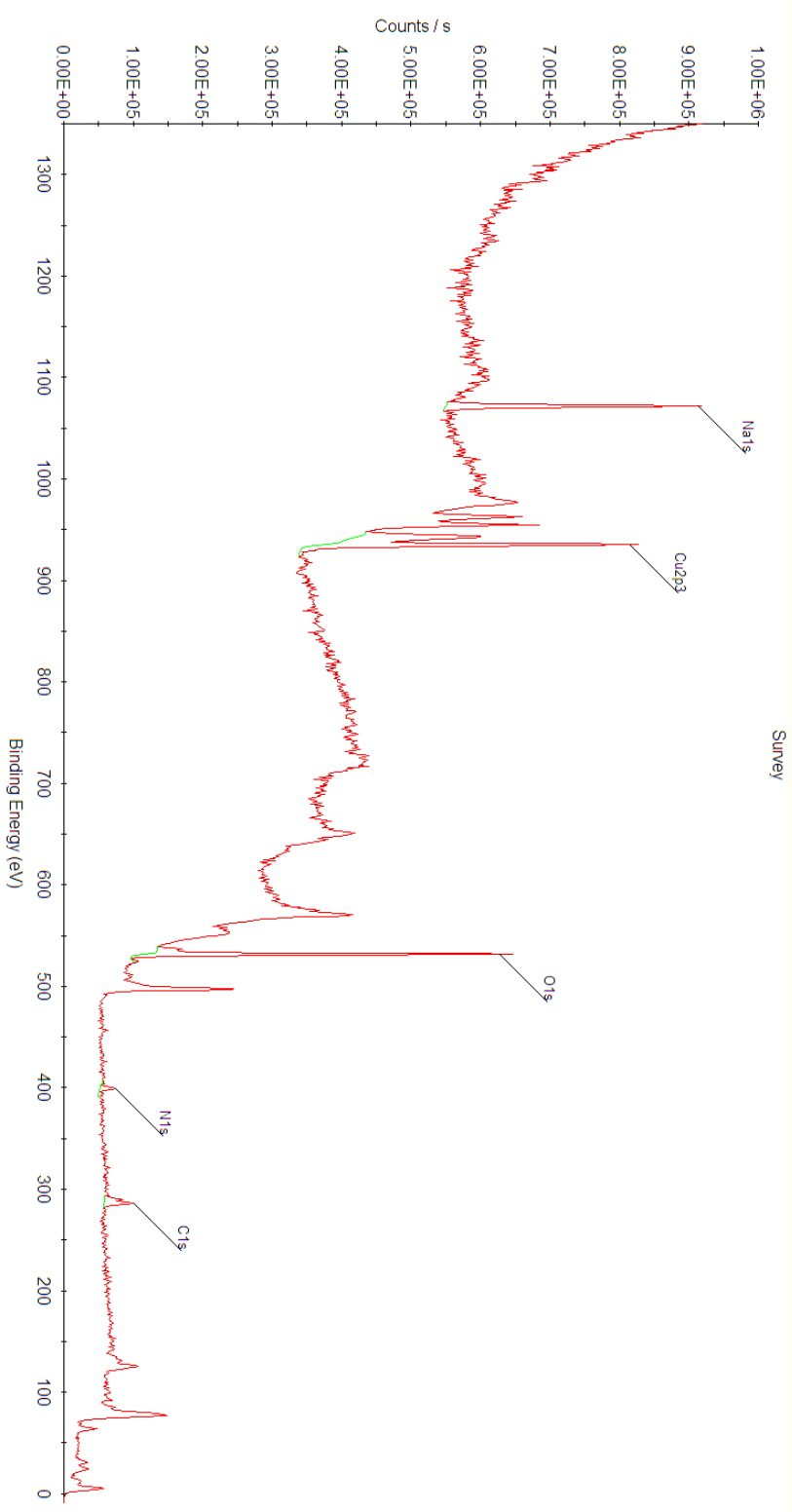

Figure B-17. Survey x-ray photoelectron spectrum of Cu electrode post-electropolishing.

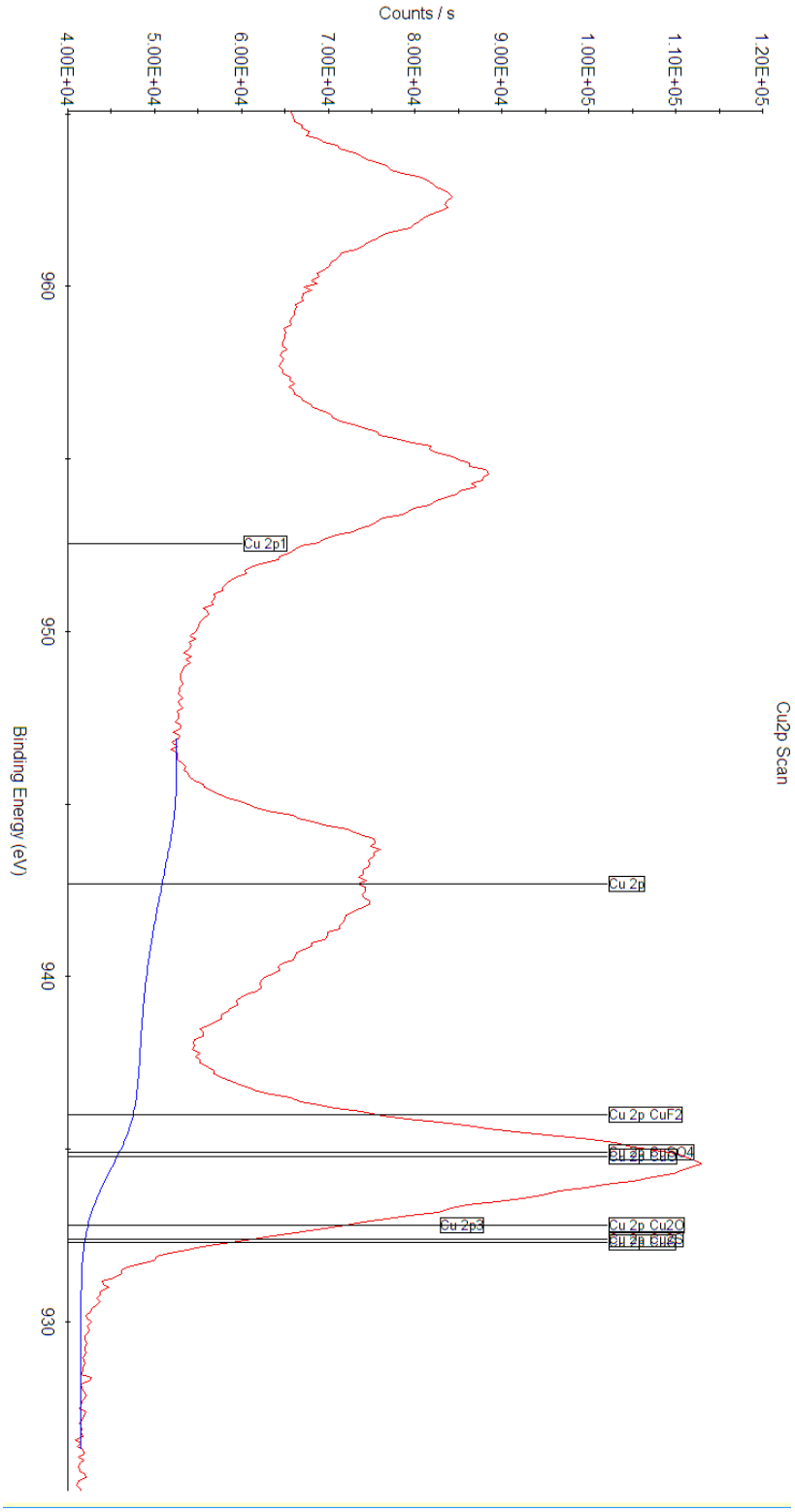

Figure B-18. Copper 2p x-ray photoelectron spectrum of Cu electrode post-electropolishing.

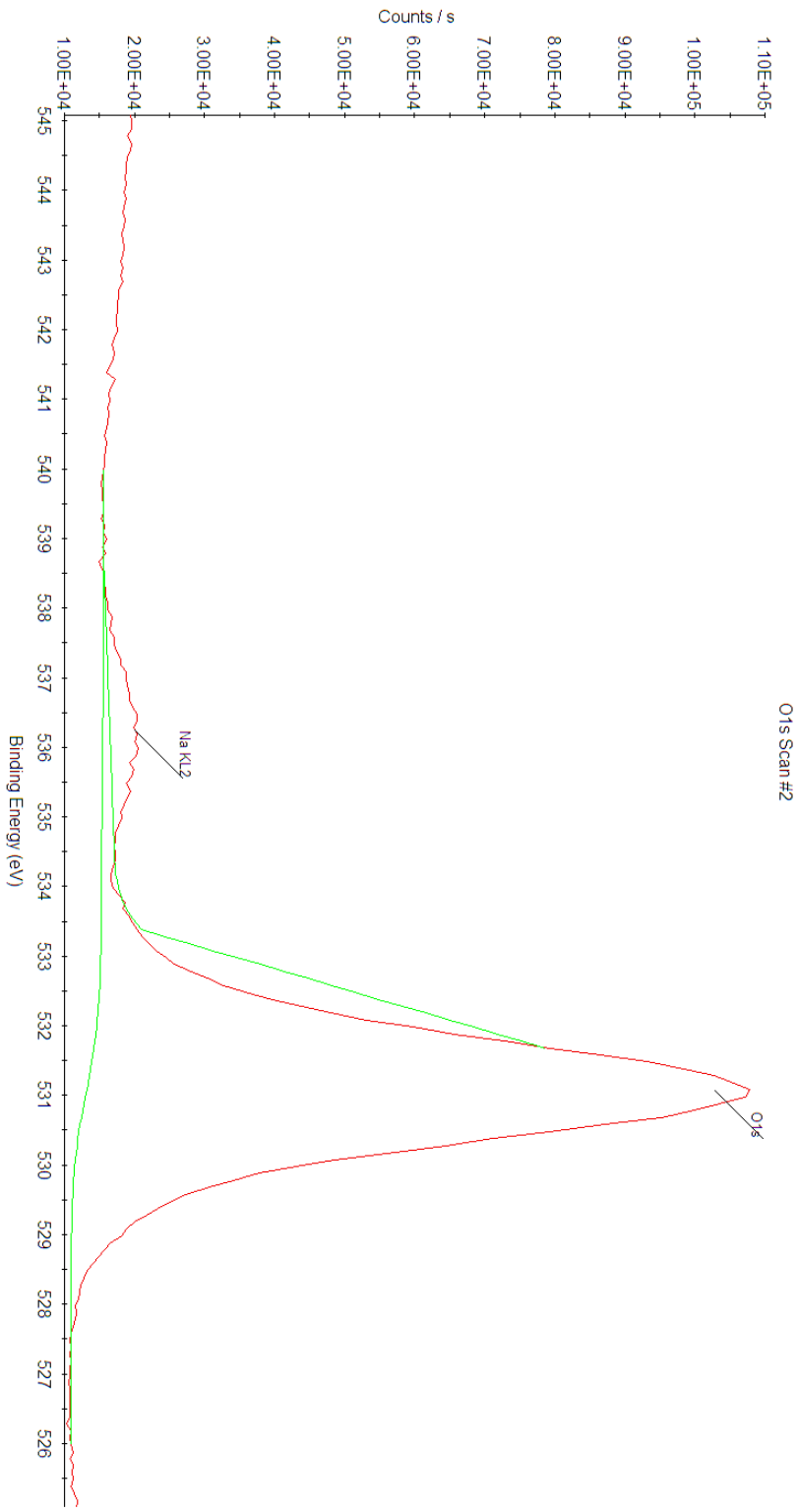

Figure B-19. Oxygen 1s x-ray photoelectron spectrum of Cu electrode post-electropolishing.

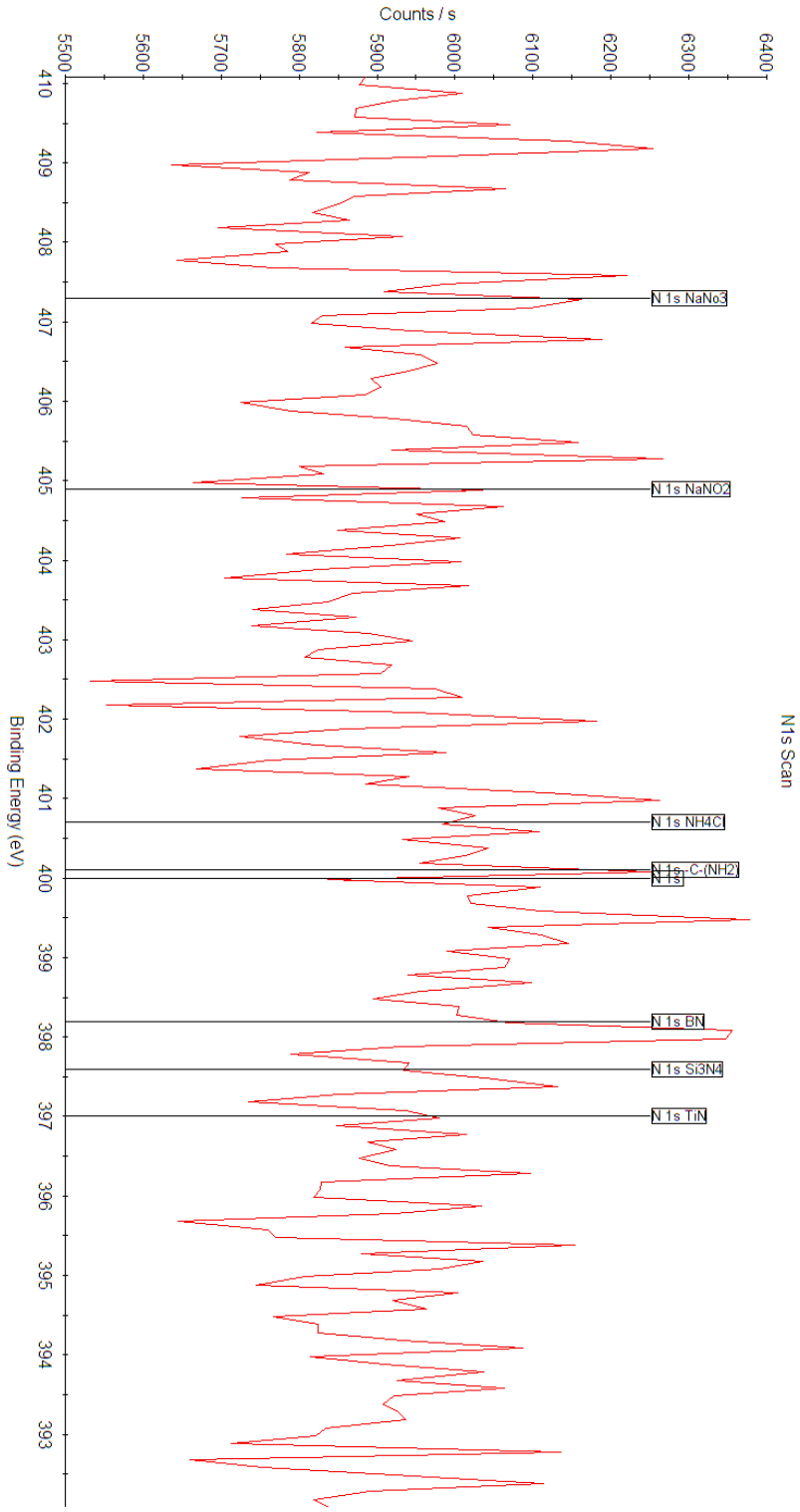

Figure B-20. Nitrogen 1s x-ray photoelectron spectrum of Cu electrode post-electropolishing.

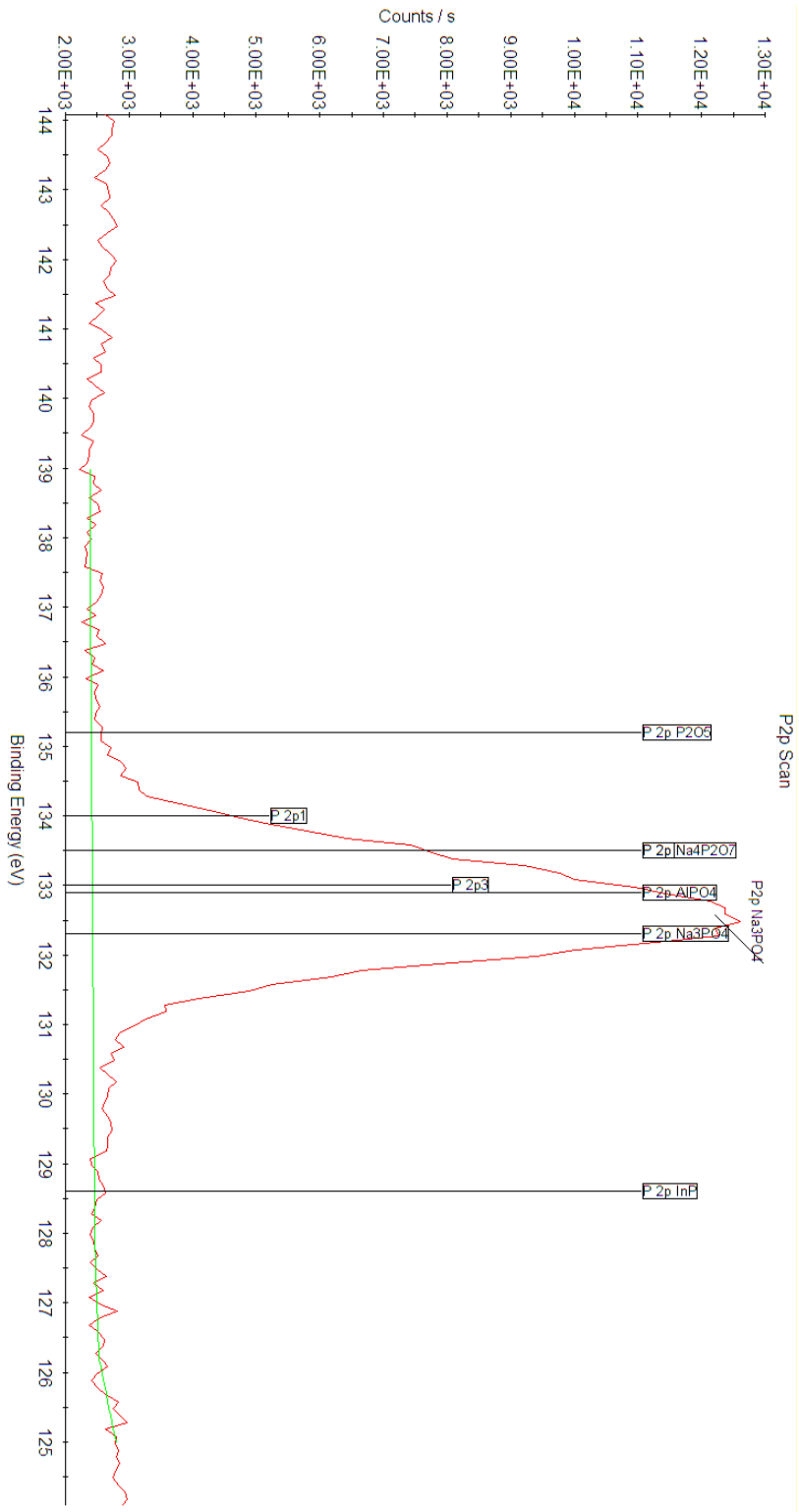

Figure B-21. Phosphorus 2p x-ray photoelectron spectrum of Cu electrode post-electropolishing.

B.4.1.3 Post-Reaction Copper Electrode

Electropolished copper electrode from previous experiment was tested for NRR by bulk electrolysis at $10\,\mathrm{mA{\cdot}cm^{-2}}$ in $1\,\mathrm{M}$ aq. KOH solution at 1000 psi N_2 for 8 hours.

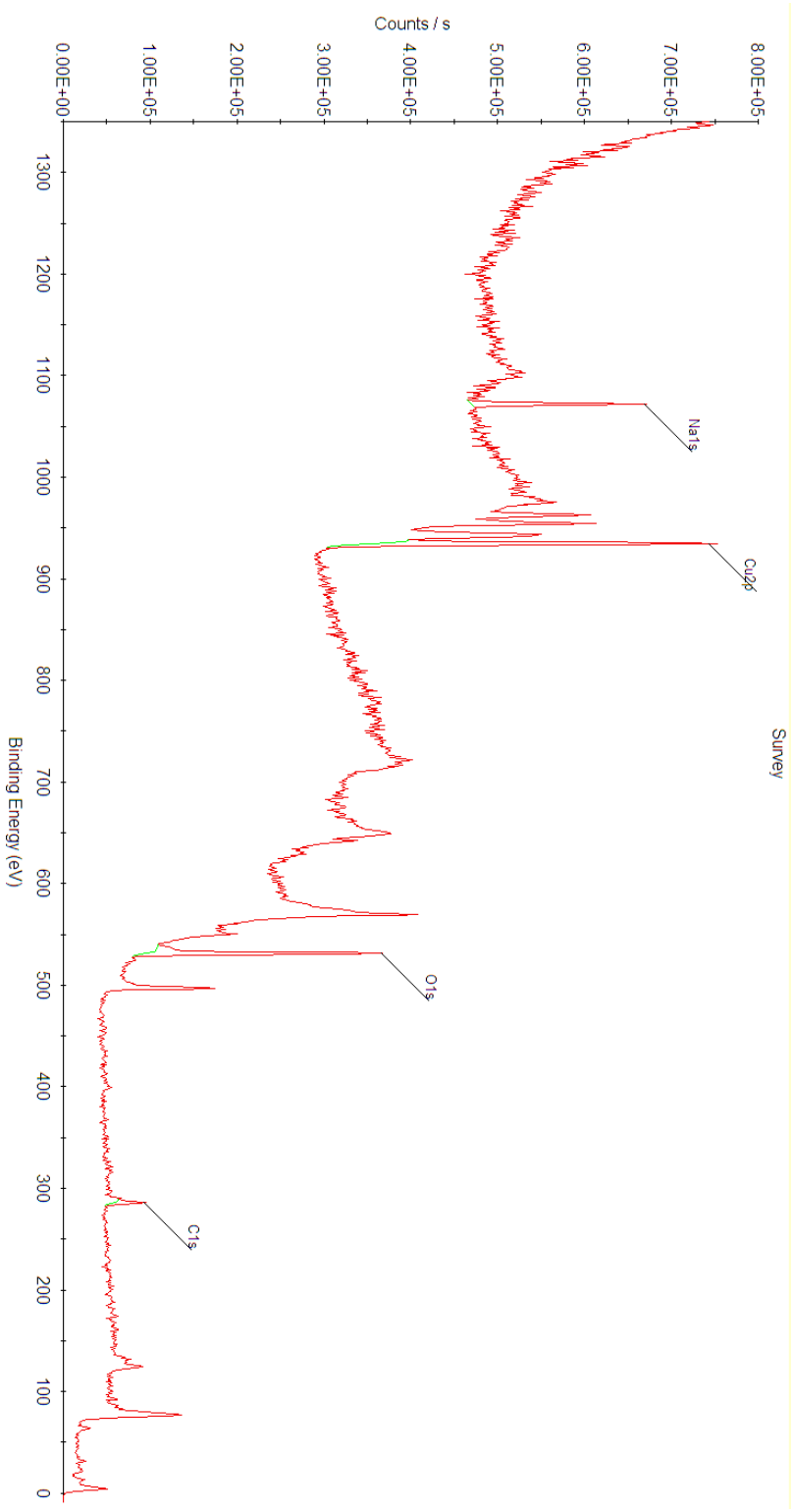

Figure B-22. Survey x-ray photoelectron spectrum of Cu electrode post-reaction.

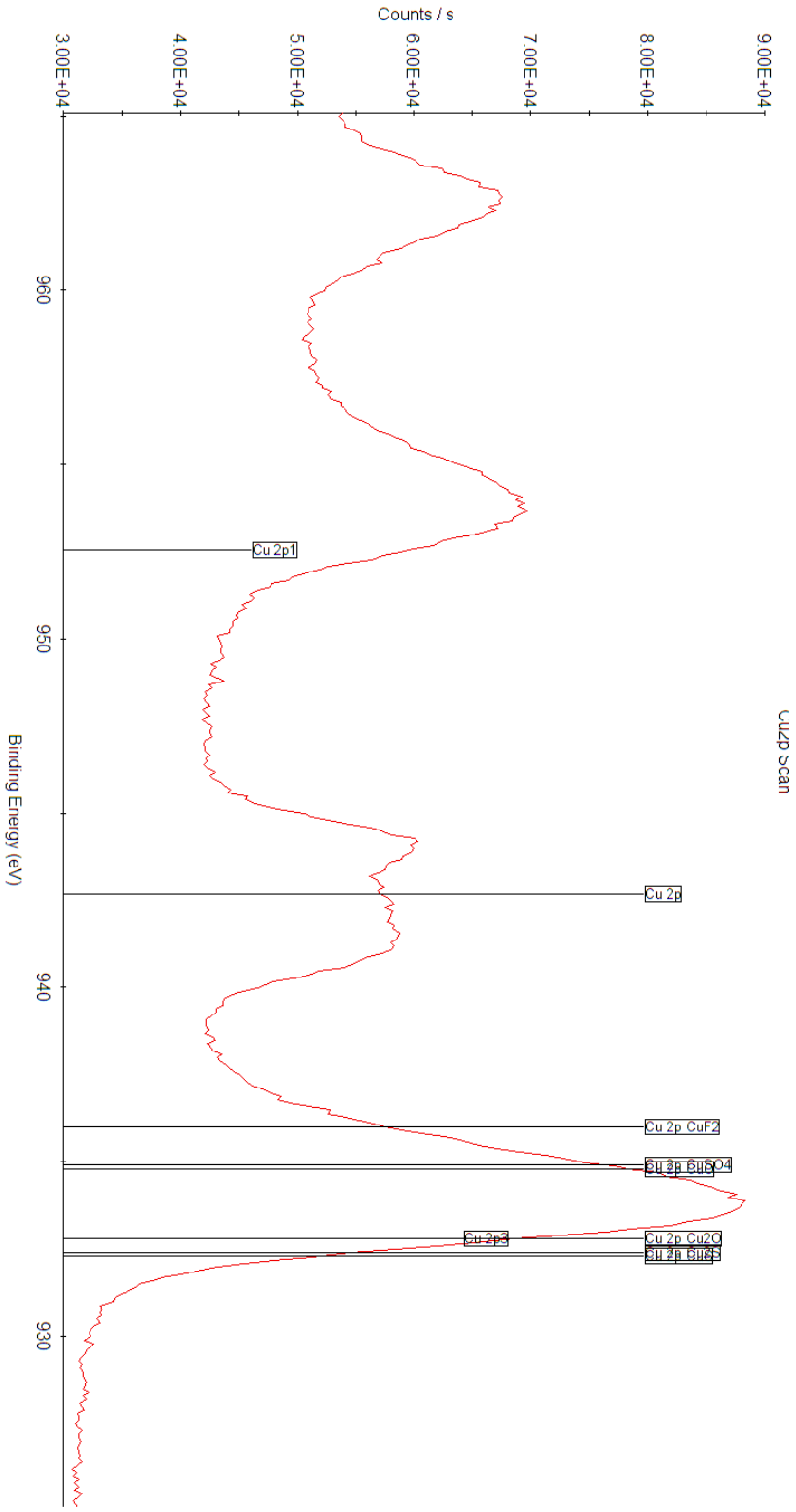

Figure B-23. Copper 2p x-ray photoelectron spectrum of Cu electrode post-reaction.

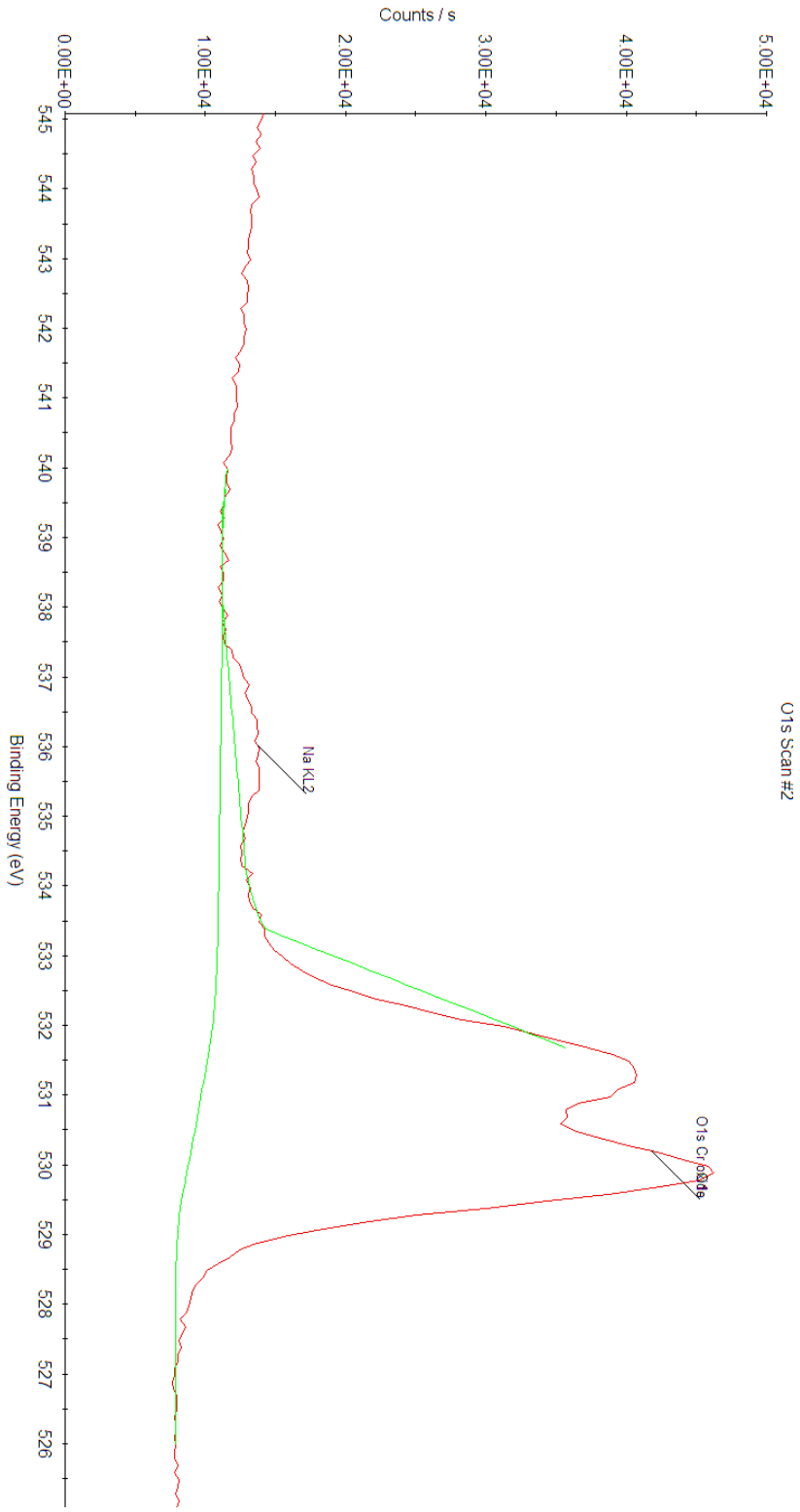

Figure B-24. Oxygen 1s x-ray photoelectron spectrum of Cu electrode post-reaction.

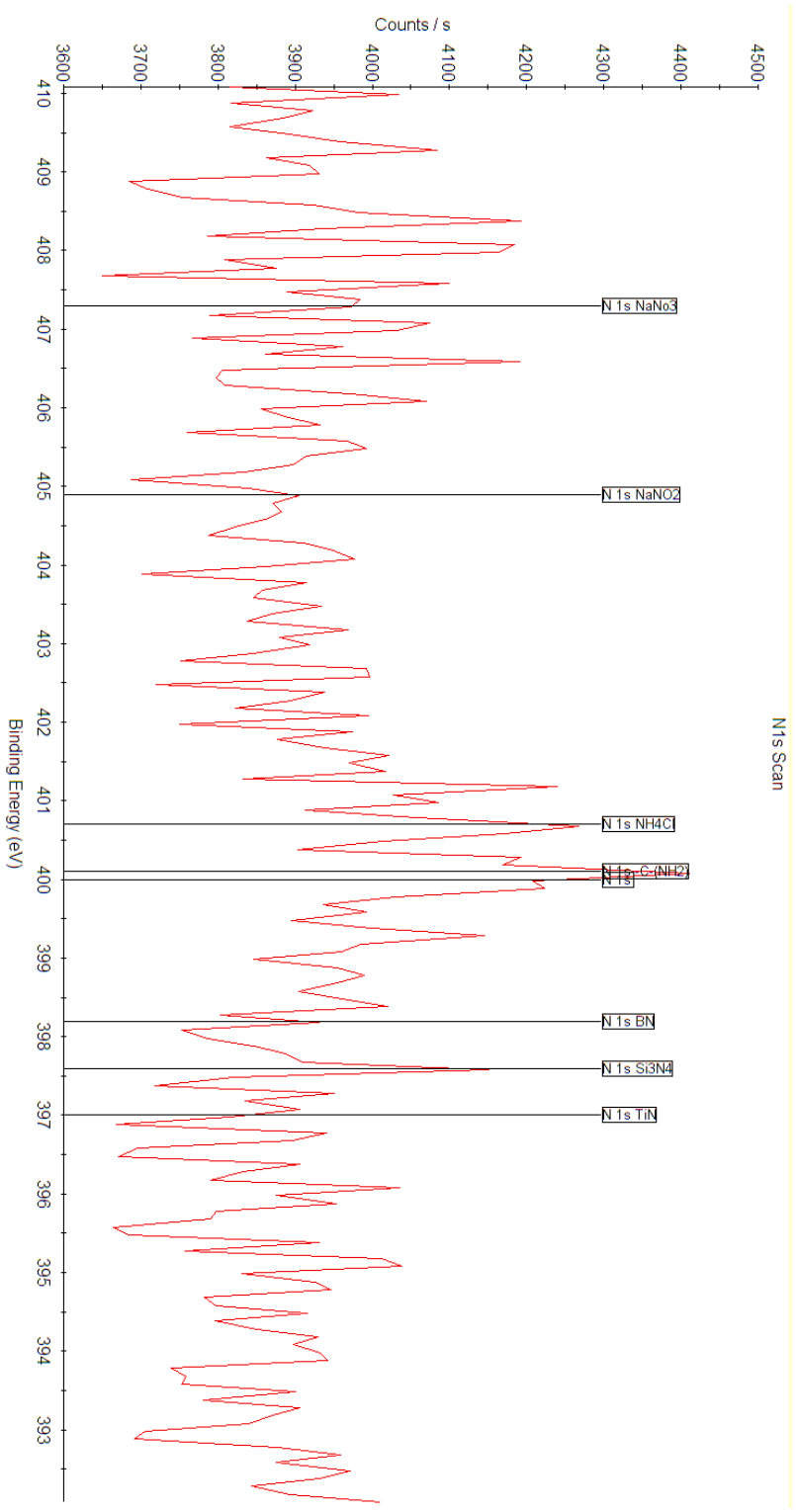

Figure B-25. Nitrogen 1s x-ray photoelectron spectrum of Cu electrode post-reaction.

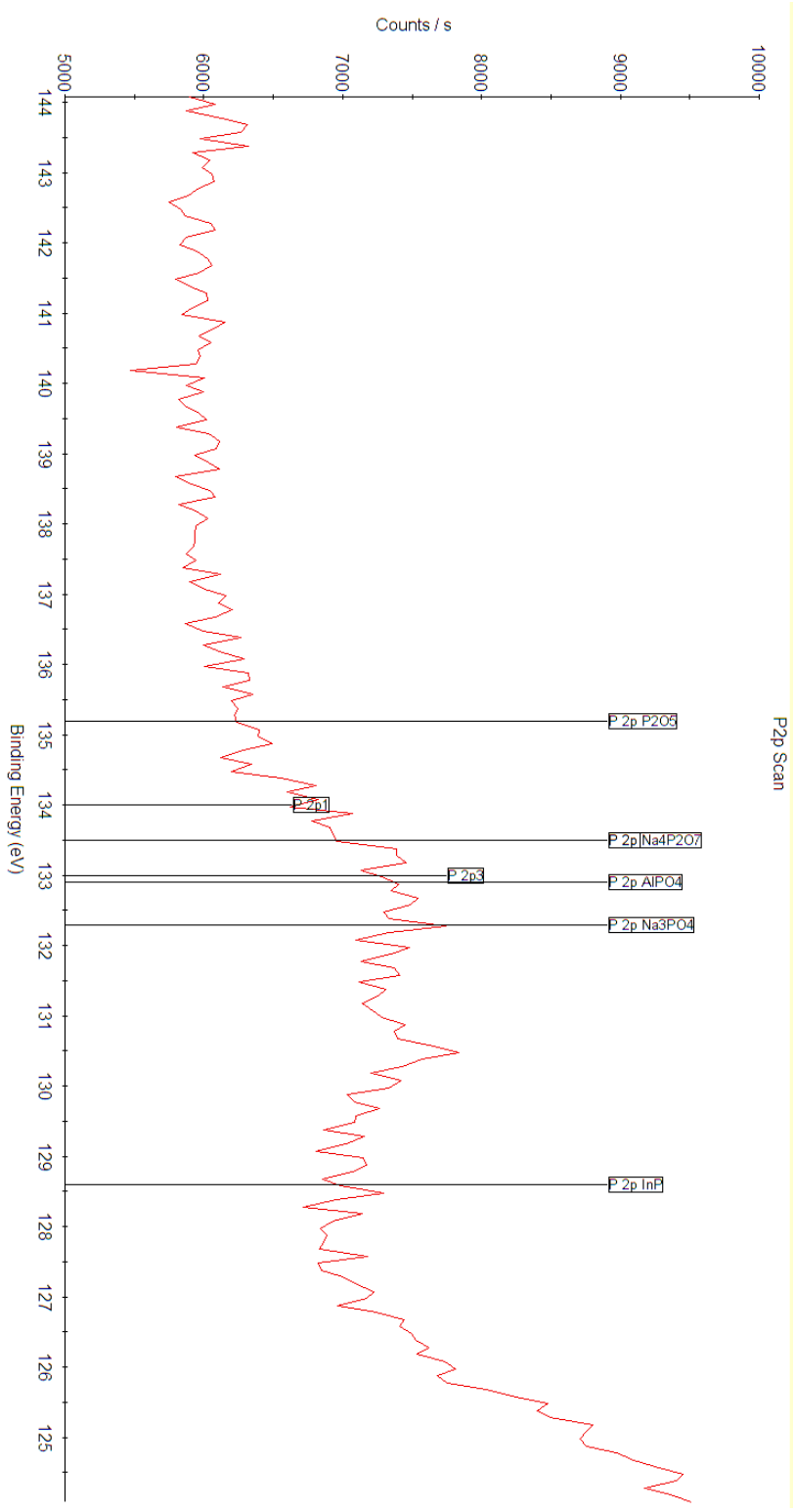

Figure B-26. Phosphorus 2p x-ray photoelectron spectrum of Cu electrode post-reaction.

B.4.2 Copper Nitride

B.4.2.1 Sodium Amide Synthesis

Copper foil, thickness 1.0 mm, 99.999% trace metals basis from Millipore Sigma was nitridated by sodium amide prep as described in **Section 3.4.4.1** on page 143. Etching was accomplished by argon-ion sputtering was performed by built in ion gun at 1 keV for 5-minute increments.

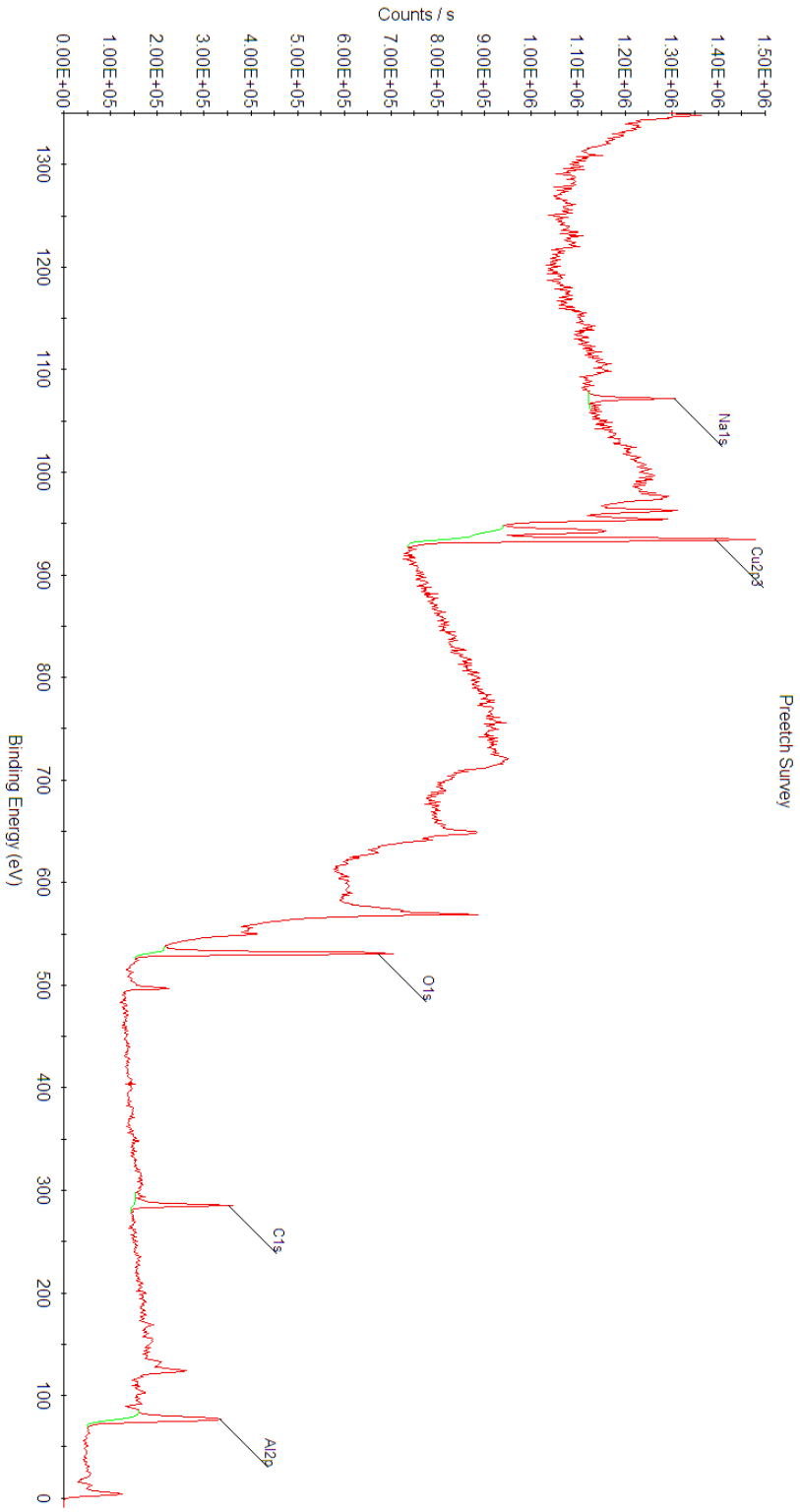

Figure B-27. Surface survey x-ray photoelectron spectrum of Cu_3N foil prepared by sodium amide prep.

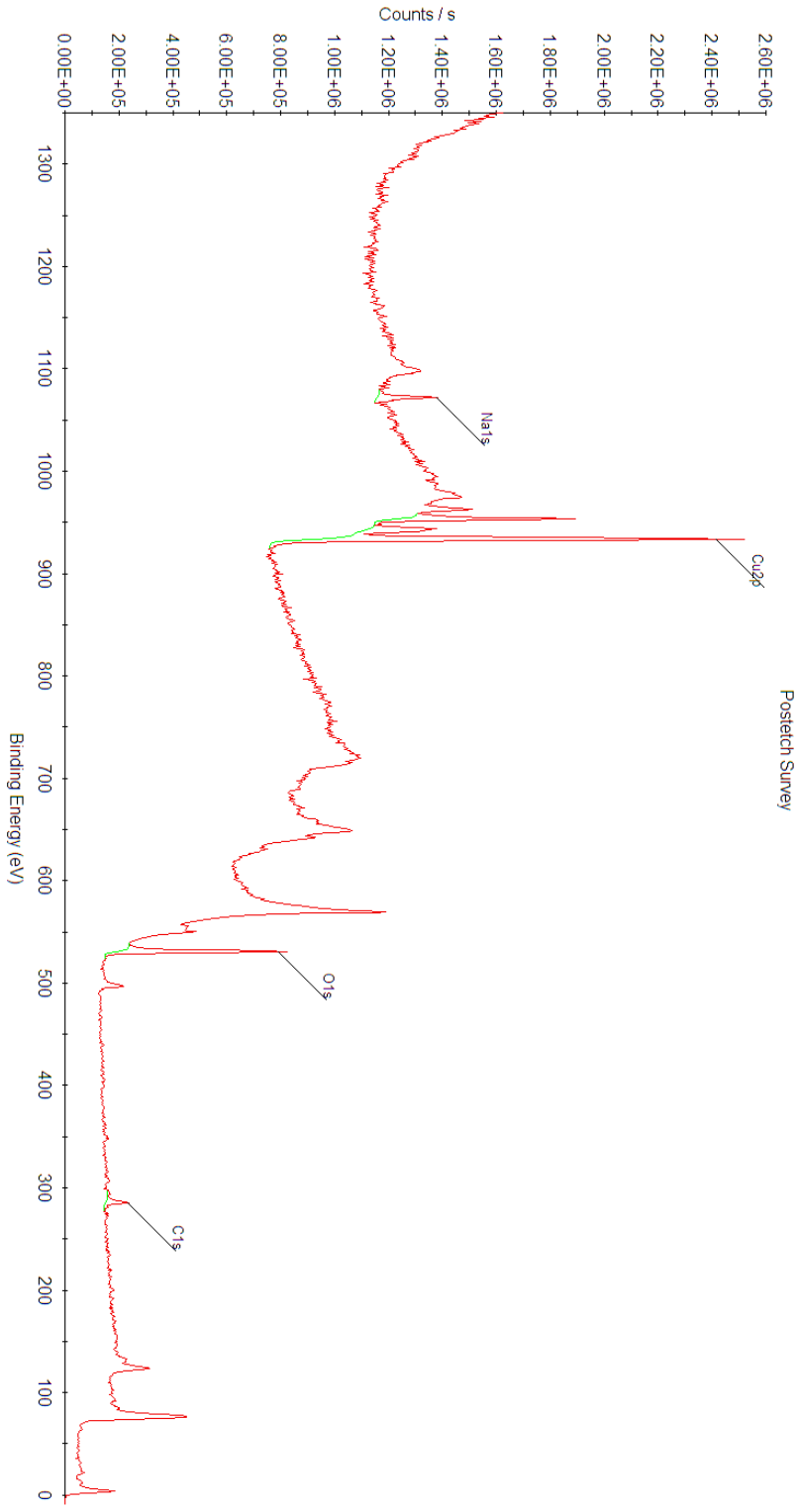

Figure B-28. Subsurface survey x-ray photoelectron spectrum of etched Cu_3N foil prepared by sodium amide prep.

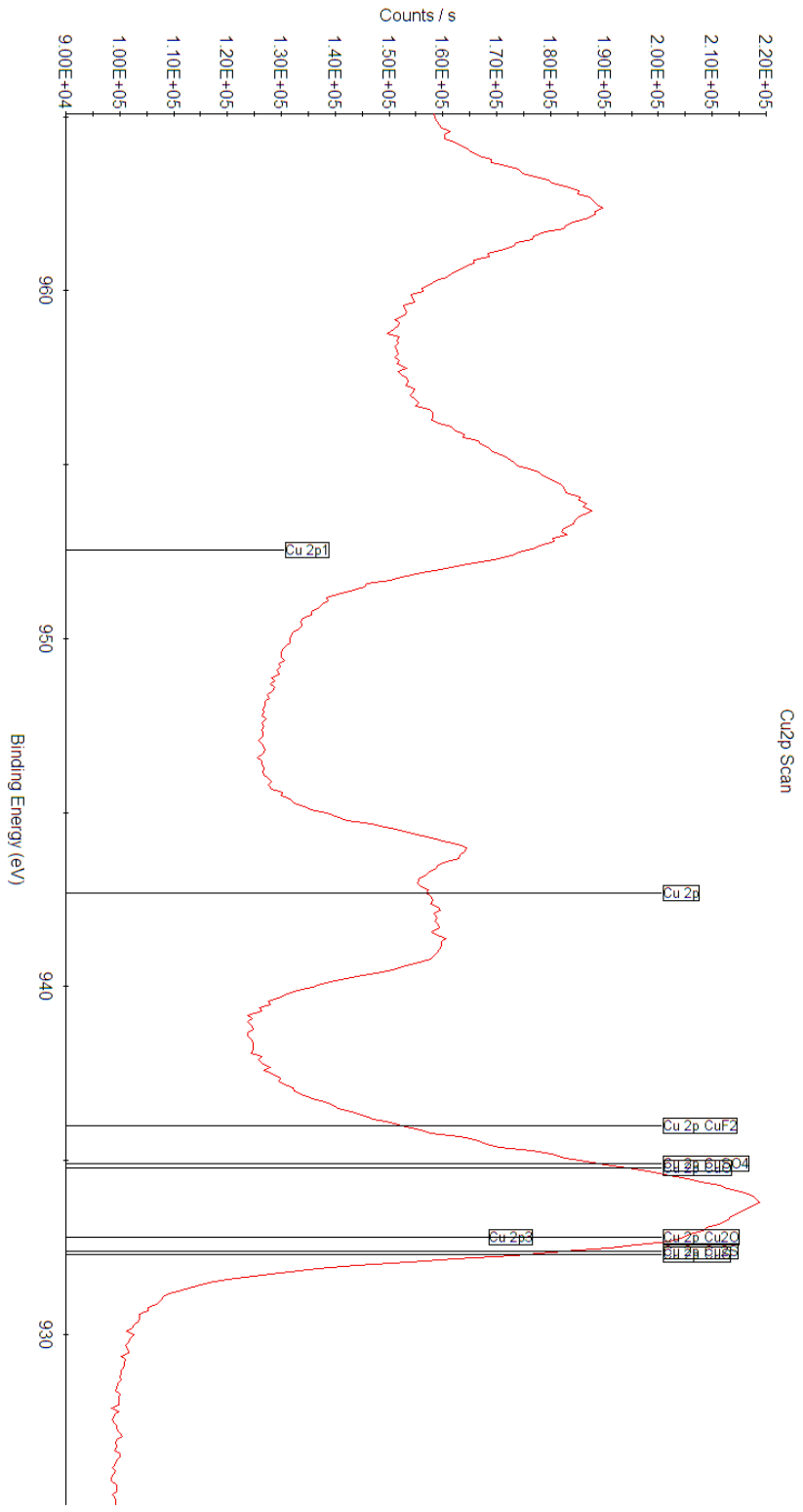

Figure B-29. Surface copper 2p x-ray photoelectron spectrum of Cu_3N foil prepared by sodium amide prep.

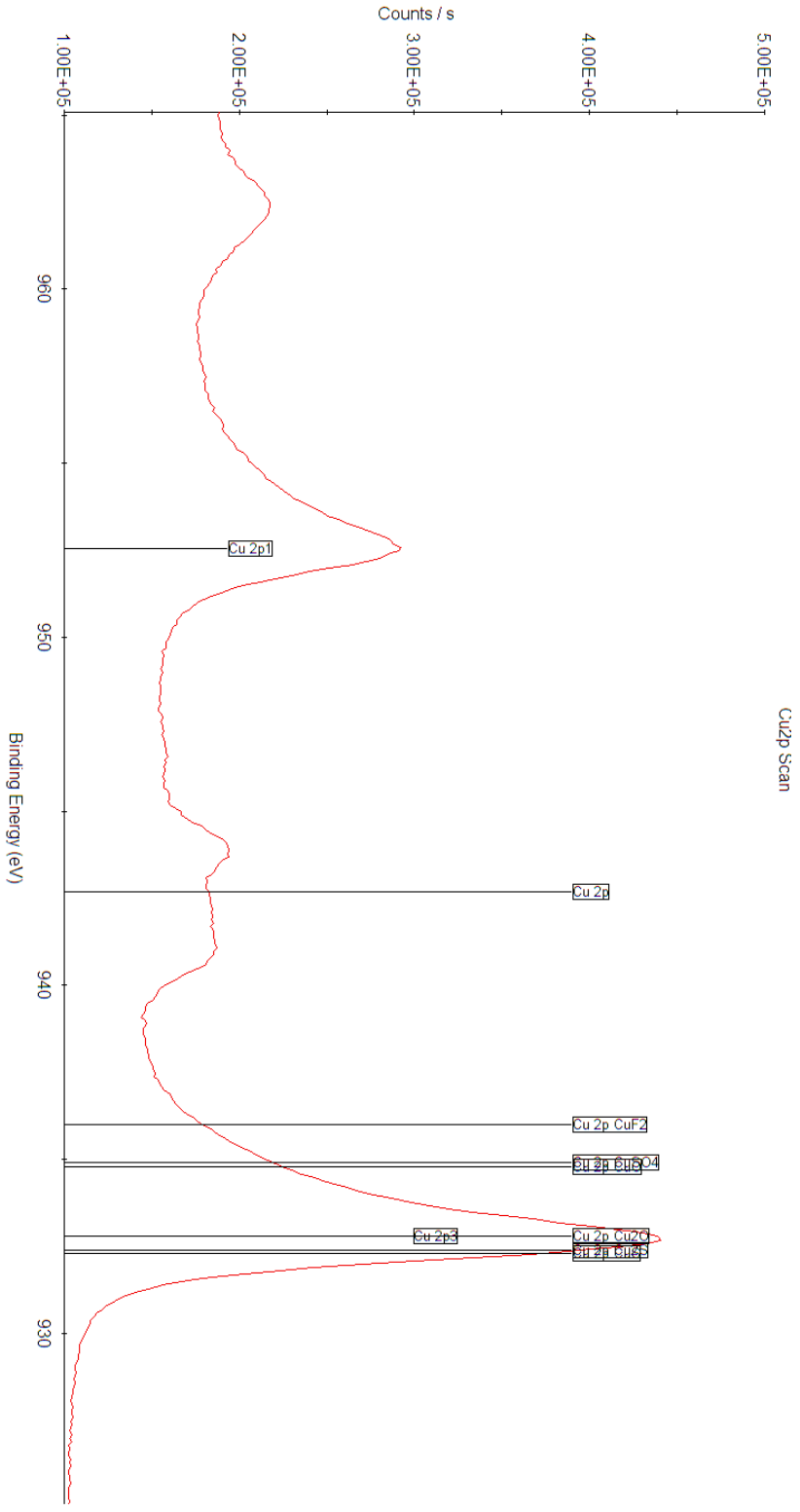

Figure B-30. Subsurface copper 2p x-ray photoelectron spectrum of etched Cu_3N foil prepared by sodium amide prep.

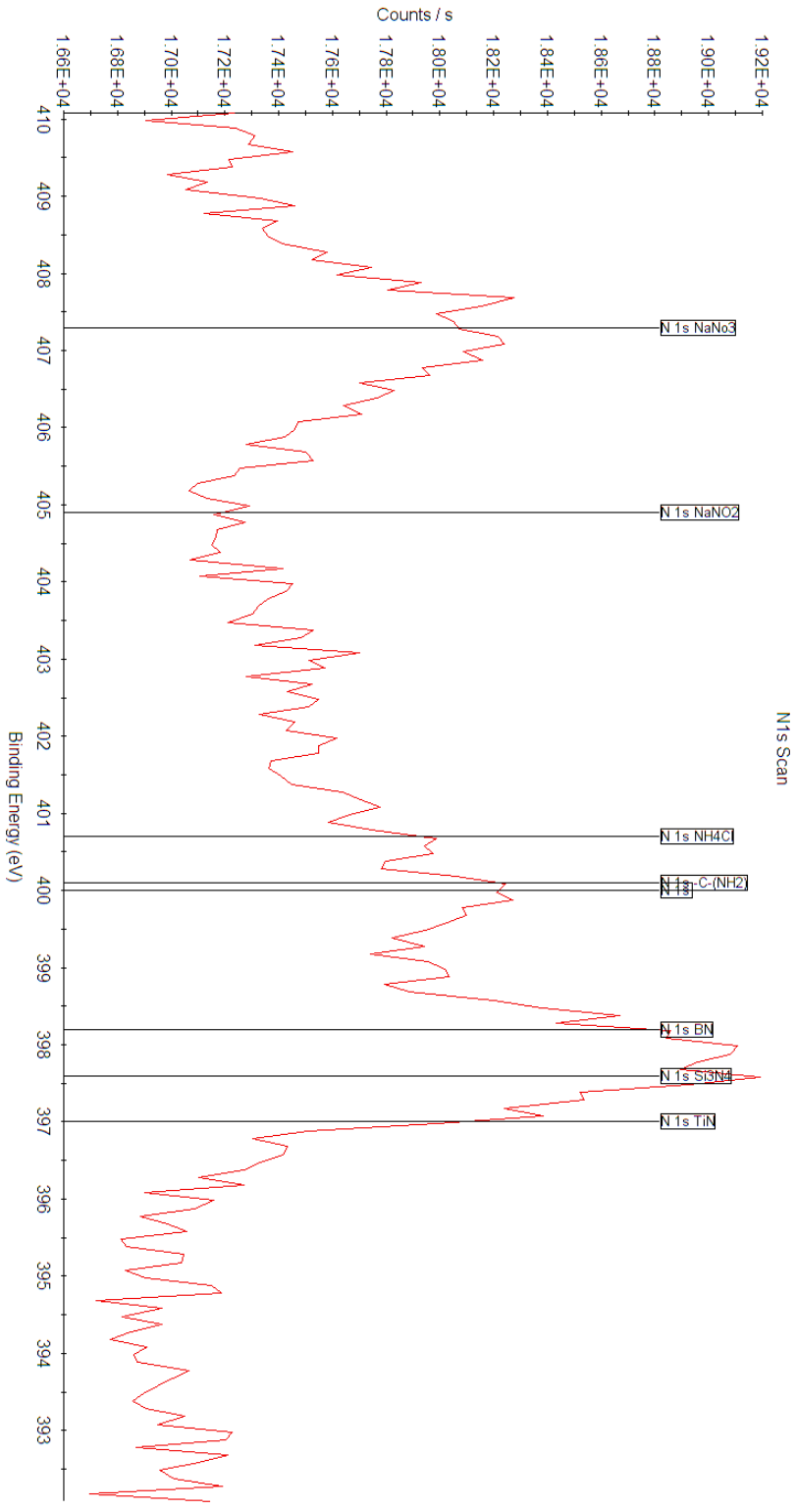

Figure B-31. Surface nitrogen 1s x-ray photoelectron spectrum of Cu_3N foil prepared by sodium amide prep.

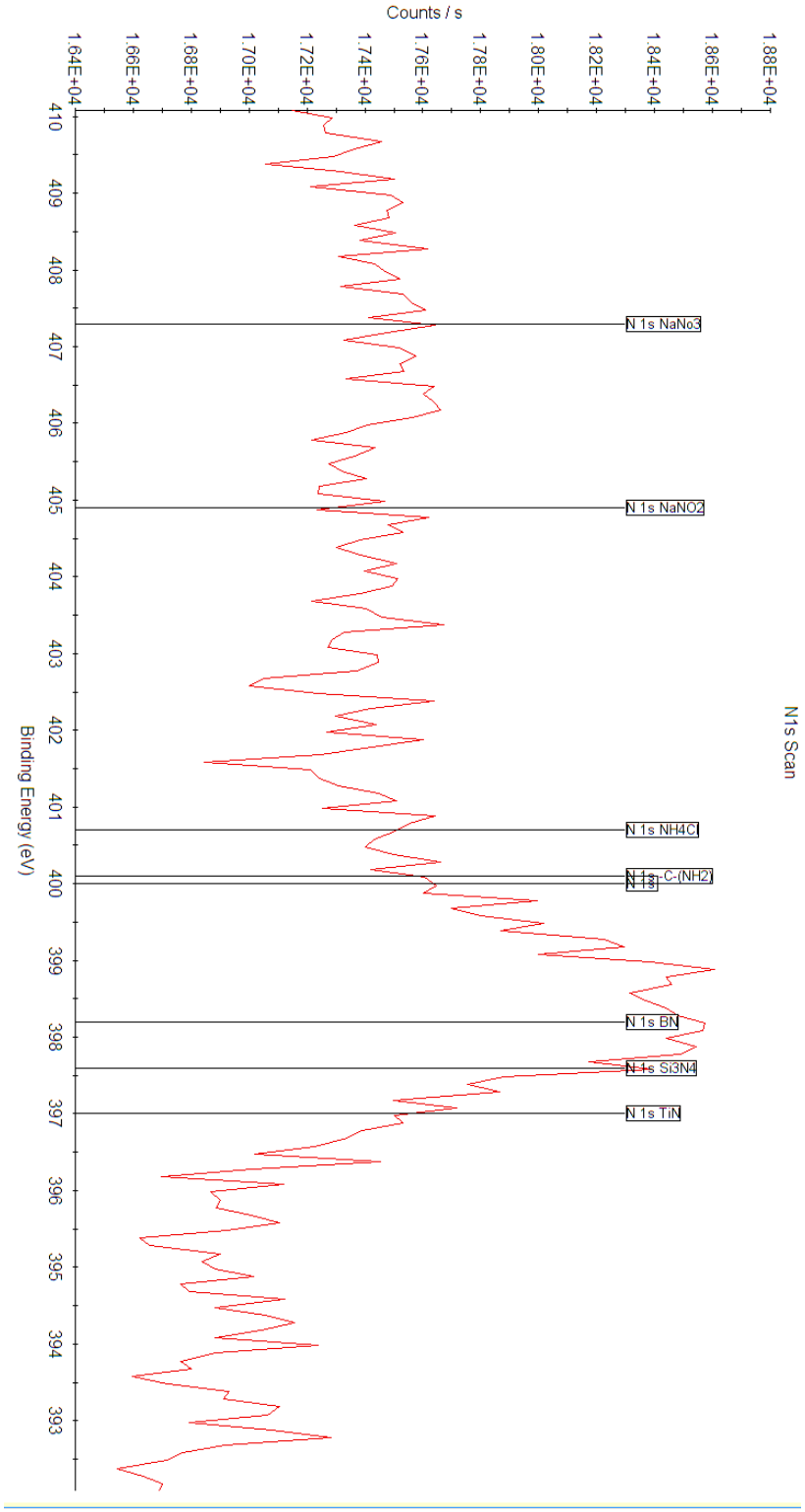

Figure B-32. Subsurface nitrogen 1s x-ray photoelectron spectrum of etched Cu_3N foil prepared by sodium amide prep.

B.4.2.2 Flowing Ammonia Synthesis

Copper foil, thickness 1.0 mm, 99.999% trace metals basis from Millipore Sigma and copper foam, 63% porous lost carbonate sintering (CU003804 from Goodfellow USA) were nitridated by flowing NH_3 prep as described in **Section 3.4.4.2** on page 143. Etching was accomplished by argon-ion sputtering was performed by built in ion gun at 1 keV for 5-minute increments.

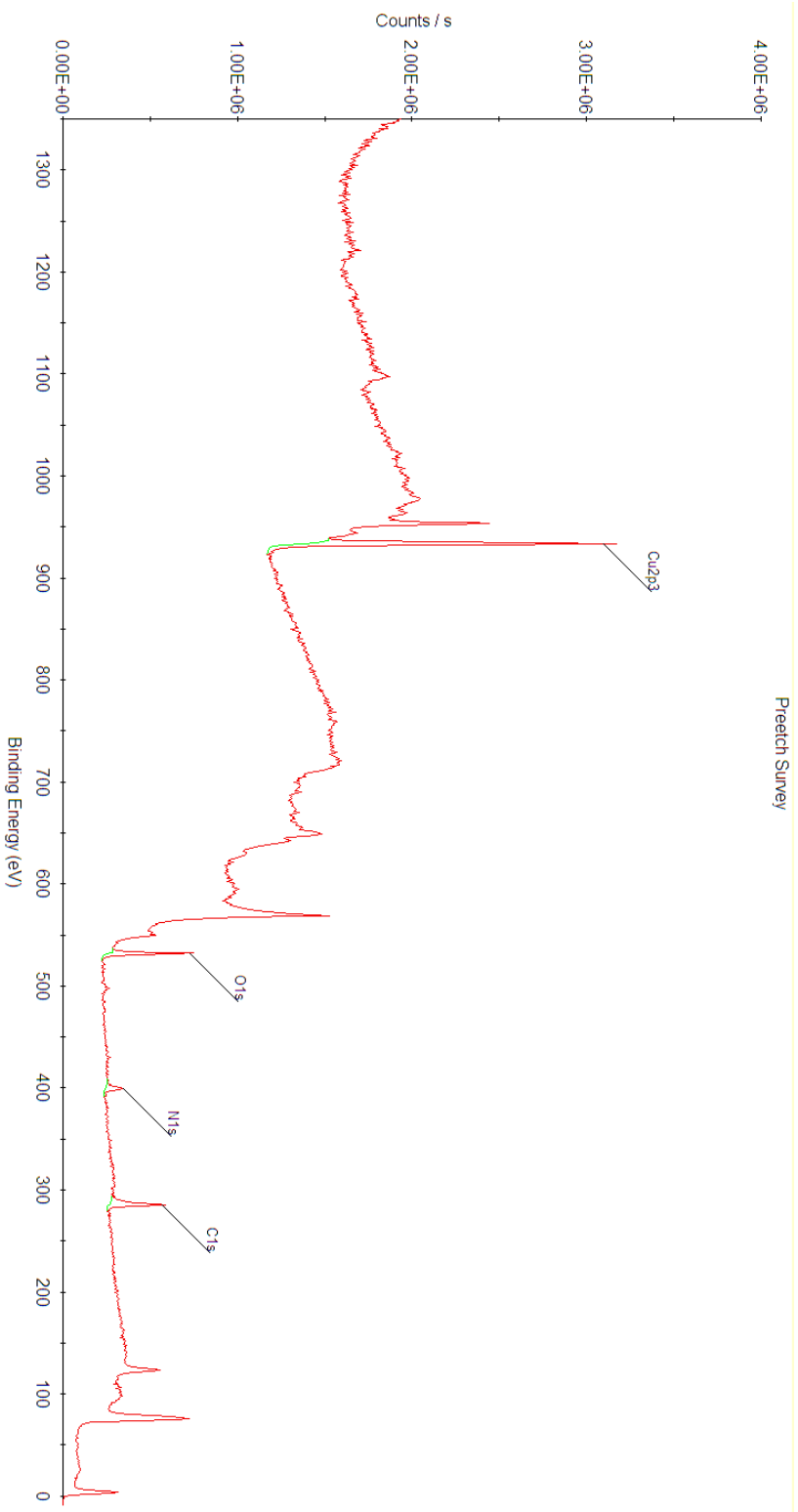

Figure B-33. Surface survey x-ray photoelectron spectrum of Cu_3N foil prepared by flowing NH_3 prep.

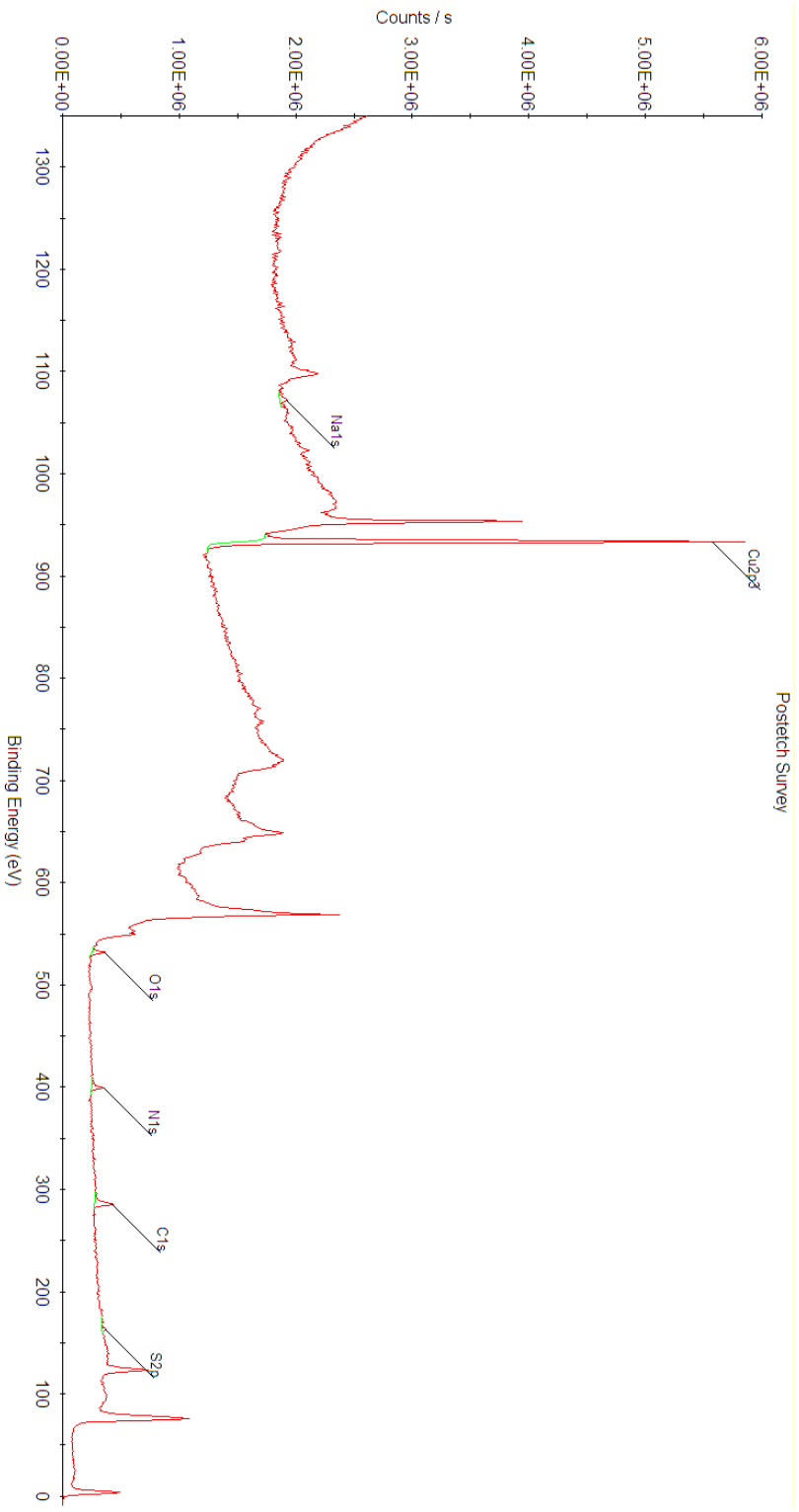

Figure B-34. Subsurface survey x-ray photoelectron spectrum of etched Cu_3N foil prepared by flowing NH_3 prep.

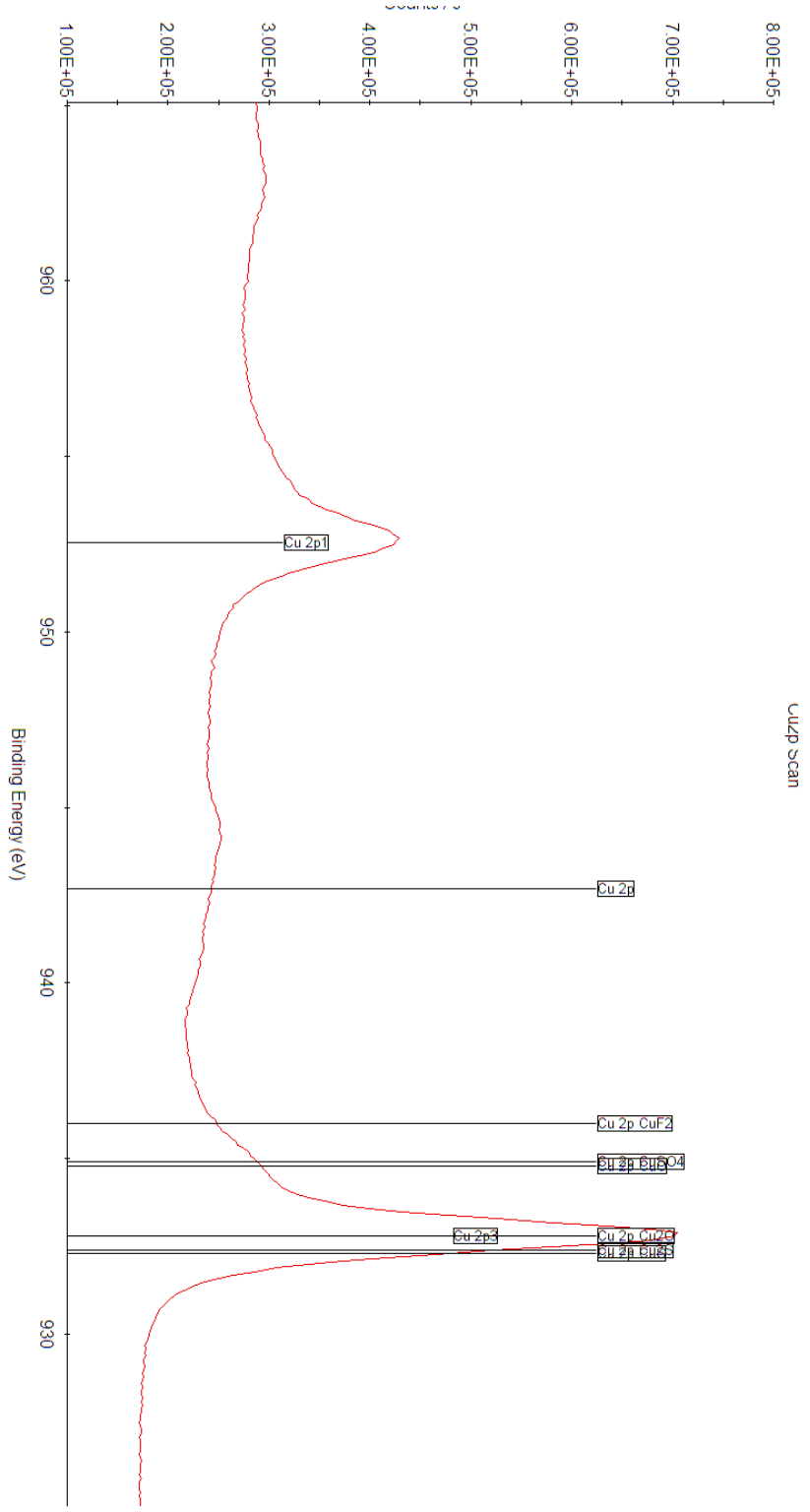

Figure B-35. Surface copper 2p x-ray photoelectron spectrum of Cu_3N foil prepared by flowing NH_3 prep.

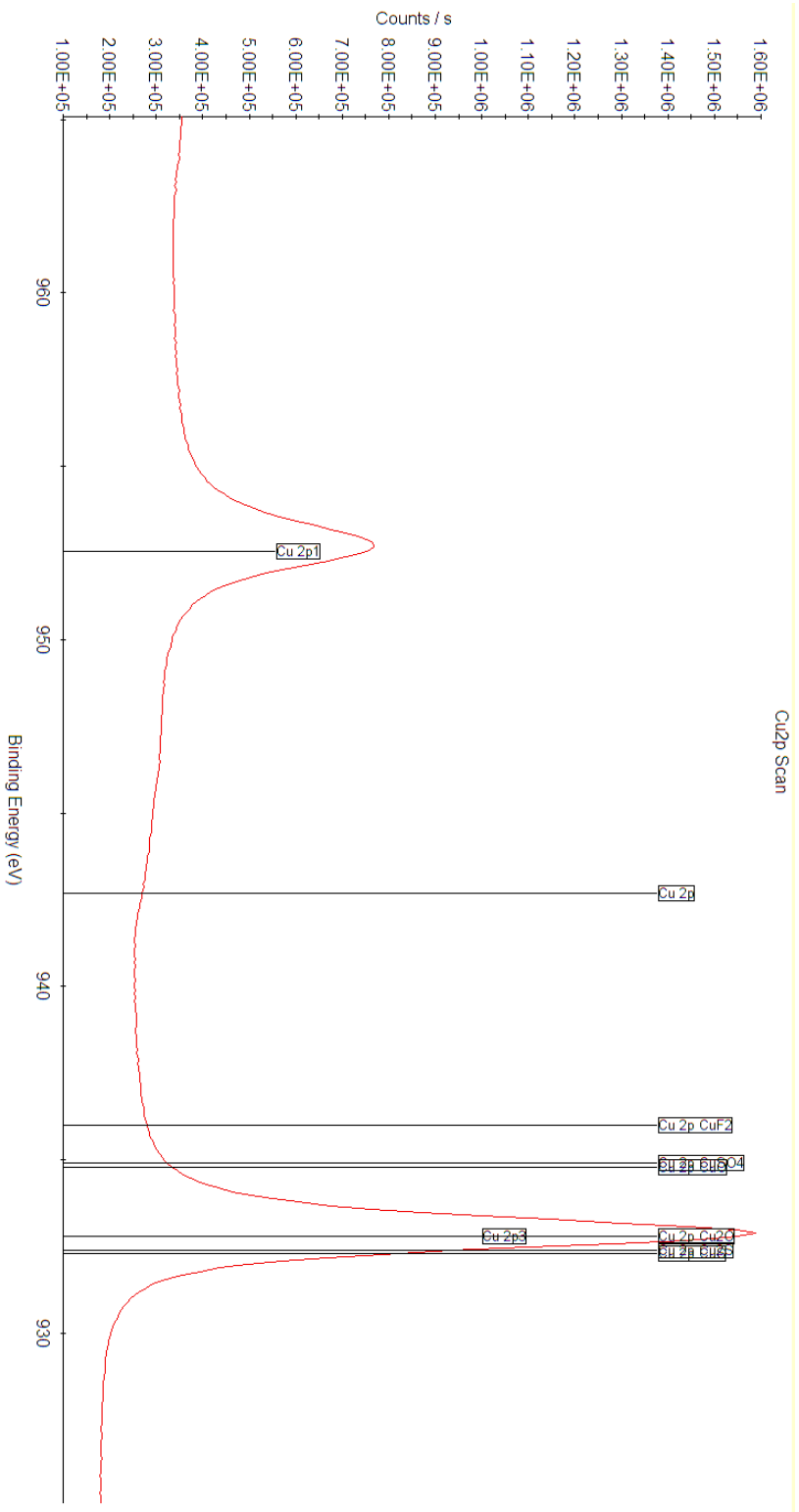

Figure B-36. Subsurface copper 2p x-ray photoelectron spectrum of etched Cu_3N foil prepared by flowing NH_3 prep.

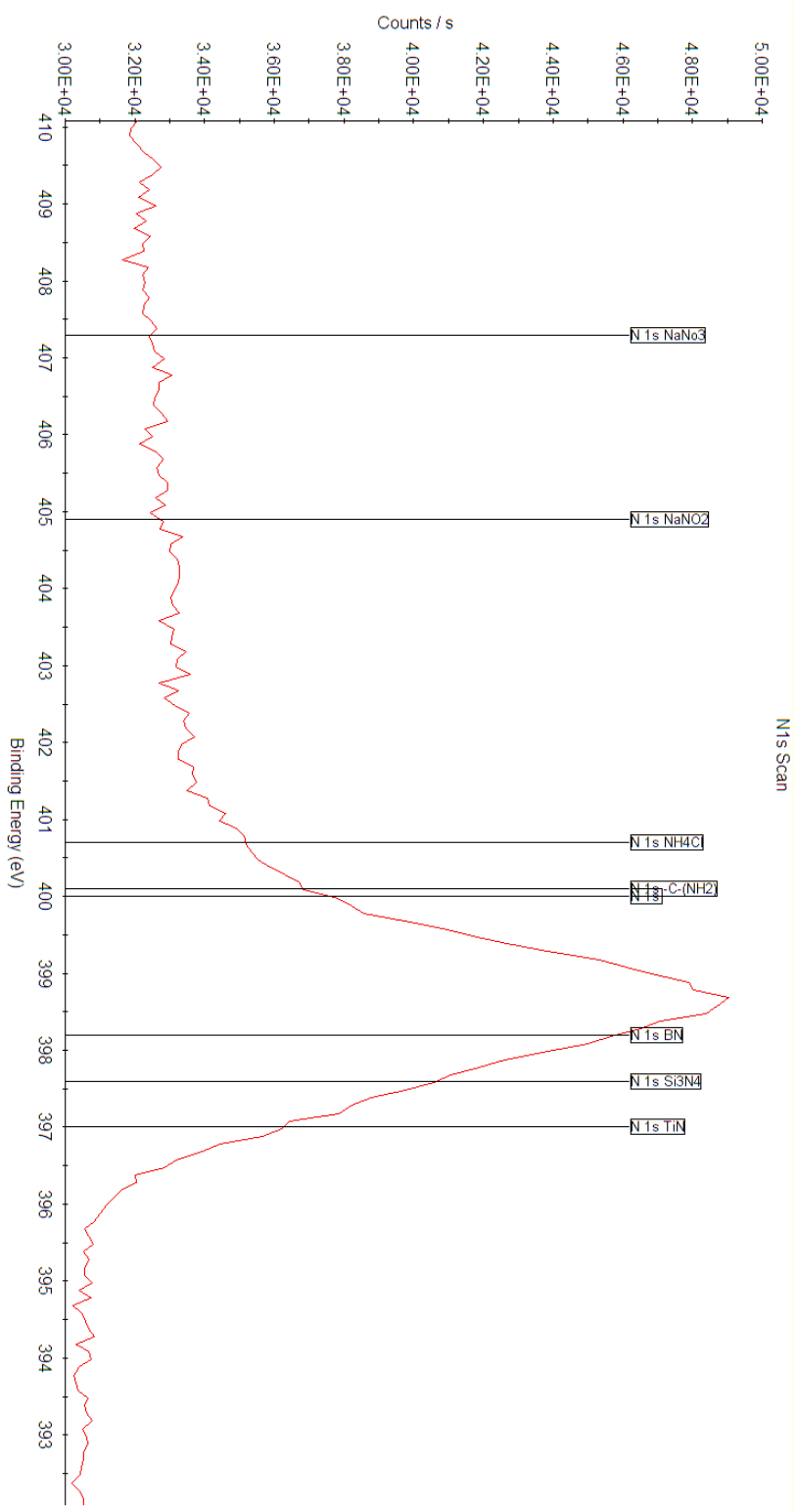

Figure B-37. Surface nitrogen 1s x-ray photoelectron spectrum of Cu_3N foil prepared by flowing NH_3 prep.

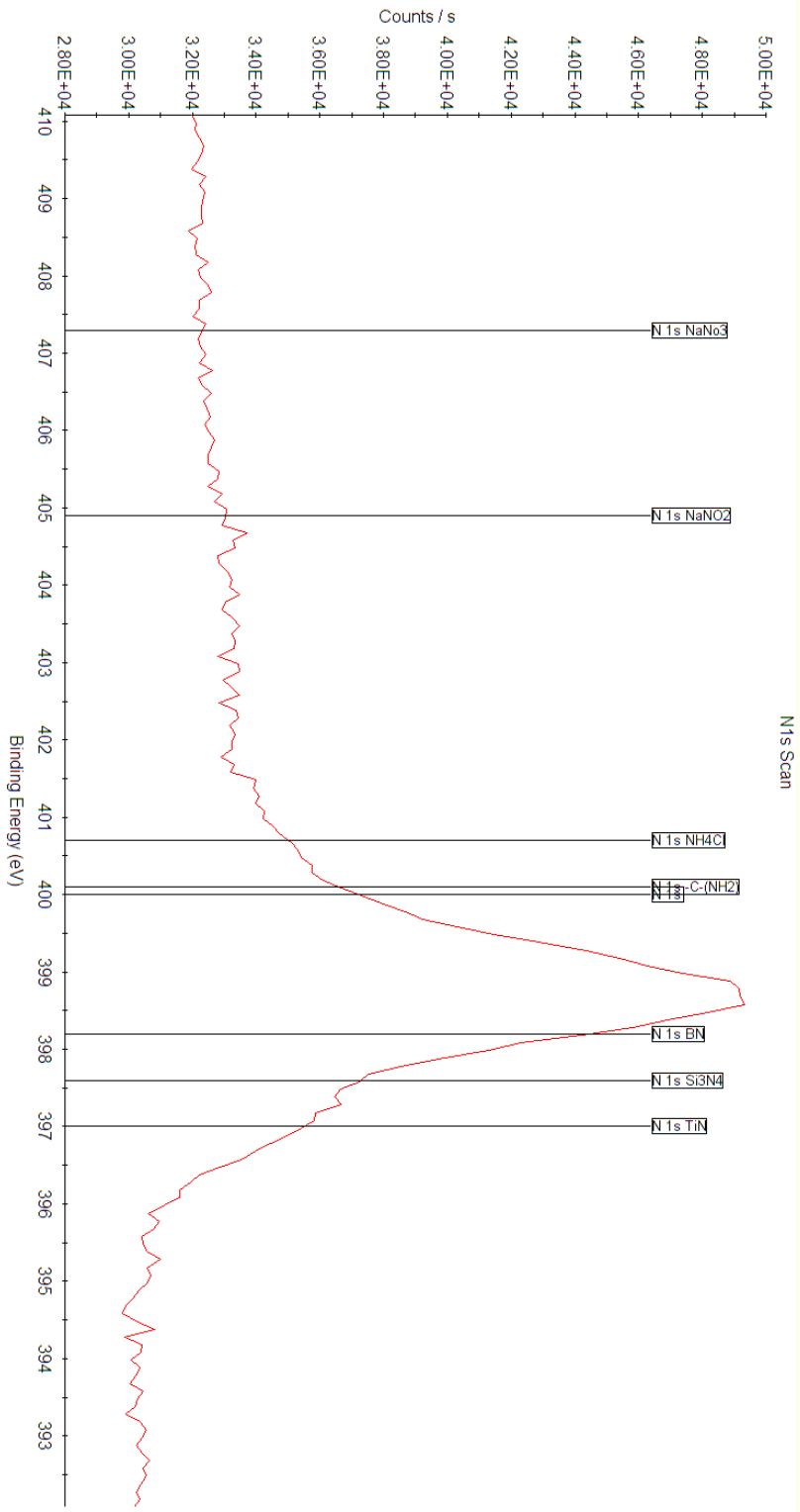

Figure B-38. Subsurface nitrogen 1s x-ray photoelectron spectrum of etched Cu_3N foil prepared by flowing NH_3 prep.

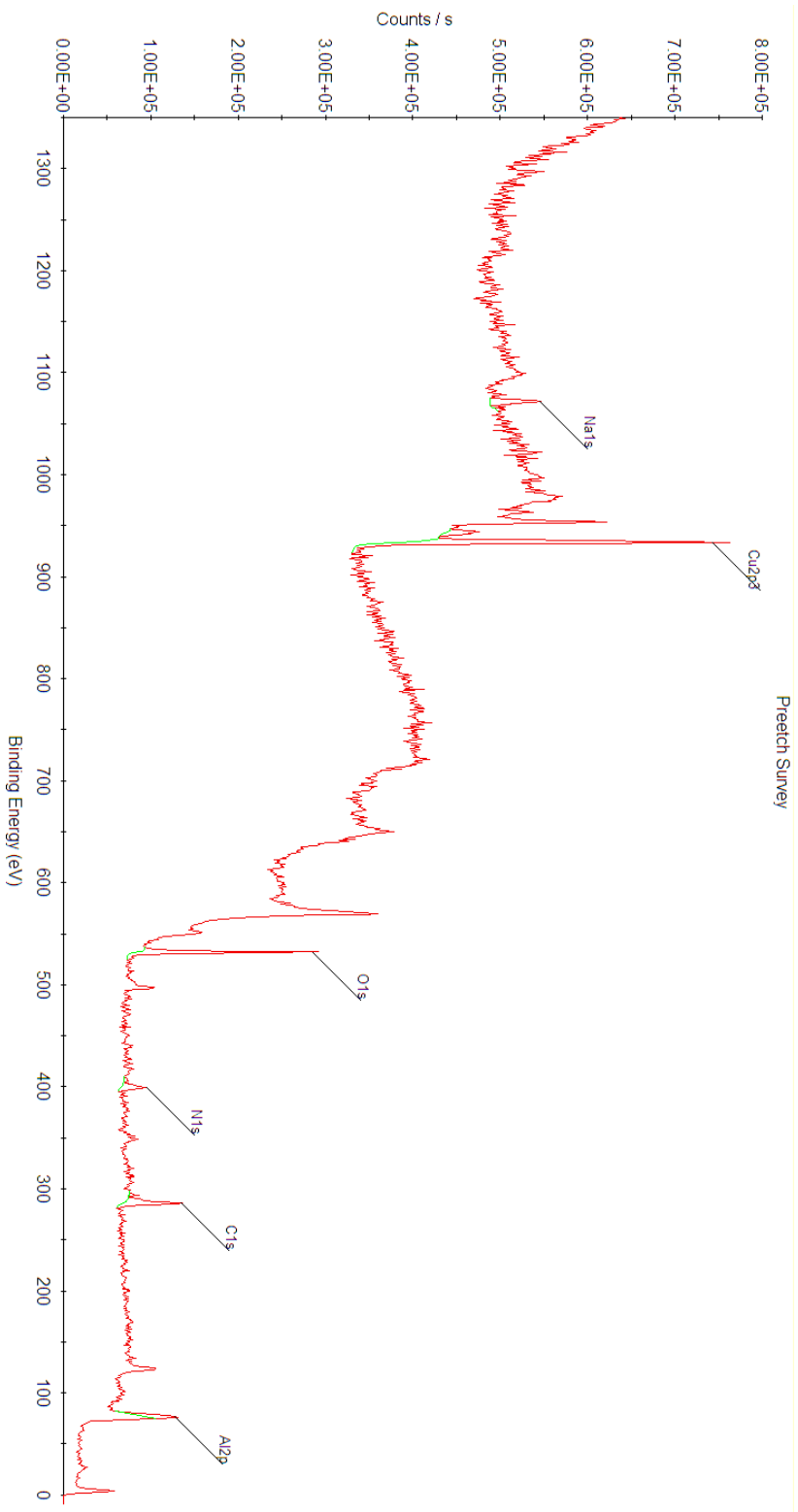

Figure B-39. Surface survey x-ray photoelectron spectrum of Cu_3N foam prepared by flowing NH_3 prep.

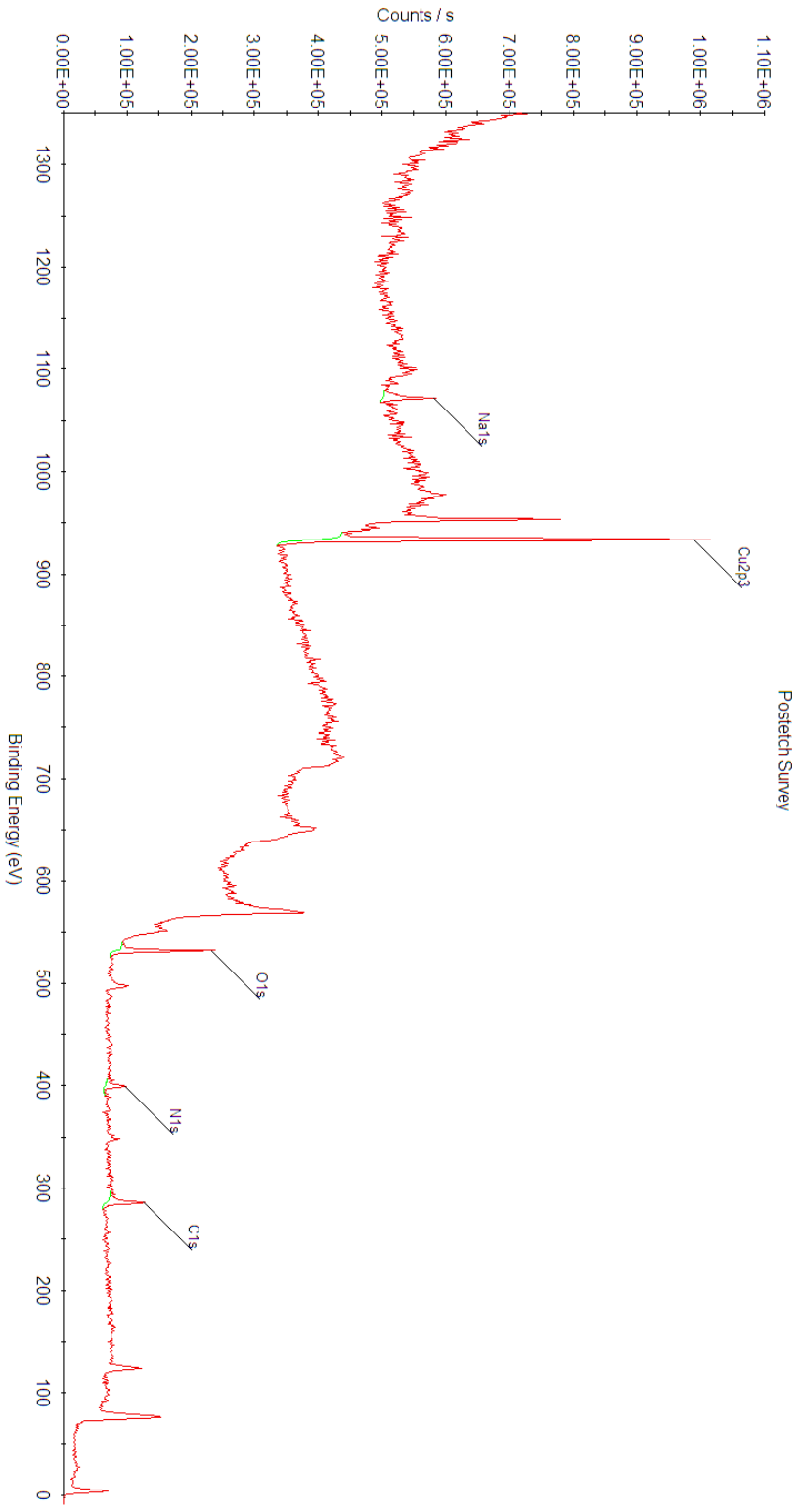

Figure B-40. Subsurface survey x-ray photoelectron spectrum of etched Cu_3N foam prepared by flowing NH_3 prep.

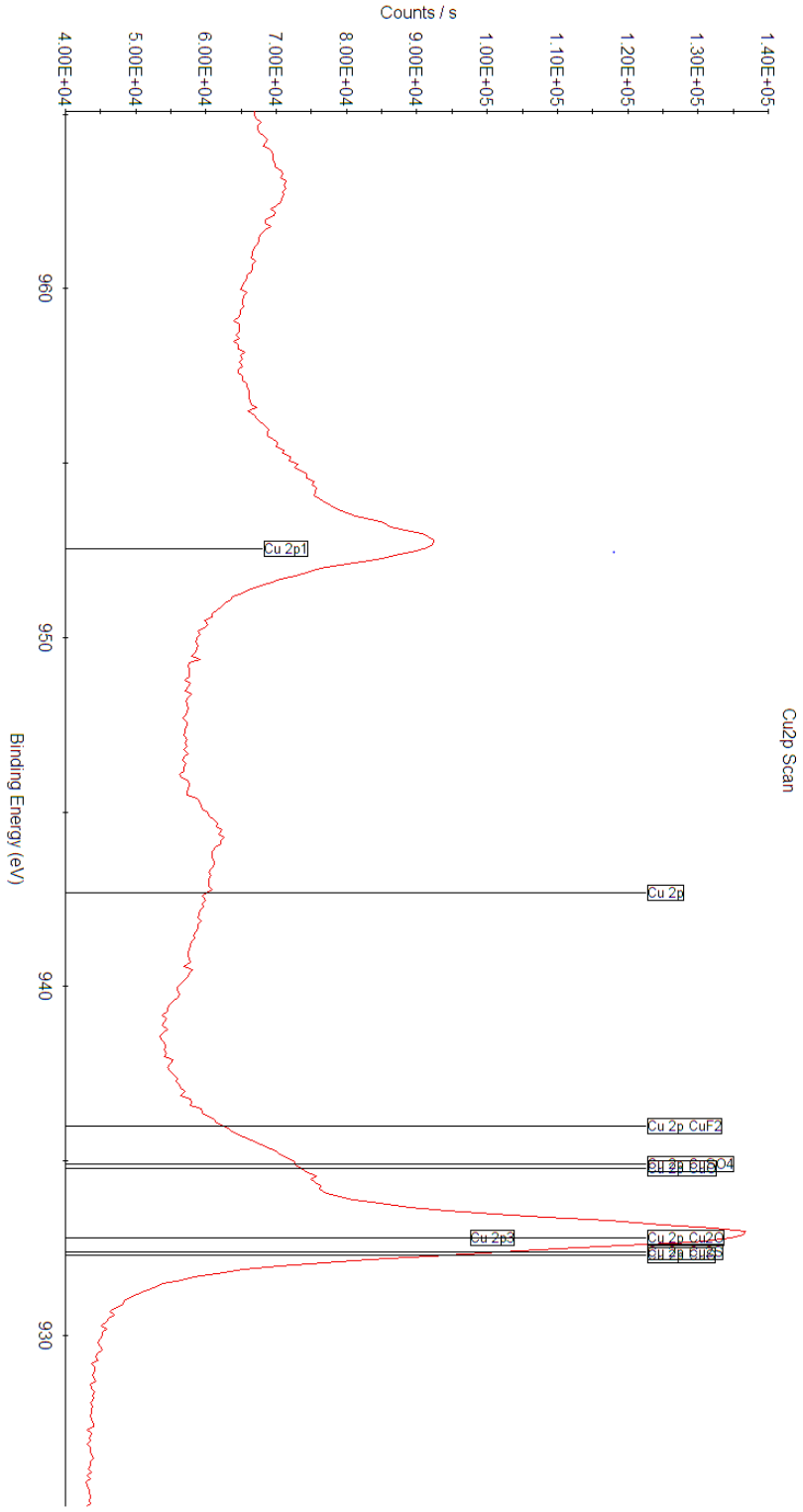

Figure B-41. Surface copper 2p x-ray photoelectron spectrum of Cu_3N foam prepared by flowing NH_3 prep.

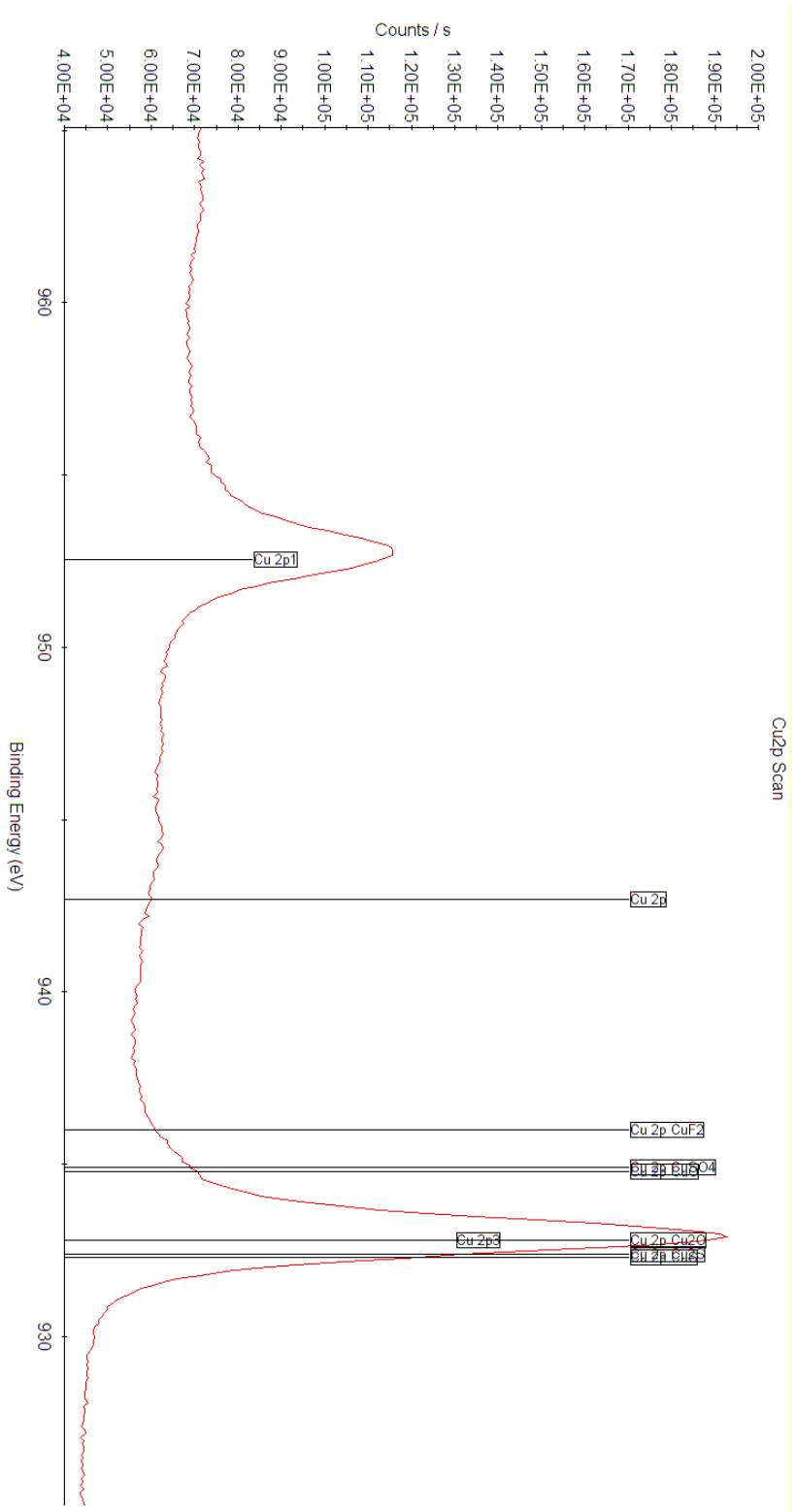

Figure B-42. Subsurface copper 2p x-ray photoelectron spectrum of etched Cu_3N foam prepared by flowing NH_3 prep.

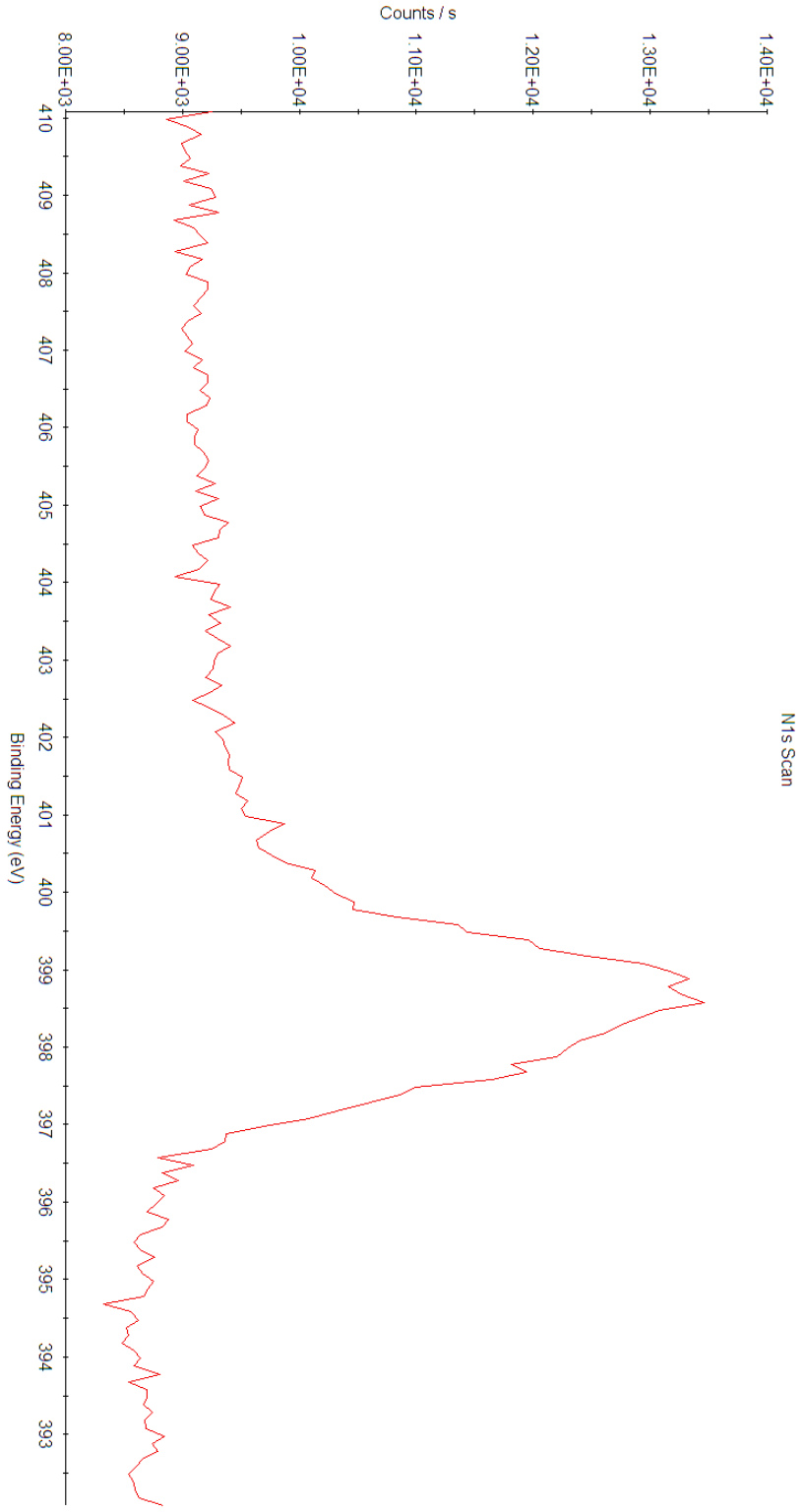

Figure B-43. Surface nitrogen 1s x-ray photoelectron spectrum of Cu_3N foam prepared by flowing NH_3 prep.

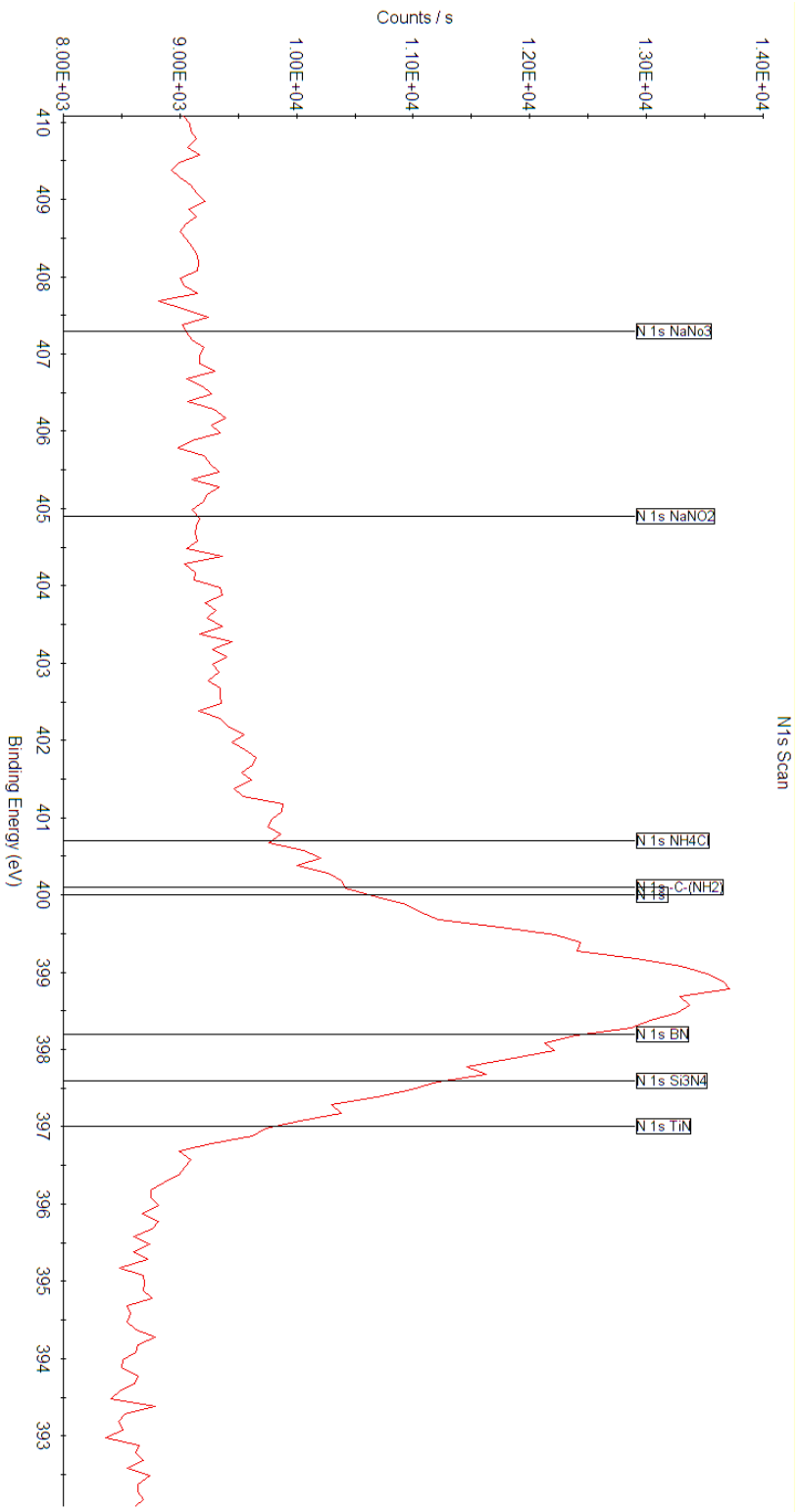

Figure B-44. Subsurface nitrogen 1s x-ray photoelectron spectrum of etched Cu_3N foam prepared by flowing NH_3 prep.

B.4.3 Vanadium Nitride

B.4.3.1 Sodium Amide Synthesis

Vanadium foil, thickness 1.0 mm, 99.999% trace metals basis from Millipore Sigma was nitridated by sodium amide prep as described in **Section 3.4.4.3** on page 144.

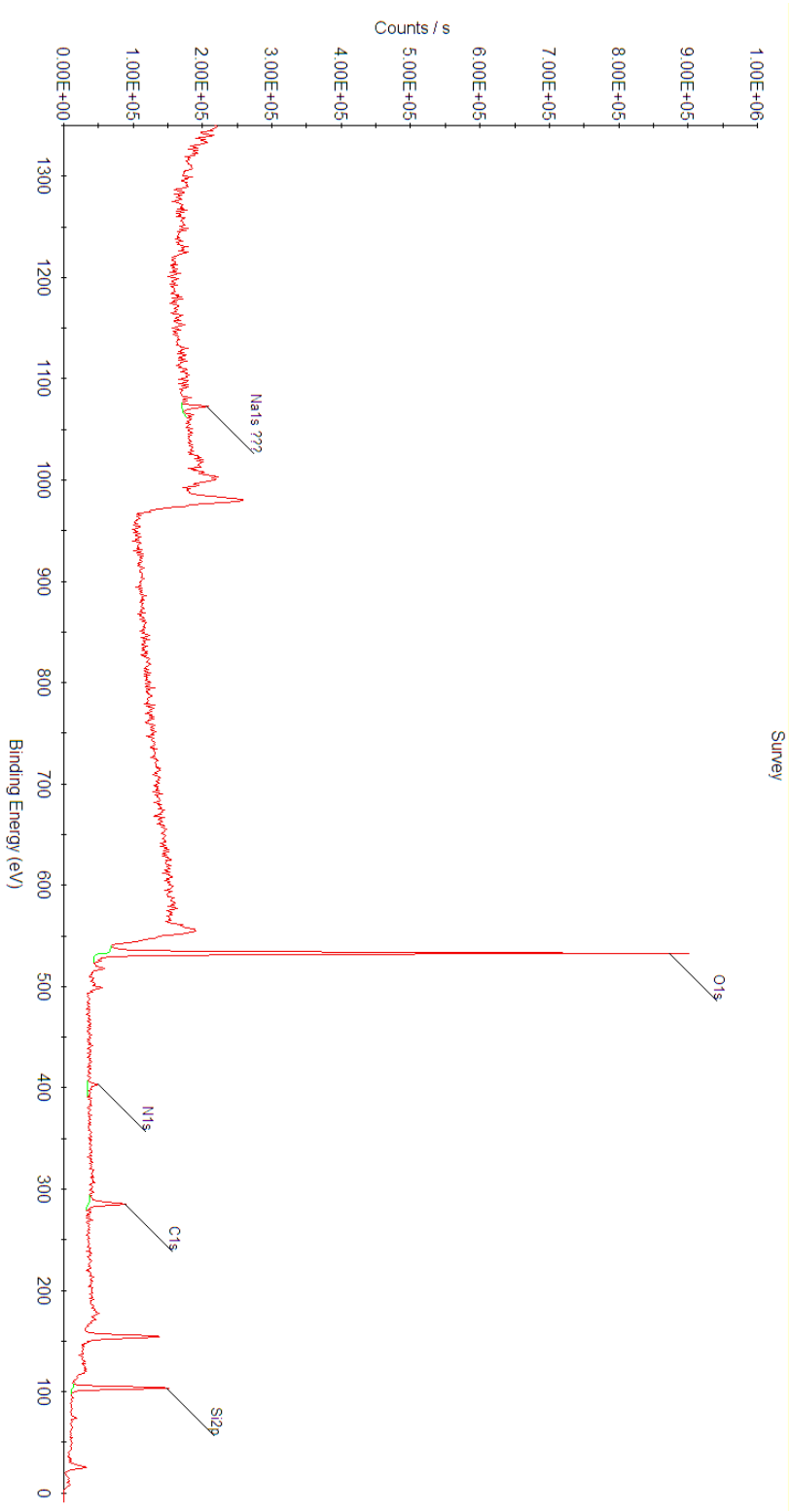

Figure B-45. Survey x-ray photoelectron spectrum of vanadium nitride electrode prepared by sodium amide prep.

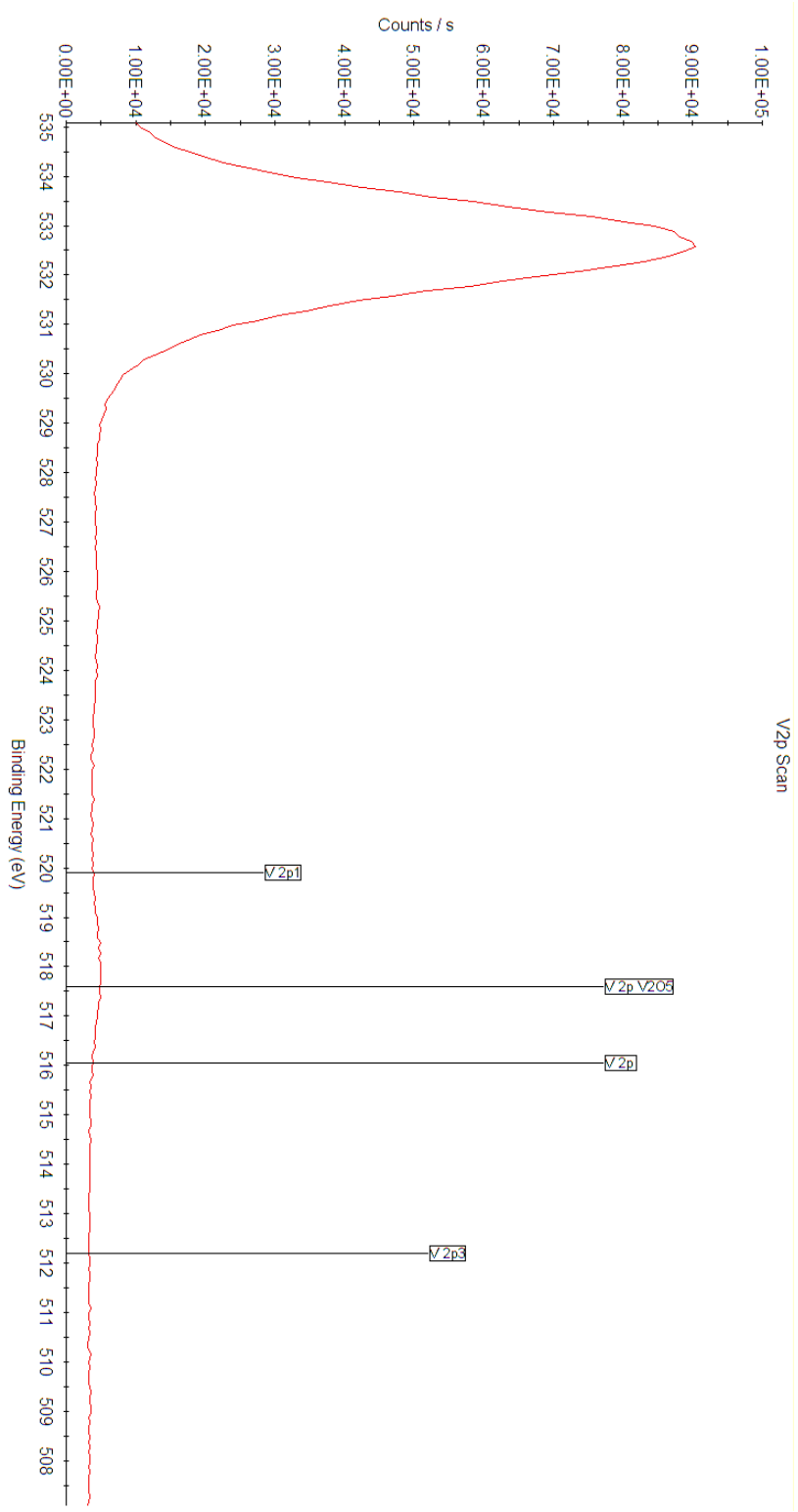

Figure B-46. Vanadium 2p x-ray photoelectron spectrum of vanadium nitride electrode prepared by sodium amide prep.

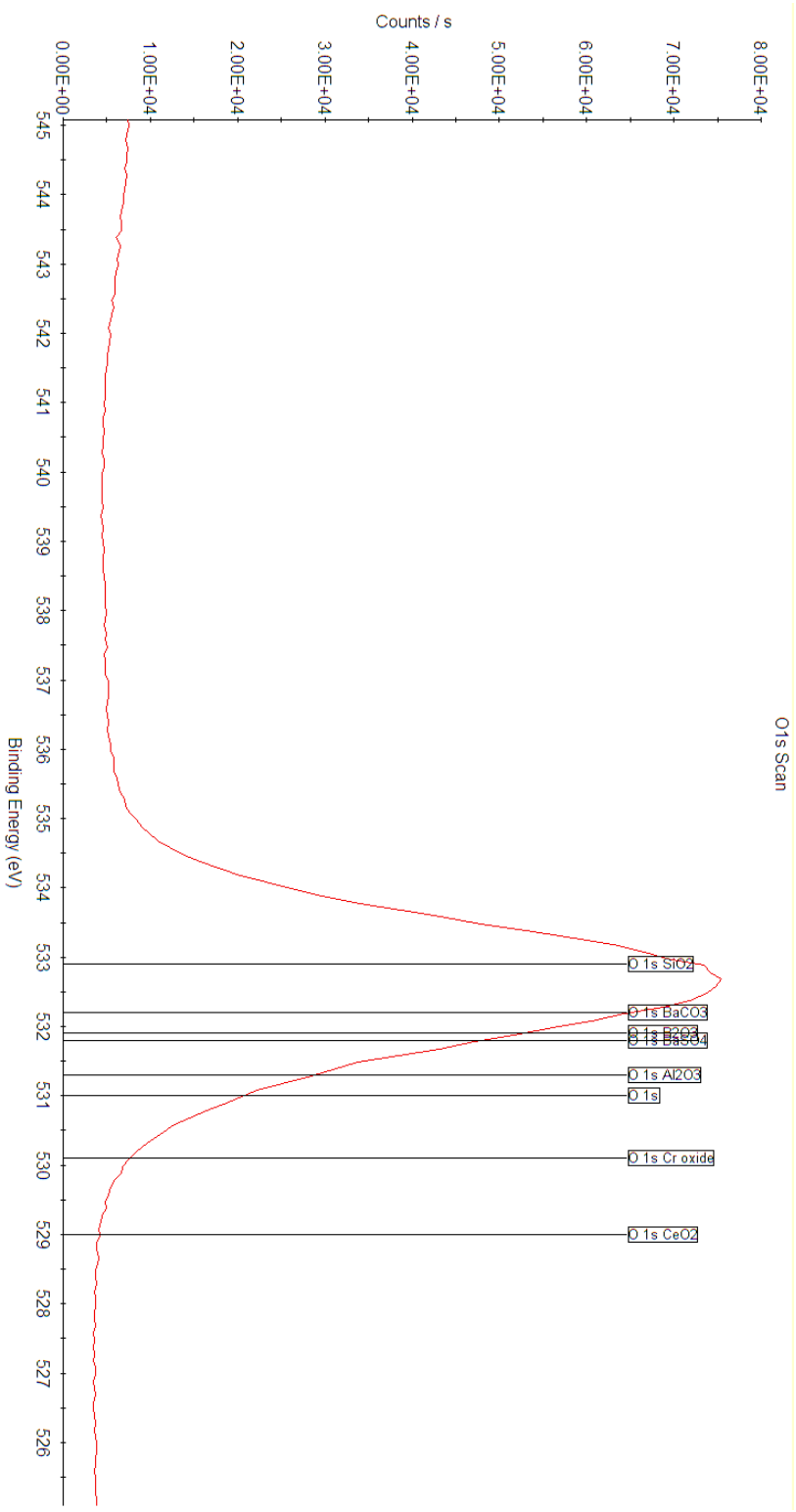

Figure B-47. Oxygen 1s x-ray photoelectron spectrum of vanadium nitride electrode prepared by sodium amide prep.

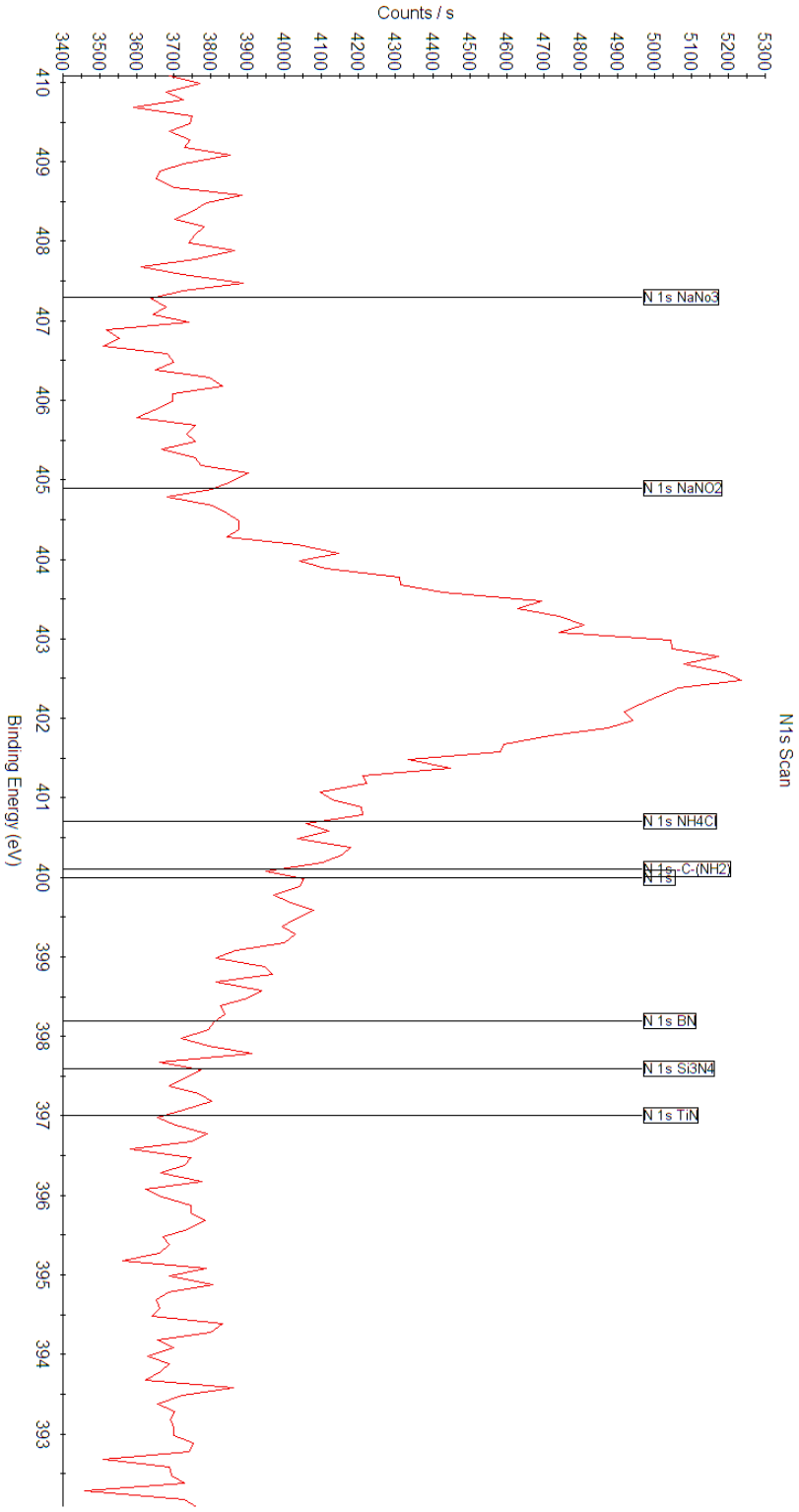

Figure B-48. Nitrogen 1s x-ray photoelectron spectrum of vanadium nitride electrode prepared by sodium amide prep.

B.4.3.2 Urea Synthesis

Vanadium foil, thickness 1.0 mm, 99.999% trace metals basis from Millipore Sigma was nitridated by urea prep as described in **Section 3.4.4.4** on page 145.

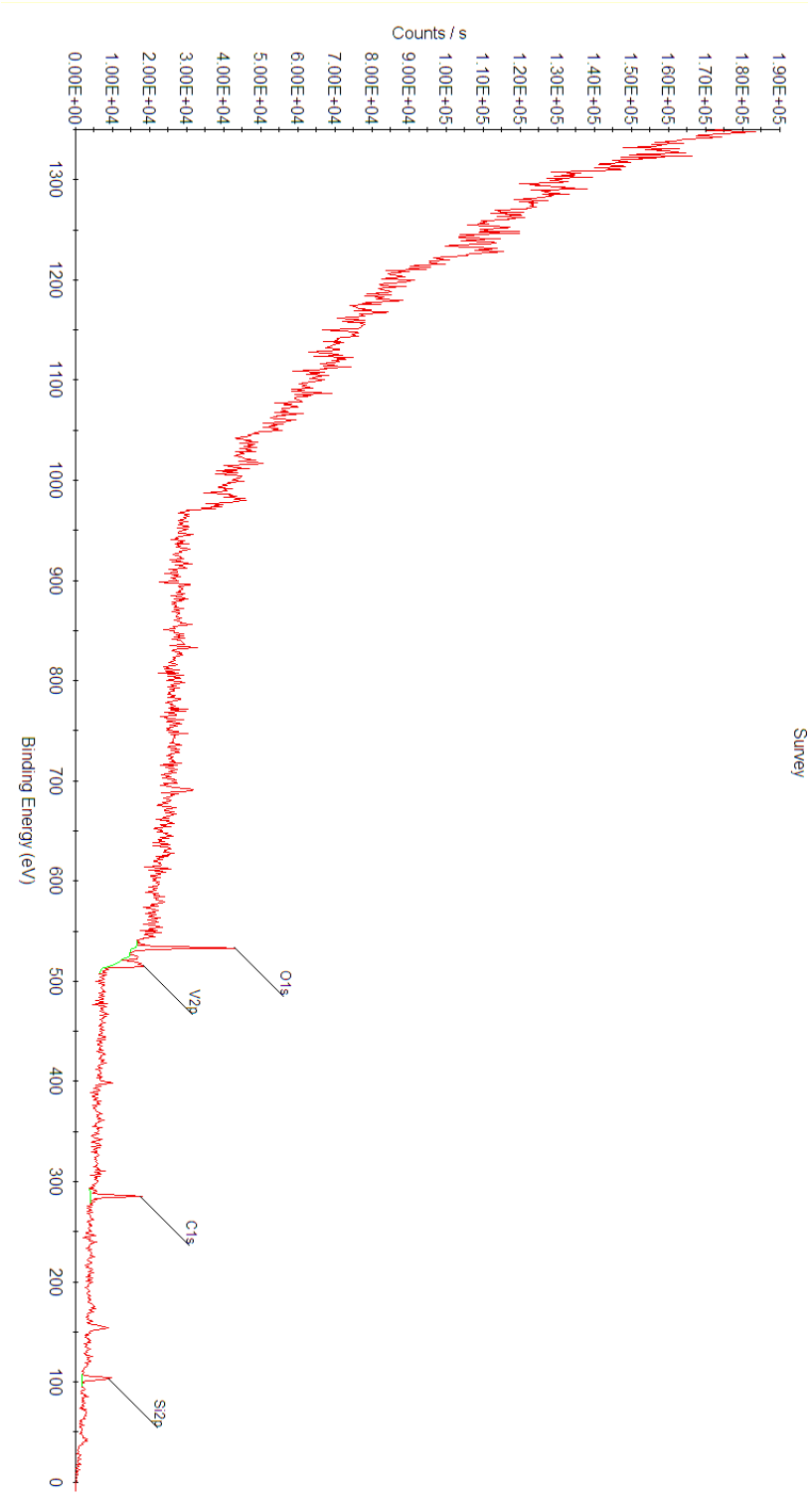

Figure B-49. Survey x-ray photoelectron spectrum of vanadium nitride electrode prepared by urea prep.

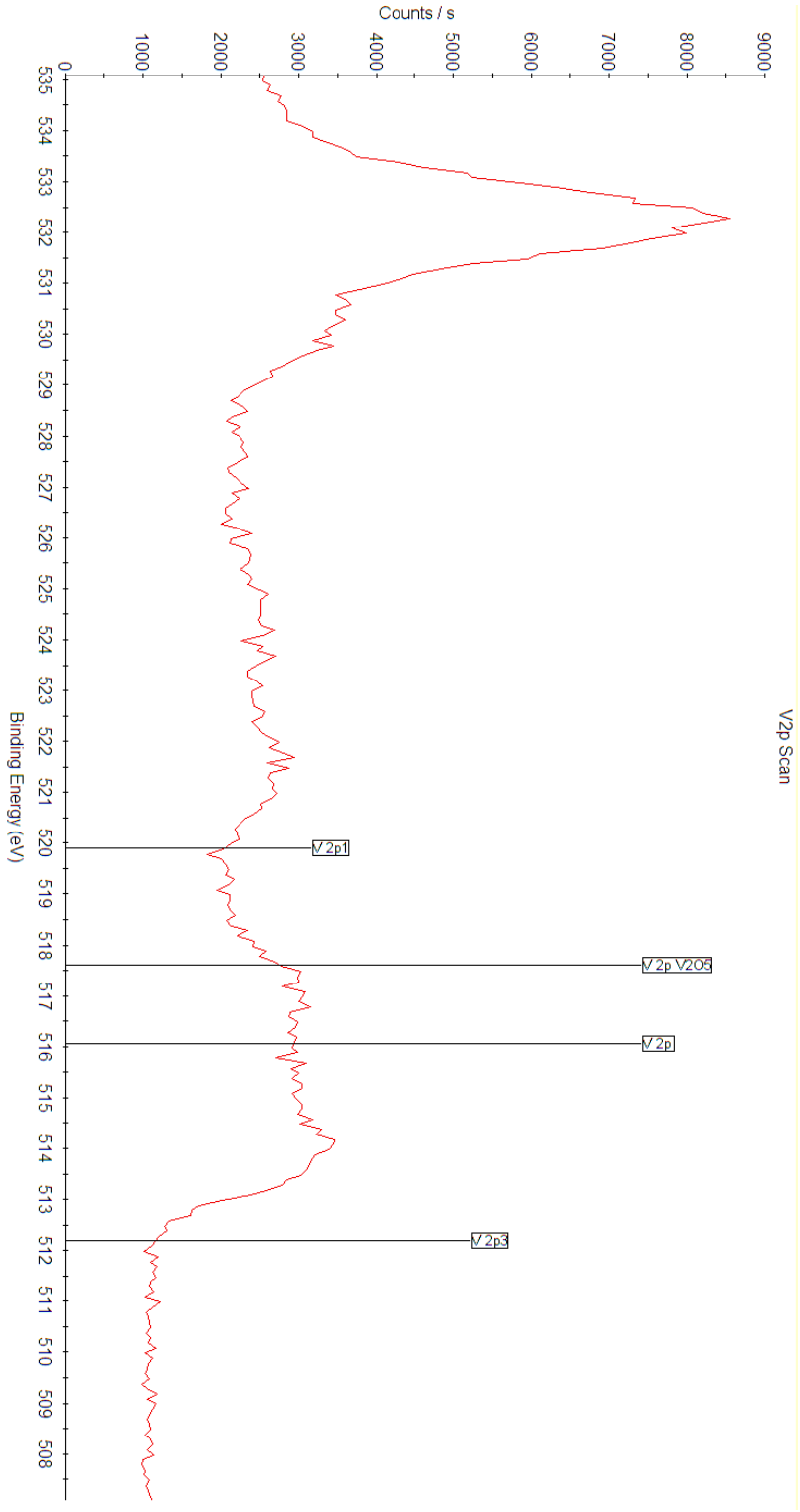

Figure B-50. Vanadium 2p x-ray photoelectron spectrum of vanadium nitride electrode prepared by urea prep.

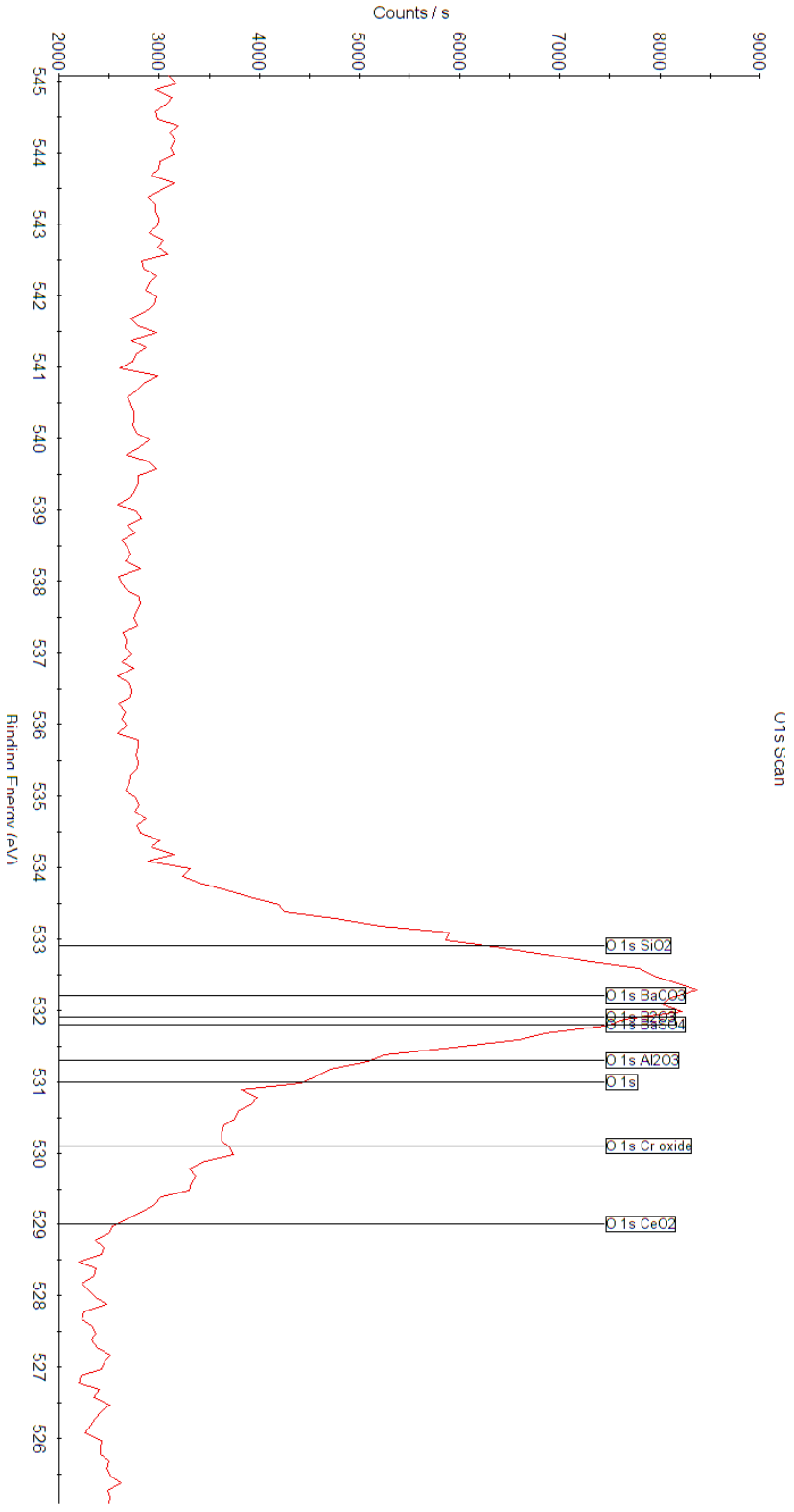

Figure B-51. Oxygen 1s x-ray photoelectron spectrum of vanadium nitride electrode prepared by urea prep.

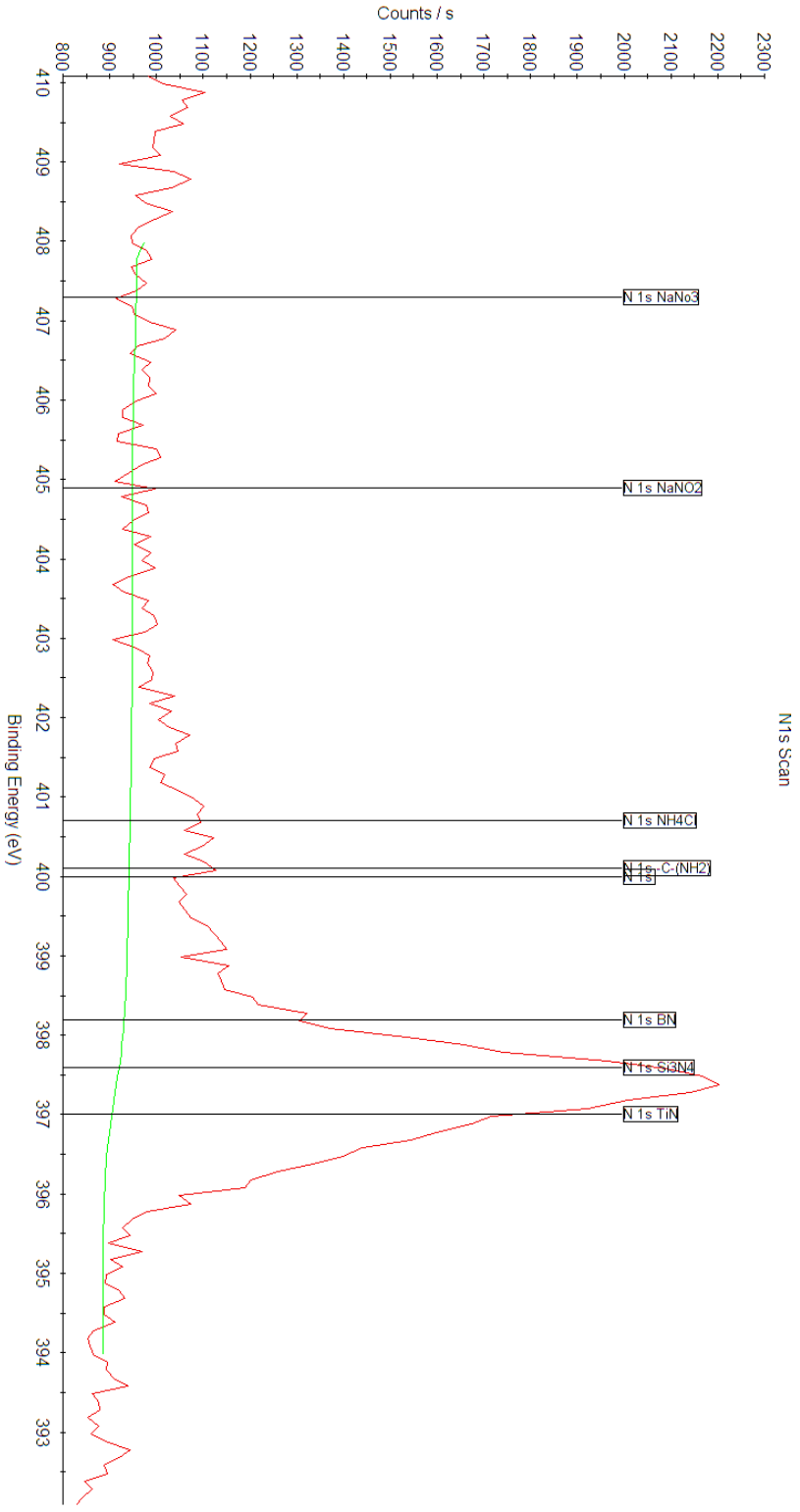

Figure B-52. Nitrogen 1s x-ray photoelectron spectrum of vanadium nitride electrode prepared by urea prep.

Appendix C

Supplementary Information on Electrochemical Methane Functionalization

Contents

C.1 ^{1}H NMR Spectra

All NMR spectra were recorded in concentrated sulfuric acid media with Bruker AVANCE-300, -400, or -500 spectrometers and processed using MestReNova software. Spectra were

collected using a benzene-d_6 internal lock capillary or using a 20% loading of $D_2SO_4 - d_2$ in H_2SO_4 as the sample medium. Presaturation solvent suppression techniques were applied to reduce the protic H_2SO_4 signals. ^{1}H NMR chemical shifts are given in ppm with respect to the internal standard ($(NH_4)_2SO_4$ δ6.15 ppm). Coupling constants are reported as J-values in Hz.

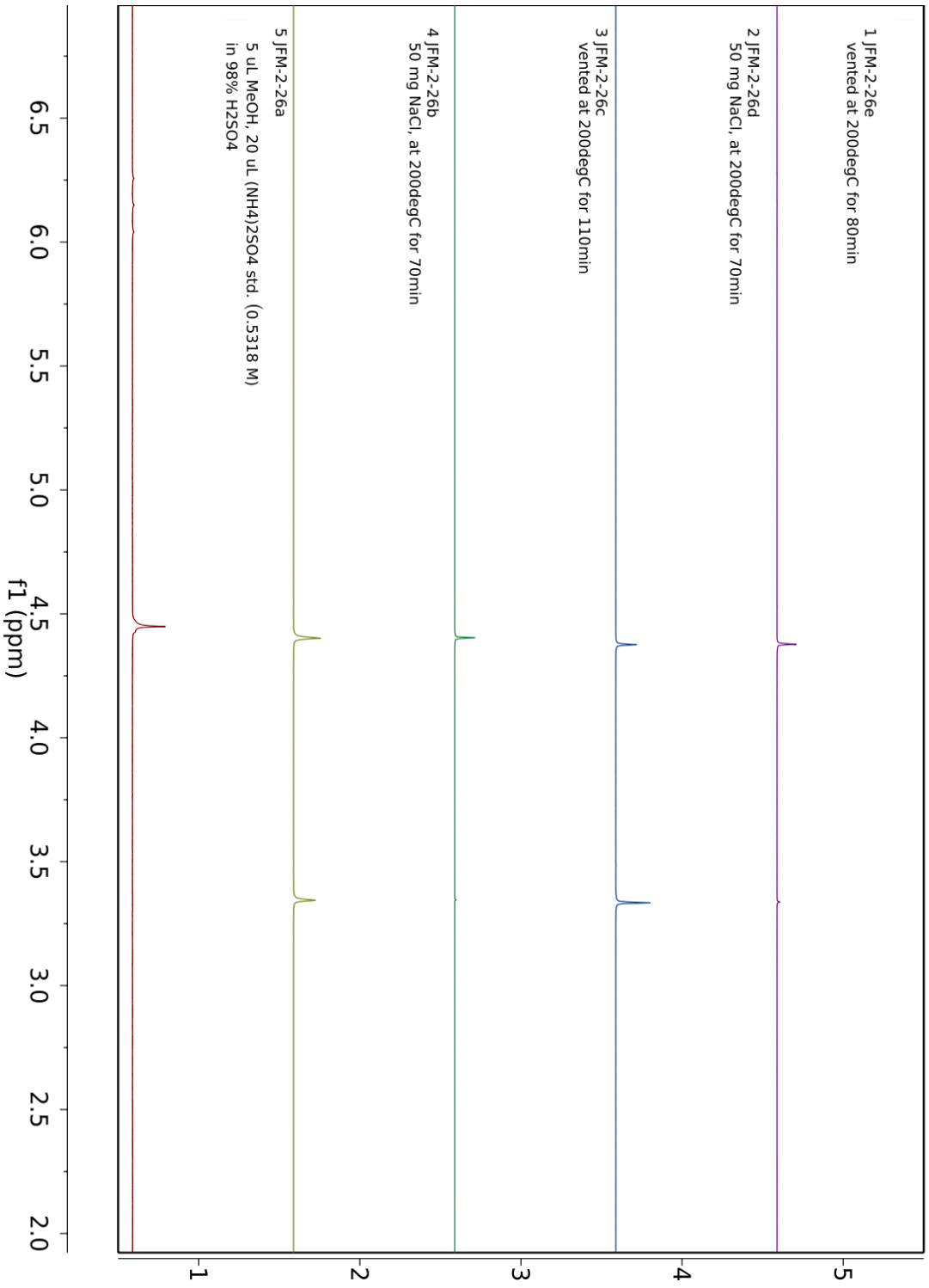

Figure C-1. Stacked ^{1}H NMR spectra of MBS in H_2SO_4, showing generation of MeCl by *in situ* HCl evolution, and subsequent removal of MeCl by venting.

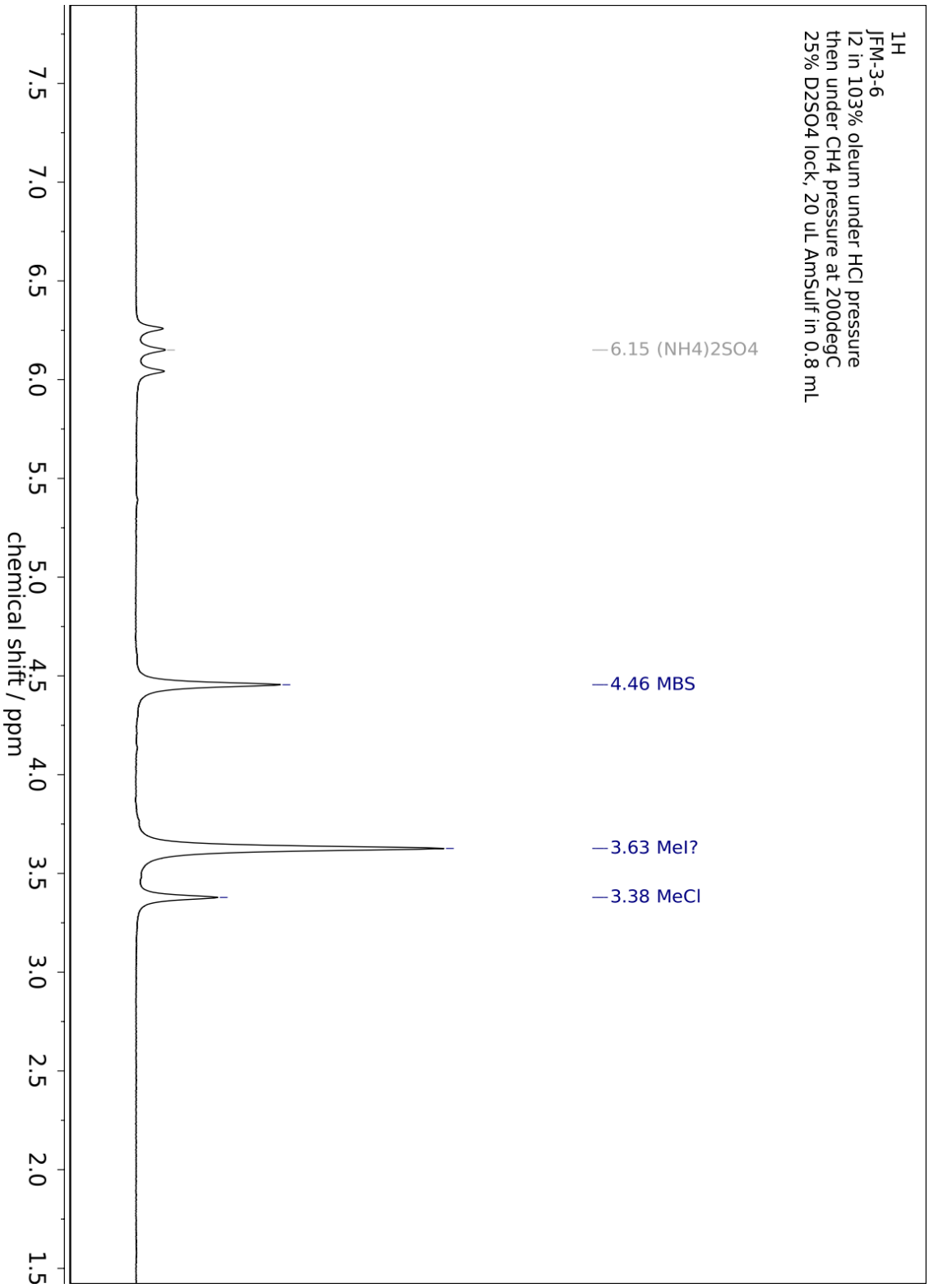

Figure C-2. ^{1}H NMR spectrum of of MBS generated by I_2 in 3% fuming H_2SO_4, showing generation of MeCl but also presumably MeI.

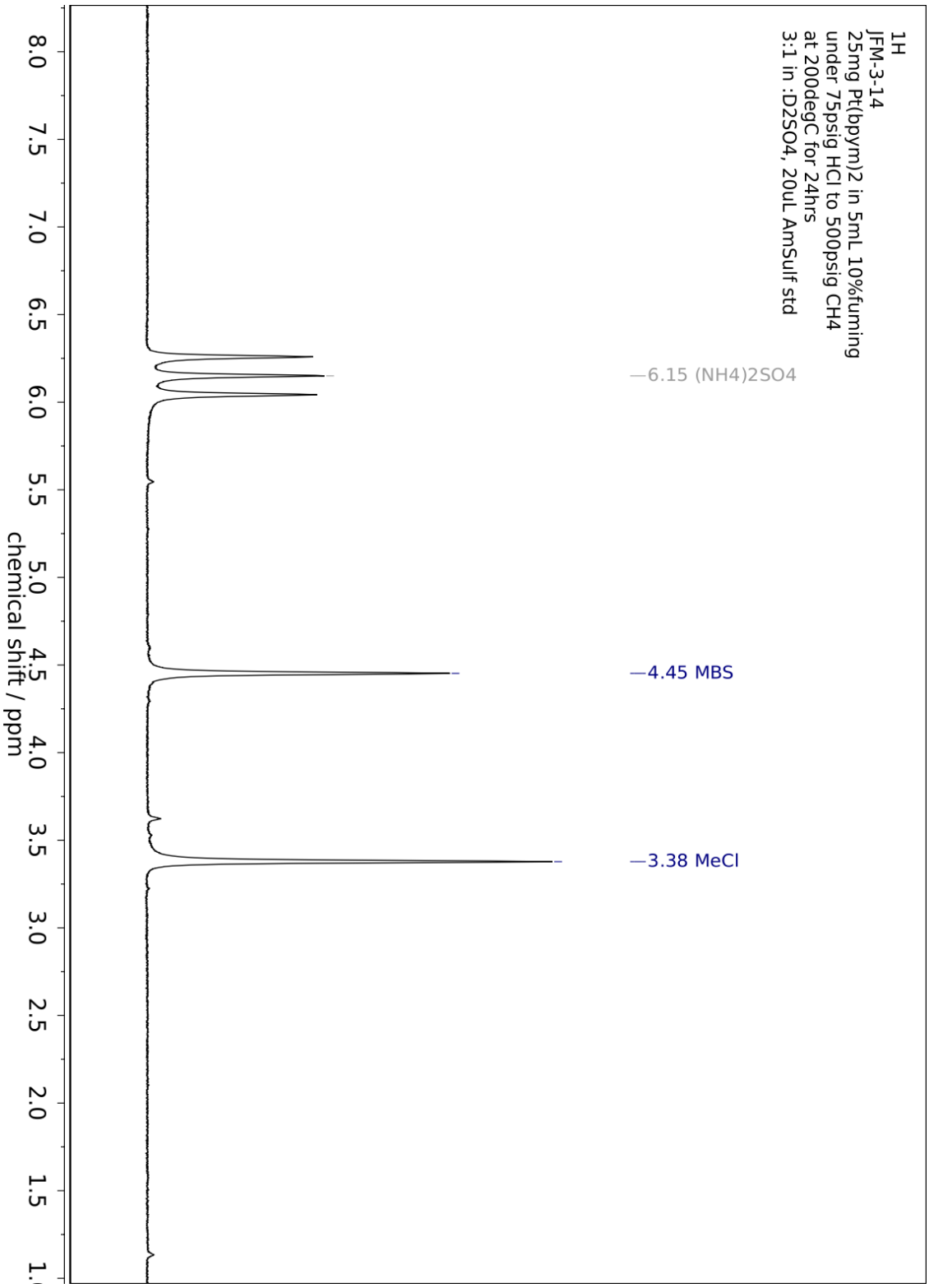

Figure C-3. ^{1}H NMR spectrum of of MBS generated by Pt(bpym)Cl_2 in 3% fuming H_2SO_4, showing generation of MeCl.

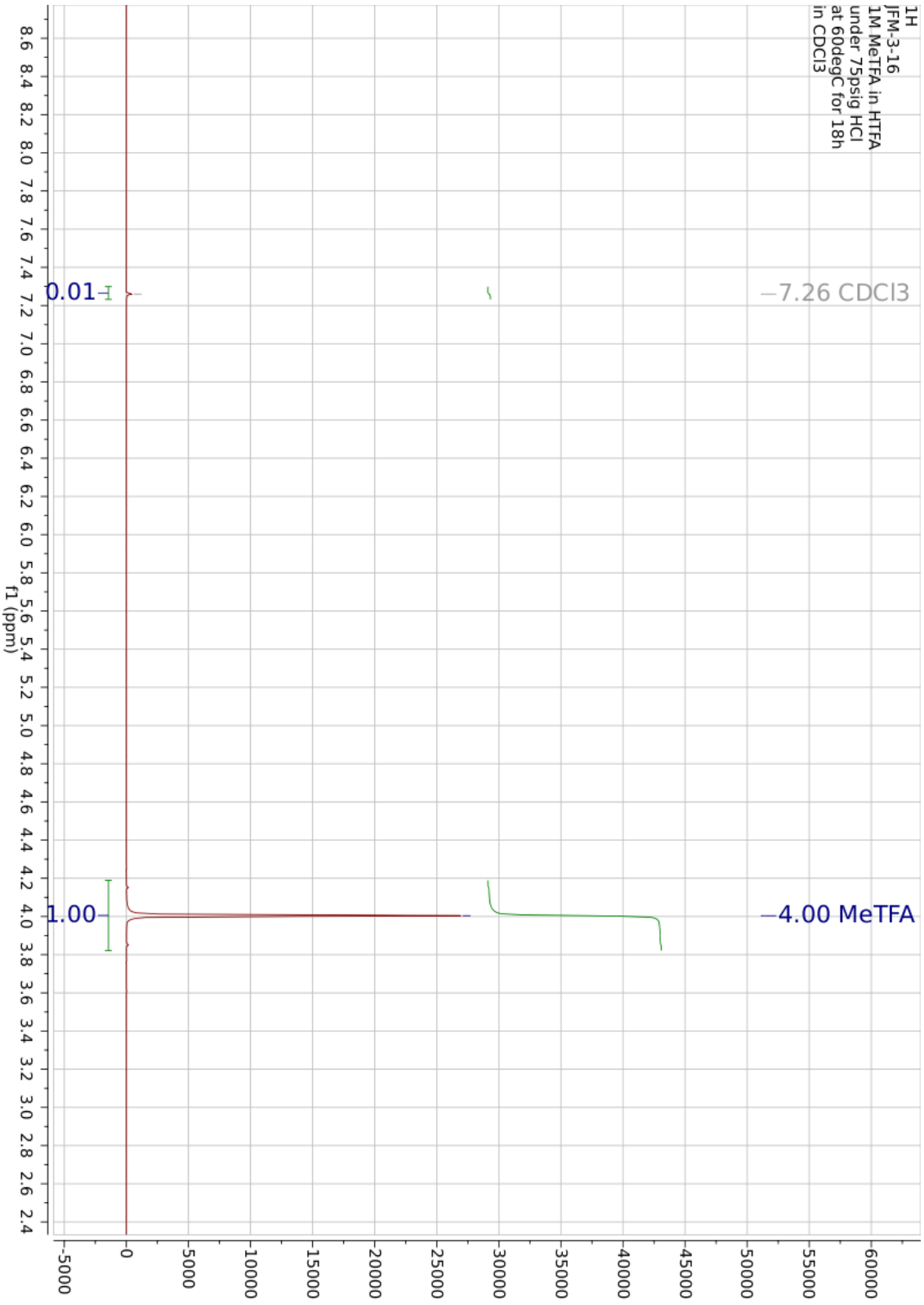

Figure C-4. ^{1}H NMR spectrum of MeTFA in HTFA under 60 psig HCl pressure, showing no appreciable conversion to MeCl.

C.2 Process Flow Diagrams for Functionalized Methane Product Separations

C.2.1 Process Flow Diagrams for Methyl Bisulfate Hydrolysis

Reactions were modeled at an inflow rate of $1\,000\,000\,\mathrm{m^3 \cdot d^{-1}}$ of natural gas at an assumed composition of 90% CH_4, 3% C_2H_6, 1% C_3H_8, 5% CO_2, 0.99% N_2, and 100 ppm H_2S. The efficiency of the electrochemical methane functionalization reactor was artifically imposed at 90% conversion of methane to methyl bisulfate, 5% overoxidation of methane to CO_2, and 5% methane left unconverted.

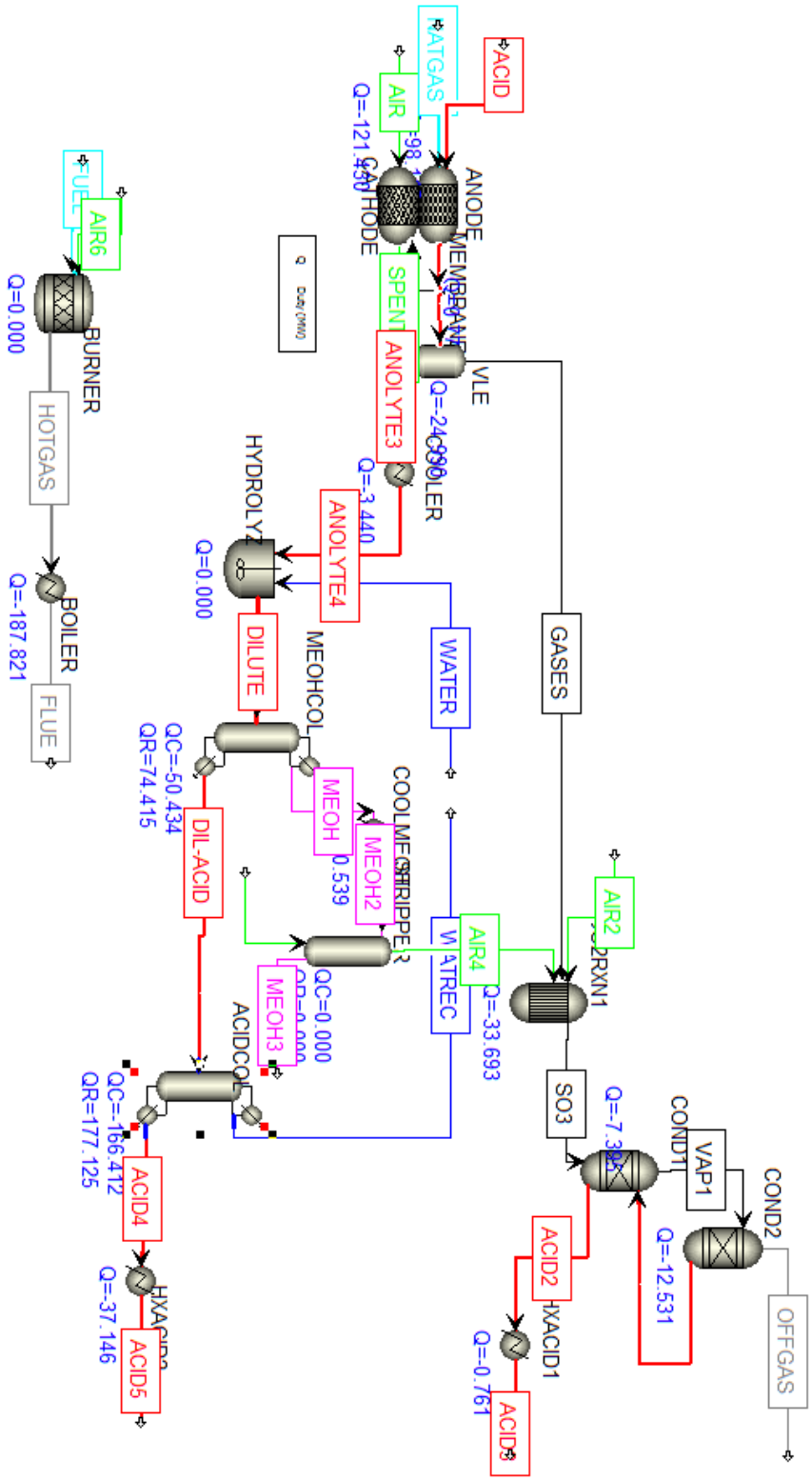

Figure C-5. Full process-flow diagram for methane gas-to-liquid conversion by electrochemical functionalization to methyl bisulfate and subsequent hydrolysis to methanol.

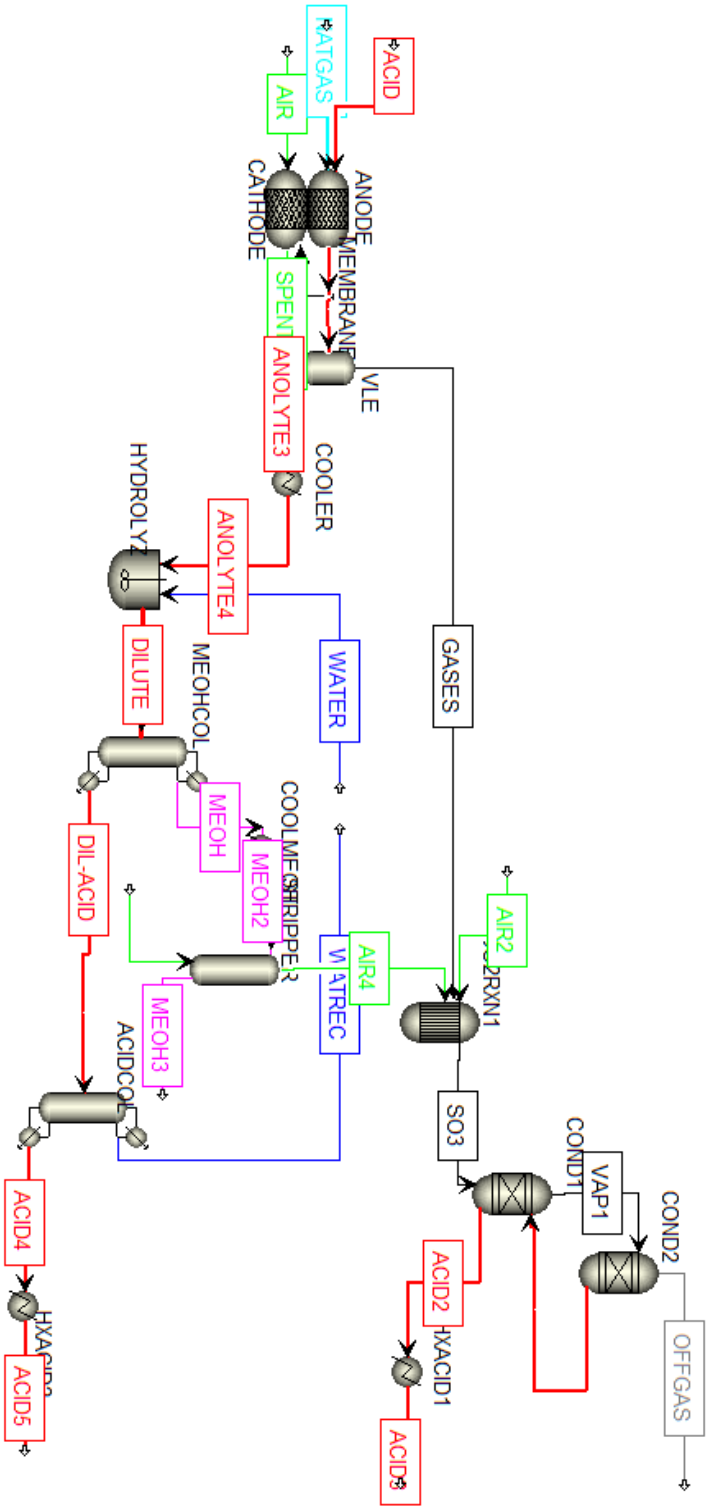

Figure C-6. Full process-flow diagram for methane gas-to-liquid conversion by electrochemical functionalization to methyl bisulfate and subsequent hydrolysis to methanol, without burners or heat balance.

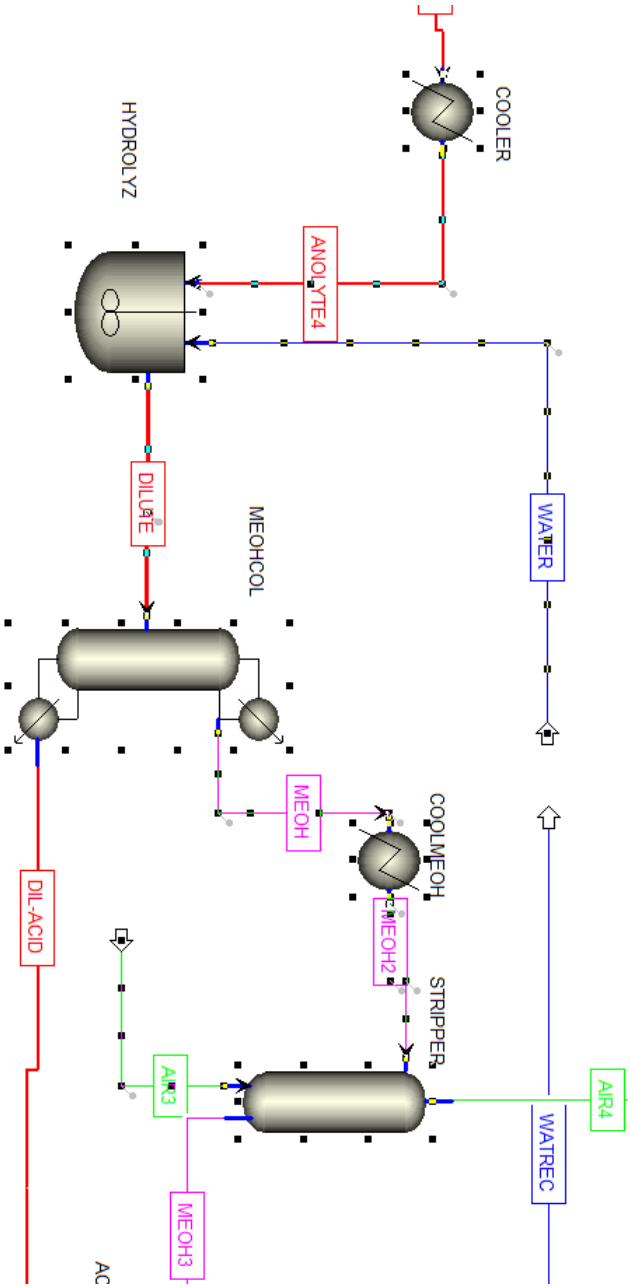

Figure C-7. Process-flow diagram for methyl bisulfate hydrolysis reactor and distillation columns.

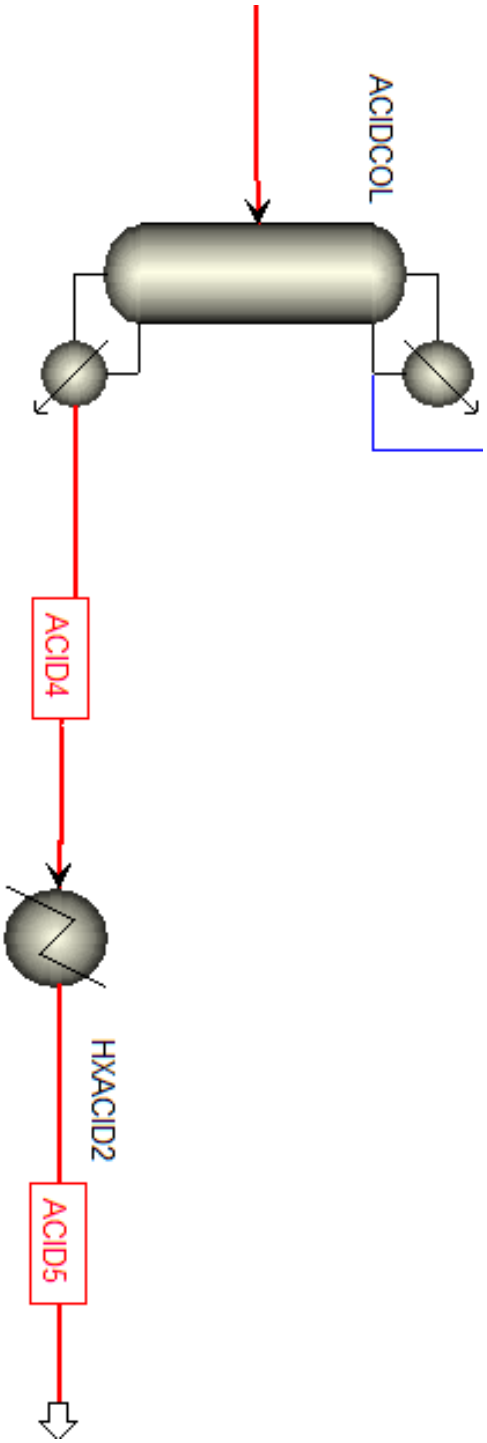

Figure C-8. Process-flow diagram for sulfuric acid reconcentration columns for methyl bisulfate hydrolysis process.

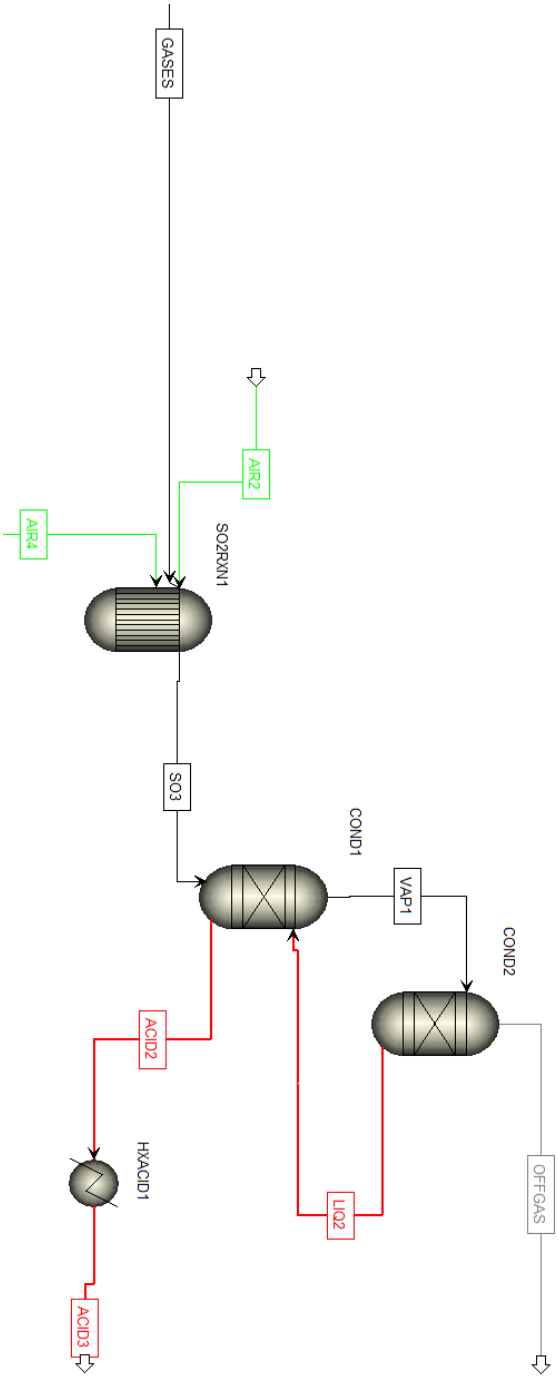

Figure C-9. Process-flow diagram for offgas stream and sulfuric acid condensers for methyl bisulfate hydrolysis process.

C.2.2 Process Flow Diagrams for Methyl Chloride Hydrolysis

Reactions were modeled at an inflow rate of $1\,000\,000\,m^3 \cdot d^{-1}$ of natural gas at an assumed composition of 94% CH_4, 5% CO_2, 0.75% N_2, and 2500 ppm H_2S. The efficiency of the electrochemical methane functionalization reactor was artifically imposed at 59% conversion of methane to methyl bisulfate and 41% methane left unconverted, and assuming that an equilibrium concentration of 3 M for methyl bisulfate in H_2SO_4 was achieved. The process was found to generate enough high-pressure steam to support its distillation & power needs. In order to minimize reactor overheads to minimize the process footprint, a 'falling-film absorber anode reactor' layout (**Figure C-10**) was proposed for the primary electrochemical reactor, combining SO_3 absorption, methane absorption, and methyl bisulfate electrogeneration into a single reactor. This reactor is modeled as a 4-stage counter-current vapor-liquid reactor with simultaneous electrolyte chemistry.

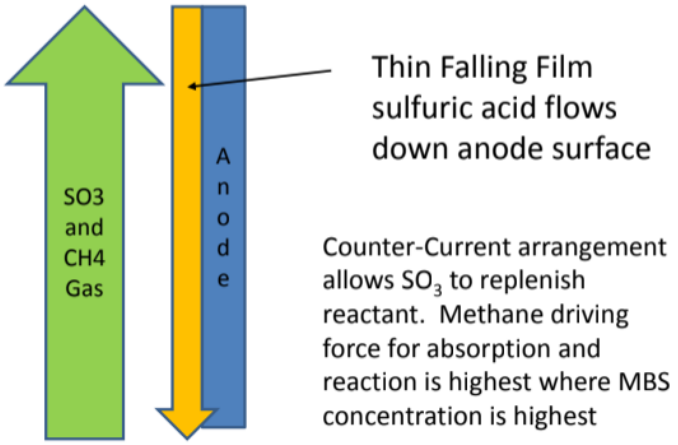

Figure C-10. Diagram of proposed falling-film absorber anode reactor layout for electrochemical conversion of methane to methyl bisulfate. Design by Randall Field.

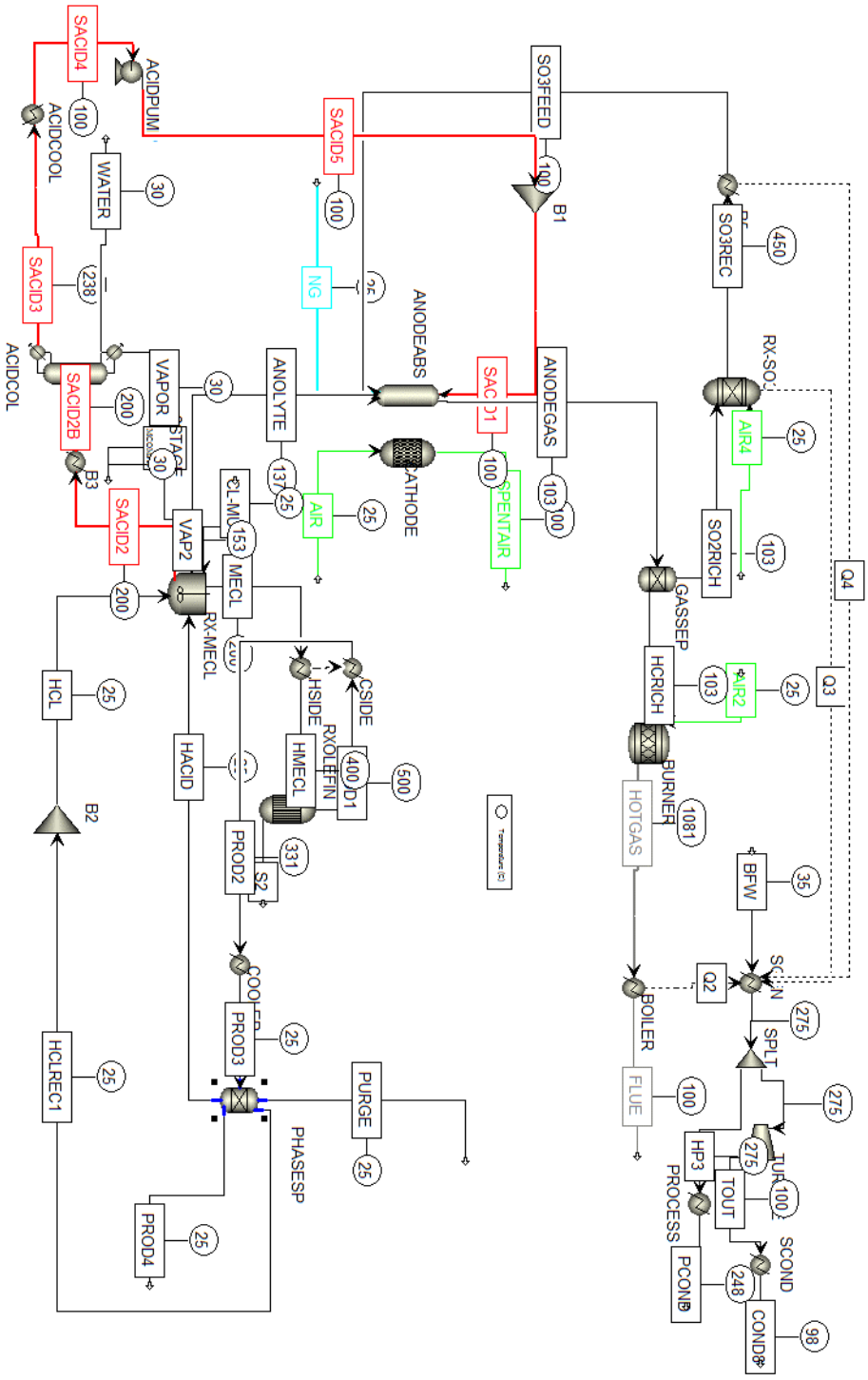

Figure C-11. Full process-flow diagram for methane gas-to-liquid conversion by electrochemical functionalization, conversion to methyl chloride, and hydrolysis to methanol.

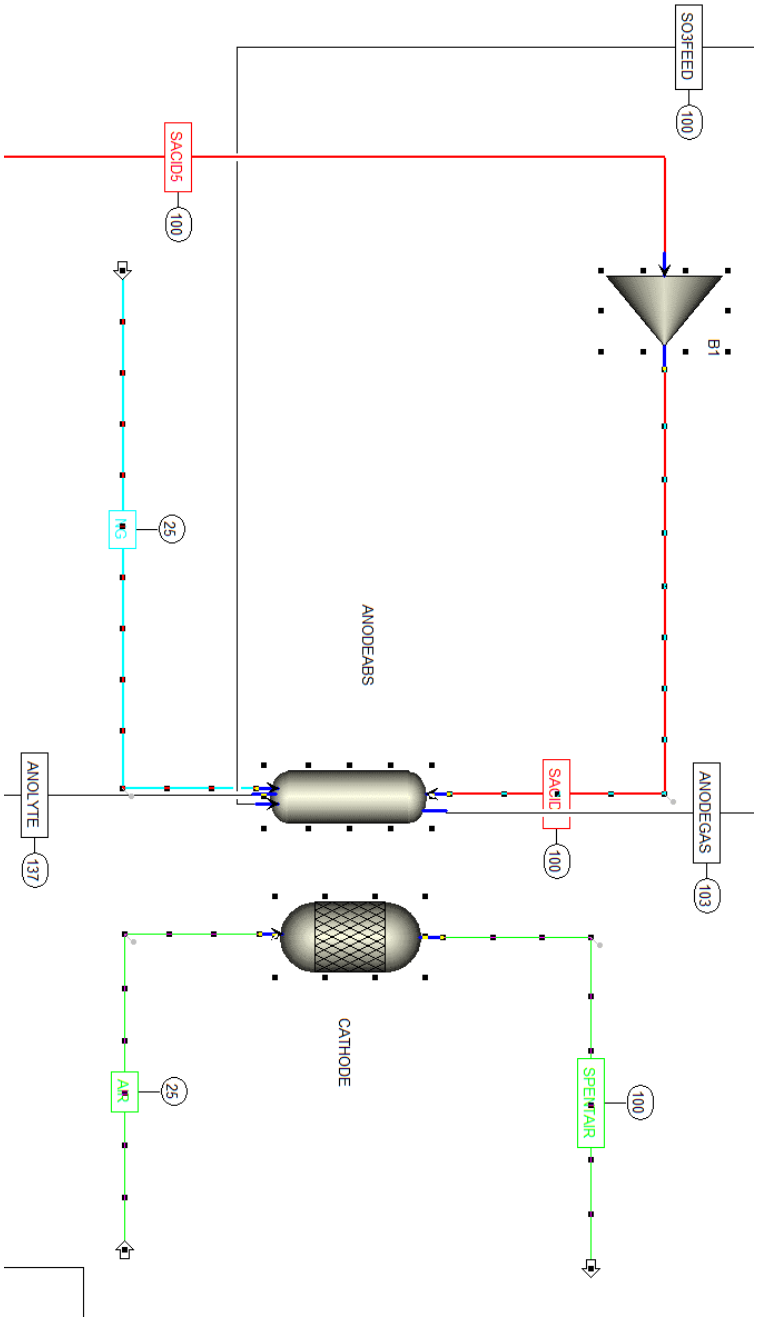

Figure C-12. Process-flow diagram for methyl bisulfate conversion reactor from methyl chloride hydrolysis gas-to-liquid process.

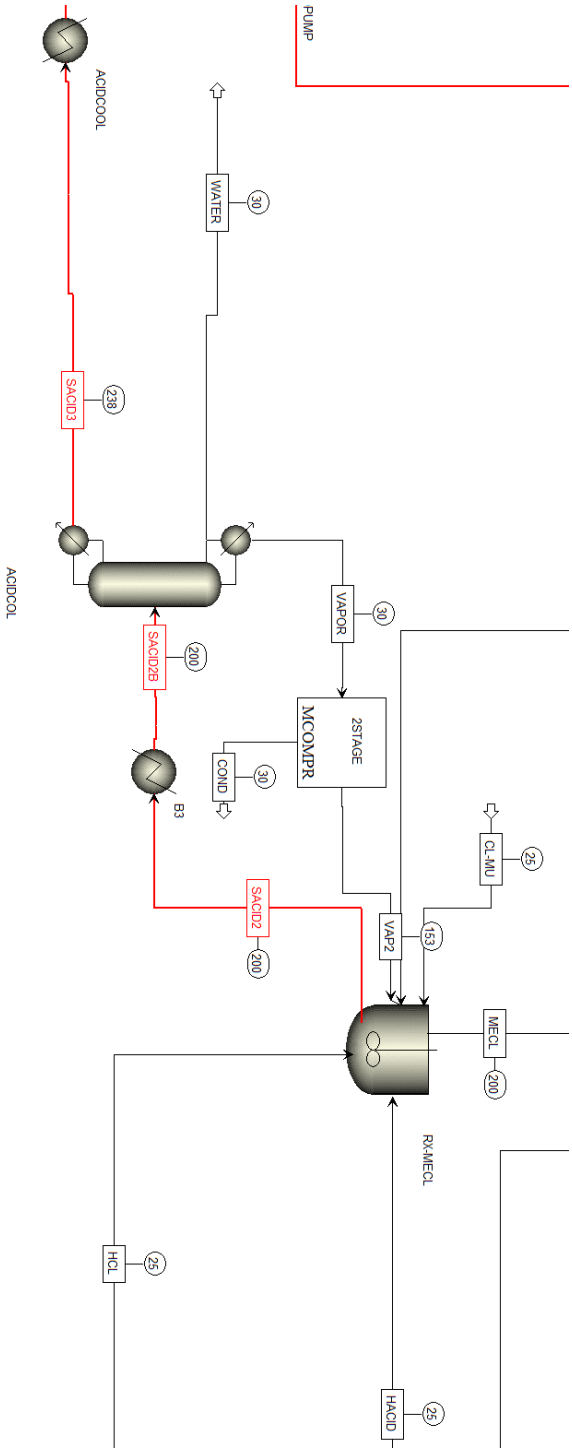

Figure C-13. Process-flow diagram for methyl chloride conversion reactor from methyl chloride hydrolysis gas-to-liquid process.

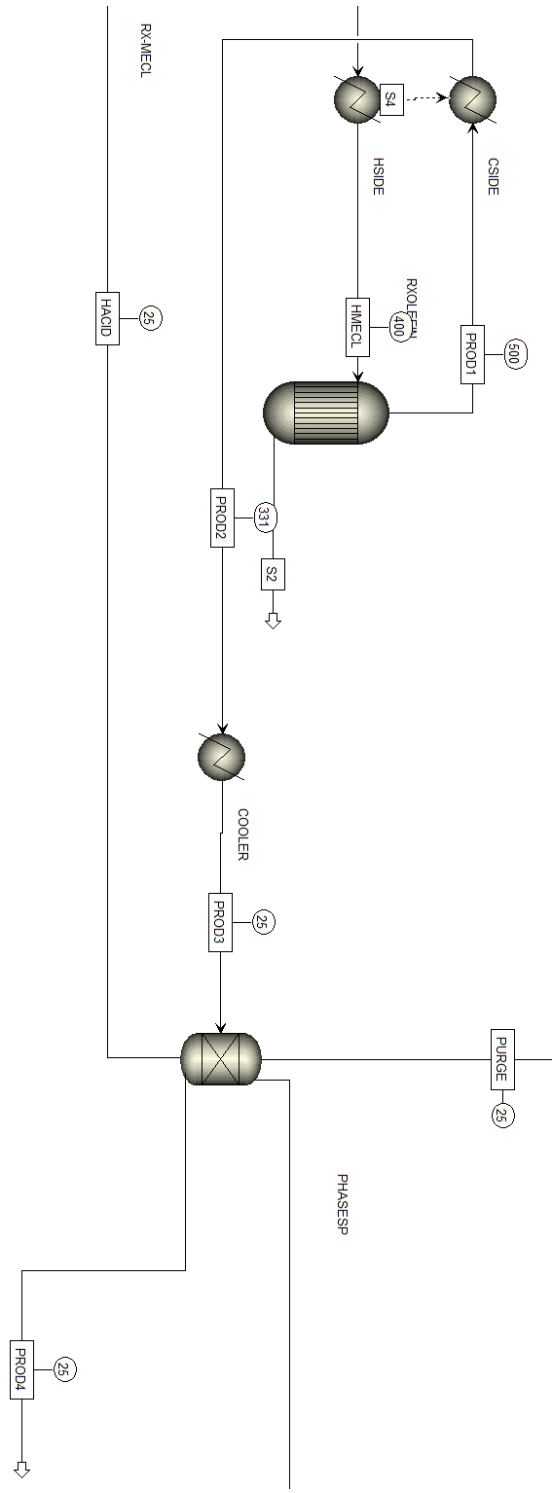

Figure C-14. Process-flow diagram for olefin conversion reactor from methyl chloride hydrolysis gas-to-liquid process.

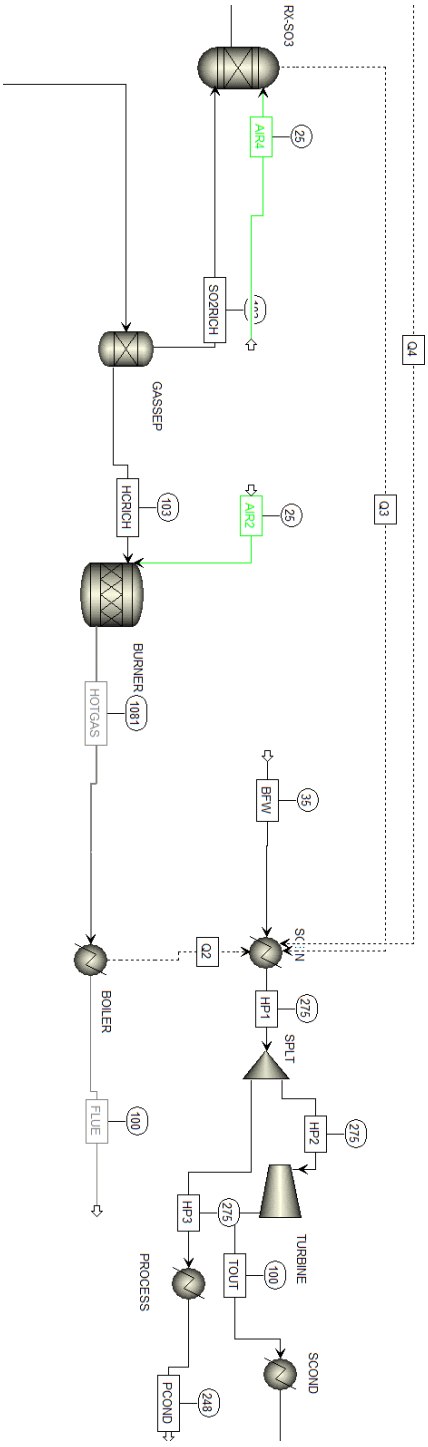

Figure C-15. Process-flow diagram for burners for methyl chloride hydrolysis gas-to-liquid process.

C.2.3 Process Flow Diagrams for Methyl Chloride Upconversion

Reactions were modeled at an inflow rate of $1\,000\,000\,m^3 \cdot d^{-1}$ of natural gas at an assumed composition of 94% CH_4, 5% CO_2, 0.75% N_2, and 2500 ppm H_2S. The efficiency of the electrochemical methane functionalization reactor was artifically imposed at 59% conversion of methane to methyl bisulfate and 41% methane left unconverted, and assuming that an equilibrium concentration of 3 M for methyl bisulfate in H_2SO_4 was achieved. The process was found to generate enough high-pressure steam to support its distillation & power needs. In order to minimize reactor overheads to minimize the process footprint, a 'falling-film absorber anode reactor' layout (**Figure C-10**) was proposed for the primary electrochemical reactor, combining SO_3 absorption, methane absorption, and methyl bisulfate electrogeneration into a single reactor. This reactor is modeled as a 4-stage counter-current vapor-liquid reactor with simultaneous electrolyte chemistry.

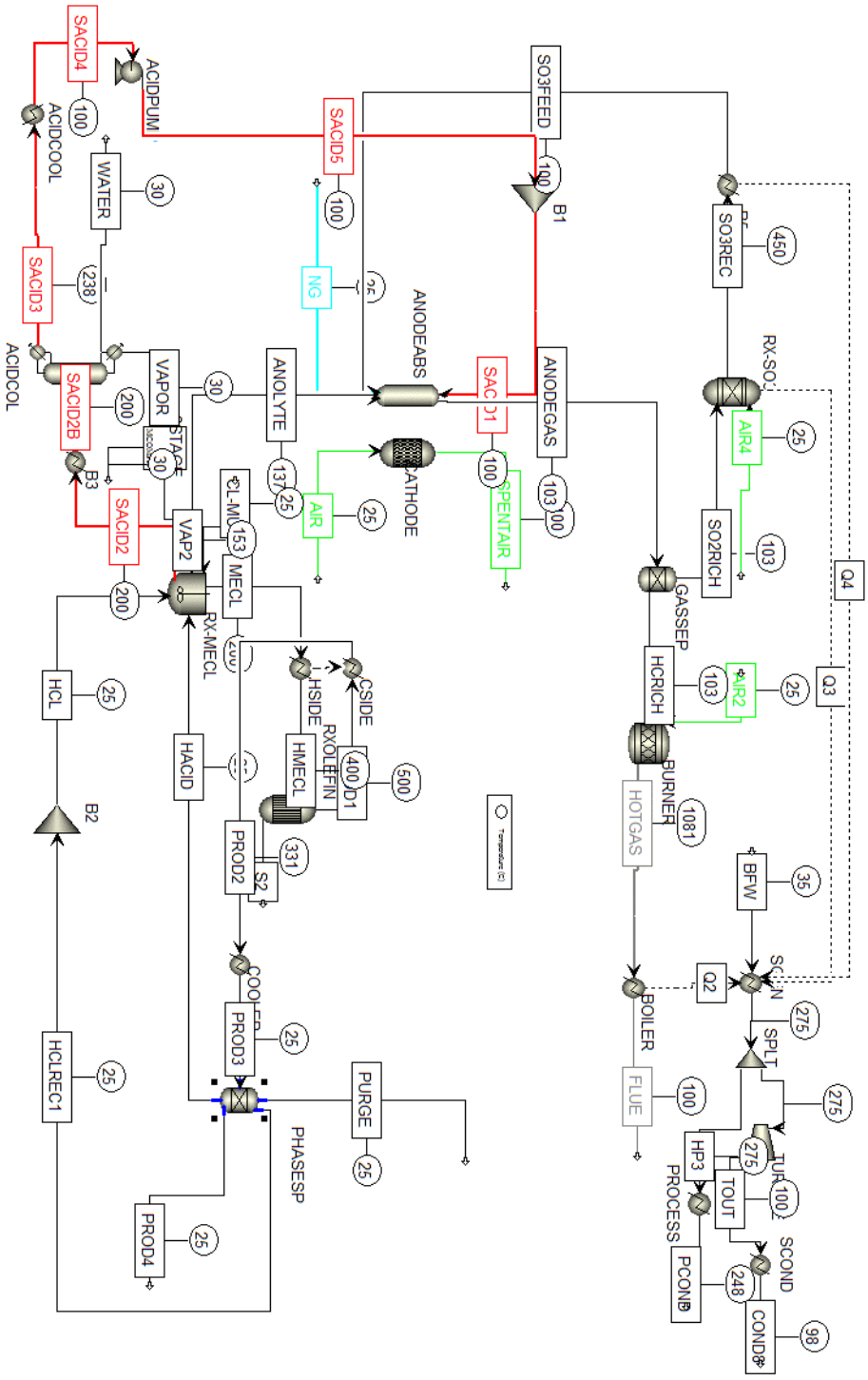

Figure C-16. Full process-flow diagram for methane gas-to-liquid conversion by electrochemical functionalization, conversion to methyl chloride, and upgrading to 1-octene.

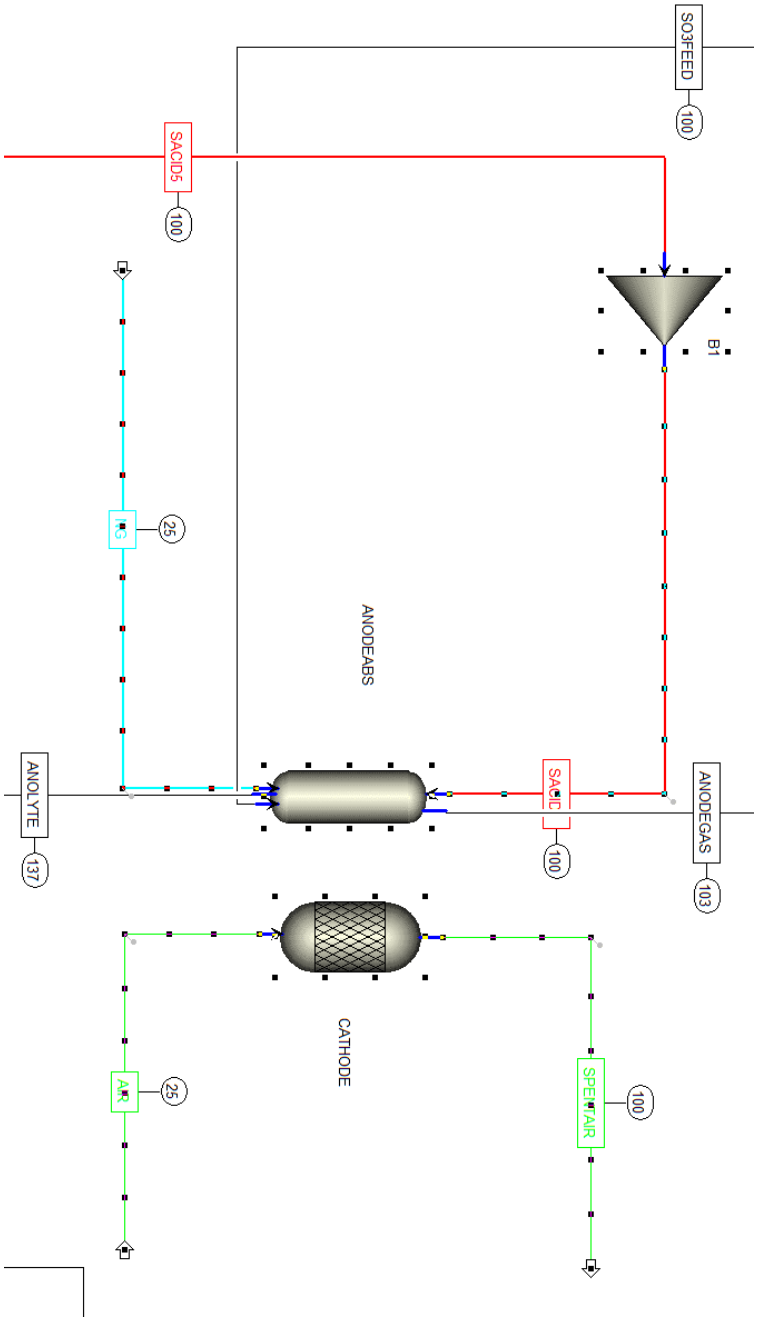

Figure C-17. Process-flow diagram for methyl bisulfate conversion reactor from methyl chloride upgrading gas-to-liquid process.

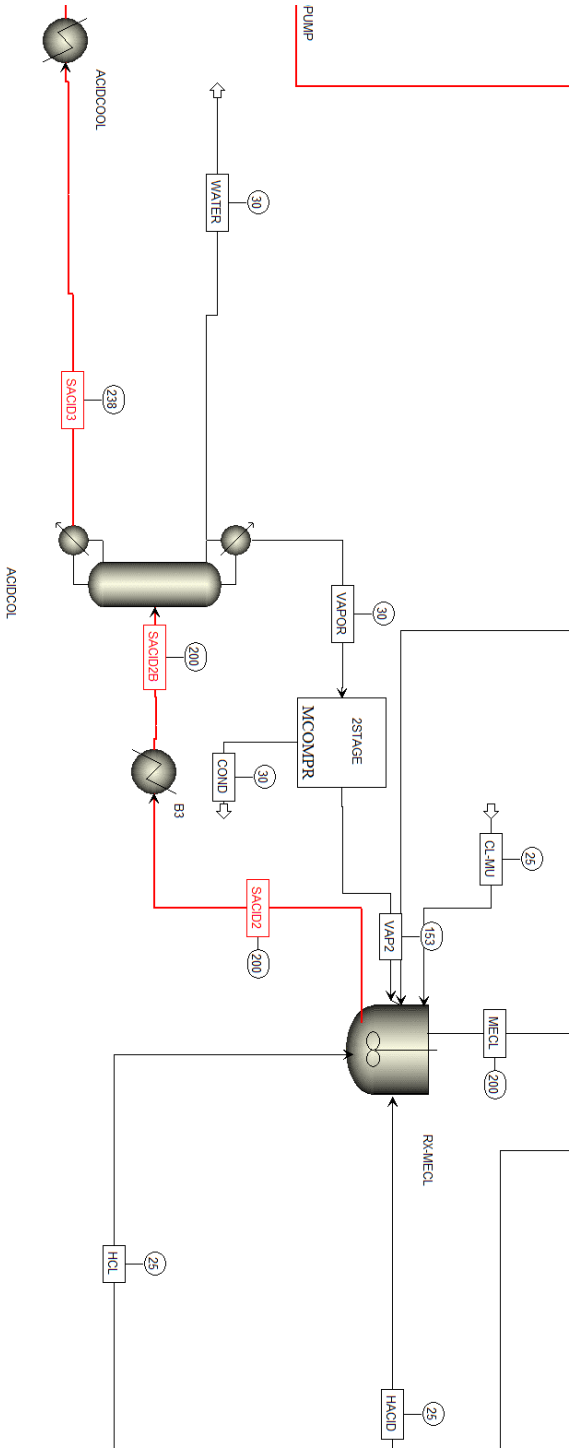

Figure C-18. Process-flow diagram for methyl chloride conversion reactor from methyl chloride upgrading gas-to-liquid process.

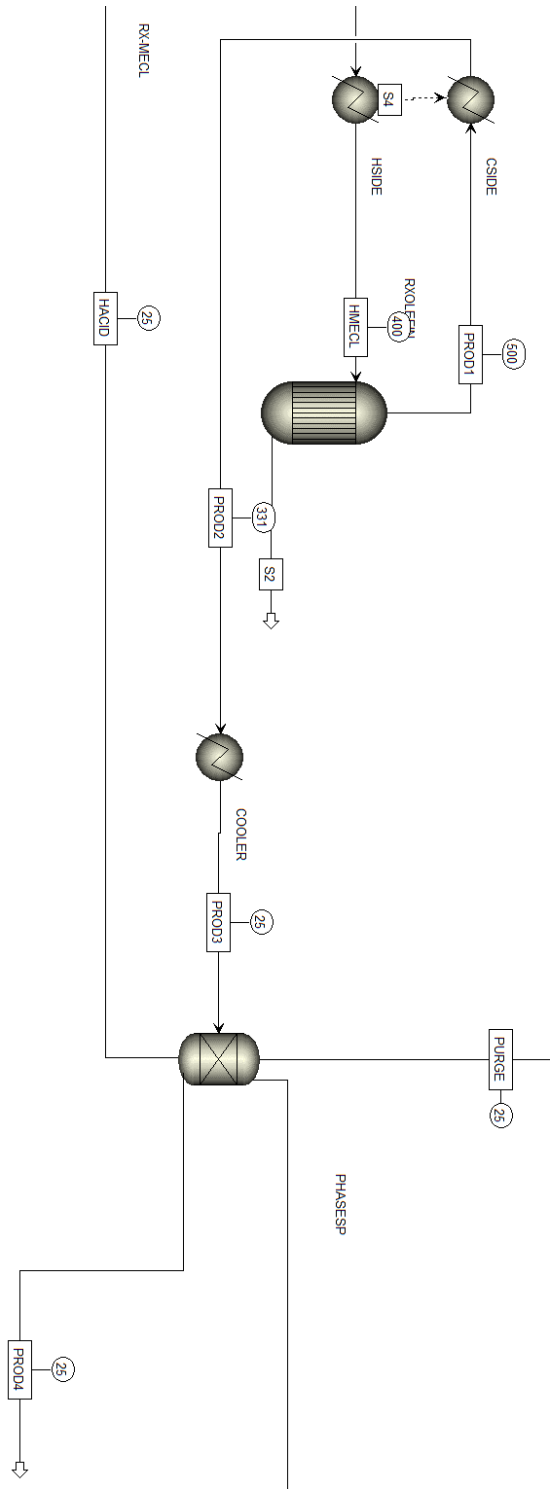

Figure C-19. Process-flow diagram for olefin conversion reactor from methyl chloride upgrading gas-to-liquid process.

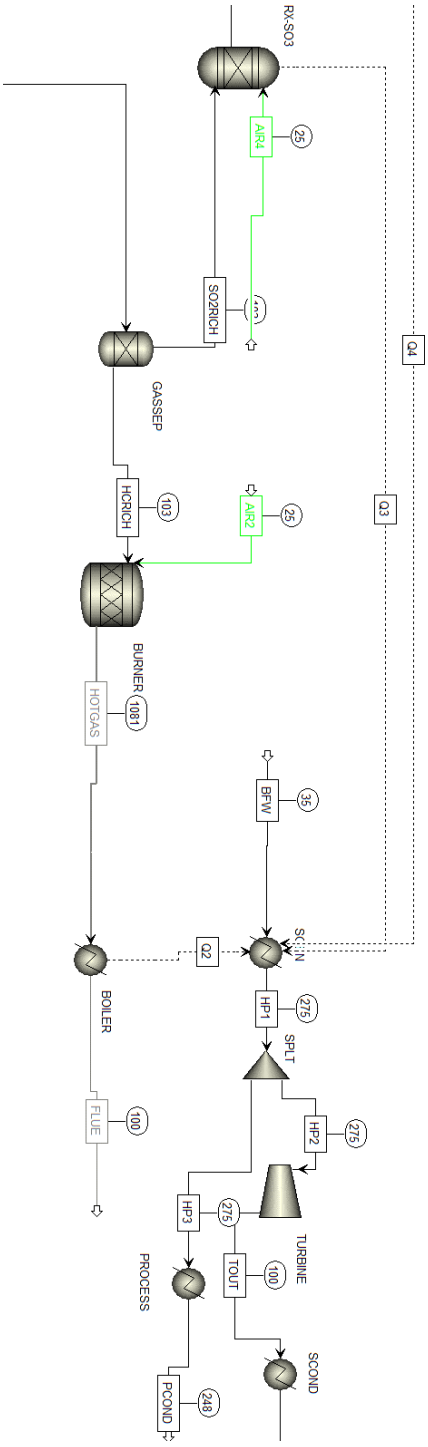

Figure C-20. Process-flow diagram for burners for methyl chloride upgrading gas-to-liquid process.

C.3 Stream Tables for Functionalized Methane Product Separations

C.3.1 Stream Table for Methyl Bisulfate Hydrolysis

[i] °C
[ii] Bar
[iii] $kmol \cdot h^{-1}$
[iv] $kg \cdot h^{-1}$
[v] $m^3 \cdot h^{-1}$
[vi] MW

	ACID	ACID2	ACID3	ACID4	ACID5
Temperature[i]	25	250	50	224.9	50
Pressure[ii]	10	1	1	0.1	1
Vapor Fraction	0	0	0	0	0
Mole Flow[iii]	2775.516	261.068	261.068	2600	2600
Mass Flow[iv]	250000	22950.301	22950.301	228405.868	228405.868
Volume Flow[v]	140.002	14.961	12.754	145.508	126.922
Enthalpy[vi]	-586.854	-51.821	-54.322	-519.756	-540.728
H_2O	277.542	33.159	33.159	332.243	332.243
H_2SO_4	2497.974	227.905	227.905	2267.757	2267.757
CH_4					
SO_3		< 0.001	< 0.001		
SO_2		< 0.001	< 0.001		
O_2		< 0.001	< 0.001		
N_2		0.001	0.001		
MBS				trace	trace
MeOH				trace	trace
H_3O^+					
H_2S		trace	trace		
C_2H_6					
C_3H_8					
CO_2		0.002	0.002		
H_2SO_4	0.98	0.974	0.974	0.974	0.974
MBS				trace	trace

Table C.1. Stream table for methane gas-to-liquid conversion by electrochemical functionalization to methyl bisulfate and hydrolysis to methanol.

	AIR	AIR2	AIR3	AIR4	ANOLYTE
Temperature	25	25	25	35	150
Pressure	1	1	1	1	1
Vapor Fraction	1	1	1	1	0.184
Mole Flow	10000	10546.741	10	13.85	6142.925
Mass Flow	288105.44	303857.356	288.105	411.792	284002.63
Volume Flow	247778.635	261325.718	247.779	353.73	39860.656
Enthalpy	-0.019	-0.02	$>$ -0.001	-0.223	-571.41
H_2O				0.016	277.542
H_2SO_4					1409.613
CH_4				0.111	586.041
SO_3					
SO_2				0.043	83.72
O_2	2000	2109.348	2	1.948	
N_2	8000	8437.393	8	7.864	13.953
MBS				trace	1004.641
MeOH				3.834	
H_3O^+					2511.603
H_2S				0.002	4.651
C_2H_6				0.001	55.813
C_3H_8				$<$ 0.001	18.604
CO_2				0.032	176.742
H_2SO_4					0.552
MBS				trace	0.397

Table C.1. Stream table for methane gas-to-liquid conversion by electrochemical functionalization to methyl bisulfate and hydrolysis to methanol.

	ANOLYTE2	ANOLYTE3	ANOLYTE4	DIL-ACID	DILUTE	GASES
Temperature	150	150	35	163.1	129.9	150
Pressure	1	1	1	1	1	1
Vapor Fraction	0.341	0	0	0	0.11	1
Mole Flow	3631.322	2528.884	2528.884	7658.938	8528.884	1102.438
Mass Flow	281472.466	239182.633	239182.633	319544.044	347274.313	42289.833
Volume Flow	43562.301	158.767	144.733	220.327	31458.859	38692.705
Enthalpy	-570.433	-505.805	-518.857	-945.558	-995.259	-68.221
H_2O	277.542	260.627	260.627	5391.181	5534.764	16.915
H_2SO_4	1409.613	1409.329	1409.329	2267.757	2135.192	0.283
CH_4	586.041	0.111	0.111	trace	0.111	585.93
SO_3						
SO_2	83.72	0.351	0.351	trace	0.351	83.369
O_2						
N_2	13.953	< 0.001	< 0.001	trace	< 0.001	13.953
MBS	1004.641	858.427	858.427	trace	132.565	146.214
MeOH				trace	725.863	
H_3O^+						
H_2S	4.651	0.003	0.003	trace	0.003	4.648
C_2H_6	55.813	0.001	0.001	trace	0.001	55.813
C_3H_8	18.604	< 0.001	< 0.001	trace	< 0.001	18.604
CO_2	176.742	0.033	0.033	trace	0.033	176.709
H_2SO_4	0.574	0.578	0.578	0.696	0.652	
MBS	0.4	0.402	0.402	trace	0.043	0.388

Table C.1. Stream table for methane gas-to-liquid conversion by electrochemical functionalization to methyl bisulfate and hydrolysis to methanol.

	LIQ2	MEOH	MEOH2	MEOH3	NATGAS	OFFGAS
Temperature	100	58.5	35	33.2	25	100
Pressure	1	1	1	1	10	1
Vapor Fraction	0	0	0	0	1	1
Mole Flow	1107.615	869.946	869.946	866.096	1860.447	11399.059
Mass Flow	43865.07	27730.269	27730.269	27606.583	34004.012	323608.627
Volume Flow	29.127	36.82	35.447	35.191	4513.104	353403.165
Enthalpy	-133.922	-56.964	-57.542	-57.319	-46.789	-210.435
H_2O	808.962	11.019	11.019	11.004		1474.834
H_2SO_4	298.647	trace	trace			< 0.001
CH_4		0.111	0.111	< 0.001	1674.402	
SO_3	trace					trace
SO_2	0.001	0.351	0.351	0.309		6.653
O_2	< 0.001			0.052		378.095
N_2	0.002	< 0.001	< 0.001	0.136	13.953	8459.209
MBS		trace	trace	trace		
MeOH		858.427	858.427	854.594		
H_3O^+						
H_2S	trace	0.003	0.003	0.001	4.651	trace
C_2H_6		0.001	0.001	trace	55.813	
C_3H_8		< 0.001	< 0.001	trace	18.604	
CO_2	0.004	0.033	0.033	0.001	93.022	1080.268
H_2SO_4	0.668	0	0	0		
MBS		trace	trace	trace		

Table C.1. Stream table for methane gas-to-liquid conversion by electrochemical functionalization to methyl bisulfate and hydrolysis to methanol.

	PROTONS	SO3	SPENTAIR	VAP1	WATER	WATREC
Temperature	150	450	150	250	25	45.8
Pressure	1	1	1	1	1	0.1
Vapor Fraction	0	1	1	1	0	0
Mole Flow	2511.603	11853.825	10627.901	12511.055	6000	5058.938
Mass Flow	2530.164	346558.981	290636.986	367473.75	108091.68	91138.176
Volume Flow	< 0.001	712786.597	373827.67	544001.672	108.399	92.067
Enthalpy	0	-215.349	-73.363	-306.666	-476.378	-399.471
H_2O		1701.691	1255.802	2288.176	6000	5058.938
H_2SO_4		34.207		294.268		trace
CH_4						
SO_3		193.698		4.38		
SO_2		6.653		6.654		
O_2		378.095	1372.099	378.095		
N_2		8459.21	8000	8459.211		
MBS						trace
MeOH						trace
H_3O^+	2511.603					
H_2S		trace		trace		
C_2H_6						
C_3H_8						
CO_2		1080.27		1080.272		
H_2SO_4	0				0	0
MBS						trace

Table C.1. Stream table for methane gas-to-liquid conversion by electrochemical functionalization to methyl bisulfate and hydrolysis to methanol.

C.3.2 Stream Table for Methyl Chloride Hydrolysis

[vii] °C
[viii] Bar
[ix] $kmol \cdot h^{-1}$
[x] $kg \cdot h^{-1}$
[xi] $m^3 \cdot h^{-1}$
[xii] $Gcal \cdot h^{-1}$

	AIR	AIR2	AIR4	ANODEGAS	ANOLYTE
Temperature[vii]	25	25	25	103.2	136.8
Pressure[viii]	1	1	2	2	2
Vapor Fraction	1	1	1	1	0
Mole Flow[ix]	5000	12891.84	2959.948	7328.602	3750.422
Mass Flow[x]	144052.72	371420.932	85277.719	236417.652	305485.765
Volume Flow[xi]	123889.252	319432.091	36653.997	114449.316	210.847
Enthalpy[xii]	-0.008	-0.021	-0.009	-134.451	-580.825
H_2O				448	648.497
H_2SO_4				0.102	1470.446
CH_4				716.213	0.09
SO_3				trace	trace
SO_2				1076.345	0.7
O_2	1000	2578.368	591.99	80.991	0.001
N_2	4000	10313.472	2367.959	4763.766	0.024
MBS				17.524	1015.19
MeOH					
H_2S				4.649	0.002
CO_2				221.012	0.041
HSO_4^-					307.716
SO_4^{2-}					< 0.001
H_3O^+					307.716
MeCl				trace	trace
HCl				trace	trace
$S_2O_7^{2-}$				trace	trace
C2=					
C3=					
C4=					
C8=					
OCTANE					

Table C.2. Stream table for methane gas-to-liquid conversion by electrochemical functionalization, conversion to methyl chloride, and hydrolysis.

	BFW	CL-MU	COND	COND8	FLUE
Temperature	35	25	30	97.6	100
Pressure	40	5	0.447	1	1
Vapor Fraction	0	0	0	0	1
Mole Flow	13339.006	0.331	16.755	6669.503	16544.138
Mass Flow	240305.924	7.299	302.436	120152.962	463058.712
Volume Flow	241.309	0.008	0.304	125.181	513005.371
Enthalpy	-908.606	-0.02	-1.143	-446.875	-174.929
H_2O	13339.006	0.259	16.741	6669.503	1835.627
H_2SO_4					
CH_4			trace		
SO_3			trace		
SO_2			< 0.001		
O_2					1186.437
N_2					12695.355
MBS			0.003		
MeOH					
H_2S			trace		
CO_2			trace		826.719
HSO_4^-					
SO_4^{2-}					
H_3O^+					
MeCl			0.011		
HCl		0.072			
$S_2O_7^{2-}$					
C2=					
C3=					
C4=					
C8=					
OCTANE					

Table C.2. Stream table for methane gas-to-liquid conversion by electrochemical functionalization, conversion to methyl chloride, and upgrading to 1-octene.

	HACID	HCL	HCLREC1	HCRICH	HMECL
Temperature	25	25	25	103.2	400
Pressure	2	2	2	2	2
Vapor Fraction	0	1	1	1	1
Mole Flow	89.51	1011.846	1011.846	3652.298	1102.214
Mass Flow	2252.221	36947.19	36947.19	91637.78	53428.466
Volume Flow	1.812	12406.139	12406.139	57075.275	30773.363
Enthalpy	-5.852	-22.583	-22.583	-44.365	-20.781
H_2O	66.186	7.354	7.354	403.2	73.54
H_2SO_4	1.785				1.785
CH_4				716.213	0.09
SO_3	0.004				0.004
SO_2					0.7
O_2				40.495	0.001
N_2				2381.883	0.024
MBS	1.312				1.312
MeOH					
H_2S					0.002
CO_2				110.506	0.041
HSO_4^-					
SO_4^{2-}					
H_3O^+					
MeCl		13.565	13.565		1024.497
HCl	20.223	990.927	990.927		0.219
$S_2O_7^{2-}$	trace				trace
C2=					
C3=					
C4=					
C8=					
OCTANE					

Table C.2. Stream table for methane gas-to-liquid conversion by electrochemical functionalization, conversion to methyl chloride, and upgrading to 1-octene.

	HOTGAS	HP1	HP2	HP3	MECL	NG
Temperature	1081.4	275	275	275	200	25
Pressure	1	40	40	40	2	10
Vapor Fraction	1	1	1	1	1	1
Mole Flow	16544.138	13339.006	6669.503	6669.503	1102.214	1860.447
Mass Flow	463058.712	240305.924	120152.962	120152.962	53428.466	32699.198
Volume Flow	1863610	13107.538	6553.769	6553.769	21525.689	4522.332
Enthalpy	-44.385	-751.6	-375.8	-375.8	-23.857	-40.132
H_2O	1835.627	13339.006	6669.503	6669.503	73.54	
H_2SO_4					1.785	
CH_4					0.09	1748.82
SO_3					0.004	
SO_2					0.7	
O_2	1186.437				0.001	
N_2	12695.355				0.024	13.953
MBS					1.312	
MeOH						
H_2S					0.002	4.651
CO_2	826.719				0.041	93.022
HSO_4^-						
SO_4^{2-}						
H_3O^+						
MeCl					1024.497	
HCl					0.219	
$S_2O_7^{2-}$					trace	
C2=						
C3=						
C4=						
C8=						
OCTANE						

Table C.2. Stream table for methane gas-to-liquid conversion by electrochemical functionalization, conversion to methyl chloride, and upgrading to 1-octene.

	PCOND	PROD1	PROD2	PROD3	PROD4
Temperature	248.4	500	331.4	25	25
Pressure	40	2	2	2	2
Vapor Fraction	0	1	1	0.898	0
Mole Flow	6669.503	1228.58	1228.58	1228.58	126.366
Mass Flow	120152.962	53428.466	53428.466	53428.466	14180.213
Volume Flow	149.864	39459.778	30814.3	13528.154	19.951
Enthalpy	-427.685	-22.153	-25.229	-31.207	-3.722
H_2O	6669.503	73.54	73.54	73.54	
H_2SO_4		1.785	1.785	1.785	
CH_4		0.09	0.09	0.09	
SO_3		0.004	0.004	0.004	
SO_2		0.7	0.7	0.7	
O_2		0.001	0.001	0.001	
N_2		0.024	0.024	0.024	
MBS		1.312	1.312	1.312	
MeOH					
H_2S		0.002	0.002	0.002	
CO_2		0.041	0.041	0.041	
HSO_4^-					
SO_4^{2-}					
H_3O^+					
MeCl		13.565	13.565	13.565	
HCl		1011.15	1011.15	1011.15	
$S_2O_7^{2-}$		trace	trace	trace	
C2=		trace	trace	trace	
C3=		trace	trace	trace	
C4=		trace	trace	trace	
C8=		126.366	126.366	126.366	126.366
OCTANE					

Table C.2. Stream table for methane gas-to-liquid conversion by electrochemical functionalization, conversion to methyl chloride, and upgrading to 1-octene.

	PURGE	S2	SACID1	SACID2	SACID2B	SACID3
Temperature	25		100.2	200	200	238.2
Pressure	2	2	4	2	2	0.1
Vapor Fraction	1		0	0	0	0
Mole Flow	0.857	0	3098.073	3779.249	3779.249	3098.028
Mass Flow	48.841	0	279146.728	292654.755	292654.755	279142.736
Volume Flow	10.416	0	160.893	184.506	184.506	180.043
Enthalpy	-0.055		-558.584	-595.246	-595.246	-540.493
H_2O			0.954	99.082	959.281	308.665
H_2SO_4			2481.49	1928.968	2789.165	2789.165
CH_4	0.09			< 0.001	< 0.001	
SO_3			< 0.001	< 0.001	< 0.001	trace
SO_2	0.7			0.003	0.003	trace
O_2	0.001			trace	trace	trace
N_2	0.024			trace	trace	trace
MBS			0.197	4.186	4.186	0.197
MeOH						
H_2S	0.002			trace	trace	trace
CO_2	0.041			< 0.001	< 0.001	trace
HSO_4^-			307.715	860.195		
SO_4^{2-}			< 0.001	0.002		
H_3O^+			307.716	860.2		
MeCl			trace	26.613	26.613	trace
HCl				trace	trace	
$S_2O_7^{2-}$			< 0.001	< 0.001	< 0.001	< 0.001
C2=						
C3=						
C4=						
C8=						
OCTANE						

Table C.2. Stream table for methane gas-to-liquid conversion by electrochemical functionalization, conversion to methyl chloride, and upgrading to 1-octene.

	SACID4	SACID5	SO2RICH	SO3FEED	SO3REC
Temperature	100	100.2	103.2	100	450
Pressure	0.1	4	2	2	2
Vapor Fraction	0	0	1	1	1
Mole Flow	3098.028	3098.028	3676.304	6116.407	6116.411
Mass Flow	279142.736	279142.736	144779.872	230057.491	230057.591
Volume Flow	160.871	160.891	57368.645	94700.498	183923.179
Enthalpy	-558.596	-558.576	-90.087	-116.559	-97.801
H_2O	0.949	0.954	44.8	58.929	58.927
H_2SO_4	2481.449	2481.454	0.102	25.673	25.672
CH_4					trace
SO_3	< 0.001	< 0.001	trace	1028.419	1028.42
SO_2			1076.345	44.528	44.528
O_2			40.495	80.991	80.992
N_2			2381.883	4749.837	4749.842
MBS	0.197	0.197	17.524		trace
MeOH					trace
H_2S			4.649		trace
CO_2			110.506	128.03	128.03
HSO_4^-	307.716	307.711			
SO_4^{2-}	< 0.001	< 0.001			
H_3O^+	307.717	307.711			
MeCl	trace	trace	trace		trace
HCl			trace	trace	trace
$S_2O_7^{2-}$	< 0.001	< 0.001	trace	trace	trace
C2=					trace
C3=					trace
C4=					trace
C8=					trace
OCTANE					trace

Table C.2. Stream table for methane gas-to-liquid conversion by electrochemical functionalization, conversion to methyl chloride, and upgrading to 1-octene.

	SPENTAIR	TOUT	VAP2	VAPOR	WATER
Temperature	100	99.6	153.2	30	30
Pressure	1	1	2	0.1	0.1
Vapor Fraction	1	0.897	1	1	0
Mole Flow	5000	6669.503	29.355	46.109	635.111
Mass Flow	144052.72	120152.962	1390.79	1693.226	11818.785
Volume Flow	155121.097	182662	515.298	11607.593	11.743
Enthalpy	2.618	-388.504	-0.671	-1.677	-43.761
H_2O		6669.503	2.812	19.553	631.063
H_2SO_4					trace
CH_4			< 0.001	< 0.001	trace
SO_3			< 0.001	< 0.001	< 0.001
SO_2			0.002	0.002	< 0.001
O_2	1000		trace	trace	trace
N_2	4000		trace	trace	trace
MBS			trace	0.003	3.986
MeOH					
H_2S			trace	trace	trace
CO_2			< 0.001	< 0.001	trace
HSO_4^-					
SO_4^{2-}					
H_3O^+					
MeCl			26.541	26.551	0.061
HCl					
$S_2O_7^{2-}$			trace	trace	trace
C2=					
C3=					
C4=					
C8=					
OCTANE					

Table C.2. Stream table for methane gas-to-liquid conversion by electrochemical functionalization, conversion to methyl chloride, and upgrading to 1-octene.

	ANOLYTE4	WATER	DILUTE
Temperature	35	25	164.3
Pressure	1	1	1
Vapor Frac	0	0	0
Mole Flow	5480.746	12000	17480.746
Mass Flow	513771.714	216183.36	729955.074
Volume Flow	306.753	216.797	542.817
Enthalpy	-1131.257	-952.756	-2084.019
MBS	0.329		0.113
H_2O	555.08	12000	11783.805
H_2SO_4	3405.266		4176.541
CH_4	0.149		0.149
SO_2	12.869		12.869
N_2	0.001		0.001
MBS	1506.96		735.685
MeOH			771.275
H_2S	0.001		0.001
C_2H_6	0.007		0.007
C_3H_8	0.002		0.002
CO_2	0.41		0.41
H_2O	0.101	1	0.674
H_2SO_4	0.621	0	0.239
H_2SO_4	0.65	0	0.561
H_2SO_4	0.544	0	0.004

Table C.2. Stream table for methane gas-to-liquid conversion by electrochemical functionalization to methyl bisulfate and hydrolysis to methanol.

C.3.3 Stream Table for Methyl Chloride Upconversion

[xiii] °C
[xiv] Bar
[xv] $kmol \cdot h^{-1}$
[xvi] $kg \cdot h^{-1}$
[xvii] $m^3 \cdot h^{-1}$
[xviii] $Gcal \cdot h^{-1}$

	AIR	AIR2	AIR4	ANODEGAS	ANOLYTE
Temperature[xiii]	25	25	25	103.2	136.8
Pressure[xiv]	1	1	2	2	2
Vapor Fraction	1	1	1	1	0
Mole Flow[xv]	5000	12891.84	2959.948	7328.602	3750.422
Mass Flow[xvi]	144052.72	371420.932	85277.719	236417.652	305485.765
Volume Flow[xvii]	123889.252	319432.091	36653.997	114449.316	210.847
Enthalpy[xviii]	-0.008	-0.021	-0.009	-134.451	-580.825
H_2O				448	648.497
H_2SO_4				0.102	1470.446
CH_4				716.213	0.09
SO_3				trace	trace
SO_2				1076.345	0.7
O_2	1000	2578.368	591.99	80.991	0.001
N_2	4000	10313.472	2367.959	4763.766	0.024
MBS				17.524	1015.19
MeOH					
H_2S				4.649	0.002
CO_2				221.012	0.041
HSO_4^-					307.716
SO_4^{2-}					< 0.001
H_3O^+					307.716
MeCl				trace	trace
HCl				trace	trace
$S_2O_7^{2-}$				trace	trace
C2=					
C3=					
C4=					
C8=					
OCTANE					

Table C.3. Stream table for methane gas-to-liquid conversion by electrochemical functionalization, conversion to methyl chloride, and upgrading to 1-octene.

	BFW	CL-MU	COND	COND8	FLUE
Temperature	35	25	30	97.6	100
Pressure	40	5	0.447	1	1
Vapor Fraction	0	0	0	0	1
Mole Flow	13339.006	0.331	16.755	6669.503	16544.138
Mass Flow	240305.924	7.299	302.436	120152.962	463058.712
Volume Flow	241.309	0.008	0.304	125.181	513005.371
Enthalpy	-908.606	-0.02	-1.143	-446.875	-174.929
H_2O	13339.006	0.259	16.741	6669.503	1835.627
H_2SO_4					
CH_4			trace		
SO_3			trace		
SO_2			< 0.001		
O_2					1186.437
N_2					12695.355
MBS			0.003		
MeOH					
H_2S			trace		
CO_2			trace		826.719
HSO_4^-					
SO_4^{2-}					
H_3O^+					
MeCl			0.011		
HCl		0.072			
$S_2O_7^{2-}$					
C2=					
C3=					
C4=					
C8=					
OCTANE					

Table C.3. Stream table for methane gas-to-liquid conversion by electrochemical functionalization, conversion to methyl chloride, and upgrading to 1-octene.

	HACID	HCL	HCLREC1	HCRICH	HMECL
Temperature	25	25	25	103.2	400
Pressure	2	2	2	2	2
Vapor Fraction	0	1	1	1	1
Mole Flow	89.51	1011.846	1011.846	3652.298	1102.214
Mass Flow	2252.221	36947.19	36947.19	91637.78	53428.466
Volume Flow	1.812	12406.139	12406.139	57075.275	30773.363
Enthalpy	-5.852	-22.583	-22.583	-44.365	-20.781
H_2O	66.186	7.354	7.354	403.2	73.54
H_2SO_4	1.785				1.785
CH_4				716.213	0.09
SO_3	0.004				0.004
SO_2					0.7
O_2				40.495	0.001
N_2				2381.883	0.024
MBS	1.312				1.312
MeOH					
H_2S					0.002
CO_2				110.506	0.041
HSO_4^-					
SO_4^{2-}					
H_3O^+					
MeCl		13.565	13.565		1024.497
HCl	20.223	990.927	990.927		0.219
$S_2O_7^{2-}$	trace				trace
C2=					
C3=					
C4=					
C8=					
OCTANE					

Table C.3. Stream table for methane gas-to-liquid conversion by electrochemical functionalization, conversion to methyl chloride, and upgrading to 1-octene.

	HOTGAS	HP1	HP2	HP3	MECL	NG
Temperature	1081.4	275	275	275	200	25
Pressure	1	40	40	40	2	10
Vapor Fraction	1	1	1	1	1	1
Mole Flow	16544.138	13339.006	6669.503	6669.503	1102.214	1860.447
Mass Flow	463058.712	240305.924	120152.962	120152.962	53428.466	32699.198
Volume Flow	1863610	13107.538	6553.769	6553.769	21525.689	4522.332
Enthalpy	-44.385	-751.6	-375.8	-375.8	-23.857	-40.132
H_2O	1835.627	13339.006	6669.503	6669.503	73.54	
H_2SO_4					1.785	
CH_4					0.09	1748.82
SO_3					0.004	
SO_2					0.7	
O_2	1186.437				0.001	
N_2	12695.355				0.024	13.953
MBS					1.312	
MeOH						
H_2S					0.002	4.651
CO_2	826.719				0.041	93.022
HSO_4^-						
SO_4^{2-}						
H_3O^+						
MeCl					1024.497	
HCl					0.219	
$S_2O_7^{2-}$					trace	
C2=						
C3=						
C4=						
C8=						
OCTANE						

Table C.3. Stream table for methane gas-to-liquid conversion by electrochemical functionalization, conversion to methyl chloride, and upgrading to 1-octene.

	PCOND	PROD1	PROD2	PROD3	PROD4
Temperature	248.4	500	331.4	25	25
Pressure	40	2	2	2	2
Vapor Fraction	0	1	1	0.898	0
Mole Flow	6669.503	1228.58	1228.58	1228.58	126.366
Mass Flow	120152.962	53428.466	53428.466	53428.466	14180.213
Volume Flow	149.864	39459.778	30814.3	13528.154	19.951
Enthalpy	-427.685	-22.153	-25.229	-31.207	-3.722
H_2O	6669.503	73.54	73.54	73.54	
H_2SO_4		1.785	1.785	1.785	
CH_4		0.09	0.09	0.09	
SO_3		0.004	0.004	0.004	
SO_2		0.7	0.7	0.7	
O_2		0.001	0.001	0.001	
N_2		0.024	0.024	0.024	
MBS		1.312	1.312	1.312	
MeOH					
H_2S		0.002	0.002	0.002	
CO_2		0.041	0.041	0.041	
HSO_4^-					
SO_4^{2-}					
H_3O^+					
MeCl		13.565	13.565	13.565	
HCl		1011.15	1011.15	1011.15	
$S_2O_7^{2-}$		trace	trace	trace	
C2=		trace	trace	trace	
C3=		trace	trace	trace	
C4=		trace	trace	trace	
C8=		126.366	126.366	126.366	126.366
OCTANE					

Table C.3. Stream table for methane gas-to-liquid conversion by electrochemical functionalization, conversion to methyl chloride, and upgrading to 1-octene.

	PURGE	S2	SACID1	SACID2	SACID2B	SACID3
Temperature	25		100.2	200	200	238.2
Pressure	2	2	4	2	2	0.1
Vapor Fraction	1		0	0	0	0
Mole Flow	0.857	0	3098.073	3779.249	3779.249	3098.028
Mass Flow	48.841	0	279146.728	292654.755	292654.755	279142.736
Volume Flow	10.416	0	160.893	184.506	184.506	180.043
Enthalpy	-0.055		-558.584	-595.246	-595.246	-540.493
H_2O			0.954	99.082	959.281	308.665
H_2SO_4			2481.49	1928.968	2789.165	2789.165
CH_4	0.09			< 0.001	< 0.001	
SO_3			< 0.001	< 0.001	< 0.001	trace
SO_2	0.7			0.003	0.003	trace
O_2	0.001			trace	trace	trace
N_2	0.024			trace	trace	trace
MBS			0.197	4.186	4.186	0.197
MeOH						
H_2S	0.002			trace	trace	trace
CO_2	0.041			< 0.001	< 0.001	trace
HSO_4^-			307.715	860.195		
SO_4^{2-}			< 0.001	0.002		
H_3O^+			307.716	860.2		
MeCl			trace	26.613	26.613	trace
HCl				trace	trace	
$S_2O_7^{2-}$			< 0.001	< 0.001	< 0.001	< 0.001
C2=						
C3=						
C4=						
C8=						
OCTANE						

Table C.3. Stream table for methane gas-to-liquid conversion by electrochemical functionalization, conversion to methyl chloride, and upgrading to 1-octene.

	SACID4	SACID5	SO2RICH	SO3FEED	SO3REC
Temperature	100	100.2	103.2	100	450
Pressure	0.1	4	2	2	2
Vapor Fraction	0	0	1	1	1
Mole Flow	3098.028	3098.028	3676.304	6116.407	6116.411
Mass Flow	279142.736	279142.736	144779.872	230057.491	230057.591
Volume Flow	160.871	160.891	57368.645	94700.498	183923.179
Enthalpy	-558.596	-558.576	-90.087	-116.559	-97.801
H_2O	0.949	0.954	44.8	58.929	58.927
H_2SO_4	2481.449	2481.454	0.102	25.673	25.672
CH_4					trace
SO_3	< 0.001	< 0.001	trace	1028.419	1028.42
SO_2			1076.345	44.528	44.528
O_2			40.495	80.991	80.992
N_2			2381.883	4749.837	4749.842
MBS	0.197	0.197	17.524		trace
MeOH					trace
H_2S			4.649		trace
CO_2			110.506	128.03	128.03
HSO_4^-	307.716	307.711			
SO_4^{2-}	< 0.001	< 0.001			
H_3O^+	307.717	307.711			
MeCl	trace	trace	trace		trace
HCl			trace	trace	trace
$S_2O_7^{2-}$	< 0.001	< 0.001	trace	trace	trace
C2=					trace
C3=					trace
C4=					trace
C8=					trace
OCTANE					trace

Table C.3. Stream table for methane gas-to-liquid conversion by electrochemical functionalization, conversion to methyl chloride, and upgrading to 1-octene.

	SPENTAIR	TOUT	VAP2	VAPOR	WATER
Temperature	100	99.6	153.2	30	30
Pressure	1	1	2	0.1	0.1
Vapor Fraction	1	0.897	1	1	0
Mole Flow	5000	6669.503	29.355	46.109	635.111
Mass Flow	144052.72	120152.962	1390.79	1693.226	11818.785
Volume Flow	155121.097	182662	515.298	11607.593	11.743
Enthalpy	2.618	-388.504	-0.671	-1.677	-43.761
H_2O		6669.503	2.812	19.553	631.063
H_2SO_4					trace
CH_4			< 0.001	< 0.001	trace
SO_3			< 0.001	< 0.001	< 0.001
SO_2			0.002	0.002	< 0.001
O_2	1000		trace	trace	trace
N_2	4000		trace	trace	trace
MBS			trace	0.003	3.986
MeOH					
H_2S			trace	trace	trace
CO_2			< 0.001	< 0.001	trace
HSO_4^-					
SO_4^{2-}					
H_3O^+					
MeCl			26.541	26.551	0.061
HCl					
$S_2O_7^{2-}$			trace	trace	trace
C2=					
C3=					
C4=					
C8=					
OCTANE					

Table C.3. Stream table for methane gas-to-liquid conversion by electrochemical functionalization, conversion to methyl chloride, and upgrading to 1-octene.